UNIVERSIDAD POLITÉCNICA DE MADRID

ESCUELA TÉCNICA SUPERIOR DE
INGENIEROS DE CAMINOS, CANALES Y PUERTOS

Computational Micromechanics Models for Damage and Fracture of Fiber-Reinforced Polymers

TESIS DOCTORAL

MIGUEL HERRÁEZ MATESANZ

Ingeniero Industrial

2018

Departamento de Ciencia de Materiales

Escuela Técnica Superior de Ingenieros de
Caminos, Canales y Puertos

Universidad Politécnica de Madrid

Computational Micromechanics Models for Damage and Fracture of Fiber-Reinforced Polymers

TESIS DOCTORAL

Miguel Herráez Matesanz

Ingeniero Industrial

Directores de Tesis:

Carlos Daniel González Martínez

Dr. Ingeniero de Caminos, Canales y Puertos

Cláudio Saúl Faria Lopes

Dr. Ingeniero Aeroespacial

2018

A Ana,
a mis padres,
y a mi hermano

Agradecimientos

Quiero aprovechar estos párrafos no solo para agradecer, sino también para despedirme y dejar atrás esta etapa tan importante de mi vida que ha sido trabajar realizando la tesis doctoral en IMDEA Materiales.

Esta historia comienza a mediados de 2013. En ese momento disfrutaba de una beca en Airbus Military en Getafe (Madrid). El contrato terminaría unos meses más tarde y yo no tenía nada claro qué hacer con mi futuro. Recapitulando, llegué a la conclusión de que lo que más me había gustado hasta entonces era estudiar y analizar problemas, en definitiva: aprender. Así que tras pedir consejo a mis antiguos directores del proyecto de fin de carrera, Ever Barbero (WVU) y Carlos Navarro (UC3M), decidí ponerme en contacto con Carlos González de IMDEA con intención de empezar el doctorado. A los pocos días, tuve una entrevista con Carlos y Cláudio. Y una semana más tarde nos reunimos con Javier Llorca para darme la oportunidad y comprometerme a llevar a cabo el doctorado en IMDEA Materiales durante los 4 años siguientes.

En primer lugar, deseo expresar mi agradecimiento a mis directores de tesis: Carlos González y Cláudio Lopes. Aunque suene tópico, insisto en reivindicar el inestimable papel que juega el director de una tesis en el desarrollo y elaboración de ésta. A lo largo de este período no solo han potenciado mi curiosidad hacia los problemas técnicos que he tratado en la tesis y hacia muchos otros, sino que han ayudado a convertirme en una persona más madura e independiente. Son los principales responsables de que haya disfrutado tanto de la investigación, y de que quiera seguir dedicándome a ello. Quiero también dar las gracias a Javier Llorca e Ignacio Romero por su gran ayuda y consejo a la hora de afrontar el futuro próximo.

En segundo lugar, quiero dar las gracias... (wait a second, some of them will not understand very much in Spanish). Secondly, I want to express my gratitude to all of the people at NASA Langley Research Center and the National Institute of Aeronautics (NIA) who made my stay there such an amazing and unforgettable time. Firstly, to Carlos Dávila and his whole family, especially to Maritza, who made me feel like at home much more than they would ever imagine in every single dinner or event. Of course, many thanks to Andrew Bergan as well, not only for the priceless talks and all of the lessons learned, but also for sharing such wonderful times (carving pumpkins, "trick-or-treating" in Halloween...), who together with his wife Kelsey, made me enjoy and build up great memories. I would also like to express my gratitude to Frank Leone and his family, as well as Nelson Carvalho for the funny moments during the football games at lunch time. I would like to acknowledge again my advisors, Carlos and Cláudio, who made this dream come true: working at NASA!

(Back to Spanish...) Gracias a mis padres, en especial a mi madre por acordarse y preocuparse por mí en todo momento (no solo por el "táper" de comida que diariamente me ha preparado durante los últimos 18 años).

Ana. No sabría por dónde empezar... Espero no haberte desesperado demasiado durante estos últimos años, en los que no te he dedicado todo el tiempo que te mereces. Y a pesar de ello, siempre has estado ahí, comprensiva y paciente. ¡Muchas gracias! Deseo que lo que esté por llegar nos permita disfrutar un poco más del tiempo juntos.

Quiero agradecer a todo IMDEA Materiales la confianza, gratitud y amabilidad que me ha mostrado desde el primer día que puse un pie en Tecnogetafe. Primeramente quiero acordarme y agradecer todo el apoyo, no solo científico-técnico, sino también moral (e incluso psicológico), de los miembros del grupo que fueron, han sido y son: Raúl, Sergio, Diego M., Quim, Paqui, Fernando, Álex, Mohammad, Juanjo T., Olben, Jian Xu, Jaime, Peyman, Momchil, Sandip, Andrea F., Théo, Wilko, Bas, Jerome, Diego G., Joseba, Carlos Gamir, Héctor, Yunfu, Abrar, Mostafa, María A., Virginia, André, Joshua, Cristina e Iker. No puedo olvidarme de la inestimable ayuda y consejo de todos los técnicos que han sido y son: José Luis, Vanesa, Juan Carlos R., David, Víctor, Marcos A., Miguel de la Cruz, Miguel C., Pepe, Fernando y Ángel. Y aunque estrictamente no forman parte del equipo de técnicos, su soporte (cada uno a su manera) ha permitido que esta tesis, al igual que todas las demás en IMDEA, llegue a buen término: muchas gracias Raúl y Nico.

Lo que viene a continuación quizás sea lo más complicado. Han sido muchos años, pero muchísimas más han sido las personas, compañer@s y amig@s con los que he tenido la suerte de coincidir y compartir tantos y tan buenos momentos dentro y fuera de IMDEA (cafés, cenas, partidos de fútbol y otras celebraciones). En especial quiero mencionar a Andrea G., Almudena, Marta, Paqui, Laura, Elena, Anna y María B. Y aunque no puedo mencionar a todos los demás (Juan Pedro, Miguel M., Sarra, Soundes, Eva, Bárbara, Gustavo, Juan Carlos F., Carmen, Verónica, Elisa, Pablo G., Pablo A., Cristina G., Sergio L., Rudi, Arturo, Alfonso, Hugo, Xaquín, Miguel V., Marcos C., Álex R., Ángel A., Daniel P., Marcos J., Evgeny, Belén, Carmen C., Pablo R., Luis H., Alberto P., Raúl S., Hangbo, Tomeu, Jeromy, Irene, Gema, Paco, Álvaro, José, Deng, Na Li, Jingya, Chuanyun, Lu Zhang, Can Fu, Xiaolin, Ignacio, Javier Ll., Roberto, Jon, Javier S., Ilchat, Srdjan, Rubén, Teresa, Juanjo V., Fede, Damien), muchas gracias a todos.

El lunes 14 de octubre de 2013 entré en IMDEA como estudiante de doctorado. En pie, junto a mi mesa, miré alrededor. Vi muchas caras, todas nuevas evidentemente. Hoy vuelvo a hacer lo mismo, y, aunque parece que el tiempo no ha pasado, ahora no encuentro una sola de aquellas caras que vi entonces. Sé lo que eso significa. Lo he visto muchas veces, aunque en todas ellas yo era un simple espectador. Pero hoy no. Es la hora, es tiempo de terminar: defender la tesis y despedirse.

Hasta siempre Imdea

Miguel Herráez Matesanz
Madrid, Mayo de 2018

Resumen

En la actualidad, el empleo de materiales compuestos poliméricos reforzados con fibras (FRP) se ha intensificado en aplicaciones que requieren materiales con altas propiedades específicas. Numerosos modelos constitutivos fenomenológicos y con base física han sido propuestos en la literatura para predecir la respuesta mecánica de láminas unidireccionales de estos materiales. No obstante, los parámetros requeridos por dichos modelos hacen necesaria la ejecución de extensas y costosas campañas experimentales. Es por esto que los ensayos virtuales de materiales compuestos aparecen como una alternativa prometedora para reducir los programas experimentales dedicados a la caracterización mecánica de los mismos. Además, dado que el fallo de los FRPs está controlado por fenómenos que tienen su origen a escala microscópica, es fundamental adoptar una estrategia basada en la multiescala, capaz de capturarlos mediante modelos micromecánicos.

Cabe destacar que esta tesis forma parte de la estrategia multiescala desarrollada por el Grupo de Materiales Compuestos del Instituto IMDEA Materiales durante los últimos años.

En esta tesis, se amplía la capacidad de la micromecánica computacional (CMM) para establecer predicciones virtuales de diferents procesos de fractura en compuestos unidireccionales reforzados con fibras con respecto al estado del arte. Para ello, las propiedades mecánicas de los constituyentes del material compuesto son determinadas mediante micromecánica experimental. A este respecto, se han desarrollado dos nuevas técnicas experimentales para la caracterización longitudinal de las fibras. La primera consiste en ensayos de tracción en fibras individuales a las que se les ha realizado una entalla para medir su tenacidad de fractura; mientras que la segunda técnica se basa en la compresión de micropilares tallados en la sección transversal de fibras con los que obtener su resistencia a compresión.

Se ha evaluado el efecto de la sección transversal de la fibra sobre la resistencia transversal de una lámina unidireccional mediante CMM, haciendo uso de elementos representativos de volumen (RVE) con condiciones de contorno periódicas (PBC). El despegue de la intercara fibra/matriz se representa a través de un modelo de zona cohesiva (CZM) con una ley de tracción-separación, mientras que un modelo elasto-plástico, dependiente de la presión hidrostática, que incluye daño por tracción y compresión se emplea para capturar el comportamiento no lineal de la matriz polimérica. El comportamiento mecánico de ambos constituyentes se calibra utilizando las propiedades obtenidas por medio de los ensayos micromecánicos mencionados anteriormente.

Aprovechando la estrategia CMM, se ha analizado el fenómeno de *kinking* de las fibras que tiene lugar cuando una lámina unidireccional es sometida a cargas de compresión en la dirección de las fibras. Un RVE de un apilamiento de láminas a $\pm 45°$ y un modelo 3-D con una sola fibra se han empleado conjuntamente para estimar la resistencia a compresión de una lámina unidireccional y compararla con las predicciones de la teoría de *kinking* de fibras (FKT). Adicionalmente, los resultados en régimen de post-fallo del modelo CMM han sido comparados con las predicciones de un modelo de daño continuo (CDM) para modelos de mesomecánica computacional desarrollado por Bergan and Leone (2016) del NASA Langley Research Center. Cabe destacar que el modelo CMM se ha empleado para predecir los parámetros de entrada requeridos por el modelo CDM.

En esta tesis, las capacidades de la micromecánica computacional se han ampliado desde la predicción de las propiedades elásticas y resistencias hasta la simulación de procesos de fractura en materiales compuestos. Para caracterizar la tenacidad de microestructuras heterogéneas, se ha desarrollado una estrategia original para el estudio de procesos de fractura en materiales quasi-frágiles. Este método se basa en la aplicación del campo de desaplazamientos alrededor de la punta de una grieta proporcionado por la mecánica de fractura elástica lineal (LEFM) en modo I. Esta técnica se aplica al análisis virtual de la propagación de una grieta intralaminar sometida a tracción mediante un modelo 2-D de celda embebida. El proceso de fractura es capturado con gran precisión, no sólo por la energía de fractura intralaminar, sino también por la forma característica de la curva de crecimiento de grieta (curva-R). A continuación, la respuesta a fractura de la microestructura es homogeneizada mediante una ley de ablandamiento equivalente, que puede ser empleada en modelos constitutivos en escalas superiores (mesomecánica computacional).

Todas las microestructuras han sido obtenidas numéricamente a partir de una metodología nueva y muy versátil que ha sido incluida en una interfaz de usuario desarrollada por el autor llamada `Viper`, acelerando la fase de pre-proceso en éste y futuros trabajos.

Abstract

Nowadays, fiber-reinforced polymers (FRP) are extensively used in applications where outstanding specific mechanical properties are required. Some phenomenological and physically-based failure models have been proposed in the literature to predict the mechanical performance of classical unidirectional composite plies. Unfortunately, their input parameters need to be obtained by means of costly and time-consuming experimental campaigns. For this reason, virtual testing of composite materials stands out as a promising strategy to reduce the experimental programs devoted to the characterization of these materials. Nevertheless, as failure of FRP is controlled by phenomena that take place at the microscale, there is a need to adopt a multiscale scheme which captures them by means of micromechanical models.

It must be highlighted that this thesis is embedded within the bottom-up multiscale approach developed by the Composite Materials Group of IMDEA Materials during the last years.

In this thesis, the potential of *computational micromechanics* (CMM) to make virtual predictions of some fracture processes in unidirectional fiber reinforced composites is extended with respect to the state of the art. To this end, the mechanical properties of the material constituents are determined through experimental micromechanics. In this regard, two novel experimental techniques devoted to the longitudinal characterization of the reinforcement fibers were developed. The first one consists of tensile testing single filaments of notched fibers to measure their fracture toughness; whereas, the second technique is based on the compression of micropillars milled on the cross section of individual fibers to obtain its compressive strength.

The effect of the fiber cross section on the transverse strength of a unidirectional ply was studied by means of CMM, making use of representative volume

elements (RVE) under periodic boundary conditions (PBC). Fiber/matrix interface debonding is represented by means of a cohesive zone model (CZM) with a traction-separation law, whereas a pressure dependent, elasto-plastic model that includes tensile and compressive damage is employed to capture the nonlinear behavior of the polymer matrix. The mechanical response of both constituents is calibrated using the properties obtained by the micromechanical tests mentioned previously.

Taking advantage of the CMM strategy, the fiber kinking phenomenon that takes place when a unidirectional ply is loaded under longitudinal compression was analyzed beyond the state of the art. An RVE of a $\pm 45°$ stacking of plies and a single-fiber 3-D model are combined to give an estimate of the compressive strength and are compared to the fiber kinking theory (FKT) predictions. In addition, the results of the post-peak response of the CMM model are compared to the predictions of a continuum damage model (CDM) for computational mesomechanics modeling developed by Bergan and Leone (2016) from NASA Langley Research Center. More importantly, the CMM model is also used to predict the input parameters for the CDM model.

In this thesis, the capabilities of computational micromechanics are extended from the prediction of elastic and strength properties to the simulation of fracture processes in composite materials. To characterize the toughness of composite microstructures, an original framework to study fracture processes in quasi-brittle materials was developed. This approach is based on the linear elastic fracture mechanics (LEFM) solution of the displacement field around a crack tip under mode I loading. The methodology is applied to the virtual analysis of the intralaminar transverse crack propagation under tension by means of a 2-D embedded cell model. The fracture process is accurately characterized, not only by the intralaminar fracture energy, but also the shape of the crack resistance curve (R-curve). Afterwards, the fracture response of the microstructure is homogenized into an equivalent softening law, that may be used in higher scale constitutive models (computational mesomechanics).

All the microstructures employed in this thesis were obtained numerically from a novel and versatile algorithm. This was embedded in an in-house developed user-interface called `Viper`, thus, speeding up the pre-processing stage and making it available for other users.

Glossary of terms

In general, the superscripts ^{f}, ^{m}, ^{c} are referred to quantities of the fiber, matrix and fiber/matrix cohesive interface respectively. Whereas the subscripts $_t$, $_c$ indicate tensile and compressive quantities.

x_1	Longitudinal direction (parallel to the fibers)
x_2	Transverse direction
x_3	Through-the-thickness direction
ε	Strain tensor
$\Delta\varepsilon$	Strain increment tensor
$\tilde{\varepsilon}_t^{\mathrm{pl}}$, $\tilde{\varepsilon}_c^{\mathrm{pl}}$	Equivalent plastic strain under tension and compression
ε^0	Strain at damage initiation
ε^u	Strain at ultimate failure
σ	Nominal stress tensor
$\tilde{\sigma}$	Effective stress tensor
$\mathbf{S}$	Compliance tensor
$\mathbf{Q}$	Stiffness tensor
$\mathbf{C}_T$	Tangent constitutive tensor
$\mathbf{I}$	Identity tensor
$\mathbf{M}$	Damage evolution tensor
P	Load
H	Hardness
A_c	Contact area of indentation
E^m	Elastic modulus of the matrix
ν^m	Poisson ratio of the matrix
c^m	Cohesion parameter of the matrix (Drucker-Prager model)
ϕ^m	Internal friction angle of the matrix (Drucker-Prager model)
σ_t^m	Uniaxial tensile strength of the matrix
G_t^m	Fracture energy of the matrix under uniaxial tension

σ_{yc}^m	Uniaxial compressive yield strength of the matrix
σ_{uc}^m	Uniaxial ultimate compressive strength of the matrix
$D_t^m,\ D_c^m$	Damage variables under tension/compression of the matrix
ψ^m	Dilation angle of the material model of the matrix
ϵ^m	Eccentricity parameter of the material model of the matrix
$\sigma_{b_0}/\sigma_{c_0}$	Biaxial to uniaxial compressive ratio of the material model of the matrix
K_c^m	Tensile and compressive meridian yield condition ratio of the matrix
μ^m	Viscosity of the material model of the matrix
α^m	Coefficient of thermal expansion of the matrix
N^c	Normal tensile strength of the interface
S^c	Shear strength of the interface
$G_n^c,\ G_s^c$	Fracture energies under modes I and II of the interface
μ^c	Friction coefficient of the interface
$t_n,\ \delta_n$	Normal cohesive traction and displacement jump
$t_s,\ \delta_s$	Longitudinal shear cohesive traction and displacement jump
δ_0	Separation at damage initiation
δ_u	Separation at ultimate failure
k_{nn}^c	Penalty stiffness in the normal direction of the interface
k_{ss}^c	Penalty stiffness in the shear direction of the interface
η_{BK}^c	Benzeggagh-Kenane power exponent of the interface
D^c	Damage variable of the interface
V_f	Fiber volume fraction
E_1^f	Longitudinal elastic modulus of the fiber
E_1^{0f}	Initial longitudinal elastic modulus of the fiber of the nonlinear model
c_f	Nonlinear parameter of the longitudinal elastic modulus
E_2^f	Transverse elastic modulus of the fiber
G_{12}^f	Longitudinal shear modulus of the fiber
G_{23}^f	In-plane shear modulus of the fiber

ν_{12}^f	Longitudinal Poisson ratio of the fiber
ν_{23}^f	In-plane Poisson ratio of the fiber
$X_t^f,\ G_t^f$	Strength and fracture energy under longitudinal tension of the fiber
$X_c^f,\ G_c^f$	Strength and fracture energy under longitudinal compression of the fiber
α_1^f	Coefficient of thermal expansion in the longitudinal direction of the fiber
α_2^f	Coefficient of thermal expansion in the transverse direction of the fiber
d	Fiber diameter (circumscribed diameter of non-circular fibers)
d_{eff}	Equivalent fiber diameter (non-circular fibers)
d_v	Diameter of the channels or "islands" of hollow fibers
I_x^f	Second moment of inertia of the cross section of the fiber
n_l	Number of lobes of a lobular fiber
n_e	Number of edges of a polygonal fiber
χ	Smoothing ratio of a smooth polygonal fiber
ξ	Hollowness ratio of a C-shaped fiber
θ	Angular amplitude of a C-shaped fiber
L_0	Reference length in the Weibull distribution for fiber strength
σ_0	Weibull strength
m	Weibull shape parameter
F	Weibull cumulative density function (cdf)
a	Crack length
a_0	Initial crack length
Δa	Crack propagation length
K_{I}	Stress intensity factor under mode I
K_{IC}	Critical stress intensity factor under mode I
K_{IC}^f	Mode I fracture toughness of the fiber
σ_∞	Remote stress
Y	Non-dimensional stress intensity factor
G_{I}	Energy release rate under Mode I

G_{IC}^{f}	Critical energy release rate under Mode I of the fiber
W	Elastic strain energy density
$\vec{t}$	Traction vector
$\vec{u}$	Displacement vector
Γ	J-integral contour
E^{*}	Effective elastic modulus
l_p	Plastic process zone length
ρ	Volumetric density
λ	Linear density
$d_p,\ h_p$	Micropillar diameter and height
θ_p	Taper angle of the micropillar
$\dot{\varepsilon}$	Strain rate
σ_c	Compressive stress
ε_c	Compressive strain
k_0	Linear elastic stiffness during the micropillar compression test
$\tilde{\delta}$	Tolerance minimum distance between adjacent fibers
A_i	Cross section area of fiber i
A_{ij}	Overlapping cross sectional area of fibers i and j
Υ	Potential defined to evaluate fiber overlapping
t_{exec}	Execution time
V_f^{loc}	Local fiber volume fraction
s_r	Sampling radius
$P(x,y)$	Sampling point with coordinates (x,y)
c_v	Coefficient of variation of the Voronoi cells area
A_i^{v}	Voronoi cell area of fiber i
$\delta_1,\ \delta_2$	Distance to the first and second nearest neighbors
θ_1	Orientation of the first nearest neighbor
$g(r)$	Radial distribution function

$K(r)$	Second-order intensity function
$\boldsymbol{x}$	Position vector
$S_2(\boldsymbol{x})$	Two-point probability function
$S_2^{ij}(\boldsymbol{x_A}, \boldsymbol{x_B})$	General two-point probability function
$\mathrm{D}^i(\alpha)$	Domain covered by phase i of sample $alpha$
$\chi^i(\boldsymbol{x_A}, \alpha)$	Characteristic function
Ω	Area of the sample
W, H	Dimensions in pixels of a bitmap of the microstructure
N_a	Number of fibers per unit area
$\hat{I}_i(r)$	Indicator function
$\hat{K}_{\mathrm{ref}}(r)$	Second-order intensity function of a CSR dispersion
$\hat{L}(r)$	Besag's function
ΔT	Temperature drop during the cool down process
$\overrightarrow{U_k}$	Displacement of master node k
u_i	Displacement in the i direction
l^*	Characteristic element length
$E_{11},\ E_{22}$	Longitudinal and transverse elastic modulus of the ply
$\nu_{12},\ \nu_{23}$	Longitudinal and transverse Poisson ratio of the ply
$G_{12},\ G_{23}$	Longitudinal and transverse shear modulus of the ply
$\kappa,\ \mu$	Parameters for the small scale bridging analytical model
G_{2+}	Intralaminar tensile fracture energy
l_c	Characteristic length of the fracture process zone (FPZ)
w_c	Critical separation of a cohesive law
$R(\Delta a)$	Resistance curve (R-curve)
φ_0	Initial fiber misalignment
φ	Fiber rotation
$\varphi^{\max},\ \varphi^{\mathrm{avg}}$	Maximum and average fiber rotation of the single-fiber CMM model
w_{kb}	Width of the kink band

ω_{kb}	Relative kink band size
$\alpha,\ \eta$	Parameters of a Ramberg-Osgood nonlinear curve (Ch. 6)
τ_Y	Shear yield limit of a perfectly-plastic constitutive model
τ_L	Shear yield limit assumed for a nonlinear constitutive model
σ_r	Residual crushing stress during fiber kinking
β	Angle of the kink band
J_2	Second invariant of the stress tensor
f_{CL}	Constitutive law relating shear strain to shear stress
γ^c	Shear strain to failure upon fiber kinking
E_1^*	Longitudinal elastic modulus of the ply (nonlinear model)
c_l	Parameter of the nonlinear longitudinal elastic modulus model
α_R	Coefficient of Rayleigh damping
τ_μ	Frictional shear stress at the interface
D	Damage variable
$F_{1+},\ F_{1-}$	Damage activation functions under longitudinal tension and compression
$\phi_{1+},\ \phi_{1-}$	Loading functions under longitudinal tension and compression
$r_{1+},\ r_{1-}$	Elastic domain thresholds under longitudinal tension and compression

List of acronyms

FRP	Fiber reinforced polymer
CFRP	Carbon fiber reinforced polymer
CDM	Continuum damage mechanics
CMM	Computational micromechanics
CMG	Composite Materials Group (IMDEA Materials)
ICME	Integrated computational materials engineering
UD	Unidirectional
FE	Finite element
RVE	Representative volume element
PBC	Periodic boundary conditions
MN	Master node
ROI	Region of interest
FIB	Focused Ion Beam
SEM	Scanning electron microscopy
AFM	Atomic force microscopy
SFT	Single-fiber test
LEFM	Linear elastic fracture mechanics
FPZ	Fracture process zone
PAN	Polyacrylonitrile
PE	Polyethylene
RSA	Random sequential adsorption
HCM	Hard-core model
NNA	Nearest-neighbor algorithm
CSR	Complete spatial random
PDF	Probability density function
CDF	Cumulative density function
DFT	Discrete Fourier transform

IDFT	Inverse of the discrete Fourier transform
FFT	Fast Fourier transform
ILSS	Interlaminar shear strength
BK	Benzeggagh-Kenane
ISS	Interface shear stress (t_s)
INS	Interface normal stress (t_n)
INS$^+$	Interface normal tensile stress
INS$^-$	Interface normal compressive stress
SENT	Single-edge notched test
FPM	Field projection method
FKT	Fiber kinking theory
UMAT	User material subroutine in Abaqus/Standard
VUMAT	User material subroutine in Abaqus/Explicit
DGD	Deformation gradient decomposition
ASTM	American Society for Testing and Materials
EPP	Elastic perfectly-plastic

"You know, life is difficult".
Fernando Naya (2015)

Contents

Introduction and objectives 1

In the present state of technological development, small diameter fibers as carbon, glass, aramid or polyethylene, stand among the strongest man made materials and their applications as reinforcement in composites have specially grown in lightweight applications due to their excellent strength and stiffness to weight ratio. Fibers are normally embedded in a matrix made of metal, ceramic or polymer, which plays the role to maintain the fibers adequately oriented according to specific design directions while providing them with an effective protection in harsh environments.

Fiber-reinforced polymers, or FRPs, are preferred candidates in structural applications where the strength to weight ratio leads the structural design process. One of the main drawbacks regarding the use of these materials is their complex mechanical behaviour, hardly predictable, which depends on the properties of the constituents (fibers, matrix and interfaces) as well as on their spatial distribution within the material. Manufacturing conditions also play an important role and are responsible for the generation of defects in the form of voids, interface debonding, resin pockets or dry fiber areas which are considered detrimental for the final performance of the material. The mechanical response of FRPs is, obviously, strongly influenced by the mechanical properties of the high performance fibers used (carbon, glass, aramid, etc.) albeit their spatial distribution, tow architecture and cross section governs the basic deformation and failure mechanisms (González and Llorca, 2007a).

1.1 Composite materials and industry requirements

Composite materials, shortened to composites for brevity, are defined as complex materials made from two or more constituents with significantly different physical or chemical properties. Smart combinations of different constituents can provide a desired response of the composite making it perfect for a particular given application. For this reason, man-made composites have a long history, e.g. Egyptians already built houses using wattle and daub and ancient Mesopotamians realized that gluing wood at different angles the resulting plywood exhibited better properties than the ordinary ones. Owing to this tailoring capability, different types of composites can be found nowadays in aerospace, energy, automobile, construction, sports and many other technological industries.

Regarding lightweight structural applications, such as spacecraft and aircraft structures, fiber reinforced polymers are the most extensively used among all the high performance composites. FRPs are made of a polymer matrix reinforced with stiff and strong continuous fibers that can be weaved, knitted or braided in order to create a textile sheet that will ease the manufacturing process. However, for high-end applications requiring superior strength and stiffness, composite laminates made by stacking several unidirectional (UD) plies are still the reference architecture. Each ply has millions of fibers running in a single direction, and the resulting material is highly anisotropic. The fibers are the load-bearing phase, while the matrix is mainly used to maintain the fibers oriented according to the design direction. The properties of the final laminate will depend on the stacking sequence of the individual plies. Therefore, there exists an enormous freedom for the custom design of composite laminates in order to fully exploit their mechanical performance. However, predicting the mechanical performance of composite materials is not straight forward due to their anisotropy and heterogeneity, so strategies like the multiscale approach are extremely useful to face their analysis in a systematic and efficient manner.

1.2 Multiscale strategy

The hierarchical structure of fiber-reinforced composite materials makes them ideal candidates to apply multiscale strategies in their analysis. It is well known that their mechanical properties at the millimeter scale are controlled by the constituent properties and the distribution of the reinforcement fibers, whose cross section is of the order of micrometers.

A classical strategy is the so called *top-down multiscale* approach, where material testing begins studying the composite structure and identifying the weakest regions where damage is most likely to occur. Then, these sections are subjected to further refined analysis using more sophisticated constitutive models to predict the material response up to the final fracture. Nevertheless, this strategy often relies on phenomenological models whose constitutive relations may depend on the calibration tests. Indeed, due to the phenomenological nature of these models, the input parameters need to be characterized for each material configuration, thus, the results obtained for a given material system cannot be extrapolated to a material with different fiber volume fraction, ply thickness or laminate stacking sequence. In conclusion, this multiscale approach requires a massive investment on experimental testing in case of considering different material systems, manufacturing processes, loading conditions, composite configurations and architectures, etc.

A more efficient strategy is the *bottom-up multiscale* strategy (Llorca et al., 2011) which aims to predict the mechanical behavior of the material starting from the scale of the constituents (fiber, matrix and interfaces), moving up to the scale of an individual ply, laminate, component and the final structure, as illustrated in Figure 1.1.

This strategy takes advantage of the fact that composite structures are made up of laminates which in turn are obtained by stacking individual plies with different fiber orientation. This leads to the analysis of three different entities (ply, laminates and components) whose mechanical behavior is characterized at three different length scales, namely fiber diameter, ply and laminate thickness, respectively. Fiber diameters are of the order of a few µm, whereas the ply thickness ranges from modern ultra-thin plies of ~ 30 µm up to conventional plies of $150 \sim 300$ µm, and standard laminates may have a few millimeters in thickness. This clear separation between length scales enables the usage of multiscale modeling by computing the properties of one entity (e.g. the microstructure) at a given length scale, and passing this information to the simulations at the next length scale to study the mechanical performance of the larger entity (e.g. an individual ply).

Following this approach, virtual testing of composites up to the component level is carried out in successive steps within the framework of the finite element method (FEM). Firstly, *computational micromechanics* (CMM) is employed to predict the ply properties from the experimental characterization of the mechanical properties of the constituents (matrix, interface and fiber), together with the volume fraction and spatial distribution of fibers within the ply.

Once the ply properties (stiffness, strength and toughness) have been derived from micromechanical virtual tests, *computational mesomechanics* is then employed

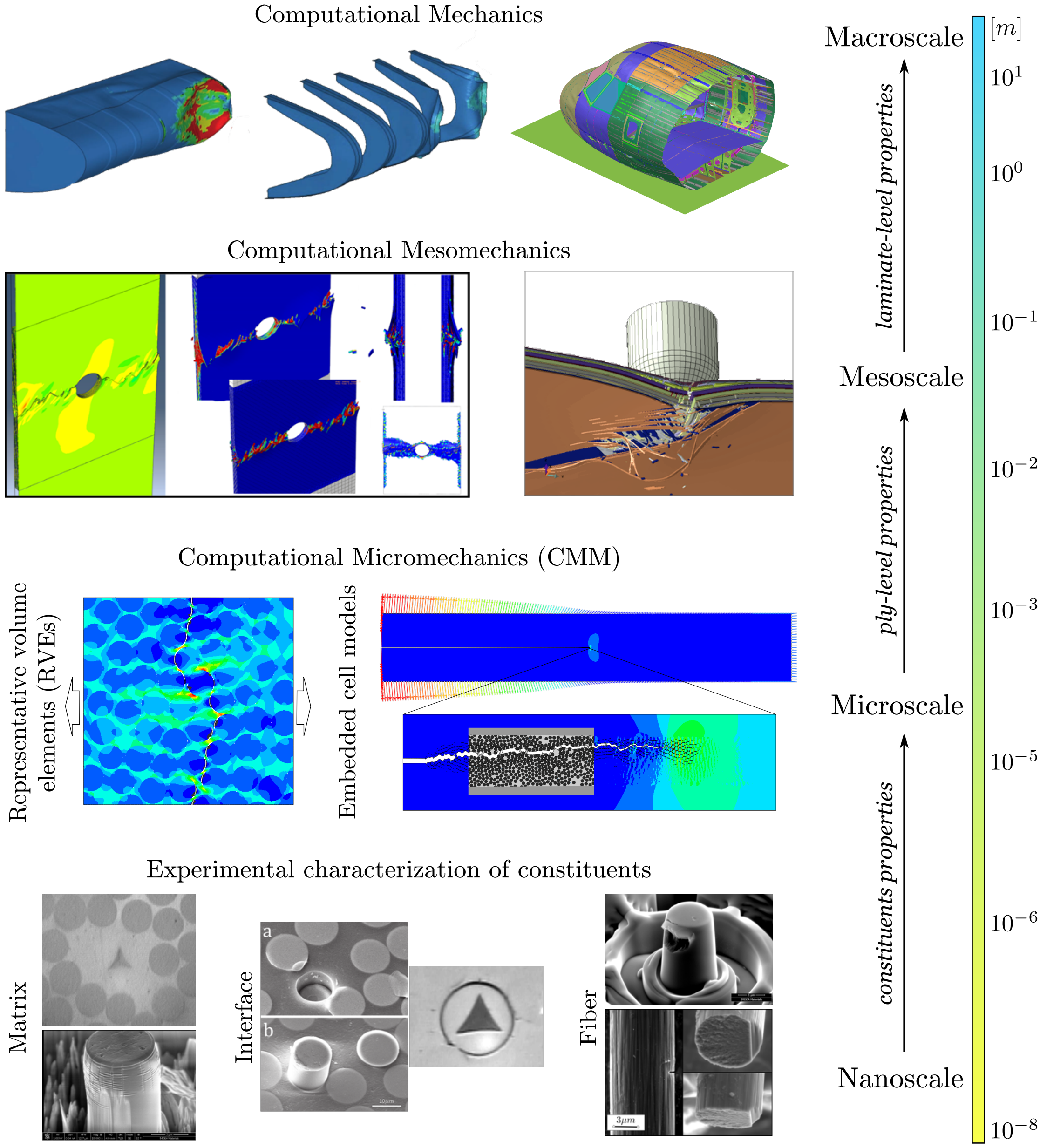

Figure 1.1: Bottom-up multiscale simulation scheme to perform virtual mechanical tests of fiber-reinforced composite materials.

to determine the homogenized mechanical behavior of the laminate, together with the interlaminar behavior between adjacent plies. The global mechanical response of the laminate is homogenized again and forwarded to macroscale models (*computational mechanics*). These latter models consider multiple subcomponents or subassemblies that are usually represented by means of planar elements (shells).

This thesis focuses on the initial stages of the bottom-up multiscale strategy:

first, the experimental characterization of the composite constituents; and later, the development of micromechanical models for the analysis of various failure mechanisms in unidirectional fiber-reinforced composites.

1.2.1 Constituents characterization

Thorough characterization of the constituents is crucial to obtain reliable input properties for simulations relying on these values. As observed previously, in a FRP composite not only the fibers and the matrix need to be characterized, but also their interface which exhibits different properties and controls the damage mechanism known as fiber/matrix debonding.

Matrix and fiber/matrix interface determine, mainly, the mechanical performance of the composite in the direction perpendicular to the fibers, as well as the shear deformation modes. Thus, experimental characterization of the matrix and the fiber/matrix interface is required to accomplish precise results from virtual tests. Characterization of the matrix has been pursuit by testing neat resin coupons (Fiedler et al., 2001). Nevertheless, this kind of tests does not take into account the local residual stresses due to the manufacturing/curing process of the composite ply. Similarly, *ad hoc* fabricated specimens for the characterization of the interface have been developed over the last decades, e.g. the drop test (Miller et al., 1987), and the fragmentation test (Kelly and Tyson, 1965), among others. However, they lack the same features as the neat resin coupons: the unrealistic stress state of the dedicated specimens, missing the constraining effect of the surrounding fibers, as well as the residual thermal stresses. Novel techniques based on the experimental technique of nanoindentation have been developed to carry out *in situ* microtests to characterize the polymer matrix (Fiedler et al., 2001; Rodríguez et al., 2012b; Naya, 2017) and the interface (Canal et al., 2012a; Rodríguez et al., 2012a).

Long fibers are intended to provide high strength and stiffness in the longitudinal direction in an FRP. Therefore, experimental characterization of the fibers is typically focused on their longitudinal properties (Tagawa and Miyata, 1997; Tsai and Daniel, 1999; Cheng et al., 2005; Kant and Penumadu, 2013; Herráez et al., 2016a). *Ex situ* testing of individual filaments has become the most popular strategy adopted by the research groups in the field.

It is important to note that some fibers, like carbon fibers, exhibit a strong anisotropy due to their internal morphology. For that reason, the longitudinal characterization of this type of fibers is not sufficient to fully describe their elastic behavior in the transverse direction or under shear loads. However, experimental testing of the transverse properties of these small-diameter fibers is challenging, and just a few works in the literature face this problem (Hadley et al., 1965; Phoenix and Skelton, 1974), to the best knowledge of the author.

A review of the most remarkable state-of-the-art experimental techniques devoted to the characterization of the FRP constituents (matrix, fibers and interface) is carried out in Chapter 2, together with a complete methodology to characterize the longitudinal properties of high performance fibers.

1.2.2 Computational micromechanics

Computational micromechanics has emerged in recent years as a powerful tool to predict the influence of the constituent properties on the ply behaviour under different loading conditions. This approach is based on the numerical simulation of the mechanical response of models where the constituents of the material are explicitly represented, such as periodic *representative volume elements* (RVE) of the composite microstructure (González and Llorca, 2007a; Totry et al., 2008a,b; Vaughan, 2011; Herráez et al., 2015; Naya et al., 2017a,b) and embedded cell models (Canal et al., 2012b; Herráez et al., 2018b) by means of the finite element method (FEM). As a result, this numerical strategy considers detailed information of the microstructure and constituent properties, inherited from micromechanical characterization of the fiber, matrix and interface.

Periodic representative volume elements

In these methods, the inhomogeneous material is approximated by an infinite model made of a periodic arrangement of the phases (fibers and matrix). The resulting periodic microfields are evaluated by analyzing the repeating cell of the microstructure, which may describe geometries ranging from rather simplistic to highly complex representations of the real microstructure of the composite.

Periodic microfield approaches are often used to obtain constitutive equations for composite materials in the nonlinear regime. Nevertheless, these methods become invalid when the nonlinear phenomenon is associated with a inhomogeneous process, such as a strain localization problem (e.g. cracking). In these cases, the stress vs. strain response obtained from the model during the damage propagation regime depends on the size of the RVE (Bazant and Planas, 1997).

Several strategies have been developed to handle the analysis of heterogeneous materials at the microlevel. The pioneer approach called *method of the cells* was developed by Aboudi (1989). In this method, an analytical approximation is employed to obtain the stress and strain fields over a microstructure that corresponds to a square arrangement of fibers. Another examples of analytical methods to solve the unit cell problem are the *transformation field analysis* (Dvorak, 1992) or the high-fidelity generalized method of cells (Aboudi, 2004). Although these analytical approaches use highly idealized microstructures and provide limited information about the microscopic field, they are useful to obtain constitutive models at an extremely low computational cost. Besides the previous simplistic approximations, the analysis of composites through periodic microfield strategies is often tackled through more complex and realistic cells which are solved by means of numerical tools such as FEM.

The mechanical behavior of composite materials can be studied through the numerical simulation of a *representative volume element* (RVE) of the microstructure. The RVE was originally defined by Hill (1963) as the smallest volume element of a heterogeneous material for which the average stress and strain microfields converge to an asymptotic value which is size independent and represents the effective macroscopic constitutive response. Therefore, the RVE should exceed a minimum size to ensure that the simulation results are independent of the size and spatial distribution of the reinforcements within the RVE. There are no procedures to predict the size of the RVE for the analysis of a particular composite, instead it should be confirmed by sensitivity study. It was demonstrated that only a few dozens of fibers or particles in an RVE are sufficient to simulate the mechanical behavior of metal-matrix composites (Segurado and Llorca, 2002) and FRPs (Totry et al., 2010; Trias et al., 2006).

In the multiparticle cell models, the computational micromechanical process to simulate the behavior of the composite begins with the creation of an RVE. The microstructure of a composite is usually idealized as a random dispersion of spheres, ellipsis, circles, or any other geometrical shape which represents the cross section of the reinforcement. To analyze the transverse behavior of unidirectional FRPs, assuming infinitely long straight fibers, the microstructure is idealized as a dispersion of circles which represent the fibers cross section. This fibers distribution should be representative of the actual transverse section of the composite ply. Different methodologies have been proposed to attain this goal, ranging from the replication

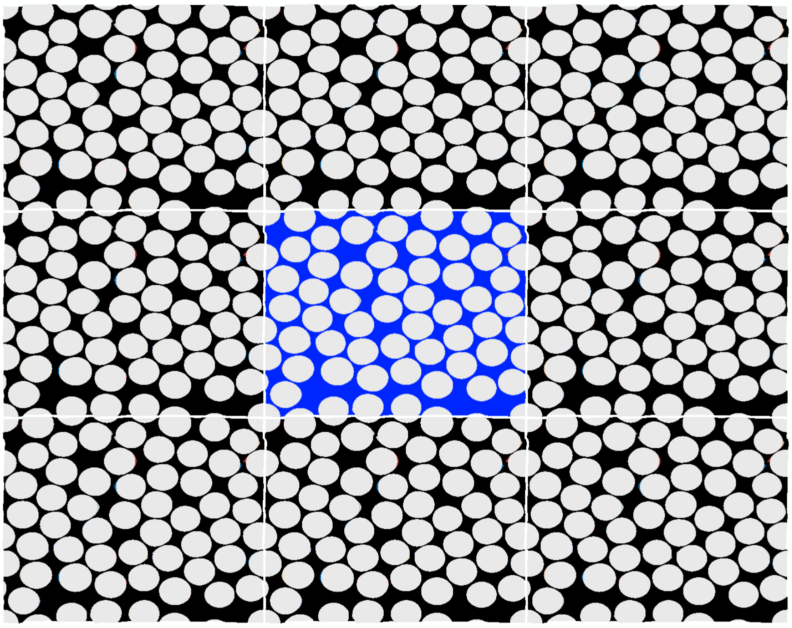

Figure 1.2: Unit cell containing an RVE with randomly distributed fibers subjected to uniaxial compression in the vertical direction and the periodic microstructure generated by the repetition of the unit cell.

of the images of a real microstructure (Trias, 2005), the reproduction of statistical spatial descriptors (Vaughan and McCarthy, 2010) or direct techniques to obtain an idealized random isotropic microstructure (Segurado and Llorca, 2002; Melro et al., 2008). The latter has become the most efficient and was proven to be sufficient to reproduce the response of the composite ply under transverse loads (Trias et al., 2006; Melro et al., 2008; Naya et al., 2017a).

A review of the most remarkable algorithms devoted to the numerical generation of heterogeneous microstructures is performed in Chapter 3. This is followed by the presentation of a novel strategy for the generation of arbitrary 2-D artificial microstructures and the statistical evaluation of various microstructures generated through this method. Finally, a user-interface application called `Viper` integrating multiple capabilities for the generation of arbitrary microstructures, and evaluation of spatial descriptors is presented in Chapter 3.

The RVE together with the boundary conditions must generate a valid stress microfield regardless of the RVE size and the edges effect. The boundary conditions applied play a key role on the assessment of the homogenized properties. The two most common types of boundary conditions are: uniform boundary displacements or isostrain (Hill-Reuss), and uniform boundary tractions or isostress (Hill-Voigt).

Though simple to implement and cheap in terms of computational cost, these boundary conditions are not representative of real stress states, as the edges of the model induce artificial stress concentrations. In addition, the stiffness of the RVE tends to be overestimated and underestimated, for the isostrain and isostress boundary conditions respectively (Benssousan et al., 1978). Instead, *periodic boundary conditions* (PBC) are considered to be a more general way to introduce far-field loads into the RVE. The application of PBC along the edges of the RVE guarantees the continuity between adjacent RVEs which deform like tiles of a jigsaw puzzle, see Figure 1.2. However, the use of PBC requires the RVE to be periodic, such that a fiber intersecting one of the edges must find its complementary fiber twin on the opposite edge.

In Chapter 4, 2-D models consisting of periodic RVEs including PBC are employed to evaluate the effect of the fiber cross section on the transverse compressive and tensile strengths of a unidirectional FRP ply.

A 3-D single-fiber RVE with PBC is employed in Chapter 6 to address the fiber kinking phenomenon, which takes place when a unidirectional FRP ply is loaded under longitudinal compression due to the shear stress induced in the polymer matrix.

Embedded cell models

The embedded cell method consists of a model representing a specimen with two different material descriptions. First of all, a *region of interest* (ROI) where the microstructure is resolved with a high level of detail, including the matrix, fibers and interfaces. This domain is embedded in a region where the material is considered as a homogeneous domain. The embedding outer region is responsible for transmitting the far-field loads to the ROI, where the stress and strain fields are resolved at the microstructure level. This strategy enables the simulation of strain localization problems such as crack propagation and other fracture processes. This approach was successfully applied by Canal et al. (2012b) on the intralaminar transverse crack propagation on FRP through a three-point bending test as illustrated in Figure 1.3.

Depending on the consideration of the outer region, Böhm (1998) came up with the following two main types of embedded cell methods:

- Models in which the ROI and the embedding region represent explicitly the microstructure, but where the discretization size is different (Sautter et al.,

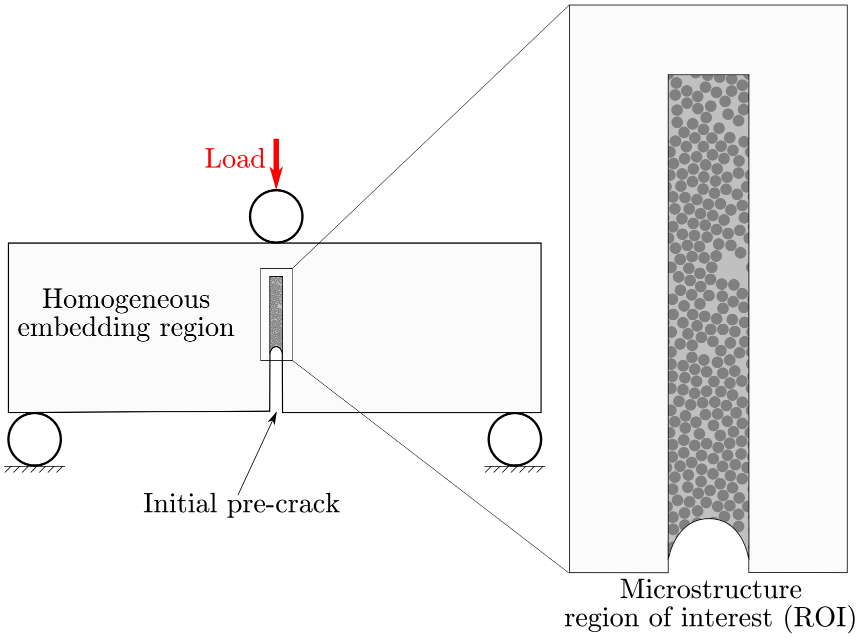

Figure 1.3: Schematic of the embedded model employed to simulate a three-point bending test on a unidirectional FRP (Canal et al., 2012b).

1993). These models avoid layer effects generated at the interface between both regions, nonetheless, this type of model involves a very high computational cost.

- Models which represent the embedding region through a homogeneous material whose constitutive response is defined a priori based on empirical, analytical or numerical approaches. These models are specially suited to study the localization and growth of cracks in heterogeneous materials (Wulf et al., 1996; González and Llorca, 2007b; Canal et al., 2012b; Mortell et al., 2017) or the stress concentrations around the crack tips (Aoki et al., 1996) or around local defects (Xia et al., 2001).

The embedded cell method employing a homogeneous linear elastic material model for the embedding region is used in Chapter 5 to analyze the intralaminar transverse crack propagation in a fiber-reinforced polymer.

1.3 Motivation for the research

Despite UD composite laminates being the most simple architecture among FRPs, predicting their mechanical performance is a complex task. Their strong anisotropy and heterogeneity are the origin of the different failure mechanisms exhibited for different loading conditions.

Figure 1.4 illustrates the failure mechanisms suffered by a UD composite ply under pure stress states (uniaxial tension, uniaxial compression and pure shear). When a UD ply is loaded under uniaxial tension in the longitudinal direction, x, the failure mechanism is fibers tensile failure. Whereas, under longitudinal compression, the ply failure is dictated by the mechanism known as fiber kinking. This phenomenon is triggered by the shear yielding of the matrix leading to an unstable stress state resolved by the sudden rotation and breakage of the fibers along a narrow band at an inclination angle β. Regarding the transverse loading cases, under tension ($\sigma_{22} > 0$) ply failure is frequently determined by the failure of the fiber/matrix interfaces, or debonding, followed by the tensile failure of the remaining polymer matrix ligaments. In transverse compression, shear banding of the matrix, together with interface debonding are responsible for the failure of the composite ply. In-plane shear loads not only promote fiber debonding, but also large plastic deformation of the matrix and fiber/matrix friction. The combination of all of these phenomena provokes a remarked nonlinear response of the UD ply under in-plane shear (Hahn and Tsai, 1973).

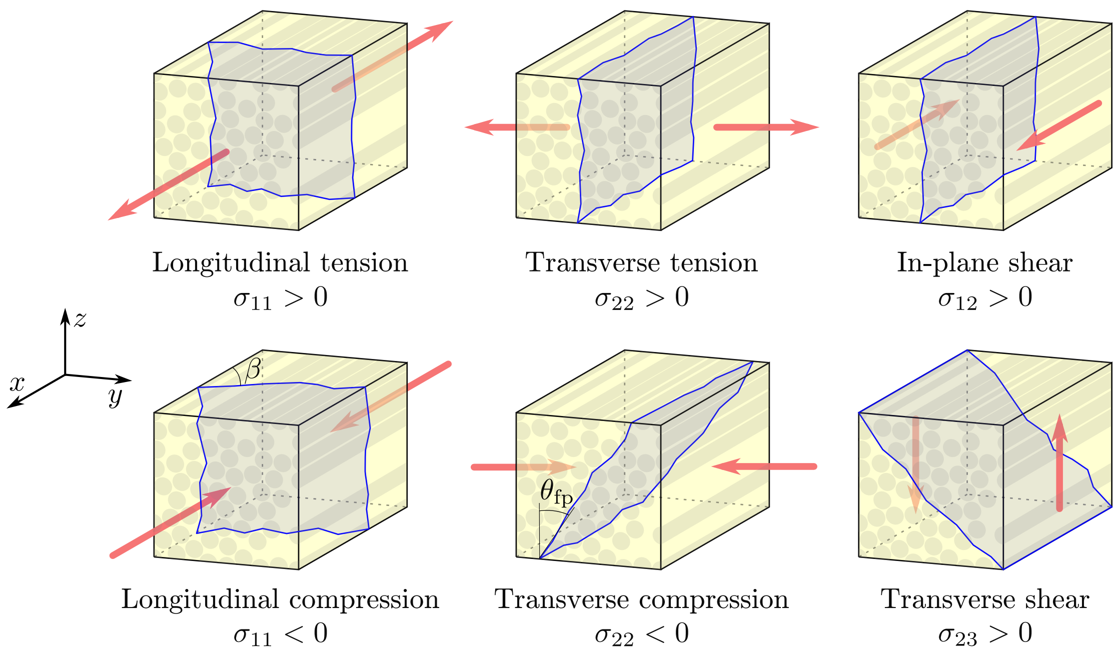

Figure 1.4: Schematics of the different failure mechanisms in unidirectional fiber-reinforced composite plies under pure stress states.

Over the last decades a number of constitutive models to predict these failure modes and their interactions have been developed. It was Hashin (1980) who first distinguished between matrix-dominated and fiber-dominated failure mechanisms. Followed by Puck and Schürmann (2004), who extended Hashin's criteria by identifying distinct fracture planes, θ_{fp}, according to different loading conditions. And finally the different versions of the LaRC (Langley Research Center) criteria: LaRC02/03 (Dávila et al., 2003; Camanho et al., 2003; Dávila, 2005) and LaRC04 (Pinho et al., 2005).

1.4 Objectives of this thesis

Over the last years, the Composite Materials Group at IMDEA Materials has worked intensely in the development of a multiscale strategy to evaluate the mechanical performance of composite laminated materials (Llorca et al., 2011; Lopes et al., 2016).

On one hand, precise characterization of the FRP constituents at the microscale has been pursuit. Experimental characterization of the interface and the matrix was successfully achieved by *in situ* microtests. Fiber push-in (Rodríguez et al., 2012a) and push-out (Canal et al., 2012b) tests were developed to obtain the interface shear strength, whereas instrumented nanoindentation on resin pockets (Rodríguez et al., 2012b) and resin micropillars compression (Naya, 2017) were employed to characterize the elasto-plastic behavior of the polymer matrix. However, there are still some gaps in terms of characterization of constituent properties like the interface toughness, and the fiber strength (in tension and compression), among others.

On the other hand, an extensive work on the computational micromechanics field have been carried out to analyze the different failure mechanisms of UD composite plies (Totry et al., 2008a; Naya et al., 2017a,b). The use of CMM tools enables the analysis of unfeasible, or at least complex, experimental setups, which allow for a deeper understanding of the underlying deformation mechanisms, and the influence of many different variables (multiaxial stress states, material properties, etc). Additionally, the CMM models are used to compute the mechanical properties of the ply (stiffness and strength), so that they are passed to the constitutive models of the homogenized ply at higher scales (*computational mesomechanics*). Nevertheless, these constitutive models also require the stress vs. strain evolution after damage initiation as an input parameter for each of the different failure modes. In this regard, an effort is required to design strategies capable of capturing the material response during the damage evolution process (e.g. crack propagation, shear bands yielding, fiber kinking...).

This thesis covers some of the gaps presented above. To accomplish this, the following objectives are defined:

- *Experimental characterization of fibers.* To characterize the longitudinal mechanical properties of reinforcement fibers. In this regard, two novel experimental techniques were developed to measure the longitudinal fracture toughness and compressive strength of high performance fibers.
- *Analysis of fracture and damage mechanisms of UD plies by means of computational micromechanics.* To exploit the potential of CMM models to study fracture processes in the post-peak regime. One of the failure mechanisms considered in this work was the transverse failure, first attending to the effect of the fiber cross section on the transverse strength, followed by the detailed analysis of the intralaminar crack propagation under transverse tension. Later, the fiber kinking phenomenon was addressed through CMM based on the model of Naya et al. (2017b) and was employed to evaluate a homogeneous CDM constitutive model developed externally by Bergan and Leone (2016). In addition, a versatile algorithm to generate arbitrary 2-D microstructures was developed and integrated into a user-interface called `Viper` in order to facilitate and speed up the pre-processing stage of CMM analysis.
- *Multiscaling softening laws from the micro to the mesoscale.* To obtain the equivalent softening laws (stress vs. strain) or cohesive laws (tracion vs. separation) that reproduce the fracture response of the microstructure through the characteristic R-curve. The procedure is illustrated in Figure 1.5: elastic properties (E) and strength (Y) are obtained from RVE models, whereas the fracture energy (G) and the R-curve are computed through embedded cell models. From the R-curve predicted through CMM (blue shade), the softening curve is inferred and can be applied to mesoscale models. Due to the computational cost that 3-D models involve and the size of the RVEs required to capture fracture processes properly, this homogenization procedure was applied to a simplified 2-D model to study the intralaminar transverse crack propagation.

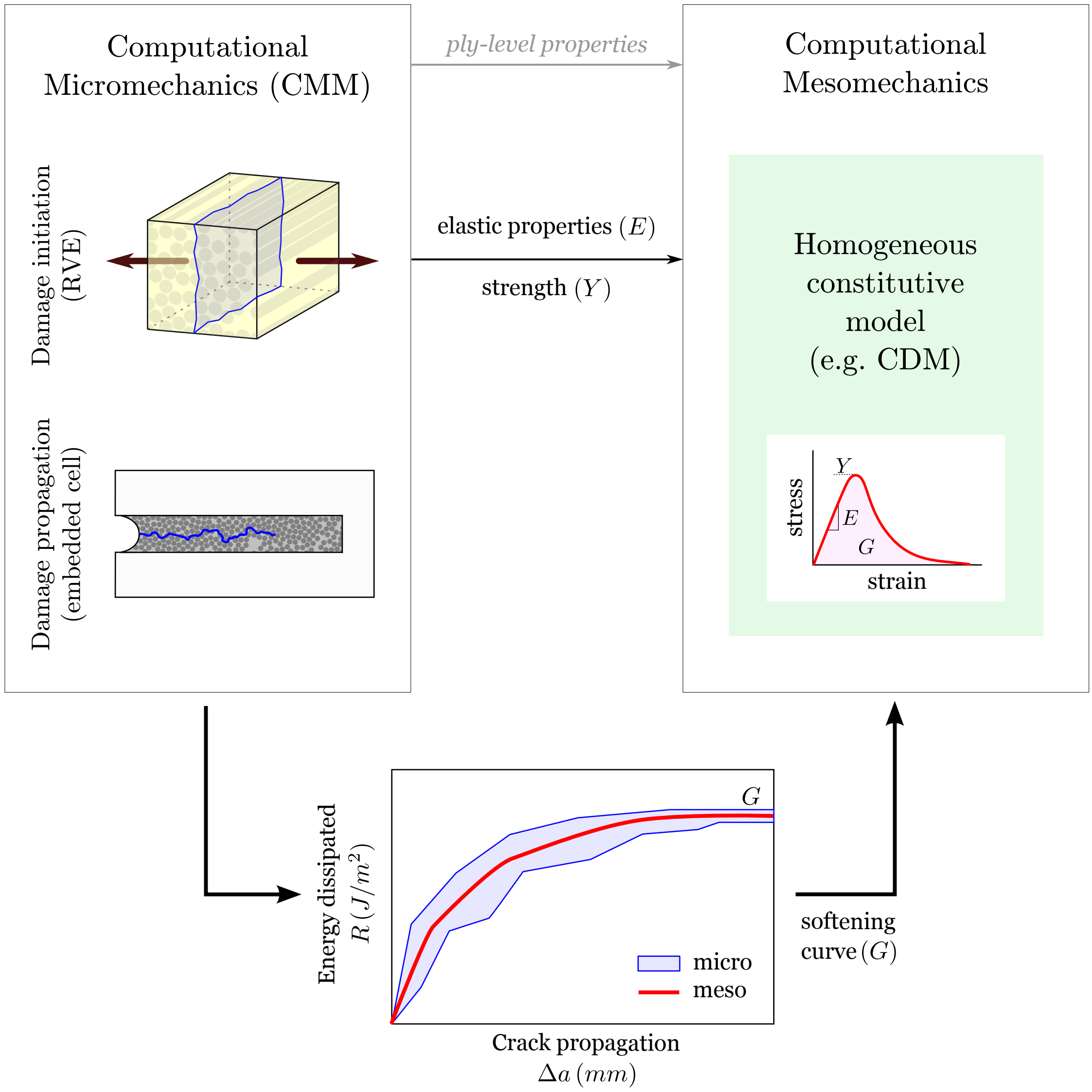

Figure 1.5: Homogenization procedure following a bottom-up multiscale scheme from the micro to the mesoscale for the intralaminar failure mode under transverse tension.

1.5 Outline of the dissertation

The outline of this dissertation is as follows:

Chapter 2 presents a review of the state-of-the-art on the experimental techniques devoted to the characterization of the FRP constituents (matrix, interface and fiber). In the second part of the chapter, two novel techniques for the experimental determination of the fracture toughness and compressive strength of fibers are proposed. The results obtained with these techniques to different materials are presented.

Chapter 3 starts with a literature review of the numerical algorithms to generate artificial microstructures. Afterwards, a new versatile approach based upon solving fibers overlapping is presented for the generation of 2-D microstructures with arbitrary fiber shapes and sizes reaching high fiber volume fractions. The analysis of some spatial descriptors was carried out over a number of artificial microstructures to validate this new algorithm. Finally, an in-house developed user interface for the generation and statistical analysis of 2-D microstructures is presented: `Viper`.

In Chapter 4, the effect of the fiber shape on the transverse tension and compression strengths is analyzed by means of computational micromechanics (CMM). For this purpose, periodic *representative volume elements* with different fiber cross sections were virtually tested. The influence of the residual thermal stresses was also addressed.

In Chapter 5, a numerical framework for the analysis of fracture processes within quasi-brittle materials is presented. The strategy is applied to the characterization of the intralaminar fracture process of a unidirectional FRP composite through a CMM *embedded cell model*. The characteristic crack resistance curve (R-curve) of the failure process is captured and homogenized into an equivalent cohesive law that can be introduced in mesoscale constitutive models.

The fiber kinking failure mechanism is addressed in Chapter 6. A high fidelity CMM model is developed to compare and validate a mesoscale *continuum damage mechanics* (CDM) model developed by A.C. Bergan (NASA Langley Research Center). The CMM model is exploited to assess the assumptions and simplifications of the mesoscale model for fiber kinking.

The thesis concludes in Chapter 7 with an exposition of the main remarks drawn through all of the previous chapters. The benefits and opportunities offered by the bottom-up multiscale strategy are highlighted from the perspective of *computational micromechanics* to analyze in detail phenomena based upon the constituents scale. In this final chapter, a perspective on potential future research topics to be addressed is presented.

2 Experimental techniques for micromechanical characterization

In this chapter, a brief review of the micromechanical experimental techniques devoted to the characterization of the microconstituents of FRPs is presented. Afterwards, a full experimental procedure for the longitudinal characterization of high performance fibers is described in detail in Section 2.2. This procedure includes two new experimental techniques, developed in this thesis, focused on the compressive strength and fracture toughness characterization of fibers. A discussion on the current state-of-the-art experimental techniques is drawn in Section 2.3 addressing the main material properties that have not been characterized yet and its estimation to be used in numerical models. The chapter concludes with Section 2.4 summarizing the contributions of this thesis to the current state of the art and the potential impact of the properties for which no experiments have been developed yet.

2.1 State of the art

In general, mechanical characterization of the FRP constituents, namely matrix, interface and fibers, is a complex task due to their inherent small scale (Herráez et al., 2017). Although, some mechanical properties may be inferred from macroscale tests, like some of the elastic properties, micromechanical tests are required to evaluate other properties like strength and toughness.

Some mechanical properties can be obtained from *ex situ* tests such as neat resin coupons, or the fiber drop test (see Section 2.1.2). However, this approach may not be entirely representative of the actual properties within the real composite because of differences in the manufacturing process, curing conditions and the initial residual stress state. In view of this, a more representative solution relies on the use of *in situ* micromechanical testing techniques in order to characterize the matrix, interface and fibers within the *as manufactured* composite material.

2.1.1 Matrix characterization

As a first approximation, mechanical characterization of the elastic properties of the isotropic polymeric matrix, E^m and ν^m, and the tensile strength, σ_t^m, may be done through macroscale coupons of neat resin. Nevertheless, the most adequate strategy to obtain the sophisticated elasto-plastic mechanical response of the matrix consists of *in situ* microtesting. Along this section, the instrumented nanoindentation (Rodríguez et al., 2012b) and micropillar compression techniques (Naya, 2017) are briefly explained for the sake of completeness. In addition, the mechanical properties of Hexcel 8552 epoxy resin obtained through experimental characterization are gathered in Table 2.1.

Instrumented nanoindentation

Instrumented nanoindentation is an experimental technique that consists of penetrating the surface of a material, using a spherical, conical or pyramidal rigid indenter, see Figure 2.1b. This methodology was originally developed by Tabor (1951) who by measuring the applied load P and the contact area A_c, obtained the material hardness as $H = P/A_c$. Nevertheless, estimation of the contact area is not trivial from nanoindentation.

Although a methodology to estimate the contact area from the stiffness of the unloading curve was developed by Oliver and Pharr (1992), its application to frictional materials, such as polymers, is not straightforward, due to the pile-up and sink-in phenomena (Figure 2.1a) which mask the contact area predicted by this method. This problem was analyzed in detail by Rodríguez et al. (2012b) to determine the full constitutive behavior of several polymers and bulk metallic glasses.

Epoxy resins behave as frictional materials, which means they are brittle under tensile loads, while in compression, they exhibit a pronounced plastic behavior. Since the yield surface is dependent on the hydrostatic pressure, it can be modeled using a Drucker-Prager yield criterion assuming isotropic elasto-plastic behavior (Drucker and Prager, 1952). This constitutive law requires four mechanical properties to

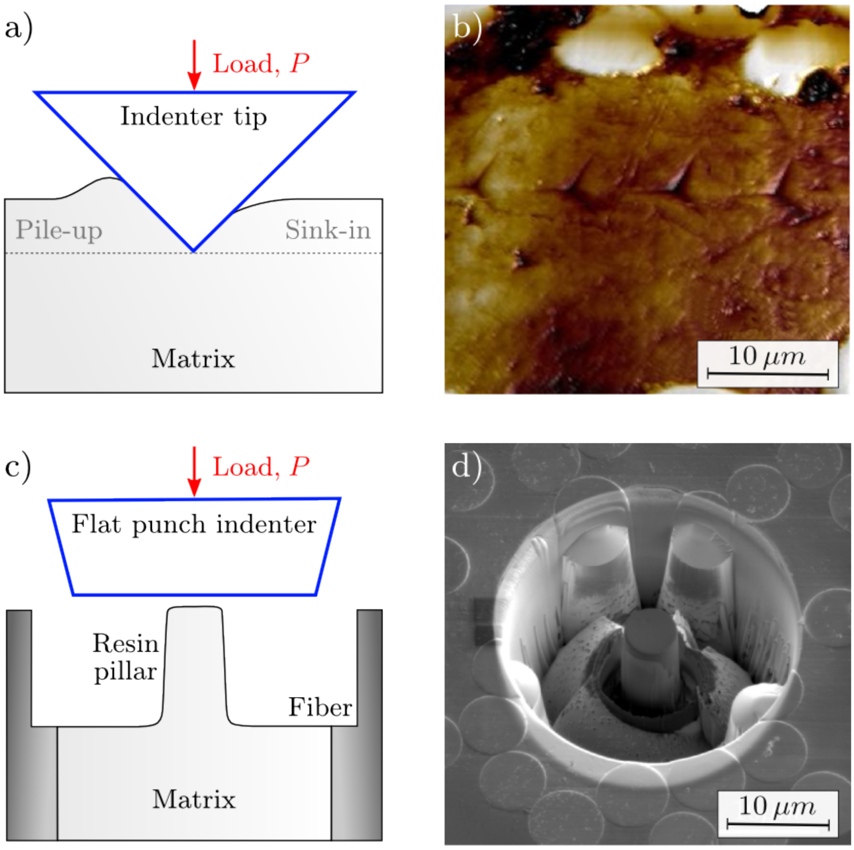

Figure 2.1: Experimental techniques for polymer matrix characterization: a) schematics of instrumented nanoindentation technique illustrating the pile-up and sink-in phenomena, b) atomic force microscope (AFM) image of a group of nanoindentation footprints in a resin pocket (Naya, 2017), c) sketch of the matrix micropillar compression test, d) scanning electron microscope (SEM) image of an FIB milled resin micropillar (Herráez et al., 2017).

describe the constitutive response of the material: the elastic modulus (E^m) and Poisson's ratio (ν^m) which characterize the elastic regime, and the cohesion (c^m) and the internal friction angle (ϕ^m) which determine the plastic yield surface.

The study carried out by Rodríguez et al. (2012b) through numerical finite element (FE) models concluded that the analysis of the load-displacement indentation curves alone cannot provide, independently, the information required to determine all of the parameters that describe the constitutive behavior of the polymer when pile-up/sink-in phenomena are present. This problem might be tackled carrying out complementary tests to obtain one of the matrix properties independently. In

Table 2.1: Mechanical properties of the 8552 epoxy resin obtained from *in situ* micromechanical characterization through instrumented nanoindentation and micropillar compression tests (Rodríguez et al., 2012b; Naya et al., 2017a).

E^m [GPa]	σ_{yc}^m [MPa]	ϕ^m [°]
5.1 ± 0.3	176 ± 3	31 ± 1

this regard, a new micromechanical test, the resin micropillar compression, has been recently proposed by Naya (2017) to measure the compressive yield strength of the matrix, σ_{yc}^m, independently, so the frictional behavior of the resin can be obtained jointly with the methodology proposed by Rodríguez et al. (2012b).

Micropillar compression test

The aim of this experimental technique is to get a direct stress-strain curve of the polymer under a uniaxial compression stress state. The main advantage of this method with respect to an equivalent macroscopic test is that there is no need of neat resin to manufacture *ad hoc* specimens. Micropillars are carved *in situ* on the cross section of a unidirectional FRP ply sample using a Focused Ion Beam (FIB) and then they are compressed using a flat punch tip indenter, as shown in Figure 2.1c and d. However, the load-displacement curve obtained from the experiment needs to be corrected to account for geometrical features of the carved pillar as the conical shape tapered angle, and substrate compliance (Yang et al., 2009). In addition, other issue of this test is the formation of a stiffer skin as a result of the FIB milling process (Wang et al., 2012). The stiffening effect of the micropillar skin was also corrected by Naya (2017) fabricating pillars of different diameters.

This technique provides a direct measurement of E^m and σ_{yc}^m from the stress-strain curve. Both experimental techniques, micropillar compression and instrumented nanoindentation, were combined by Naya (2017) to fully characterize the elasto-plastic constitutive behavior of the matrix. The compressive yield strength, σ_{yc}^m, obtained through the compression of resin micropillars was combined with the nanoindentation loading curve to determine the internal friction angle, ϕ^m. Details of the methodology were presented by Rodríguez et al. (2012b). The mechanical properties obtained with this technique for the 8552 epoxy matrix are collected in Table 2.1.

2.1.2 Interface characterization

As it was mentioned previously, fiber/matrix interface characterization in FRPs requires either the manufacturing of *ad hoc* coupons or the development of *in situ* micromechanical tests. In the first group of techniques, the most popular one reported in the literature are: the single-fiber fragmentation test, the fiber pull-out test and the single compression test. On the second group, the most efficient *in situ* micromechanical tests are the fiber push-in (Rodríguez et al., 2012a) and push-out tests (Canal et al., 2012b).

Ad hoc micromechanical tests

Kelly and Tyson (1965) originally developed the *fiber fragmentation test* to characterize the fiber/matrix interface shear strength, S^c, of a tungsten fiber embedded in copper matrix. The fundamentals of this technique relay on the study of the fragmentation process of a single fiber embedded in a dog-bone coupon made of the polymer matrix when tested under uniaxial tension in the fiber direction, as shown in Figure 2.2a. During the test, a longitudinal tensile stress in the fiber is developed. As load keeps increasing, progressive fragmentation events will take place until all remaining loaded fiber segments are too short to sustain the tensile stress transferred through shear stresses at the fiber/matrix interface (Herrera-Franco and Drzal, 1992). Analytical models accounting for load transfer between the fiber and the matrix are employed to derive the interface shear strength based upon the progressive fiber breakage process and the length of the fiber fragments (Cox, 1952). However, some important drawbacks affect the accuracy of the predicted interface strength. For instance, the matrix is assumed not to yield during the fiber fragmentation test, such that the whole process is fully governed by the interface and fiber failure (Bascom and Jensen, 1986). Another issue arises from the typically brittle epoxy matrices employed in the FRP composites, which may not reach the strain required to continuously break the fiber into small fragments.

The fiber *pull-out test* consists of a fiber partially embedded in a matrix block, that is loaded under tension while the matrix block is fixed, see Figure 2.2b. The force applied to the fiber is recorded during the test as well as the fiber end displacement, so the shear stress along the fiber/matrix interface can be estimated using a simple shear-lag model (Cox, 1952). More sophisticated FE micromechanical models were also developed to improve the understanding of the physical mechanisms governing the fiber/matrix interface debonding during the fiber pull-out process (Beck-

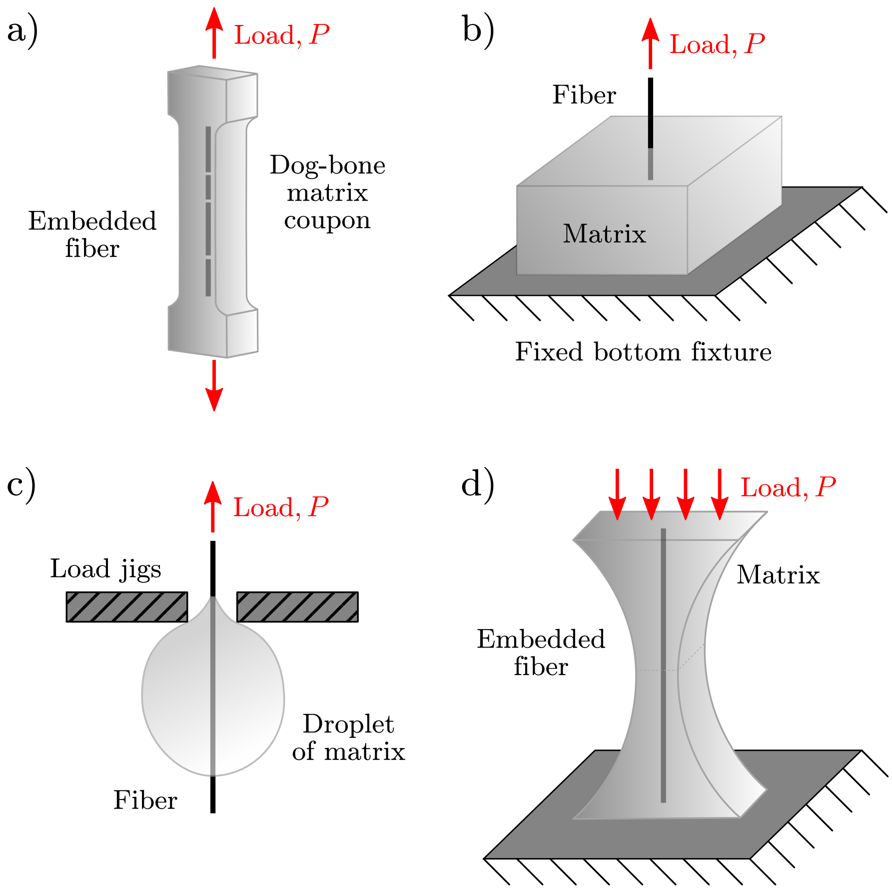

Figure 2.2: Schematics of *ad hoc* micromechanical tests to characterize the fiber/matrix interface strength: a) single-fiber fragmentation test (Kelly and Tyson, 1965), b) pull-out test with fixed bottom configuration, c) microbond test (Miller et al., 1987), and d) single compression test with smooth curvature (Broutman, 1969).

ert and Lauke, 1998). Nevertheless, there is an important practical difficulty from the experimental point of view. For typical values of the interface shear strength, to prevent fiber fracture the embedded pull-out length should be lower than ∼1 mm, and, from the experimental point of view, this is difficult to achieve and control (Kim et al., 1992).

The *microbond test*, also known as *drop test*, appeared as a modified version of the fiber pull-out test to deal with some of the problems from the latter (Miller et al., 1987). In this case, the fiber is pulled-out from a droplet of previously cured resin as illustrated in Figure 2.2c. Although this method allows for testing small diameter fibers, due to the reduced size of the droplets, it presents other disadvantages. The complex geometry of the droplet hinders the precise measurement of the embedded fiber length, bringing out inaccurate strength values (Herrera-Franco and Drzal, 1992). In addition, matrix cracking is frequently triggered by the "loading jigs" configuration prior to interface failure, and the manufacturing of specimens is hardly controllable, so repeatability of the results is jeopardized.

The *single compression test* of a dog-bone shaped specimen with smooth curvature was developed by Broutman (1969) to overcome the main limitation of the experimental procedures described previously: complex stress states around the fiber interface. This method is based on a single fiber embedded in a matrix specimen that is loaded under uniaxial compression, as shown in Figure 2.2d. Interface debonding initiates from the region where shear stress is maximum. However, the different elastic properties of the constituents induce a transverse tensile stress state at the center plane of the coupon, while the shear stresses are close to zero due to the symmetry (Ageorges et al., 1999). It was Schüller et al. (2000) who, by means of numerical models, observed the stress state along the fiber interface is more complex than expected. The analytical expressions derived by Broutman do not account for the important influence of residual stresses, neck shape effect of the specimen geometry and fiber anisotropy. Although, this technique became obsolete due to the significant uncertainties in the prediction of the interface strength, it provided important insights for further developments using analogous single fiber composites (Kim and Mai, 1998).

In situ micromechanical tests

In this section, *in situ* micromechanical tests to measure the interface strength are described in detail, namely the push-in and push-out tests. The main advantage of this type of experimental techniques is that they account for the real constraining effect of the surrounding fibers and the resin curing process is that of the actual composite.

The *push-in* test makes use of specimens extracted from the *as manufactured* composite and therefore, the resulting interface properties are more representative of the final material (Marshall, 1984). In this test, a single fiber in a given cross-section of a bulk specimen of the laminate is pushed in by means of a flat-punch indenter until interface debonding takes place as it is shown in Figure 2.3a. The main advantage of this technique relies, probably, on the sample preparation, which only requires fine polishing of the composite lamina cross section. On the other hand, interpretation of the results is somehow difficult because the length of the debonded interface is not measurable below the surface. In addition, fiber/matrix friction is also present after debonding. Originally, all these issues were tackled by means of analytical shear lag models (Cox, 1952; Kelly and Tyson, 1965; Mandell et al., 1980). Nevertheless, analytical models often require crude simplifications, like averaged regular fibers distribution or axial symmetry, which often lead to errors in the determination of the interface strength. To avoid those problems, computational micromechanics was employed to correlate the experimental results with FE virtual tests (Molina-Aldareguía et al., 2011; Rodríguez et al., 2012a). The sequence of events during fiber push-in is presented in Figure 2.3b: debonding onset is observed at the beginning of the indentation process (i), as load increases interface debonding keeps propagating stably (ii-iii), until the whole interface is fully debonded throughout some fiber length (iv). The interface shear strength, S^c, can be obtained by means of FE modeling from the load-displacement curves, and the results for AS4/8552 are shown in Table 2.2.

The *push-out test* also allows for testing the interface of fibers embedded in a composite manufactured by conventional techniques. The physical mechanism governing fiber push-out is similar to that of fiber push-in, but it is performed on a thin slice of the composite cross section of a few fiber diameters in thickness. As in the push-in test, the fiber is pushed with a flat-punch indenter while the load-displacement curve is monitored. The slenderness of the specimen promotes full interface debonding of the fiber pushed out through the plate, as represented in Figure 2.3c and d. In this test, interpretation of the results is straightforward: the interface shear strength is directly calculated from the peak load and the interface surface. However, the complexity of the test is found on the sample preparation: slicing/polishing of the sample down to such small thickness values ($20 - 30$ µm) is extremely difficult and time consuming due to the brittleness of the composite material. Moreover, the slicing process may lead to significant relaxation of the residual stresses that could modify the mechanical response of the fiber/matrix interface.

Nevertheless, these experimental techniques are only intended to obtain the interface shear strength, S^c, whereas the normal interface strength, N^c, which may differ from the shear strength, cannot be obtained by any of the last two methods. As an approximation, in this work the interface normal strength was estimated as $N^c = 2/3 \cdot S^c$, in accordance with experimental results on cruciform specimens carried out by Ogihara and Koyanagi (2010), see Table 2.2.

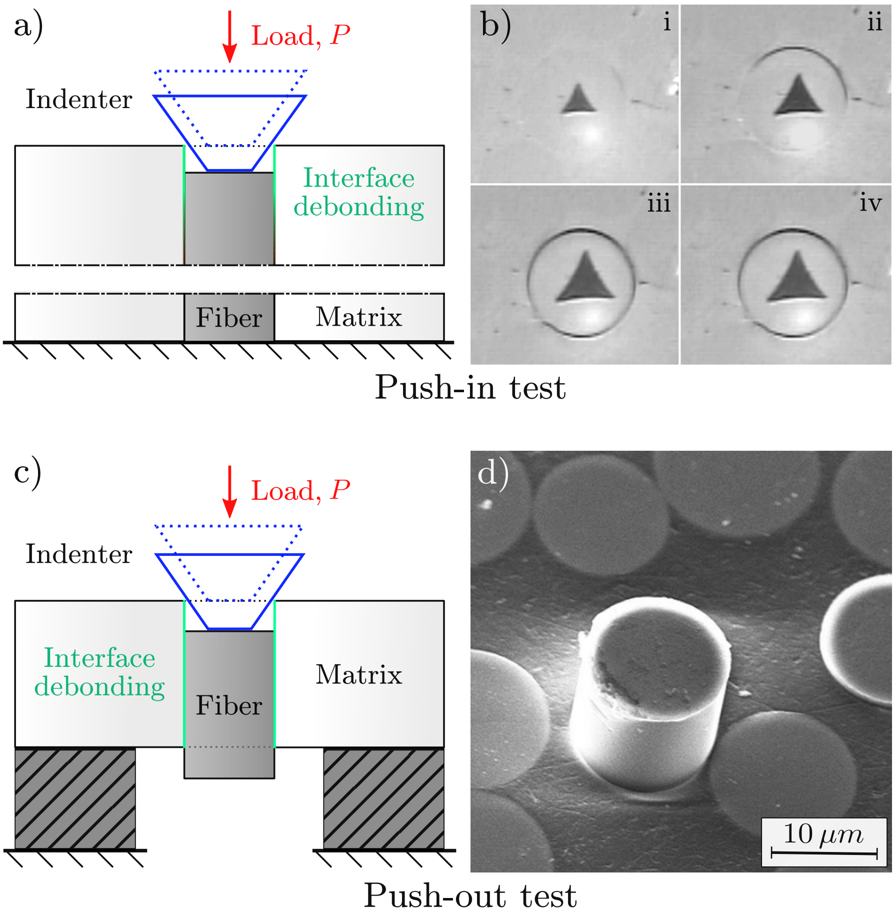

Figure 2.3: Schematics of *in situ* micromechanical tests to characterize the fiber/matrix interface strength: a) push-in test, b) SEM view of a pushed-in E-glass fiber at different load stages (Molina-Aldareguía et al., 2011), c) push-out test, d) SEM view of the back side of a pushed-out E-glass fiber (Canal et al., 2012b).

Not only the normal interface strength, but, to the best knowledge of the authors, there are also other mechanical properties of the interface that cannot be obtained through *in situ* micromechanical testing like the interface fracture toughness in mode I and II, namely G_n^c and G_s^c, and the friction coefficient, μ^c. For instance, characterization of the interface fracture energy is crucial to develop representative micromechanical models of the composite, see Section 5.4.1, but it is out of the scope of the present thesis.

2.1.3 Fiber characterization

The role of fibers in a reinforced polymer composite is to provide stiffness and strength to the material in the fiber direction. This is why the stacking sequence

Table 2.2: Mechanical properties of fiber/matrix interface for AS4/8552 composite from *in situ* micromechanical push-in tests (Rodríguez et al., 2012a; Naya et al., 2017a). $^*N^c$ is calculated based on S^c (Ogihara and Koyanagi, 2010).

N^c [MPa]	S^c [MPa]
$42^* \pm 2$	63 ± 3

of a laminate includes plies with different fiber orientations, in a simple way, to sustain loads in different directions according to a given design. For this reason most of the fiber characterization techniques available in the literature are focused on the longitudinal direction properties, mainly on the strength and stiffness. We can divide fiber characterization into tensile and compressive loading due to the enormous differences in the experimental testing strategies between both. Moreover, glass fibers behave as isotropic solids due to their amorphous structure, while carbon fibers are highly anisotropic due to the intrinsic microstructure of aligned graphene platelets. Thus, carbon fibers are typically represented as transversely isotropic solids.

Tensile loading

Numerous authors have measured the longitudinal properties under tensile loading of reinforcement fibers like carbon, glass, aramid and natural fibers among others from direct testing of filaments and/or tows. The longitudinal elastic modulus and strength of fibers can be obtained by straining, up to failure, individual filaments (single-fiber test, SFT) or tows containing thousands of fibers while monitoring the load-displacement curve, according to ASTM C1557-14 (2014) and ASTM D4018-17 (2017) respectively. When testing a tow with thousands of fibers, the cross section of fibers is estimated from the linear density of the tow. Nevertheless, in situ techniques are available to measure the diameter of one fiber during SFT, like the frequency method (ASTM D1577-07, 2012). In this manner the stress vs. strain curve of the fiber under longitudinal tension can be obtained, from which the longitudinal elastic modulus, E_1^f, and the fiber tensile strength, X_t^f, are derived. It must be remarked that some types of fibers, like carbon and aramid fibers, exhibit a nonlinear elastic behavior under longitudinal loading: with an increasing tangent modulus under tension and decreasing in compression (Peterson and Murphey, 2016; Le Goff et al., 2017). The experimental procedure for the characterization of the nonlinear elastic response of fibers is described in Section 2.2.1.

Although the Young modulus can be assumed to be constant along the fiber, fiber failure under longitudinal tension is dependent on the fiber length as it is triggered by the most critical defect (Reynolds and Sharp, 1974). This phenomenon is explained through the *weakest link theory* (Zweben and Rosen, 1970; Manders and Chou, 1983; Hitchon and Phillips, 1979) and has been typically modeled using the Weibull statistical distribution (Weibull, 1939). The Weibull cumulative density function, F, is defined as,

$$F(\sigma, L; \sigma_0, m, L_0) = 1 - \exp\left(-\frac{L}{L_0}\left(\frac{\sigma}{\sigma_0}\right)^m\right) \tag{2.1}$$

where σ_0 is the Weibull strength, m is the Weibull modulus which represents the strength dispersion, and L_0 is the gauge length of the specimens tested. This statistical distribution considers the coupon length, L, to represent the size effect upon the strength, σ.

Fiber strength dependency on the gauge length can be overcome by employing a fracture mechanics approach, instead of a stress-based strategy if the population of defects is known a priori. The application of a fracture mechanics criterion assumes that fiber failure occurs at a defect/flaw which plays the role of a small pre-crack. The variable defined for this criterion by the linear elastic fracture mechanics (LEFM) is the *stress intensity factor*, K_{I}, which is traditionally defined as,

$$K_{\mathrm{I}}(\sigma_\infty, a, \text{geometry}) = Y(a, \text{geometry}) \cdot \sigma_\infty \cdot \sqrt{\pi a} \tag{2.2}$$

where σ_∞ is the remote stress, a is the crack/notch length, 'geometry' represents the specimen geometry and boundary conditions, and Y is known as the non-dimensional stress intensity factor. The material property that is required by this criterion is the fracture toughness, K_{IC}. Therefore, material failure happens when the stress intensity factor at the crack tip, K_{I}, induced by the remote loading, σ_∞, reaches the material fracture toughness, $K_{\mathrm{I}} = K_{\mathrm{IC}}$. Thus, to characterize this property, specimens with *a priori* known crack/notch lengths are needed.

The recent development of high resolution milling techniques, like the Focus Ion Beam (FIB), has enabled a whole new range of possible experiments from a micromechanical perspective. This is the case of the single-fiber tensile test of notched fibers (Ogihara et al., 2009), which allows for the calculation of the mode I fracture toughness of the fiber, K_{IC}^{f}. This technique has been successfully applied to carbon (Kant and Penumadu, 2013; Tanaka et al., 2014) and other ceramic fibers (Ochiai et al., 2010). The application of this technique to measure experimentally the toughness of carbon, glass and aramid fibers is detailed in Section 2.2.3.

Compressive loading

A number of experimental techniques have been developed to measure the compressive strength of carbon fibers as reported by Waas and Schultheisz (1996). Among them we find i) the elastic loop test, ii) microcomposites testing, iii) the fiber recoil method, iv) micro-beam bending, and v) direct fiber compression, as illustrated in Figure 2.4.

In the *elastica loop method* (i) a fiber is bent into a loop, then the ends of the loop are pulled until the fiber breaks by compressive kinking as shown in Figure 2.4a. Although this method was originally developed by Sinclair (1950) as a mean for determining the tensile strength of fibers, the compressive stress in the loop may actually induce the failure of the fiber (Fukuda et al., 1999; López Jiménez and Pellegrino, 2012).

Microcomposites testing (ii) is a popular strategy in the literature to perform *ad hoc* microtests and extract mechanical properties at the constituents level. In general, the samples are manufactured including a single fiber. For instance, Hawthorne and Teghtsoonian (1975) carried out uniaxial compression tests on single-carbon fiber epoxy composites, as sketched in Figure 2.4b. They found an inverse relation between the elastic modulus and compressive strength for carbon fibers, as occurs in longitudinal tension for rayon-based and polyacrionitrile-based (PAN) fibers.

The *fiber recoil method* (iii) was introduced by Allen (1987) for the measurement of the compressive strength of polymer fibers. This technique consists of stretching a fiber at a certain tensile stress and then cut it in the middle. The resulting elastic wave from the cut travels to the fixed ends of the specimen and is reflected inducing a compressive stress in the fiber direction, see Figure 2.4c. Nonetheless, this procedure is prone to induce buckling along the fiber as large gauge lengths are required, and interpretation of the test results is not direct.

The *bending method* (iv) includes different test configurations to induce compressive stress in single fibers. DeTeresa (1985) employed a three-point bending setup,

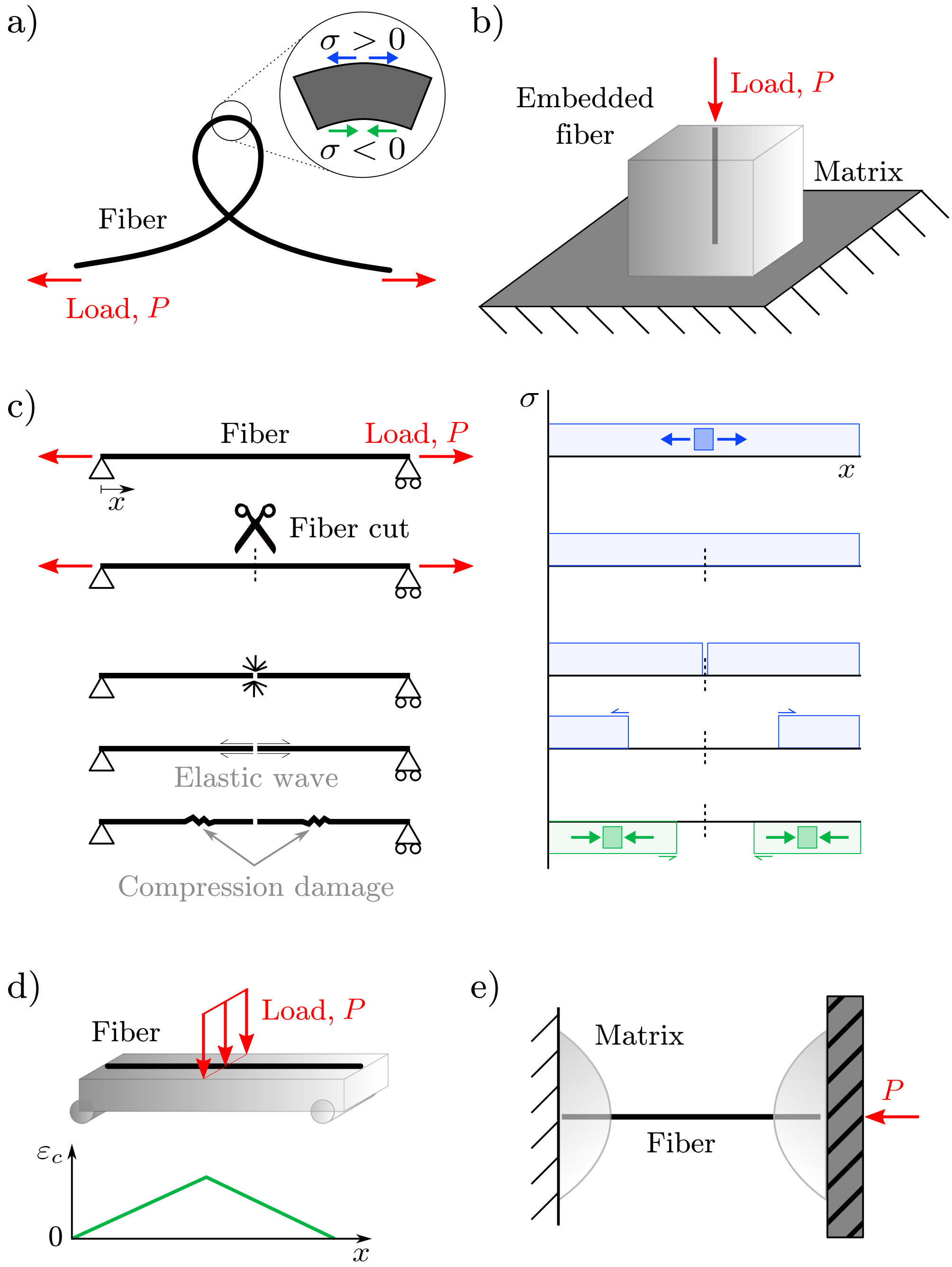

Figure 2.4: Experimental techniques to measure the fiber compressive strength: a) elastica loop test, b) microcomposite compression, c) fiber recoil method, d) micro-beam bending, and e) direct fiber compression.

as the schematic shown in Figure 2.4d, to induce a linear strain distribution along the beam-fiber until the fiber was broken. A different scheme was adopted by other authors selecting a four-point bending configuration with a single-fiber attached to the coupon face under compression (Ohsawa et al., 1990; Miwa et al., 1991).

Direct compression of single carbon fibers (v) was accomplished by Macturk et al. (1991) fixing the fiber ends to the loading fixtures with epoxy resin, see Figure 2.4e. The most sensitive variable to obtain the fiber compressive strength with this method is the fiber gauge length: if the fiber is too long it will buckle, while if it is too small the stress field will not be homogeneous and will be affected by the boundary conditions. Oya and Johnson (2001) performed a similar test to measure the compressive strength of different types of carbon fibers and found an important effect of the fixtures in the fiber failure.

Anisotropic behavior

Ceramic and polymer fibers exhibit a strong anisotropy due to their internal morphology. That is why its stiffness in the transverse direction is much lower than in the longitudinal direction, $E_2^f \ll E_1^f$. To the best knowledge of the author, the only available technique in the literature to characterize the transverse modulus of the fiber is the single-filament transversal compression test, (Hadley et al., 1965; Phoenix and Skelton, 1974). However, determination of the transverse modulus of the fiber from the load-displacement curve is inaccurate due to the uncertainty in the variables involved in the process. The most extended strategy consists of reverse engineering the fiber transverse elastic modulus from the transverse stiffness of a unidirectional ply through analytical expressions based on homogenization theories (Chamis, 1983; Mori and Tanaka, 1973) or computational micromechanics models (Totry et al., 2008b).

Regarding the shear stiffness of fibers, an original experimental method was reported by Tsai and Daniel (1999), in which a single-filament torsional pendulum was employed to measure the torsional stiffness of the fiber and thus its longitudinal shear modulus, G_{12}^f, based on the oscillation period.

2.2 New experimental techniques for fiber characterization

In this section, an experimental methodology for the longitudinal characterization of high performance fibers is presented. This procedure was applied on the characterization of three common structural fibers used in composites manufacturing: i) AS4 (Hexcel, 2018a) is a high strength carbon fiber manufactured from PAN (Polyacrylonitrile) precursor commonly used in prepregs and dry fabrics for aerospace structural applications; ii) aluminum-borosilicate E-glass fiber (54% SiO_2 - 15% Al_2O_3 - 12% CaO) is arguably the most common reinforcement for composites because of its low cost, high stiffness and strength, and the high temperature resistance; and iii) Kevlar KM2 (poly-paraphenylene terephthalamide branded by Dupont) is an organic synthetic fiber of the aromatic polyamide family (aramid) with high strength, modulus, and toughness used to develop protections against fragments impacts.

Firstly, the characterization of the elastic properties of the fibers is performed by means of single-fiber tests (SFT) in Section 2.2.1. The nonlinear response of carbon and aramid fibers is explicitly considered as well by means of an additional parameter, c_f.

Then, the experimental techniques employed for the characterization of the tensile and compressive strengths are described in Section 2.2.2. The tensile strength, X_t^f, is obtained by means of SFT and the experimental results are reduced through the Weibull's statistical distribution (see eq. 2.1), whereas the compressive strength, X_c^f, is addressed by means of a novel technique consisting of the *in situ* compression of fiber micropillars. The micropillar compression technique was only applied to AS4 carbon fibers.

Finally, the effective fracture toughness of the fibers under mode I loading, K_{IC}^f, is achieved by means of single-fiber tensile testing of notched fibers, see Section 2.2.3.

2.2.1 Characterization of the elastic behavior

Typically, structural fibers are assumed to behave as linear elastic solids for the sake of simplicity. Nevertheless, some kinds of fibers, like carbon and aramid fibers, exhibit some stiffening as tensile strain increases and this phenomenon can be captured through SFT tests. Although, some models in the literature distinguish between tension and compression loading (Montagnier and Hochard, 2005), a simple analytical model with a single parameter, c_f, to represent the nonlinear elastic response of the fibers was proposed by Kowalski (1988) as,

$$E_1^f(\varepsilon_{11}) = E_1^{0f} \cdot (1 + c_f\, \varepsilon_{11}) \tag{2.3}$$

where c_f is the nonlinear parameter and E_1^{0f} is the elastic modulus of the fiber at $\varepsilon_{11} = 0$. This nonlinear elastic response of the fibers is transferred to the mechanical response of a unidirectional ply in the reinforcement direction through the rule of mixtures as, $c_l \approx V_f\, c_f$, assuming the matrix is linear elastic (Peterson and Murphey,

Table 2.3: Longitudinal elastic properties of structural fibers for the linear and nonlinear elastic models. *Glass fibers showed a perfectly linear elastic behavior.

Fiber	Linear density λ [10^{-3} tex]	Diameter d [µm]	Linear model E_1^f [GPa]	Nonlinear model E_1^{0f} [GPa]	c_f
AS4 carbon	69 ± 4	7.1 ± 0.2	231 ± 10	211 ± 9	18.7
E-glass	310 ± 20	12.4 ± 0.4	68 ± 2	-*	-*
Kevlar KM2	164 ± 11	11.8 ± 0.4	84 ± 3	75 ± 3	7.2

2016; Le Goff et al., 2017). Integrating eq. 2.3 under uniaxial tension, a quadratic stress-strain relation is found in the longitudinal direction,

$$\sigma_{11}(\varepsilon_{11}) = \int_0^{\varepsilon_{11}} E_1^f(\varepsilon) \cdot d\varepsilon = E_1^{0f} \cdot \left(\varepsilon_{11} + \frac{c_f}{2}\,\varepsilon_{11}^2\right) \tag{2.4}$$

where c_f and E_1^{0f} can be extracted from least squares fitting of the stress-strain curves obtained from SFT.

The characterization of the elastic response of the fibers under analysis (AS4 carbon, E-glass and Kevlar KM2) was carried out by means of the following experimental procedure. The fiber ends were bonded with cyanoacrylate adhesive on cardboard with a 20 mm free-gauge length, with the embedded length being previously determined to eliminate sliding during the tests. The cardboard was directly connected to the mechanical grips of the fiber tensile test apparatus (Favimat+, Textechno$^{\text{TM}}$) and then subjected to uniaxial straining up to failure under stroke control at 1 mm/min, leading to strain rates of the order of $\sim 10^{-3}$ s^{-1}. The linear density of the fibers, λ, was determined by the fiber-tester system by using the frequency method according to the ASTM D1577-07 (2012) standard. The fiber is pre-loaded in this method to a given force in the range of $0.45 \sim 0.70$ cN/tex ([tex] = [g/km]). Then, the natural frequencies are extracted to determine linear density and, subsequently, the fiber cross section. The bulk density assumed for each of the fiber types was ρ = 1750, 2570 and 1500 kg/m^3 for the carbon, glass and aramid fibers respectively. All the tests were carried out at room temperature. A minimum of 30 fibers were dedicated to the elastic characterization of each type of fiber.

The resulting curves from the experimental SFT on AS4 carbon fibers are shown as red lines in Figure 2.5, together with the linear and nonlinear models fittings. Strain stiffening is observed under tension, while fiber stiffness reduction is predicted

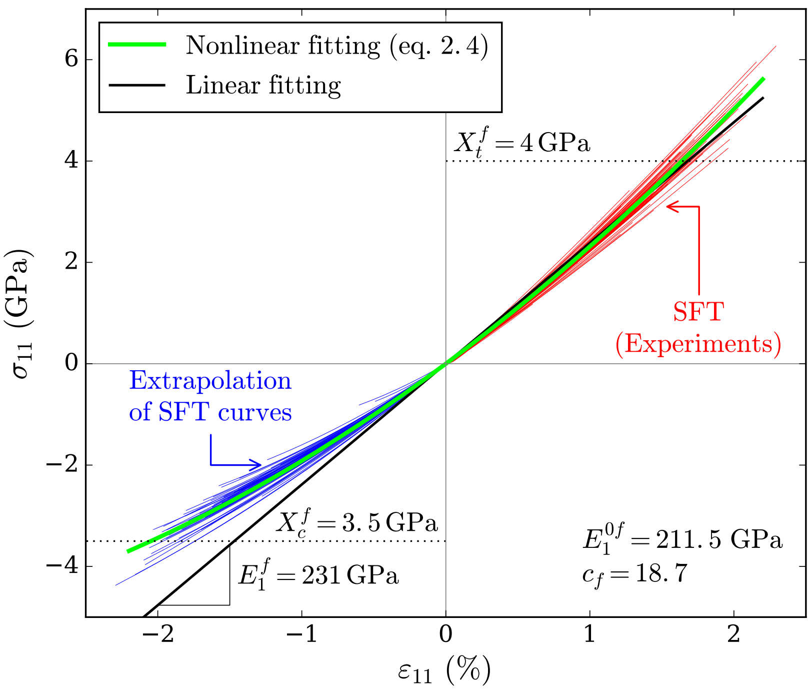

Figure 2.5: Stress vs. strain curves from SFT tests on AS4 carbon fibers (red lines), nonlinear (green) and linear (black) least squares fitting. Extrapolation of the SFT curves for the compression regime are shown (blue). Average strength values under tension, X_t^f, and compression, X_c^f, are displayed (see Section 2.2.2).

by extrapolation of the tensile results in compression. If the mechanical response of the fibers is assumed to be linear (black line), the stress prediction under tensile loading will not fall into remarkable errors, but compressive stresses will be largely overpredicted, specially for high compression strain values. The parameters obtained from the least squares fitting of the curves are gathered in Table 2.3. Peterson and Murphey (2016) reported experimental values of the same order for the nonlinear parameter under tension of IM10 carbon fiber, $c_f = 23.6 \pm 1.2$. Aramid fiber (Kevlar KM2) exhibited some nonlinearity as well ($c_f = 7.2$), whereas E-glass fiber described a perfectly linear elastic behavior ($c_f \approx 0$).

2.2.2 Longitudinal strengths characterization

Longitudinal tensile strength, X_t^f

The longitudinal tensile strength of the fibers was obtained from the SFT tests carried out up to failure as described in Section 2.2.1.

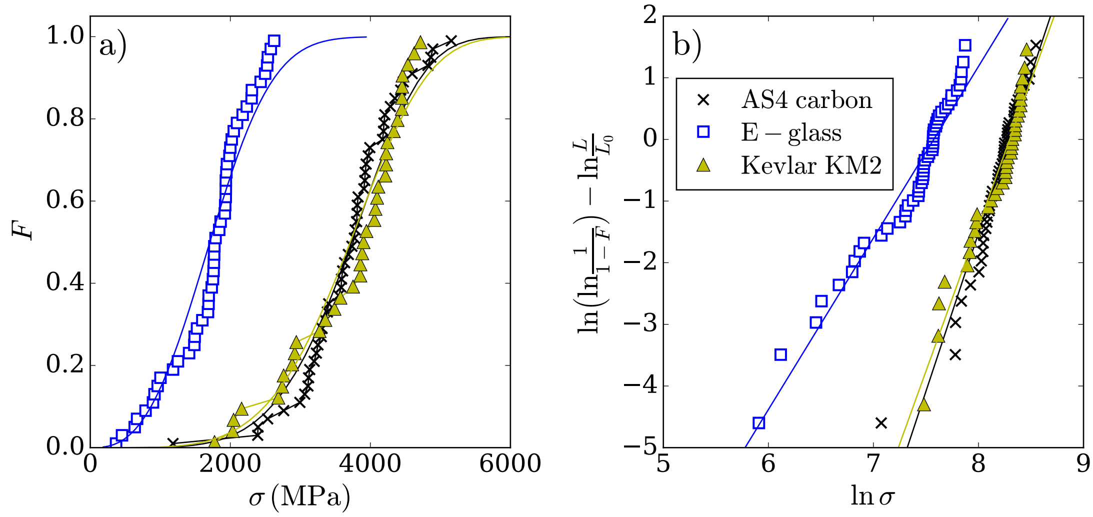

Figure 2.6: Experimental characterization of the fiber tensile strength through Weibull model: a) cumulative density function, F (eq. 2.1), and b) linear fitting of Weibull parameters (σ_0 and m).

The resulting tensile strengths, X_t^f, measured from 30 realizations of each type of fiber are shown in Table 2.4. The population of strength values obtained experimentally were fitted to a Weibull distribution according to eq. 2.1. The longitudinal elastic modulus, E_1^f, reported in Table 2.4 corresponds to a linear fitting of the SFT stress vs. strain curves.

The strength was determined with the maximum load achieved during SFT. The strength data σ of each group of fibers was arranged in ascending order and the failure probability $(i-0.5)/N$ was assigned to each individual strength as shown in Figure 2.6a, where i is the rank position and N the total number of fibers population. According to the Weibull statistics, the cumulative fracture density function, F, eq. 2.1, can be rearranged as

$$\ln\left(\ln\frac{1}{1-F}\right) - \ln\frac{L}{L_0} = m\ln\sigma - m\ln\sigma_0 \tag{2.5}$$

where the unknowns are the Weibull strength, σ_0, and the Weibull modulus, m, which were estimated by linear regression of eq. 2.5 as depicted in Figure 2.6b.

Table 2.4: Weibull parameters of the fibers tested by fitting eq. 2.5. The reference fiber length was $L_0 = 20$ mm.

Fiber	Weibull strength	Weibull modulus
	σ_0 [GPa]	m [-]
AS4 carbon	4.0	6.5
E-glass	1.9	4.1
Kevlar KM2	4.1	6.5

Longitudinal compressive strength, X_c^f

Longitudinal compressive strength of AS4 carbon fiber was measured through *in situ* fiber micropillar compression tests. A FEI Helios NanoLab DualBeam 600i equipped with a Focused Ion Beam (FIB) was used to manufacture micropillars at the center of carbon fibers on the composite cross section (Figure 2.7a). Specimens of 1.5 µm in diameter (d_p) and 3 µm in height (h_p) were fabricated using annular milling which resulted into pillars with a taper angle lower than 3° (θ_p) as shown schematically in Figure 2.8a. Beam currents were selected in order to produce suitable pillar geometries while keeping reasonable milling times, starting with an initial electric current of $I = 0.79$ nA down to $I = 80$ pA for the last milling step.

Samples were then mounted on a special holder for easy transfer between the FIB and the nanoindenter instrument. Compression tests were conducted using a Hysitron TI 950 TriboIndenter equipped with a 10 µm diameter flat punch. The experiments were carried out under displacement control at a constant displacement rate of $\dot{u} = 12$ nm/s. Considering the height of the pillars was around 3 µm, the tests speed guarantees quasi-static conditions ($\dot{\varepsilon} \approx 10^{-3}$ s^{-1}). A total of 13 fiber pillars were milled along the composite cross section and tested. Evidence of implantation of Ga^+ ions on the micropillar skin was not observed in this case, as compared to the FIB-milled micropillars on epoxy resin (Naya, 2017). The typical stress vs. displacement curves obtained during the compression tests are plotted in Figure 2.8b. All curves present the same features, identifying three different regions. The initial nonlinear region corresponds to the contact stage between the indenter tip and the top face of the pillar, followed by a linear region during elastic deformation of the fiber pillar and the surrounding material. This second stage turns into a smooth softening of the load promoted by fiber pillar splitting that eventually collapses, see Figure 2.7d and e. The compressive strength of pillars was obtained

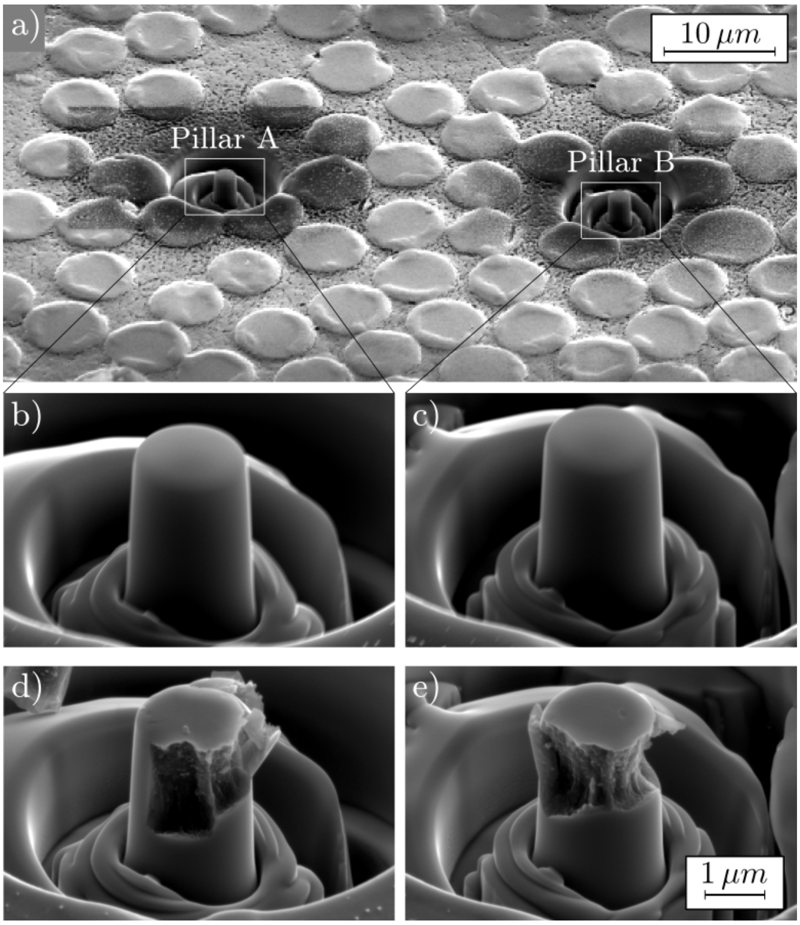

Figure 2.7: a) View of two pillars, A and B, FIB-milled on carbon fibers on the cross section of a CFRP before compression, b) premortem close view of pillar A, and c) pillar B, d) postmortem view of pillar A, and e) pillar B.

based on the loss of linearity of the loading curve from the second to the third stage. The resulting average compressive strength of AS4 carbon fibers was 3.5 GPa with a standard deviation of 0.2 GPa.

2.2.3 Fiber toughness characterization

The most common methodology to estimate the toughness of small diameter fibers is based on the direct observation of the fracture surfaces of post mortem specimens. The fracture surface of the fibers often exhibits some remains, in the form of mirror, mist and hackle textures, that allow to determine the defect size producing the failure, and consequently, the fracture toughness estimation (Honjo, 2003). However, this methodology introduces large experimental scatter due to the uncertainty in

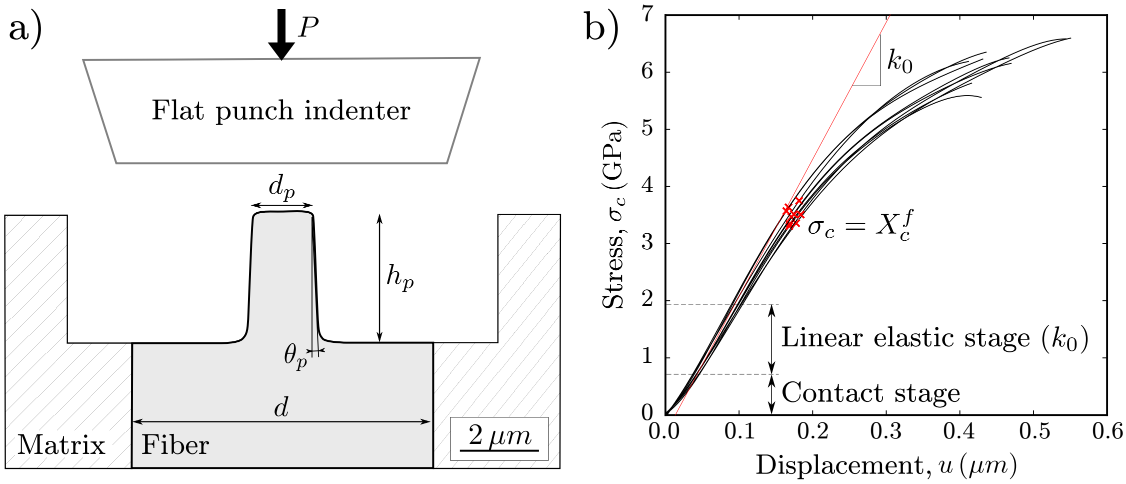

Figure 2.8: a) Schematics of the pillar compression test and b) stress-displacement curves obtained from AS4 carbon fibers micropillars compression on the composite cross section, where red crosses denote initial fiber failure.

the determination of the exact defect size that caused the final failure during the experiment.

Focus Ion Beam (FIB) opens revolutionary opportunities for testing materials at the microscale by selective removing/carving material generating complex geometries adequate for testing (Mueller et al., 2015; Slusarksi et al., 2014). Almost all materials can be structured by FIB, ranging from soft matter (polymers) to ultra hard material (diamond). This methodology permits to control precisely the geometry of the notch in terms of its depth and tip radius. The mode I fracture toughness, K_{IC}^f, is then inferred from the maximum strength of the notched fibers and the geometry of the notch.

This technique was applied to obtain the fracture toughness of the three fiber types previously tested for longitudinal elastic and tensile strength characterization, namely AS4 carbon, E-glass and aramid KM2.

Fiber toughness was determined through dedicated tensile testing notched fibers. The fibers were first extracted carefully with mechanical tweezers from tows previously separated from the woven fabrics for the three cases analyzed. Special care was taken to avoid damage while handling and mounting fibers for testing.

The fibers were first mounted on a cardboard, ensuring the edges were carefully connected to a metal holder by using copper tape to provide the appropriate electrical paths required during the fiber-milling operation. A FEI Helios NanoLab

Table 2.5: Residual strength and toughness of the fibers analyzed

Fiber	a_0/d [%]	σ_∞ [GPa]	G^f_{IC} [J/m^2]	K^f_{IC} [MPa m$^{1/2}$]	l_p/d [%]
AS4 carbon	12 ± 3	1.3 ± 0.3	50 ± 20	2.1 ± 0.4	0.95
E-glass	11 ± 2	0.5 ± 0.1	4 ± 1	1.08 ± 0.14	1.3
Kevlar KM2	10 ± 3	3.2 ± 0.4	1100 ± 200	6.6 ± 0.6	8.1

DualBeam 600i system equipped with an FIB was used to introduce the artificial notches in the fibers that acted as fracture initiators during the tensile test. Ga^+ ions were accelerated in the FIB system by using 30 kV of potential, with the beam current being adjusted to 80 pA for the carbon fibers and 24 µA for the aramid and glass, respectively. The selection of the appropriate beam current was carried out to avoid microstructural changes due to ion impingement during milling operations. Straight and sharp notches perpendicular to the fiber axis (a straight-fronted edge crack) were introduced in the three structural fibers analyzed with a depth, a_0, to diameter, d, ratio of approximately $a_0/d \approx 0.1$, see Figure 2.9a. The notch radius at the tip resulting from the FIB milling process was approximately ~ 50 nm. The fibers were submitted to an uniaxial tensile test up to failure by using the experimental setup previously described. After the tensile tests, the fracture surface was observed by scanning electron microscopy (SEM) to confirm the fracture location and check the quality of the notch, as shown in Figure 2.9b. The surface texture agrees with the brittle fracture behavior, and the fracture process starting from the FIB-milled crack tip.

The residual strength of the notched fiber, σ_∞, was determined from the failure load and the fiber cross section, Table 2.5. A preliminary comparison of the effect of the notch on the strength of the fiber suggests a higher defect sensitivity in carbon and glass fibers with respect to aramid ones which can be interpreted as a lower material toughness for the first ones.

The toughness of the fibers was evaluated from their residual strength and notch size, based on the Linear Elastic Fracture Mechanics (LEFM) postulates. Consequently, it was assumed that, neither the small crack tip radius (≈ 50 nm) nor the possible material modification induced during Focus Ion Beam milling operations excessively affected the fracture behavior of the fiber and, thus, the result can be considered a good approximation of an intrinsic material property. Under the LEFM

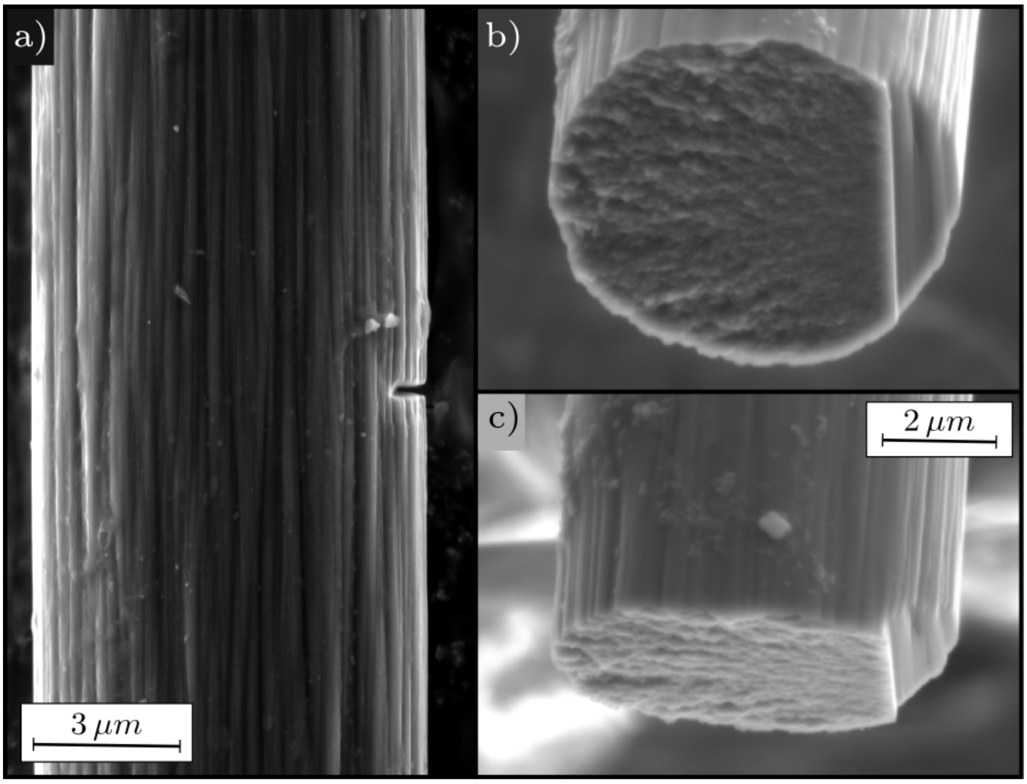

Figure 2.9: a) Longitudinal view of an AS4 carbon fiber after the introduction of a straight notch perpendicular to the axis, b) fracture surface of a notched AS4 carbon fiber after tensile test, and c) detail of the fracture surface texture.

premises, the cracked fiber is stable under specific loading conditions if the stress intensity of the singular stress field around the crack tip (stress intensity factor, K_{I}) is below a given material property known as fracture toughness in normal opening mode I, K^f_{IC}. As a result, the failure of the fiber is dictated by

$$K_I(a, a/d, \sigma) = Y(a/d) \cdot \sigma_\infty \cdot \sqrt{\pi a} = K_{IC} \tag{2.6}$$

where K_{I} stands for the stress intensity factor that is determined from the specimen geometry, the crack depth, a, and the far field stress applied, σ_∞. The factor $Y(a/d)$ is also known as non-dimensional stress intensity factor or shape factor.

Although analytical estimations are found in the literature of the non-dimensional stress intensity factor for linear elastic isotropic solids with a straight-fronted edge crack introduced in a cylinder subjected to uniaxial tension along its axis (Guinea et al., 2004; Toribio et al., 2009), it was decided to determine it numerically using the finite element method because carbon and aramid fibers show a strong anisotropy.

The geometry of the specimen is plotted in Figure 2.10a. A planar straight-fronted crack of depth a_0 is set perpendicular to the loading axis of the fiber of diameter d. For simplicity, only a quarter of the fiber was analyzed thanks to the symmetry of the problem as it is shown in Figure 2.10b. The fiber length, $L = 5d$, was large enough to assume far field loading conditions at the boundaries where a uniform axial stress is imposed without displacements and rotations constraints at the edges. The relative crack to diameter ratio was varied in the range of $0 < a_0/d \leq 0.2$ according to the experimental results aforementioned. As commented previously, both carbon and aramid fibers exhibit a strong anisotropic behavior, mainly due to their microstructure and chains orientation, while the amorphous structure of the glass can be considered elastic isotropic. Carbon and aramid fibers were assumed to behave as transversely isotropic solids, with the directions $2-3$ defining the isotropy plane and 1 the fiber direction (Cheng et al., 2005; Bencomo-Cisneros et al., 2012). The elastic properties used in the simulation are summarized in Table 2.6. In all cases, the fibers were considered homogeneous and, hence, the spatial changes in the properties within the fibers due to their own microstructure are not accounted for (sheath/core structure, for instance).

The particular symmetry boundary conditions used to simulate a state of uniaxial tension for the cracked fiber were $u_3 = 0$ on $x_3 = 0$ and $u_1 = 0$ on the crack plane $x_1 = 0$ and $x_2 > 0$ (see Figure 2.10a). In addition, a uniform normal traction stress, σ, was imposed on the upper face of the fiber, at $x_1 = L$. The geometry of the fiber was first partitioned using a cylinder following the crack tip direction in order to enrich the discretization around the crack tip and capture adequately the large stress gradients in this region, Figure 2.10c. Swept and structured meshes were used, respectively, to discretize the cylindrical region and the remaining volume of the fiber using 8-node isoparametric brick elements in Abaqus/Standard (Simulia, 2013). A mesh sensitivity analysis was performed obtaining an error below 0.5% in the J-integral calculation. The final discretization consisted of 160,000 nodes, as illustrated in Figure 2.10b. Simulations were carried out using Abaqus/Standard within the framework of the small deformations theory (Simulia, 2013).

The evaluation of toughness for the given configuration was carried out based on the J-integral which is the standard approach to characterize the energy release rate associated with a potential crack growth in Linear Elastic Fracture Mechanics ($J = G$ in perfectly brittle materials). In such case, the energy release rate, J, is obtained by numerical integration along the contour Γ (Figure 2.10a) according to

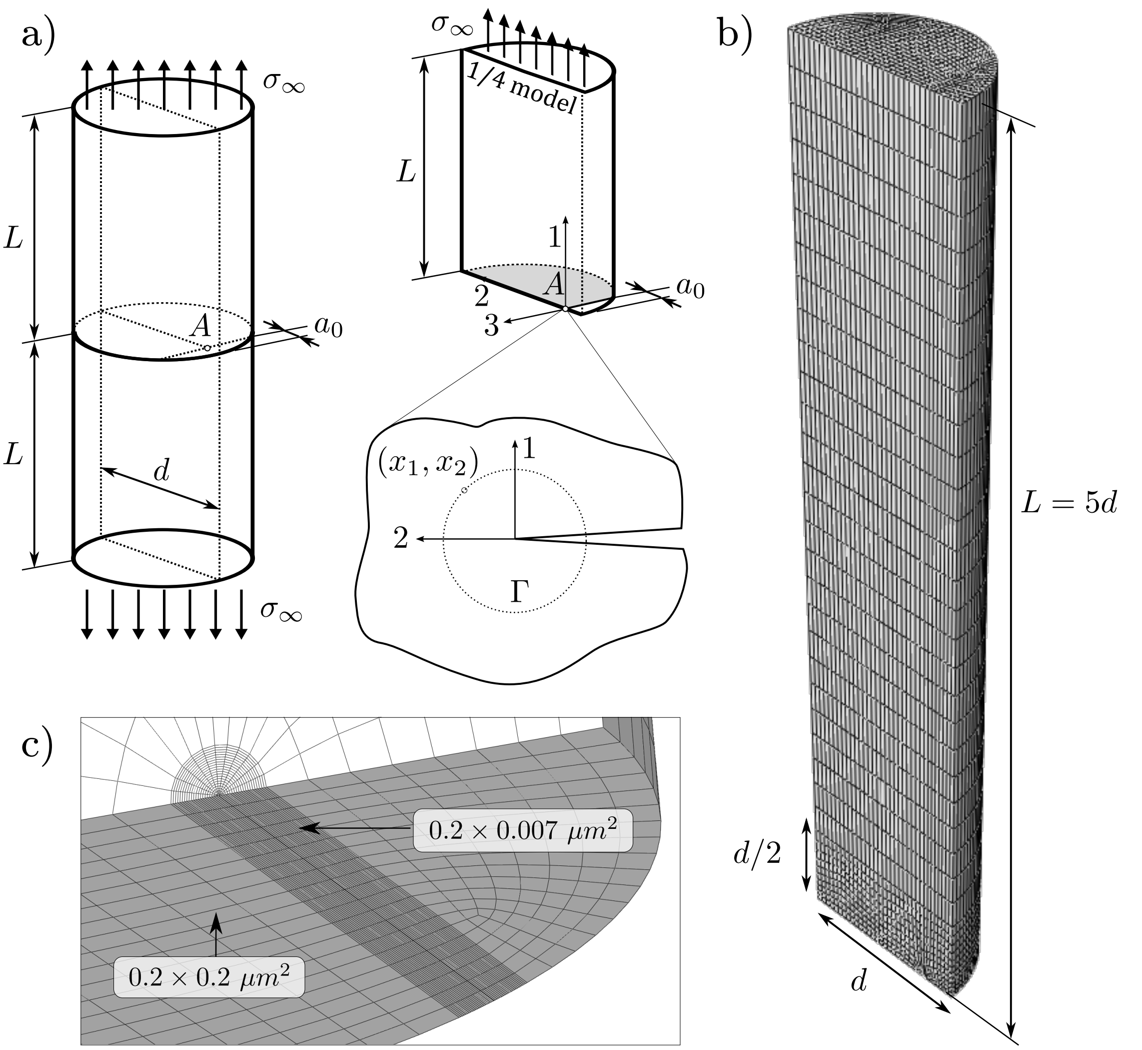

Figure 2.10: a) Geometrical model of the notched fiber and detail of the Γ contour for the J-integral evaluation, b) close view of the finite-element mesh around the crack tip region, and c) global finite-element mesh of the 1/4 model.

$$J = \int_\Gamma \left(W dx_2 - \vec{t} \cdot \frac{\delta \vec{u}}{\delta x_1} ds \right) \tag{2.7}$$

where W is the elastic strain energy density and $\vec{t}$ and $\vec{u}$ are the traction and displacement vectors along the contour Γ. Even though the energy release rate is path independent, several concentric contours surrounding the crack tip are used because of the numerical nature of the finite element solution. In addition, J-integral values are not constant along the crack length and the finite element model is focused on the maximum value which is attained at the symmetry plane (point A in

Table 2.6: Elastic properties used in the simulation of the fibers: AS4 carbon (Herráez et al., 2015), E-glass and Kevlar KM2 (Cheng et al., 2005).

Fiber	E_1 [GPa]	$E_2 = E_3$ [GPa]	$\nu_{12} = \nu_{13}$	ν_{23}	$G_{12} = G_{13}$ [GPa]	G_{23} [GPa]
AS4 carbon	231	13	0.3	0.46	11.3	4.45
E-glass	68	68	0.3	0.3	26.1	26.1
Kevlar KM2	84	1.34	0.6	0.24	24.4	0.54

Figure 2.10a and 2.11c). The stress intensity factor, K_I, at point A was determined from the J-integral using the following Irwin's like relation for anisotropic solids derived by Sih et al. (1965).

$$J = \sqrt{\left(\frac{S_{11}S_{22}}{2}\right)\left(\sqrt{\frac{S_{11}}{S_{22}}} + \frac{2S_{12} + S_{66}}{2S_{22}}\right)} K_I^2 \tag{2.8}$$

where K_I stands for the stress intensity factor in mode I and S_{ij} stand for the compliance tensor components of the anisotropic solid under plane strain conditions:

$$S_{11} = \frac{1 - \nu_{12}\nu_{21}}{E_1} \tag{2.9a}$$

$$S_{22} = \frac{1 - \nu_{21}\nu_{12}}{E_2} \tag{2.9b}$$

$$S_{12} = -\frac{\nu_{12} \cdot (1 - \nu_{23})}{E_1} \tag{2.9c}$$

$$S_{66} = \frac{1}{G_{12}} \tag{2.9d}$$

This expression yields the traditional Irwin's relation for isotropic solids $J = K^2/E^*$, where E^* is the effective elastic modulus under plane strain $E^* = E/(1 - \nu^2)$. The non-dimensional stress intensity factor, $Y(a/d)$, is plotted in Figure 2.11a for the three structural fibers analyzed in this work using the elastic constants shown in Table 2.6. The values of the fiber toughness for the given initial notch depth were determined using the corresponding non-dimensional stress intensity factors determined with the FE model and the residual strength of the fibers and are summarized in Table 2.5. The lowest toughness values were obtained for the E-glass fibers, $K_\text{IC}^f = 1.08$ MPa m$^{1/2}$, and were similar to those reported in the literature

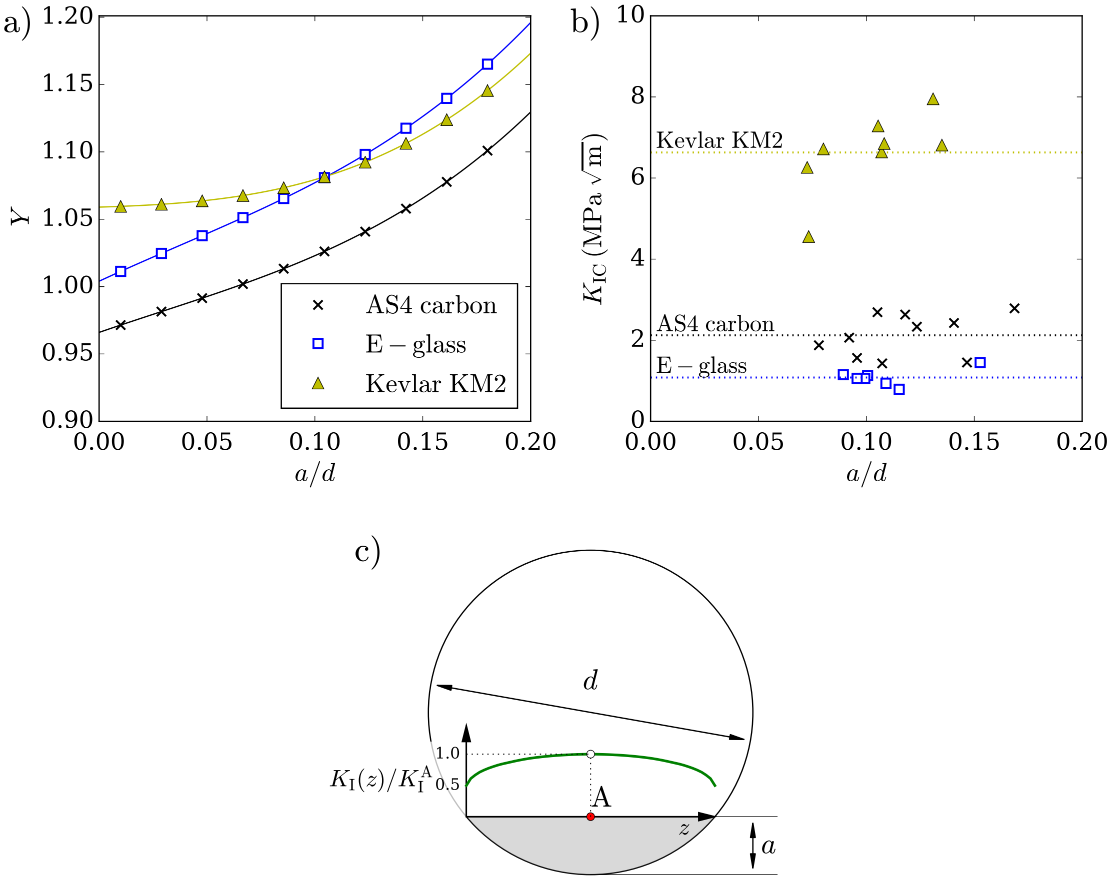

Figure 2.11: a) Non-dimensional stress intensity factors (Y) for a straight-fronted crack for three types of fibers, b) fracture toughness vs. relative notch size, and c) typical stress intensity factor (green) profile along a chordal notch. Note the maximum stress intensity factor occurs at the midpoint, A.

(Wallenberger et al., 2001), and slightly higher than soda lime glass tested by nanoindentation (Gong et al., 2001). High strength Toray T700 FIB notched carbon fibers were tested by Kant and Penumadu (2013) and the results obtained, 1.73 MPa m$^{1/2}$, were similar to those reported here for AS4 carbon fiber (2.1 MPa m$^{1/2}$), while Naito et al. (2008) determined slightly lower values of the order of 1.1 MPa m$^{1/2}$ for other PAN-based carbon fibers (high strength T800G and high modulus M30S, M40S and M50S), although the authors employed an expression for the non-dimensional factor intended for isotropic solids developed by Astiz (1986).

The results of the fracture toughness of the three fibers are plotted in Figure 2.11b, as a function of the relative notch size, to determine whether the internal structure of the fibers may affect its toughness. The calculated values of fiber toughness were almost insensitive to the notch depths for the values employed in the tests. These results are not surprising for the case of amorphous structures as in E-glass fibers, but may take place in highly anisotropic fibers as aramid and carbon which could exhibit sheath/core structures resulting from the manufacturing process. In any case, the notches introduced in the fibers in this work exceed this initial skin effect and the toughness obtained can be considered a homogeneous property corresponding to the central core of the fiber. This effect has been reported by other authors, like Kant and Penumadu (2013), suggesting a skin thickness in high strength T700 carbon fibers of the order of ~ 0.3 µm which is smaller than the average notch depth used in this study ($a_0 \approx 0.9$ µm).

The morphology of the fracture surface analyzed after fiber testing reveals the nature of the dissipation mechanisms for each fiber. The size of the damaged/plastic process zone ahead of the notch tip, l_p, can be estimated according to the well known Irwin relation as

$$l_p = \frac{1}{\pi}\left(\frac{K_{\mathrm{IC}}}{\sigma_0}\right)^2 \tag{2.10}$$

where K_{IC} stands for the fracture toughness shown in Table 2.5, and σ_0 is the average tensile strength of the Weibull distribution, Table 2.4. This estimation indicates whether or not the notched fiber strength is dictated by the stress singularity at the crack tip given by the linear elastic fracture mechanics. All the results are gathered in Table 2.5.

Not surprisingly, the plastic radius, l_p, was well below the fiber diameter, d, being the ratio $l_p/d \approx 1.3$ and 0.95% for the AS4 carbon and E-glass fibers, respectively, indicating essentially brittle behavior of both kind of fibers. In the case of E-glass fibers, the amorphous structure promotes the crack propagation through a single mirror-like cleavage plane as it is observed in Figure 2.12a, dissipating the smallest amount of energy per surface unit corresponding to a brittle fracture. The fracture surface of the AS4 carbon fibers was also flat although a smooth granular texture was observed and illustrates fairly well that the crack propagation origin is found at the midpoint of the artificial notch, as demonstrated in the numerical simulations required for the calculation of the non-dimensional stress intensity factor, see Figure 2.11c. This morphology is typical of PAN-based carbon fibers as was noticed by other authors (Kant and Penumadu, 2013; Ogihara et al., 2009).

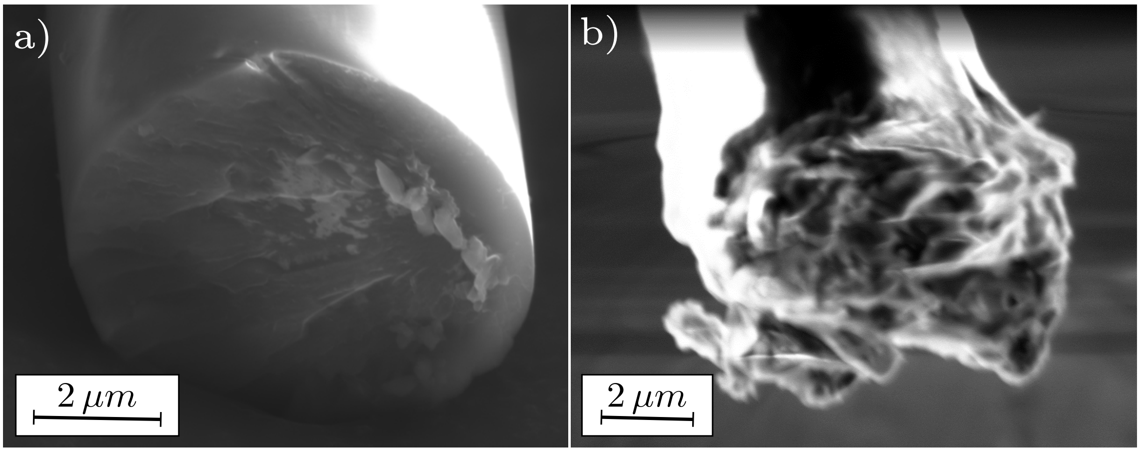

Figure 2.12: Post-mortem SEM micrographs of the fracture surface of notched fibers: a) E-glass and b) Kevlar KM2.

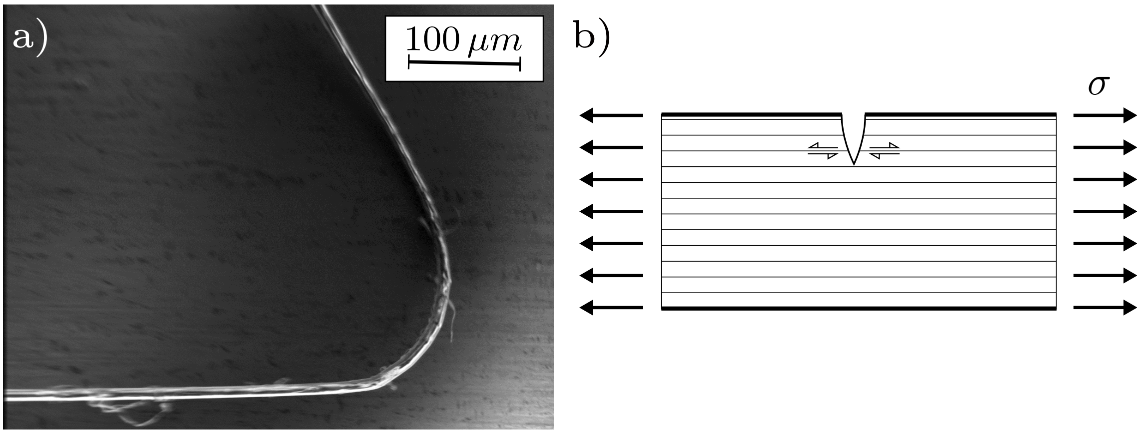

Figure 2.13: a) Coil-shaped Kevlar-KM2 fiber after fracture, and b) sketch of fibril sliding mechanisms of an aramid fiber.

The plastic zone radius of the Kevlar KM2 fibers inferred from eq. 2.10 was $l_p/d \approx 8.1\%$ which is significantly higher than the two previous fiber types studied. In this case, the residual strength of the notched fibers was not significantly affected by the presence of the defect introduced suggesting other nonlinear energy dissipation mechanisms (3.2 and 3.8 GPa for notched and unnotched strength, respectively). This notch insensitivity behavior can be attributed to the fibril structure allowing sliding mechanisms in the fiber direction that can produce in turn a homogenization of the stress field around the notch (Bencomo-Cisneros et al., 2012; Panar et al., 1983). It follows that individual fibrils bundles of aramid fiber are loaded almost homogeneously and independently of the presence of the notch resulting in a less sensitive behavior of the fiber, Figure 2.13b. As a result, Kevlar-KM2 fibers presented the highest toughness compared to carbon and glass fibers. This phenomenon is better understood observing the fractured region of these fibers shown in Figure 2.12b. In this case, the fracture process involves energy dissipation through a larger volume of fiber, not only a planar fracture surface, in the form of plastic deformation and damage around the fractured region (fibrils breakage-slippage, Figure 2.13b). The fiber takes a coiled shape after breakage that can be explained by means of the elastic shock wave generated with the fracture process, similar to a recoil test (see Section 2.1.3). This shock wave subjects the fiber to a high stress level reaching large plastic deformations and permanent bending, see Figure 2.13a.

The work presented in this section was published in Herráez et al. (2016a).

2.3 Discussion

This section presents a summary of the properties defining the mechanical behavior of the FRP constituents measured through experimental characterization, obtained from the literature or estimated based on the authors experience.

A summary of the mechanical properties of the microconstituents of a carbon fiber reinforced polymer (CFRP) is presented in Tables 2.7, 2.8 and 2.9. As noted, there are still properties that need to be derived from the literature or estimated.

Table 2.7: Summary of the mechanical properties characterization of the 8552 epoxy polymer matrix.

Property	Characterization	Value
E^m, elastic modulus	Instrumented nanoindentation, Section 2.1.1	5.1 ± 0.3 GPa
ϕ^m, internal friction angle	Instrumented nanoindentation, Section 2.1.1	$31 \pm 1°$
σ^m_{yc}, compression yield point	Micropillar compression, Section 2.1.1	176 ± 3 MPa
σ^m_t, tensile strength	Literature (Hexcel, 2013)	120 MPa
G^m_t, tensile fracture energy	Literature (Hexcel, 2013)	90 J/m^2

Table 2.8: Summary of the mechanical properties characterization of the fiber/matrix interface of AS4/8552 composite.

Property	Characterization	Value
N^c, normal strength	Assumed as in Ogihara et al. (2009)	42 ± 2 MPa
S^c, shear strength	Fiber push-in and push-out tests, Section 2.1.2	63 ± 3 MPa
G_n^c, mode I fracture energy	Estimated	2 J/m^2
G_s^c, mode II fracture energy	Estimated	30 J/m^2
μ^c, friction coefficient	Estimated	0.2 - 0.4

Regarding the matrix behavior (Table 2.7), during the last years a strong effort has been carried out in the Composite Materials Group at IMDEA Materials to perform a fine characterization of the polymer matrix at the microlevel through instrumented nanoindentation first (Rodríguez et al., 2012b) and later by resin micropillar compression (Naya, 2017). On the other hand, tensile properties of the epoxy resin can be obtained from the manufacturer data sheet (Hexcel, 2013). However, micromechanical *in situ* tests to characterize the tensile strength and associated fracture energy have not been developed yet. For more details on the constitutive model and mechanical properties employed for the epoxy matrix along the following chapters the reader is referred to Section 4.2.2.

Fiber/matrix interface is probably the most difficult constituent to characterize (Table 2.8). Essentially, we cannot refer to it as a "material", but a mechanical interaction between two phases. Therefore, its experimental characterization requires the development of *in situ* microtests. As a simplification, traction-separation laws under normal and shear stresses are assumed (see Section 4.2.2 for more details). Thus, the strength and fracture energies under both failure modes are needed. The interface shear strength, S^c, can be measured through fiber push-out (Canal et al., 2012b) and push-in tests (Rodríguez et al., 2012a), as explained in Section 2.1.2. Nonetheless, no experimental setup has been developed yet to obtain the interface normal strength, N^c. So far, it is estimated as $N^c = 2/3 \cdot S^c$ based on Ogihara and Koyanagi (2010). Finally, a robust experimental methodology to get either of the two fracture energies (mode I, G_n^c, and mode II, G_s^c) is not available in the literature, so they need to be estimated as explained in Section 4.2.2. The value for the friction

Table 2.9: Summary of the mechanical properties characterization of AS4 carbon fiber. Longitudinal elastic modulus values, E_1^f, are shown for the linear and nonlinear models.

Property	Characterization	Value
E_1^f, long. modulus (linear)	Single-fiber test, Section 2.1.3	231 ± 10 GPa ($c_f = 0$)
E_1^f, long. modulus (nonlinear)	Single-fiber test, Section 2.1.3	211 ± 9 GPa ($c_f = 18.7$)
E_2^f, transv. modulus	Estimated	12.9 GPa
G_{12}^f, long. shear modulus	Torsional pendulum test (Tsai and Daniel, 1999)	11.3 ± 0.7 GPa
ν_{12}^f, long. Poisson ratio	Estimated	0.3
ν_{23}^f, transv. Poisson ratio	Estimated	0.46
X_t^f, long. tens. strength	Single-fiber test, Section 2.1.3	4000 ± 900 MPa
X_c^f, long. comp. strength	Fiber micropillar compression, Section 2.2.2	3500 ± 200 MPa
G_t^f, long. tens. fract. energy	Notched-fiber test, Section 2.2.3	50 ± 20 J/m^2
G_c^f, long. comp. fract. energy	Estimated	500 J/m^2

coefficient, μ^c, is also estimated based upon Naya et al. (2017a).

The anisotropic structure of carbon fibers is an additional complexity for their characterization. The mechanical properties in the longitudinal direction are very different to those in the transverse direction. As a simplification, it is commonly assumed that carbon fibers behave as elastic transversely isotropic solids, see Table 2.9. On the one hand, longitudinal characterization of the fiber under tensile loads is a well known field due to their fundamental role as reinforcement within the composite material, either by means of tows containing thousands of filaments or single-fiber tests (SFT), as reported in Section 2.1.3. Longitudinal characterization of fibers was revisited in Section 2.2.3 to consider and measure the nonlinear stiffening of AS4 carbon fiber. Regarding the fracture characterization under longitudinal tensile loads, in this work, a recently developed experimental technique based upon the SFT of a notched fiber is applied not only to carbon fibers, but also to glass and aramid fibers. On the other hand, transverse characterization of fibers is an elusive topic due to the difficulty associated to the microscopic scale fibers. Typically, the transverse elastic modulus of the fibers, E_2^f, is estimated by reverse engineering of the ply transverse modulus. Whereas, the longitudinal shear modulus, G_{12}^f, can be readily derived from the single-filament torsional pendulum test (Tsai and Daniel, 1999). The Poisson coefficients are estimated as well assuming transverse incompressibility of the fiber, $\nu_{23}^f \approx 0.5$, and a typical value of 0.3 for the longitudinal Poisson ratio, ν_{12}^f. The internal morphology of carbon fibers is also responsible for its different mechanical response under compressive and tensile loading. While tensile strength is directly obtained from single-filament tensile tests, the longitudinal compressive strength of the fibers is usually measured through indirect techniques. A new methodology is proposed in this thesis to obtain this property by means of fiber micropillar compression, see Section 2.2.2.

2.4 Concluding remarks

A review of the state of the art on the characterization of FRP constituents has been presented in this chapter (matrix, interface and fiber). In addition, some novel experimental techniques devoted to the longitudinal characterization of fibers have been proposed.

The goal of the experimental characterization of the microconstituents is to apply a *bottom-up multiscale strategy* to predict and infer the mechanical behavior of the material not only at the microscale, but also at the meso and macroscales by means of numerical models and homogenization theories.

For this reason, during the last years, the Composite Materials Group at IMDEA Materials has focused its work towards the *in situ* characterization of FRP constituents (Rodríguez et al., 2012a,b; Canal et al., 2012b; Naya, 2017). This thesis is embedded within this research line and aims at developing experimental techniques for the mechanical characterization of high performance fibers. In this regard, single-fiber tensile tests were carried out on FIB-notched fibers to obtain their effective tensile fracture toughness, G_t^f, while unnotched specimens were dedicated to characterize the nonlinear elastic response of the fiber in the longitudinal direction, E_1^{0f} and c_f. Besides, micropillars were FIB-milled on the cross section of fibers in a ply to directly measure their compressive strength, X_c^f, by uniaxial compression with a flat-punch indenter. The influence of these properties, fiber elastic nonlinearity and compressive strength, on the fiber kinking mechanism will be interrogated in Chapter 6. However, there are still some gaps in terms of constituent properties characterization.

Firstly, the characterization of the matrix under tensile loads needs to be done at the microscale, as it plays a fundamental role on the transverse properties of the composite ply through the matrix ligaments generated between debonded fibers. Understanding the failure mechanisms of the polymer matrix at the microlevel, together with defects distribution, is critical to improve the virtual predictions in terms of fracture behavior and ply toughness. For instance, assuming a fracture energy value ($\approx$ 100 J/m^2) and uniaxial tensile strength ($\approx$ 100 MPa) obtained from coupon level tests in a computational micromechanics model whose elements size is around 1 µm leads to a strain to failure in the order of 200%. Thus, an *in situ* measurement of these properties is required to assess the validity of the macroscopic quantities at different spatial scales as Naya (2017) did with the compressive yield limit.

Secondly, fiber/matrix interface properties stand as the most elusive to be measured. To the best knowledge of the author, in the present there are only reliable *in situ* experimental techniques to obtain the shear strength, S^c. Characterization of the fracture energy under modes I and II, and the friction coefficient of the interface stand out as important gaps in knowledge. For instance, interface toughness plays a main role on the intralaminar and interlaminar toughness of the composite collaborating with the fiber bridging mechanism. Another example is the translaminar fracture toughness of a unidirectional FRP, which is very affected by the interface friction μ^c and fracture energy in mode II, G_s^c, during the process of fiber pull out (Bullegas et al., 2016).

In third place, classically only longitudinal failure of the fibers is considered in numerical models. Nevertheless, under some circumstances shear stresses contribute to fiber failure, as it is evidenced during the propagation of a kink band across a unidirectional FRP ply. New experimental techniques need to be developed to introduce, in a controlled manner, a measurable shear stress field along a fiber up to failure. This new technique might be based upon the torsional pendulum test proposed by Tsai and Daniel (1999) for the elastic shear modulus characterization.

Microstructures generation 3

3.1 Introduction

One of the main features required by the computational micromechanics (CMM) strategy is the artificial generation of representative microstructures. In the case of unidirectional (UD) fiber-reinforced composites, the microstructure corresponds to the fibers cross section distribution. An example of the cross section of an AS4/8552 composite system is shown in Figure 3.1. Typically, aeronautic-grade fiber-reinforced composites contain a very high fiber volume fraction ($V_f \approx 60 \sim 70\%$). However, the numerical generation of microstructures with such high volume fraction is not trivial and has been extensively studied in the literature with circular fibers.

In this chapter, the generation of 2-D microstructures representing the cross section of a fiber-reinforced composite is addressed. The chapter starts with a review of the state of the art on microstructures generation. Secondly, a novel methodology to efficiently generate microstructures with high fiber volume fraction of non-circular fibers is presented. Then, the methodology is employed to generate a variety of microstructures with a high volume fraction ($V_f = 65\%$) of non-conventional fibers, accompanied by its statistical spatial analysis. Finally, an in-house developed software package dedicated to the generation of microstructures called `Viper` is presented.

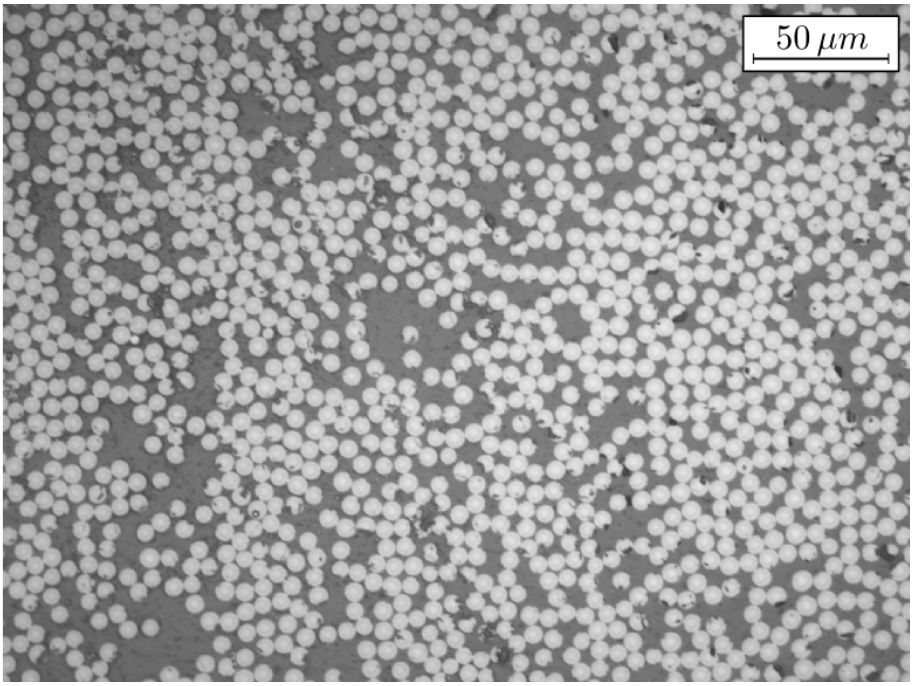

Figure 3.1: Cross section micrograph of a unidirectional AS4/8552 composite ply with $V_f \approx 68\%$.

3.2 State of the art

Artificial generation of microstructures has been a very demanding topic since the beginnings of computational micromechanics. A wide variety of algorithms to generate microstructures of circular fibers can be found in the literature. The simplest ones are based on the *random sequential adsorption* algorithm (RSA) (Rintoul and Torquato, 1997), also known as hard-core model (HCM), which lies in the sequential insertion of fibers into the RVE at arbitrary positions such that they do not overlap each other until the desired fiber volume fraction, V_f, is reached. However, this algorithm presents a jamming limit[1] around $V_f = 55\%$ (Feder, 1980; Tory et al., 1983; Buryachenko et al., 2003). To overcome this issue, similar strategies based on the RSA algorithm are found in the literature (Oh et al., 2006). Based on other statistical descriptors like the radial distribution function, $g(r)$, Bulsara et al. (1999) proposed a RSA-like methodology, but the resulting microstructure was circular, an important inconvenient for its practical application to representative load cases. Böhm (1998) and Segurado and Llorca (2002) modified the RSA strategy to generate 3-D periodic cubic cells of spherical particles with a 50% volume fraction. This is an important achievement as the jamming limit for homogeneous 3-D spheres assem-

[1] Maximum volume fraction of tightly packed homogeneous hard particles.

blies through the traditional RSA approach is around 30%. The strategy followed consists of compacting the particles towards a certain point while the RVE size is reduced. This approach was translated into 2-D periodic microstructures of circular fibers going up to $V_f = 65\%$ (Herráez et al., 2015). Other authors like Trias (2005) considered the fibers arrangement as a *complete spatial random* (CSR) pattern of a Poisson distribution avoiding the periodicity requirement. This approach was improved by Melro et al. (2008) by applying an intermediate step stirring the fibers to generate matrix rich regions where more fibers could fit resulting in volume fractions as high as 65% including the periodicity constraint. Vaughan and McCarthy (2010) were able to achieve 60% fiber volume fractions by adding fibers sequentially according to the first and second nearest neighbor distance distributions obtained from the analysis of micrographs from real microstructures. A similar approach was followed by Yang et al. (2013).

This topic has been addressed within other disciplines like those regarding granular materials such as soils, food grains or pharmaceutical powders. A triangulation-based strategy was developed by Cui and O'Sullivan (2003) to reach a high volume fraction. Nevertheless, particles size is hardly controllable with this technique.

Another approach followed in the literature to achieve even higher fiber volume fractions consists of initially considering a regular periodic pattern of particles (square or hexagonal) and progressively apply random displacements to the fibers (Gusev et al., 2000; Wongsto and Li, 2005; Catalanotti, 2016). The hexagonal packaging of circular fibers reaches the maximum possible fiber volume fraction at $V_f \approx 90\%$. However, the representativeness of the microstructures obtained through this methods is limited to circular fibers.

A different strategy, based on molecular dynamics, was implemented by Ghossein and Lévesque (2012). A fixed number of particles of zero volume are initially placed in the domain, each having a random velocity vector. The particles are then put in motion and their size increases with a given growth rate. Particle-particle and particle-face collisions are solved as elastic collisions during the analysis. The algorithm finishes when the particles volume fraction reaches a target value.

Recently, Pathan et al. (2017) made use of a different approach based on the minimization of a potential which is a function of the fibers overlapping. The procedure starts randomly placing the total number of fibers into the microstructure domain, regardless of fiber overlapping. Then, a potential is computed based on the fibers overlapping, iteratively the fibers are displaced reducing the extension of the overlapping area. These iterations are repeated until the potential is null, i.e. no fibers are overlapping and the resulting microstructure is valid.

One of the problems addressed in this thesis is the generation and analysis of microstructures made of non-circular fibers (Herráez et al., 2016b). For this reason, most of the generation algorithms previously reviewed are not appropriate to reach high fiber volume fractions with non-conventional fiber shapes or heterogeneous diameter distributions, therefore a new algorithm has been developed in this work.

3.3 Generation of microstructures with non-circular fibers

A novel versatile strategy appropriate to generate a wide variety of 2-D microstructures with high fiber volume fractions, regardless of the fibers relative shape and size, has been developed.

The generation process is illustrated in Figure 3.2. Initially, fibers are introduced within the RVE domain up to the target fiber volume fraction is achieved. Then, fibers are enlarged by a given tolerance magnitude, $\tilde{\delta}$, in order to preserve a minimum distance between them. Care is taken to preserve periodicity of the microstructure fiber-wise. At this point, massive fiber overlapping is likely to occur, especially for high fiber volume fractions, see Figure 3.2b. The overlapping of fibers is quantified through a potential, Υ, defined as the summation of the relative overlapping areas as,

$$\Upsilon = \sum_{i=1}^{N} \sum_{j \neq i}^{N} \frac{A_{ij}}{A_i} \tag{3.1}$$

where A_i is the cross section of fiber i, and A_{ij} is the overlapping area of fibers i and j. Afterwards, the overlapping of fibers is solved iteratively not only by translating the fibers, but also rotating them accordingly, as shown in Figures 3.2b, c and d. Overlapping fibers are repelled from each other such that the potential is reduced. The fibers repelling implementation was incorporated by means of the free open source 2-D physics simulator engine `Box2D` (Catto, 2017). This library was originally written in C++ by Erin Catto and published under the zlib license.

It must be remarked that fiber periodicity is preserved throughout this process. Once all the fiber overlaps are solved, beyond a specified tolerance value of the potential, $\Upsilon_{\min}$, the iterative process is finished. The final microstructure is obtained

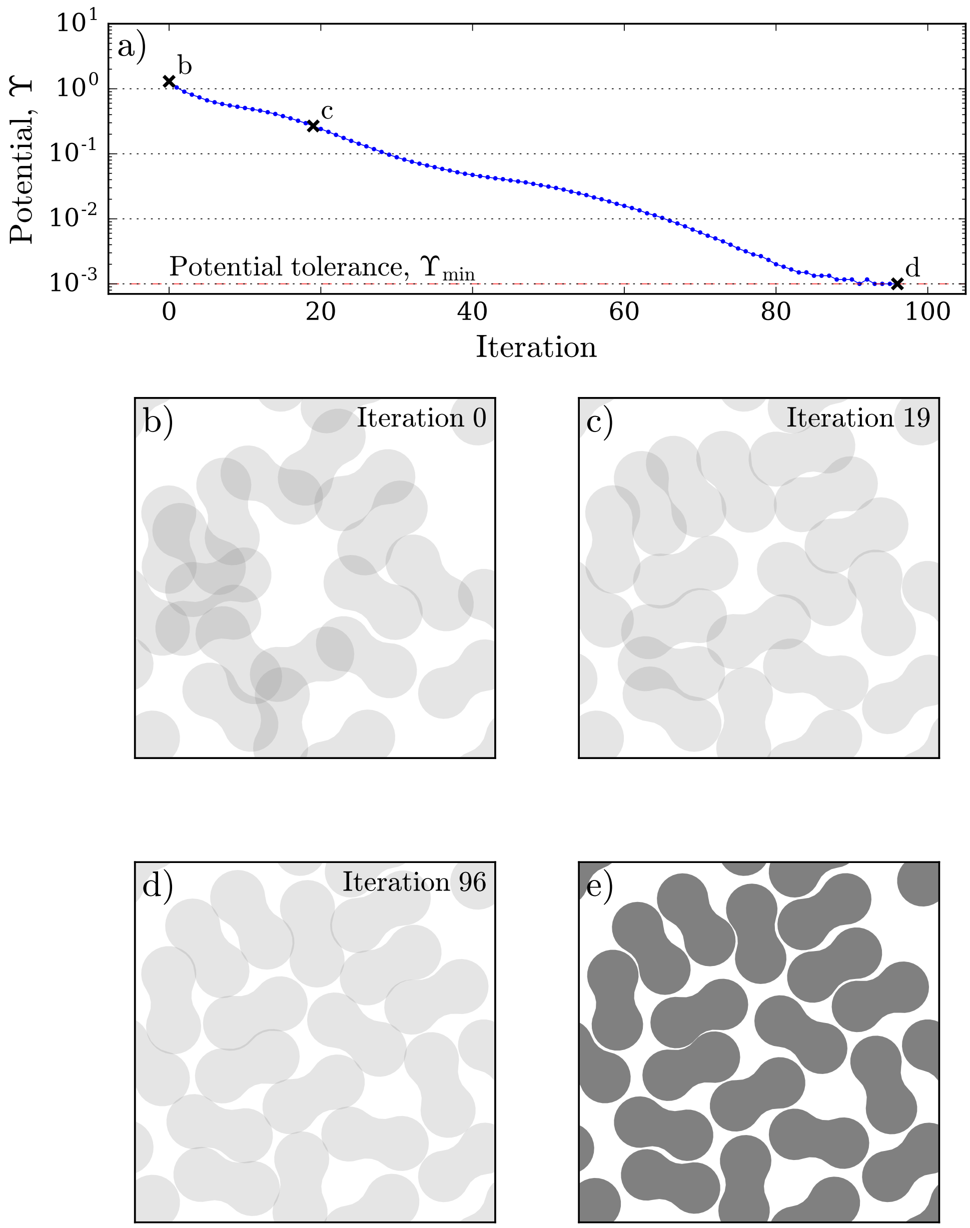

Figure 3.2: Illustration of the generation algorithm applied to a 2-lobular fibers microstructure with $V_f = 65\%$: a) evolution of the fibers overlapping residual as a function of the number of iterations, b) initial positions of the fibers, c) fibers position at increment 19, d) final position of the fibers after potential minimization, and e) final microstructure after fibers shrinking.

after shrinking the fibers by the same tolerance magnitude specified initially, $\tilde{\delta}$, see Figure 3.2e.

The fibers distribution may be heterogeneous with different shapes and sizes, so it can represent hybrid microstructures containing various fiber types.

3.3.1 Statistical analysis of microstructures

Using the algorithm presented in Section 3.3 a statistical analysis is carried out to assess the statistical representativeness of the microstructures generated using various non-circular fibers.

The statistical metrics were compared with the ideal Poisson dispersion of fibers (*complete spatial random*, CSR). The statistical descriptors reported in this section are the following:

- Execution time, t_{exec}.
- Voronoi cells area, c_v.
- Local volume fraction, V_f^{loc}.
- Nearest-neighbors distance, δ_1 and δ_2.
- Nearest-neighbor orientation, θ_1.
- Second order intensity function, $K(r)$.
- Radial distribution function, $g(r)$.
- Two-point probability function, $S_2(\boldsymbol{x})$.

The baseline microstructures have a constant fiber volume fraction of $V_f = 65\%$ with fibers of equivalent cross section regardless of their shape. The effective diameter of a non-circular fiber, d_{eff}, is defined as the diameter of the circular fiber whose cross section is equivalent. Whereas the diameter of a non-circular fiber, d, is defined as the circumscribing diameter of the cross section, i.e. for a circular fiber $d = d_{\text{eff}}$. The fibers size is not homogeneous, instead a normal distribution with a standard deviation of 5% of the effective fiber diameter is selected to introduce another source of variability in the microstructures. The size of the RVE is approximately 12 times the effective diameter of the fibers. A minimum distance between fibers was specified with a value of $\tilde{\delta} = d_{\text{eff}}/40$.

The fiber cross sections considered for this study are the following: lobular with 2, 3 and 4 lobes; polygonal fibers with 3 and 4 smoothed vertices (spolygons); elliptical fibers; C-shaped fibers; and circular fibers as reference. Details of the non-circular fibers geometry definition can be found in the Appendix A.

Table 3.1: Average execution times for microstructures with $V_f = 65\%$ for different fiber shapes and three RVE sizes. The number of fibers for the three RVE sizes is approximately 120, 330 and 2070, respectively. Standard deviation values are shown in parenthesis.

Fiber	Execution time, t_{exec} [s]		
	$L = 12\,d_{\text{eff}}$	$L = 20\,d_{\text{eff}}$	$L = 50\,d_{\text{eff}}$
Circular	2.6 (0.4)	5.9 (0.9)	35 (3)
2-Lobular	4.2 (0.7)	11.3 (1.6)	70 (14)
3-Lobular	4.9 (0.8)	11.8 (1.6)	76 (16)
4-Lobular	6.2 (1.1)	15.8 (4.2)	98 (15)
Spolygon-3	4.9 (0.8)	12.1 (2.6)	81 (10)
Spolygon-4	6.2 (2.2)	13.1 (2.9)	86 (12)
Elliptical	4.1 (0.4)	11.1 (1.4)	69 (13)
C-shaped	6.5 (1.1)	23 (4)	140 (21)

Execution time, t_{exec}

The RVEs generation algorithm was implemented in Python 2.7 and it runs in a single CPU of an Intel® Xeon® Processor E5-2680.

The execution time t_{exec} is reported in order to illustrate the additional computational effort required to deal with complex fiber geometries compared to the reference circular ones. This value is reported not only for the reference case, with RVE size $L = 12\,d_{\text{eff}}$, but also for larger RVEs ($L = 20\,d_{\text{eff}}$ and $50\,d_{\text{eff}}$).

The results are shown in Table 3.1. The lowest execution time is obtained for the microstructures of circular fibers, as expected. Computation of the fibers intersection is the most time consuming task of the generation algorithm, therefore, concave and complex cross sections increase the computational cost noticeably. It is observed that the execution time raises with the number of geometrical features of the fiber section, for instance, microstructures of lobular fibers with 4 lobes are slower to generate than those with 2 and 3 lobes, as it happens with the smoothed polygonal fibers. C-shaped fibers present the most complex geometry and in some cases present convergence issues related to their concave cross section, this effect is more accused the larger the RVE.

Nevertheless, compared to the reference circular fibers, the execution time remains in the same order of magnitude, with increment ratios between 1.5 and up to 4 for the case of C-shaped fibers. Regarding the effect of the RVE size on the computation time, as the number of particles increases with the square of the microstructure size, L, the execution time is proportional to L^2.

The execution times are considered sufficient for the generation of RVEs containing a few hundred or even thousands of fibers, as it is the case of this thesis. The efficiency could be greatly improved by the use of a compiled programming language (e.g. C++) with parallelization capabilities or introducing some modifications in the implementation strategy (e.g. conditioning the initial position the fibers).

Local volume fraction, V_f^{loc}

The local volume fraction is usually represented as a scalar field on the spatial domain of the microstructure, V_f^{loc}.

The local volume fraction can be calculated at any point $P(x, y)$ of the RVE for a given sampling radius, s_r, as the fiber volume fraction within the circle of center P and radius s_r. Figure 3.3a illustrates the procedure to compute $V_f^{\mathrm{loc}}(x, y; s_r)$ in a microstructure of circular fibers with $V_f = 65\%$ and $s_r = 4\ d$. Since the microstructure is periodic, there is no need to correct the edge effect as it is always possible to measure the volume fraction of the fibers falling into the region of interest. The resulting local volume fraction field is plotted in Figure 3.3b. It is observed that the limits of V_f^{loc}, 58.5 and 69% respectively, bound the mean value V_f. This dependence of the maximum and minimum local volume fraction on the sampling

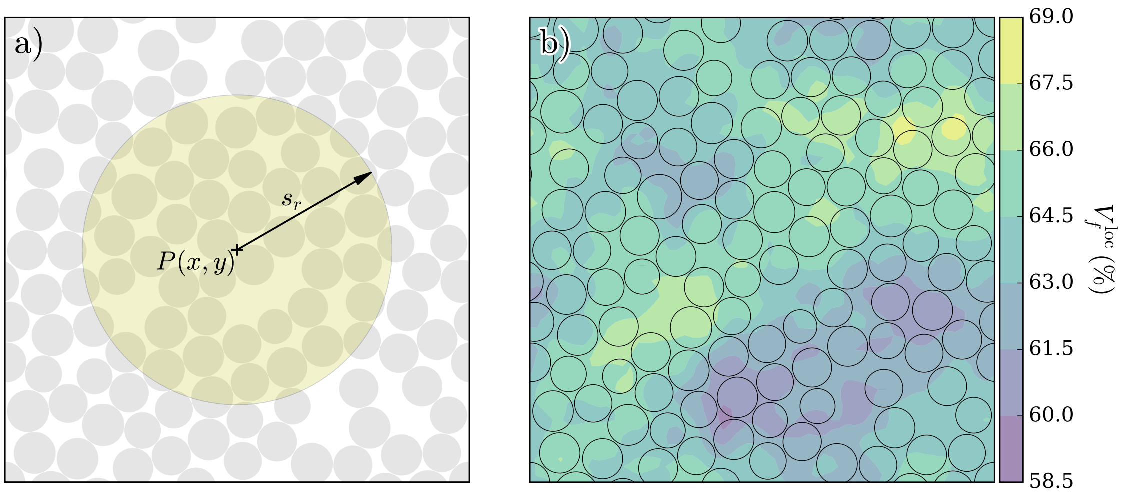

Figure 3.3: Local volume fraction description: a) computation of the V_f^{loc} at P with $s_r/d = 4$, and b) resulting field over the whole RVE with $V_f = 65\%$.

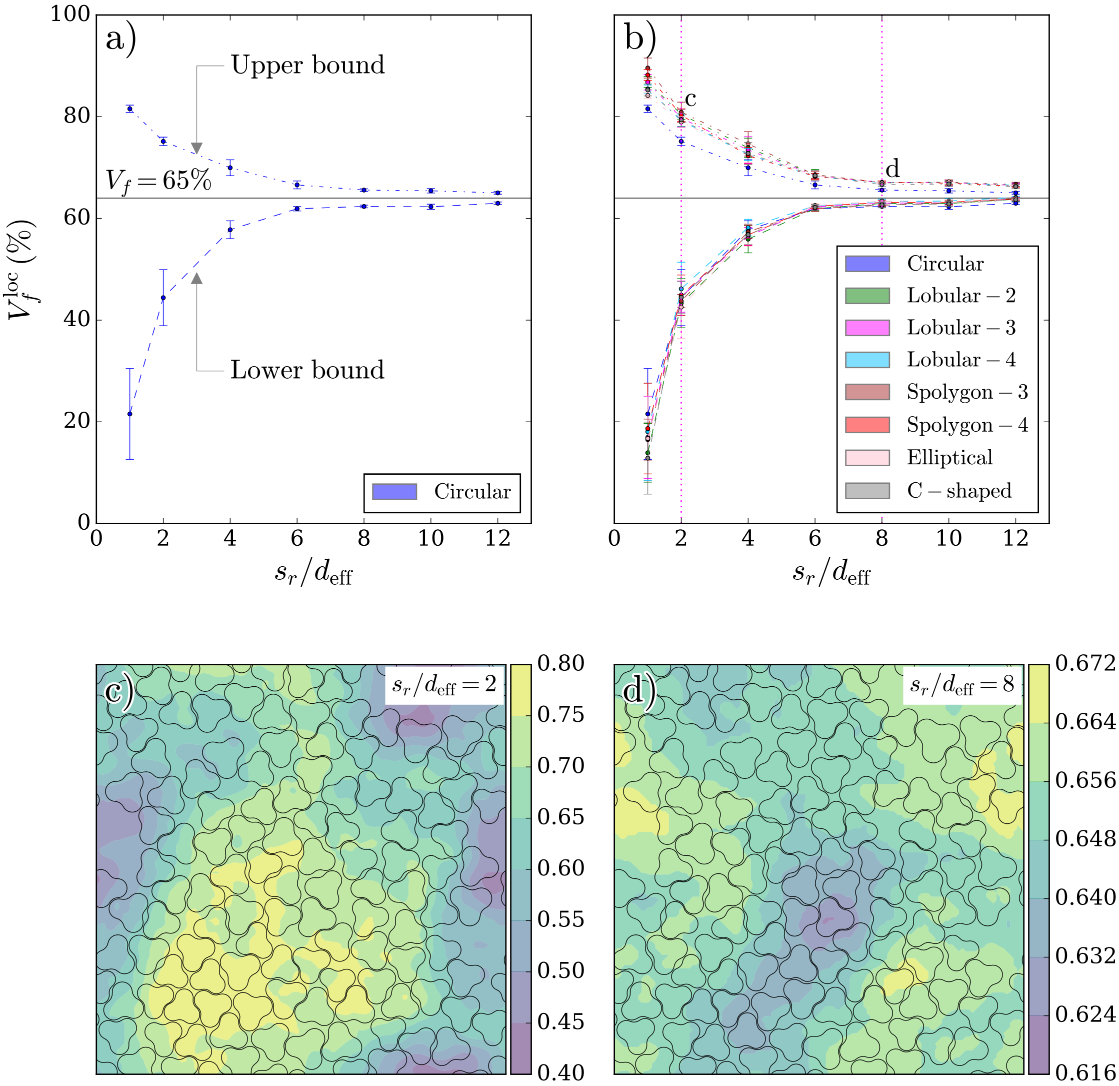

Figure 3.4: Analysis of the local volume fraction as a function of the sampling radius, s_r: a) upper and lower bounds of V_f^{loc} for 10 microstructures with circular fibers, b) comparison of the results for all the fiber cross sections under analysis, c) local fiber volume fraction field of a microstructure of 3-lobular fibers with $s_r/d_{\text{eff}} = 2$ and d) $s_r/d_{\text{eff}} = 8$.

radius can be read as a means to detect matrix rich regions and fiber clusters.

The local volume fraction descriptor was characterized by means of the resulting lower and upper bounds as a function of the sampling radius, s_r. A summary of the results obtained is shown in Figure 3.4. An example of the effect of s_r on the lower and upper bounds of V_f^{loc} is plotted in Figure 3.4a for the case with circular fibers. For very small s_r values, matrix rich regions are identified as the areas with the lowest local fiber volume fraction, as it is observed in Figure 3.4c,

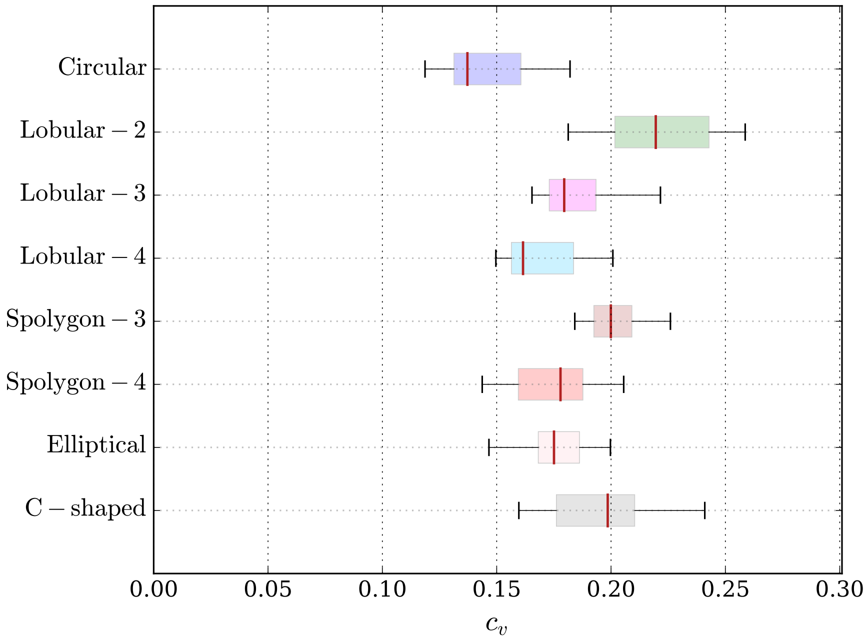

Figure 3.5: Coefficients of variation, c_v, for the microstructure systems studied. Distributions obtained from 10 equivalent realizations.

while areas with closely packed fibers read volume fraction values higher than the average, V_f. Nevertheless, for higher s_r values, both upper and lower bounds follow an asymptotic trend towards the average fiber volume fraction, see Figure 3.4d. As suggested previously, the local volume fraction descriptor can be employed to detect resin rich areas whose size is larger than the sampling radius used.

The V_f^{loc} vs. s_r/d_{eff} curves for the rest of the fiber cross sections are shown in Figure 3.4b. All of them observe the same trend and overlap, so it can be concluded that similar results in terms of fiber clustering or resin pockets are observed. This can be easily explained by the high fiber volume fraction under consideration in this study.

Voronoi cells area, c_v

The Voronoi cells area statistics was computed for all the microstructures generated. For this purpose, the RVE is divided into cells, each of them corresponding with a fiber center such that every cell contains only one fiber center and every point of the cell is closer to its center than the others. An efficient scheme to compute the Voronoi tessellation is the Bowyer-Watson algorithm (Bowyer, 1981; Watson, 1981).

Based on the Voronoi cells area, the coefficient of variation c_v is defined as,

$$c_v = \frac{\mathrm{std}(A_v^i)}{\mathrm{mean}(A_v^i)} \tag{3.2}$$

where A_v^i represents the Voronoi cell area of fiber i, mean and std are the arithmetic mean and standard deviation of the population. The coefficient of variation is a statistical descriptor that quantifies the randomness in the spatial distribution of the fibers. For instance, regular fiber arrangements, such as hexagonal or rectangular patterns, present $c_v = 0$; whereas a high c_v suggests higher randomness in the fibers distribution.

Figure 3.5 collects the distribution of c_v from 10 realizations on each microstructure type represented as box plots. The box plots are intended to describe the population of the variable of interest, in this case c_v, by means of the quartiles. The box encloses the Q1 and Q3 quartiles, whereas the red line represents the median of the distribution (Q2). The coefficients of variation obtained are in the range between 0.12 and 0.25. These values are reasonably high for such dense fiber volume fraction ($V_f = 65\%$), compared to other results reported in the literature for similar volume fractions (Catalanotti, 2016). It is observed that circular fibers show the lowest c_V values, compared to the rest of the fibers. On the other hand, the lobular-2 fibers exhibit the highest coefficient of variation, what can be explained due to their higher aspect ratio.

Nearest-neighbors distance, δ_1 and δ_2

The nearest-neighbors distance descriptors are shown through the *probability density function* (PDF) of the distance between one fiber and its first and second nearest neighbors, δ_1 and δ_2 respectively (Diggle, 1983). This statistical metric informs about the short-distance interaction between fibers.

The results obtained for the RVEs under analysis are plotted in Figure 3.6. The PDFs are obtained using the *kernel density estimation* (KDE) based on normal distributions (Scott, 1992). It is important to note that the minimum allowable distance between adjacent fibers was $\tilde{\delta} = d_{\text{eff}}/40$, the vertical grey line on the plots represents this tolerance distance. As expected, all of the microstructures observe narrow distributions of δ_1/d close to the minimum tolerance distance, $\tilde{\delta}$. Whereas the second nearest-neighbor distributions present higher scatter. Regarding, the fiber shape effect on this descriptor, it is observed that concave fibers (lobular and c-shaped) read

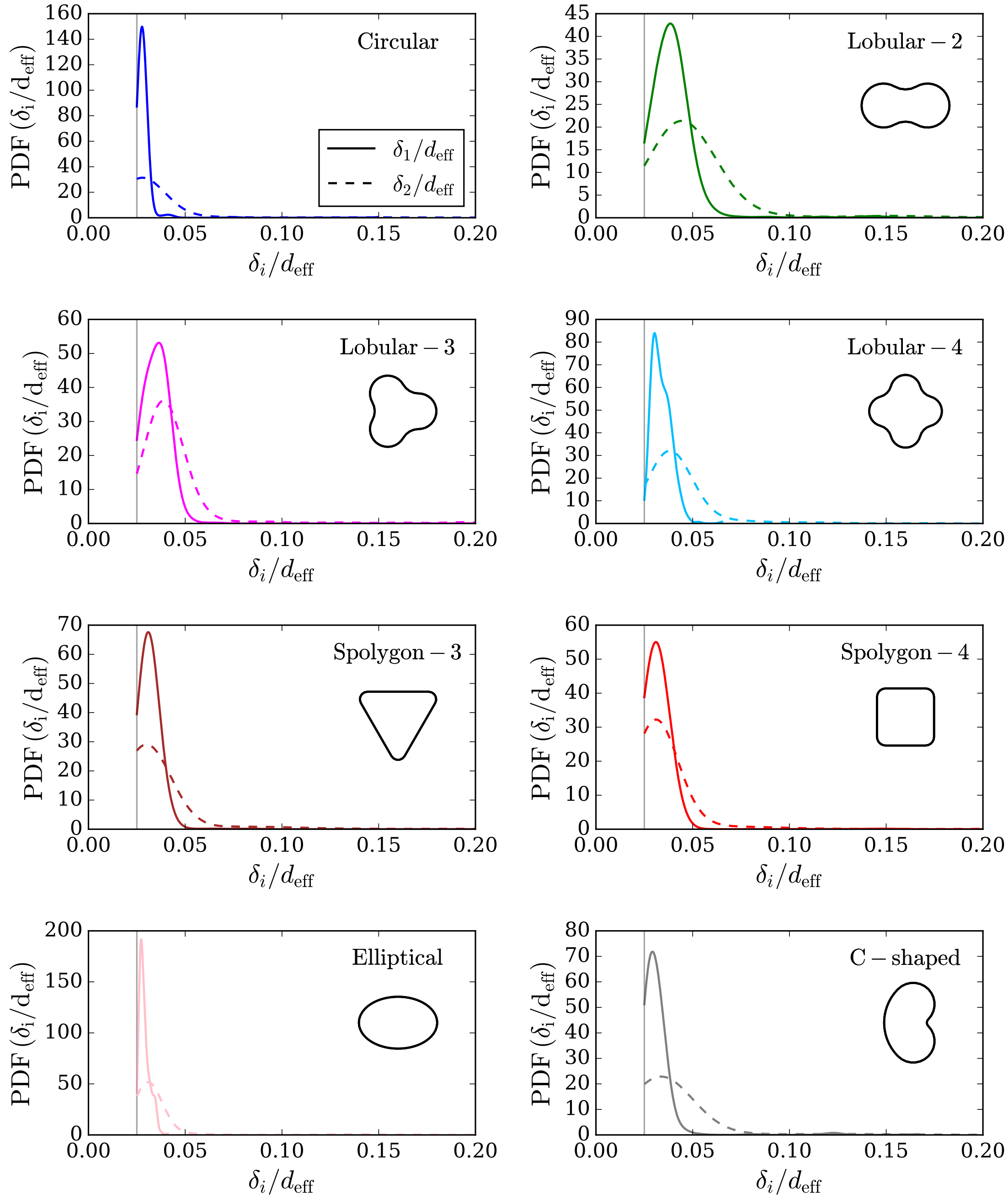

Figure 3.6: Probability density functions (PDF) of the first and second nearest-neighbors distances, δ_1 and δ_2, for the different microstructure cases over 10 realizations. The minimum distance between adjacent fibers was set to $\delta/d_{\text{eff}} = 0.025$.

a higher dispersion in both, first and second, nearest-neighbor distances. Indeed, for lobular fibers the nearest-neighbor distances decrease slightly as the number of lobes increases, due to the higher number of concave-convex entanglements.

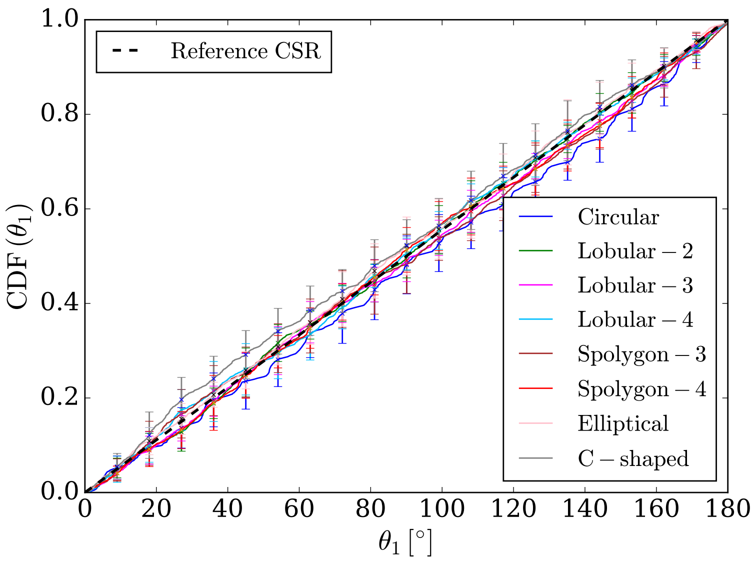

Figure 3.7: Cumulative density function (CDF) of the nearest-neighbor orientation for the different microstructure cases over 10 realizations. Ideal CDF of a complete spatial random distribution, CSR, is shown as reference (dashed line).

Nearest-neighbor orientation, θ_1

The orientations at which the nearest fiber is located, θ_1, can be used to complement the short-distance description of the nearest-neighbor distance metric and the observation of fibers packing patterns, if any. In this case, the *cumulative density function* (CDF) is employed to represent this statistical descriptor.

The CDFs of θ_1 is plotted in Figure 3.7. A CSR distribution would be represented as a straight line, standing for all of the orientations are equally alike to occur. In spite of the high fiber volume fraction, it is observed that all of the microstructures generated are remarkably random, as they follow the same trend of the theoretical CSR distribution (dashed line). For microstructures with extremely high values of fiber volume fraction ($V_f > 80\%$) it is expected to observe preferred orientations representing the hexagonal packing of fibers along the RVE.

Second order intensity function, $K(r)$

The second-order intensity function or Ripley's K-function provides insight about the pattern distribution of fibers from short to long range distances (Ripley, 1977). It is defined as the ratio between the number of extra fibers expected to lie within a radial distance r of an arbitrary point and the actual number of fibers within that

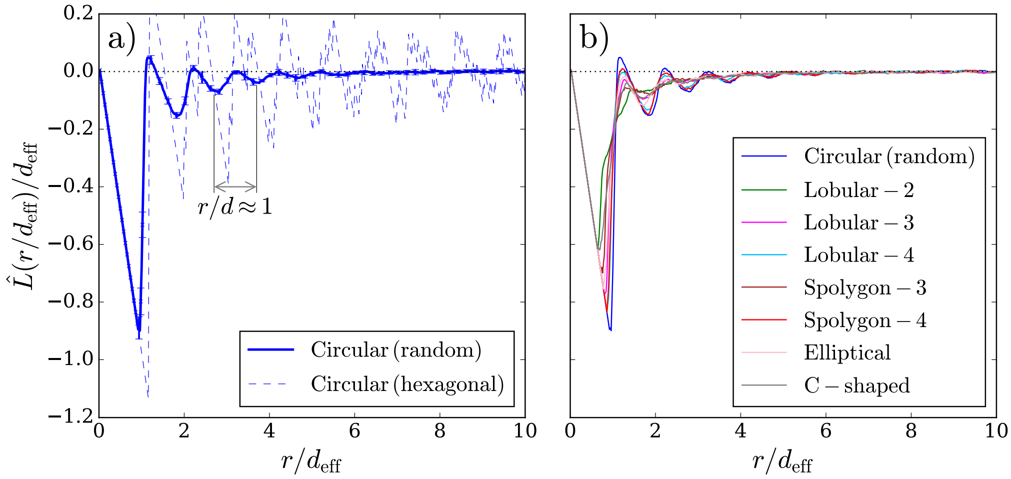

Figure 3.8: Besag's functions, $\hat{L}(r/d)$: a) comparison of a random microstructure with a regular hexagonal pattern, and b) analysis of microstructures with non-circular fibers.

area.

$$K(r) = \frac{1}{N \cdot N_a} \sum_{i=1}^{N} \hat{I}_i(r) \tag{3.3}$$

where N is the number of fibers in the RVE, N_a is the average number of fibers per unit area $N_a = N/A$, and $\hat{I}_i(r)$ is an indicator function which is 1 when the center of fiber i lies within r distance from the reference point and 0 otherwise.

The calculation of the K-function from a non-periodic microstructure requires taking into account the edge effects (Pyrz, 1994). Nevertheless, the application of equation 3.3 to a periodic microstructure is straightforward, as the RVE can be replicated in the two directions (x, y) as many times as necessary. To quantify the randomness in the fibers distribution throughout the microstructure, the resulting K-function is compared to that of a reference 2-D CSR dispersion,

$$\hat{K}_{\text{ref}}(r) = \pi r^2 \tag{3.4}$$

A proper comparison of $\hat{K}$ with $\hat{K}_{\text{ref}}$ can be achieved by the transformation of equation 3.3 by means of Besag's L-function (Besag, 1977).

$$\hat{L}(r) = \sqrt{\frac{\hat{K}(r)}{\pi}} - r \tag{3.5}$$

It is easily observed that for CSR-like distributions $\hat{L} = 0$. For interpretation, positive values of $\hat{L}(r)$ indicate clustering over that spatial scale whereas negative values indicate dispersion.

In Figure 3.8, the resulting L-functions obtained for the microstructures with circular fibers (Figure 3.8a) and for the non-circular fiber cross sections (Figure 3.8b) are shown. The results of a regular microstructure with the typical hexagonal pattern are shown to illustrate the effect of a regular fiber pattern on the L-function, where the sharp peaks and troughs evidence regularity in the fibers distribution. On the other hand, the microstructure generated with the proposed methodology (solid line) shows the typical features of a random dispersion of fibers: an initial peak around $r/d = 1$, followed by some oscillations with an approximate period of $r/d \approx 1$, which progressively decays to $\hat{L} \to 0$ for $r/d \geq 5$. The same features are observed for the non-circular fibers, verifying the long range randomness in the fibers distributions.

Radial distribution function, $g(r)$

The radial distribution function, g, computes the probability of finding the center of a fiber at a given distance r from the center of another particle. It is calculated by determining the number of fibers lying within an annular region of inner radius, r, and thickness, dr, divided by the average number of fibers per unit area, N_a, (Ripley, 1981). Taking advantage of the K-function computed previously, the radial distribution function can be written as,

$$g(r) = \frac{1}{N_a 2\pi r} \frac{dK(r)}{dr} \tag{3.6}$$

By definition, the radial distribution function of a CSR distribution is $g(r) = 1$, see equation 3.4. Thus, a random dispersion of fibers will tend to 1 for large enough r values.

The radial distribution functions computed based on the K-functions from the previous section are shown in Figure 3.9. The g function obtained from a regular hexagonal pattern of circular fibers is plotted in Figure 3.9a (dashed line), observing abrupt oscillations which evidence the regular dispersion of fibers. Nonetheless, a random dispersion of fibers result in a characteristic g function as shown by the solid line: initially, a sharp peak denotes the presence of the first nearest-neighbor ($r/d \approx 1$); followed by some oscillations representing the next rows of neighboring

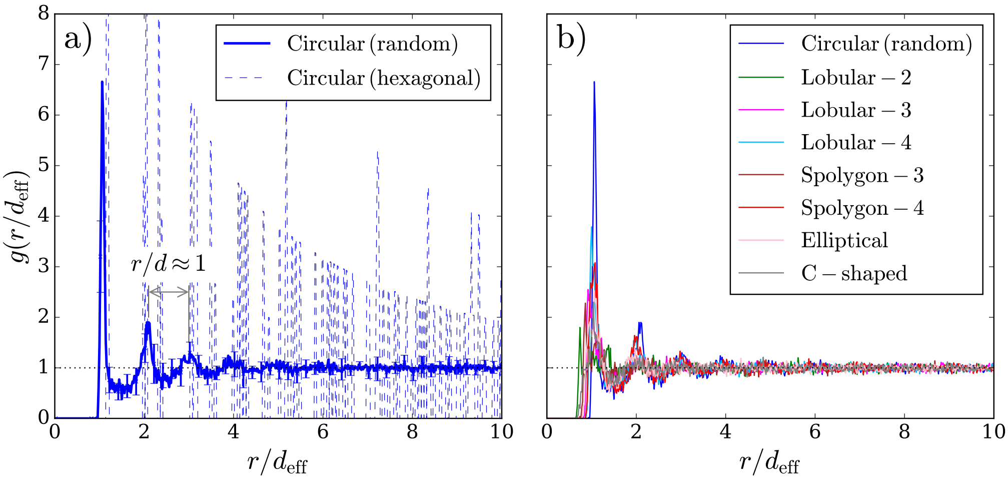

Figure 3.9: Radial distribution function $g(r/d_{\text{eff}})$: a) comparison of random distribution of circular fibers with an hexagonal regular arrangement, and b) comparison of g for microstructures with different fiber shapes.

fibers ($r/d \approx 2, 3, 4\ldots$), which finally decay towards $g = 1$. The same analysis was carried out for the microstructures with non-circular fiber shapes, see Figure 3.9b. Regardless of the fiber cross section, randomness in the fibers distribution is evidenced for long distances ($r/d_{\text{eff}} \geq 5$).

Two-point probability function, $S_2(\boldsymbol{x})$

The two-point probability function, $S_2^{ij}(\boldsymbol{x_A}, \boldsymbol{x_B})$, quantifies the probability of finding simultaneously the phase i and the phase j at two arbitrarily chosen points $\boldsymbol{x_A}$ and $\boldsymbol{x_B}$, respectively, and can be formulated as (Torquato and Stell, 1982),

$$S_2^{ij}(\boldsymbol{x_A}, \boldsymbol{x_B}) = \left\langle \chi^i(\boldsymbol{x_A}, \alpha) \cdot \chi^j(\boldsymbol{x_B}, \alpha) \right\rangle \tag{3.7}$$

where the symbol $\langle\cdot\rangle$ denotes the ensemble average of the product of characteristic functions $\chi^i(\boldsymbol{x_A}, \alpha)$ which are equal to 1 when the point $\boldsymbol{x_A}$ lies in the phase i in the sample α and equal to 0 otherwise:

$$\chi^i(\boldsymbol{x_A}, \alpha) = \begin{cases} 1, & \text{if } \boldsymbol{x_A} \in \mathrm{D}^i(\alpha) \\ 0, & \text{otherwise} \end{cases} \tag{3.8}$$

$\mathrm{D}^i(\alpha)$ represents the domain covered by phase i. In general, the evaluation of the characteristic functions for the computation of the S_2 function may be prohibitively

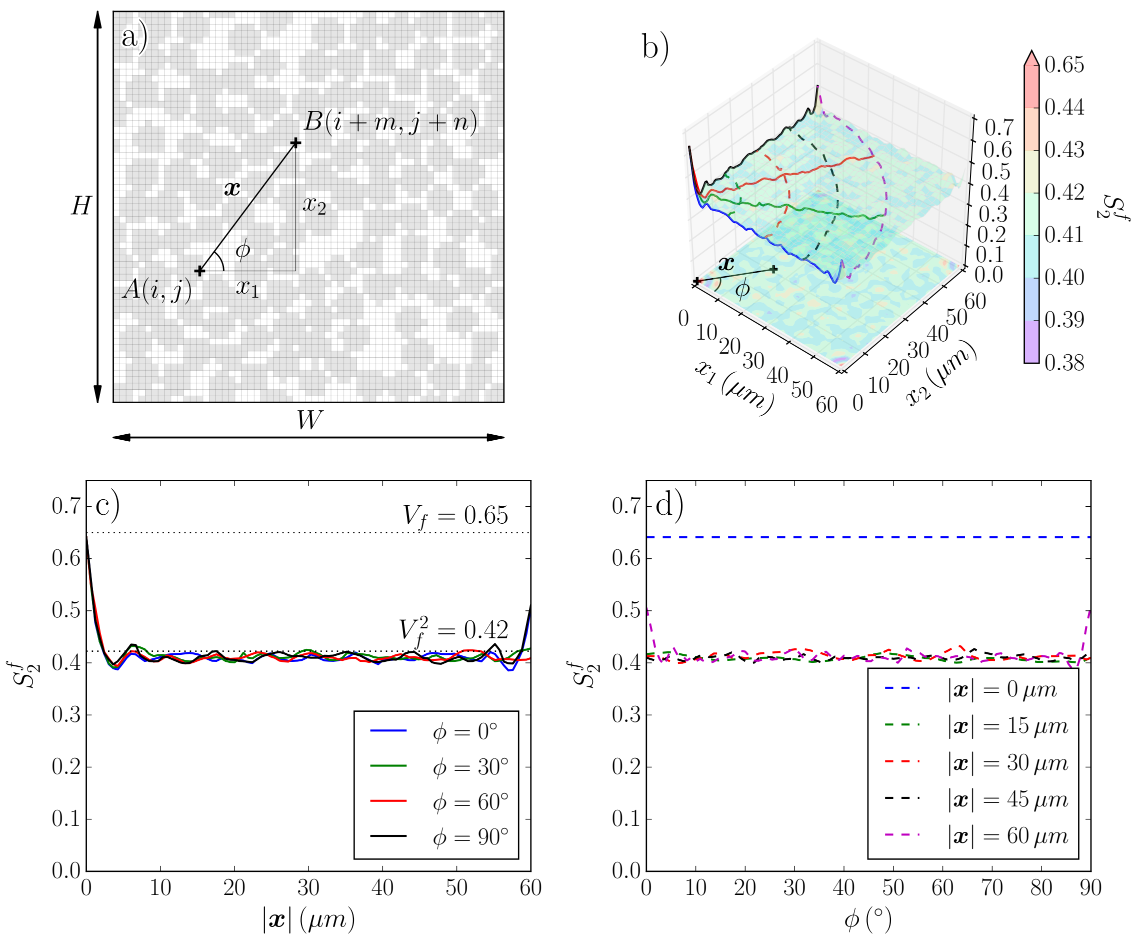

Figure 3.10: Two-point probability function: a) Bitmap discretization of a microstructure with circular fibers, b) S_2^f probability field in the 2D space, c) projection of S_2^f along different orientations (ϕ = cte), and d) projection of S_2^f along various distances ($|\boldsymbol{x}|$ = cte).

costly. Nevertheless, assuming *statistical homogeneity* of the microstructure and validity of the *ergodic hypothesis*, the two-point probability function becomes only dependent on the relative position of $\boldsymbol{x} = \boldsymbol{x_B} - \boldsymbol{x_A}$ (Torquato and Stell, 1982; Torquato, 2002), and is written as,

$$S_2^{ij}(\boldsymbol{x}) = \frac{1}{|\Omega|} \int_{\Omega} \chi^i(\boldsymbol{x}, \alpha) \cdot \chi^j(\boldsymbol{x} + \boldsymbol{y}, \alpha)\, d\boldsymbol{y} \tag{3.9}$$

where $|\Omega|$ stands for the area of the sample analyzed. A number of sampling methods can be employed to determine the values of the two-point probability function, starting from Monte-Carlo method based techniques, later refined by the sampling template approach to sample isotropic microstructures (Smith and Torquato, 1988).

To this end, a pixel-like discretization of the microstructure $W \times H$ bitmap is considered, as in Figure 3.10a. The pixel size selected was 0.5 µm, however, for clarity purposes in Figure 3.10a it is shown with 1 µm. In addition, considering the microstructure is periodic, equation 3.9 reduces to

$$S_2^f(m,n) = \frac{1}{WH} \sum_{i=1}^{W} \sum_{j=1}^{H} \chi^f(i,j) \cdot \chi^f((i+m)\,\%\,W, (j+n)\,\%\,H) \tag{3.10}$$

where % represents the *modulo* operator, and ^{f} represents the fiber phase, with S_2^f abbreviating S_2^{ff}. The summation in equation 3.10 requires an enormous number of operations, $O(W^2H^2)$, for that reason in this work, the more efficient Fourier transform procedure developed by Berryman (1985) is employed to sample the two-point probability function as,

$$S_2^f(\boldsymbol{x}) = \frac{1}{WH} \,\mathrm{IDFT}\left\{\mathrm{DFT}\{\chi^f(\boldsymbol{x})\} \cdot \overline{\mathrm{DFT}\{\chi^f(\boldsymbol{x})\}}\right\} \tag{3.11}$$

with DFT and IDFT stand for the *discrete Fourier transform*, and its inverse, and $\overline{B}$ stands for the complex conjugate of B. The number of operations needed to compute equation 3.11 is $O(WH\log(WH) + WH)$ (Berryman, 1985). The calculations were performed by means of the scientific library of Python: `scipy` (Oliphant, 2007).

The resulting S_2^f field of a random periodic microstructure is shown in Figure 3.10b. A peak of value $S_2^f = V_f$ is observed at each of the corners, representing the periodicity condition. Whereas, in most of the domain it drops to a plateau around $S_2^f = V_f^2$, evidencing there are no long-range correlations in the system, so falling of the two vector ends $\boldsymbol{x}$ into the fiber phase are independent events, each with a probability equals to V_f.

To study the two-point probability function, the S_2^f field has been projected onto $\phi = \mathrm{cte}$ and $|\boldsymbol{x}| = \mathrm{cte}$ curves. The typical curves obtained from the fibers orientation analysis, $\phi = \mathrm{cte}$, are plotted in Figure 3.10c. For all ϕ values there is an initial peak at $|\boldsymbol{x}| = 0$, since the probability to find a zero-length vector (i.e. a point) on the fiber phase is equal to the fiber volume fraction, V_f. For $\phi = 0$ and 90°, the same peak is observed at $|\boldsymbol{x}| = L$, as a result of the RVE periodicity. The plateau encountered has a value around $S_2^f = V_f^2$, as explained previously. This set of curves demonstrate the quasi-isotropic fibers distribution of the microstructure, since there are no remarkable differences between ϕ. In these cases, the elastic properties could

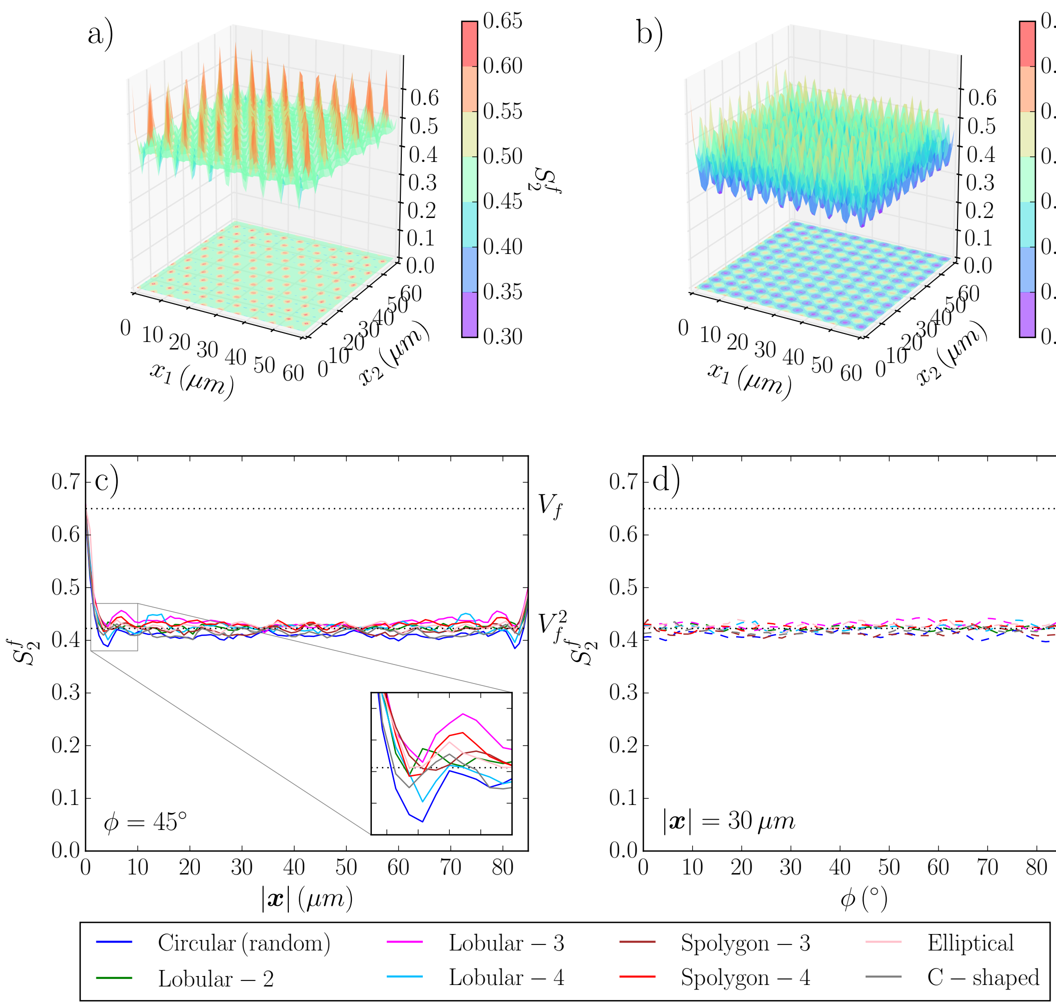

Figure 3.11: Two-point probability functions of various microstructures: S_2^f fields of regular fiber arrangements a) hexagonal and b) square, and results for microstructures with non-circular fibers for c) $\phi = 45°$ and d) $|\boldsymbol{x}| = 30\ \mu m$.

be bounded by the analytical approximation provided by Hashin and Shtrikman (1963).

Regarding the radial analysis, $|\boldsymbol{x}| = \text{cte}$, a constant value of V_f is obtained at $|\boldsymbol{x}| = 0$ as expected. The rest of $|\boldsymbol{x}|$ values experiment a constant expectancy value at $S_2^f = V_f^2$. Again, the microstructure periodicity is evidenced for $|\boldsymbol{x}| = L$ at $\phi = 0$ and 90°.

In the case of patterned microstructures, intense peaks and troughs are generated along the S_2^f field. This is illustrated for a regular hexagonal and square patterns in Figures 3.11a and b respectively. These fiber arrangements observe a regular dispersion of peaks located at the corresponding fiber centers, indicating the presence of preferred $\boldsymbol{x}$ vectors.

The analysis of the microstructures by means of the two-point probability function is collected in Figures 3.11c and d. All the microstructures show the same features as described for the circular fibers RVE: $S_2^f = V_f^2$ for all the domain excepting the RVE corners where its value is V_f. The only difference found lies in the ϕ = cte analysis, where the decay rate for small $\boldsymbol{x}$ is slightly different depending on the fiber cross section, what suggests a different short distance interaction between adjacent fibers due to their convex-concave geometry as shown in the detail in Figure 3.11c.

3.4 A microstructures generator: Viper

The algorithm developed for the generation of random microstructures with high fiber volume fraction and arbitrary fiber shape and size was embedded in a licensed user interface called `Viper`.

The user interface is a ready-to-use software package developed in Python which takes advantage of the `Box2D` library to carry out the fiber repelling process described in Section 3.3.

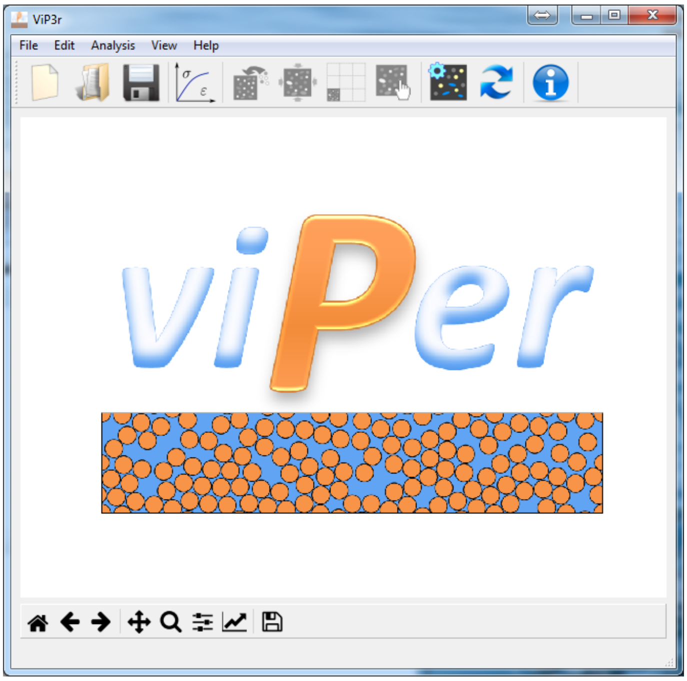

Figure 3.12: Main window of the user interface of Viper.

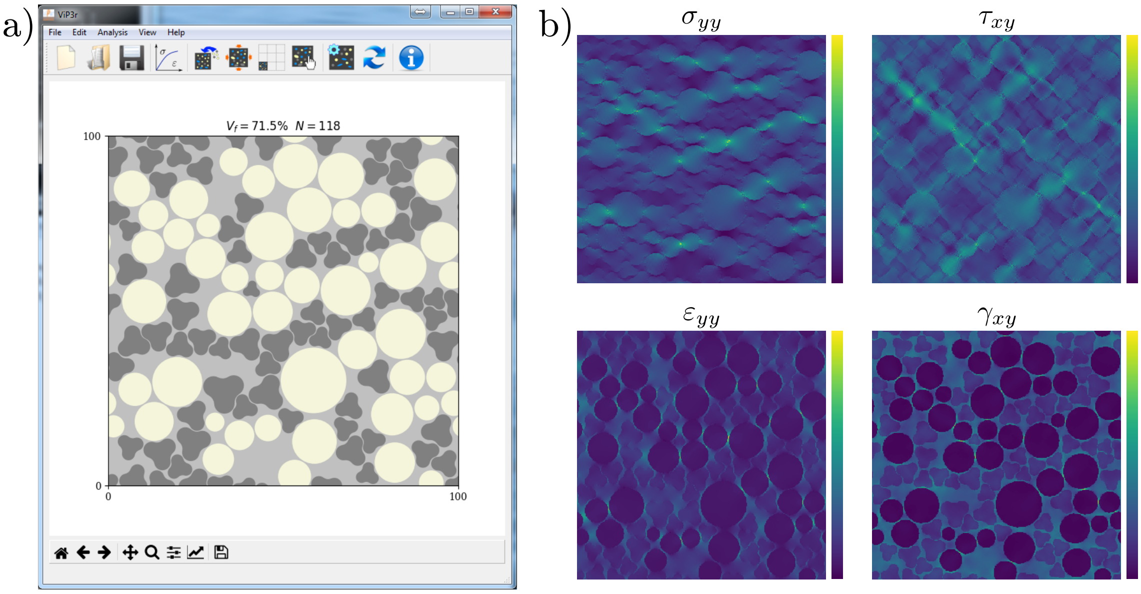

Figure 3.13: a) Illustration of a hybrid glass-carbon microstructure with non-circular fibers generated with Viper, and b) corresponding stress-strain fields obtained by DFT methods (FFT-MAD, Lucarini and Segurado (2018)).

`Viper` also includes capabilities to calculate the statistical descriptors employed in Section 3.3.1: execution time, Voronoi cells area, local volume fraction, nearest-neighbors distance, nearest-neighbors orientation, radial distribution function and two-point probability function.

Other generation algorithms are available for the user such as the *random sequential adsorption* (RSA, Segurado and Llorca (2002)) and the *nearest-neighbor algorithm* (NNA, Vaughan and McCarthy (2010)). Nevertheless, these algorithms are not suited to reach high fiber volume fractions ($V_f > 50\%$) with non-circular fibers.

An important and very time consuming phase of any analysis in CMM is building up the finite element (FE) model. To speed up this stage and make possible the design of models containing hundreds or thousands of fibers, a number of scripts were developed to generate FE models in a very automated manner in Abaqus (Simulia, 2013). Some of these scripts were integrated into a plug-in (CMG), so any user can generate a detailed computational micromechanics model in just a few seconds combining `Viper` and this custom Abaqus plug-in (Viper-CMG). First, the microstructure is generated by means of `Viper` and exported to a text file. Later, the plug-in reads the text file to obtain the microstructure description and generates the corresponding model (RVE, embedded cell model...).

In the present, the estimation of the elastic properties of microstructures by means of DFT (Discrete Fourier Transform) methods is being developed in collaboration with J. Segurado and S. Lucarini (Lucarini and Segurado, 2018), see Figure 3.13. This numerical method is highly efficient and will be extended for the analysis of the viscoelastic and elasto-plastic response of the material.

3.5 Concluding remarks

A novel strategy to artificially generate high fiber volume fraction microstructures with arbitrary fiber shapes and sizes has been developed.

Although various algorithms to generate 2-D microstructures with high fiber volume fractions can be found in the literature, most of them are intended to produce random dispersions of uniform circular fibers (Wongsto and Li, 2005; Catalanotti, 2016; Vaughan and McCarthy, 2010).

In Section 3.3.1, it has been shown the ability of this technique to efficiently generate statistically random periodic microstructures with a wide variety of fiber shapes, including concave cross sections (e.g. lobular, C-shaped). These complex fiber distributions enable the application of *integrated computational materials engineering* (ICME) on the analysis, design and optimization of virtual microstructures with improved properties.

In addition, a user interface called `Viper` was developed to facilitate the microstructures generation procedure, avoiding repetitive time consuming implementations, thus accelerating the preprocessing stage during micromechanical studies. As detailed in Section 3.4, Viper not only includes other commonly used generation algorithms (RSA and NNA), but also provides all the statistical descriptors addressed in Section 3.3.1.

In the next chapters, microstructures generated with `Viper` will be used by means of computational micromechanics (CMM) finite element models to evaluate the transverse strength (Chapter 4) and intralaminar transverse fracture energy (Chapter 5) of the composite material.

4 Effect of fiber shape on the transverse strength

4.1 Introduction

Since the discovery of high-performance carbon fibers, the composite production process has been optimized to maximize their intrinsic mechanical, thermal and electrical properties. Despite these efforts, the morphology of the reinforcing fibers has barely evolved since its discovery and most developments in this field were kept at a basic research level due to major manufacturing difficulties (Chand, 2000; Liu and Kumar, 2012). Nevertheless, some research groups have worked on the development of manufacturing processes of non-conventional fiber cross sections at lab-scale.

Pitch-based carbon fibers with different non-circular cross sections have been extensively studied by Edie and Dunham (1989). This research group determined the main manufacturing parameters, as the mesophase pitch viscosity, winding speed and temperature, controlling the fiber properties using a lab-scale set-up. Trilobal and octolobal fibers were obtained from the extrusion of the filaments through different cross section spinnerets (Edie et al., 1986, 1993). From a mechanical point of view, trilobal and round fibers respond differently to increasing process temperatures (i.e. carbonization). Trilobal fibers exhibited a higher longitudinal elastic modulus and tensile strength than standard circular ones (744 GPa and 2.72 GPa, respectively being 1900 °C the carbonization temperature). Compared to the radial fiber texture, typical of circular carbon fibers spun from mesophase pitch, the microstructure of trilobal carbon fibers does not emanate radially from a center point, but instead grows up from three lines extending from the root of each lobe.

Ribbon-shaped mesophase-pitch fibers have also been produced, obtaining a line-origin transversal texture which enhances their transport properties (Edie et al., 1993). Recent studies demonstrated the possibility to manufacture X-type fibers which theoretically can increase $3 \sim 8$ times the fracture energy of cementitious composites when compared to conventional circular fibers (Zhang and Dong, 2011).

Hollow carbon fibers can be fabricated by several methods such as coaxial electrospinning, bi-polymer blends or fiber templates. A 60% hollow carbon fiber embedded in an epoxy matrix ($V_f \approx 40\%$) can result in a composite material with a density as low as 850 Kg/m^3 as compared with the 1600 Kg/m^3 of the standard fully dense non-hollow composite demonstrating the high potential for structural lightweight applications (Liu and Kumar, 2012). The fiber manufacturer Toray developed hollow carbon fibers with tensile strength and modulus of 2.2 and 190 GPa, respectively, by carbonizing bi-component wet spun sheath-core fibers, with PAN as the sheath and PVA (polyvinyl alcohol) as the core (Liu and Kumar, 2012).

Circular, hollow and C-shaped carbon fibers were also manufactured by melt-spun of isotropic pitch (Shim et al., 2002; Park et al., 2003, 2004). Composite materials were produced by hot-press consolidation of prepregs prepared with this set of non-circular fibers by drum winding. Interlaminar shear strength specimens (ILSS) demonstrated that C-shaped CFRPs perform better as compared with circular baseline composites manufactured maintaining the same equivalent cross section. The C-shape resin contact area was 2.72 times larger that the circular cross section with the same area (Park et al., 2003). In addition, C-shaped carbon fiber composites exhibited excellent energy absorption under impact as well as better fiber wettability and thermal conductivity than circular fibers (Park et al., 2003, 2004). Patterned carbon fibers with customized surface contours were produced by Liu and Kumar (2012) and Hunt et al. (2012) using a combination of a bi-component fiber melt spinning and a sulphonation with polyethylene (PE) precursors. By properly designing the flow path and spinneret geometry, carbon fibers with trilobal, flower, and gear-shaped cross-sections in a diameter range from 0.5 to 20 µm were produced. Although carbon fibers obtained by this method have not reached yet standard mechanical properties (tensile strength 1.1 GPa and modulus 103 GPa), the customized fiber geometry may extend their application in different fields.

Manufacturing of structural composites with non-circular fibers is still kept at laboratory scale limited by the scalability of the production process as compared with conventional circular fibers. Therefore, material optimization to achieve tailored properties based on trial and error campaigns would not be suitable at this scale and a more efficient strategy based on virtual material design and Integrated Computational Materials Engineering (ICME) can be adopted instead, at least during the first stages of the evaluation process (Llorca et al., 2011).

For this purpose, computational micromechanics (CMM) emerges as the most suitable strategy to assess the influence of micromechanical variables on the mechanical performance at the ply level. Artificial microstructures are generated numerically as explained in Chapter 3 by means of `Viper` to represent the actual fibers distribution within the composite ply cross section.

In this chapter, CMM is used to ascertain the effect of the shape of reinforcing fibers on the transverse tension and compression strengths in a carbon/epoxy unidirectional ply with a 50% fiber volume fraction. The results shown in this chapter were published in (Herráez et al., 2016b).

4.2 Computational micromechanics

The micromechanical model developed is based on the analysis of a *representative volume element* (RVE) containing a periodic and random dispersion of parallel fibers embedded in a polymer matrix representing the transversal section of an unidirectional composite ply (González and Llorca, 2007a; Totry et al., 2008a,b). In this work, the volume fraction of fiber reinforcement was set to 50% in all simulations, a value that is usually attained in manufacturing of common structural FRPs. No attempt to ascertain the influence of fiber volume fraction on the transverse strength properties was done in this chapter although damage triggering mechanisms by fiber debonding and matrix shear yielding should not be strongly affected in this case.

The RVE dimensions were large enough to ensure simulation results were size independent in a statistical sense, without exceeding the computational resources, to allow fast and efficient computations. A square RVE of $L = 58$ µm in length was enough to capture the fundamental fracture mechanisms under transverse tension (interface failure) and compression (matrix shear yielding) assuming an average diameter of the fibers of $d = 7.09$ µm (representative of AS4 carbon fibers). Therefore, about 8 fibers along each of the axis of the plane of transverse isotropy ($L/d \geq 8$) are distributed (a total of 42 in the RVE for $V_f = 50\%$). A typical RVE is shown in Figure 4.1a. The RVE was extruded along the fiber axis with a thickness of $w = 0.5$ µm. The results were compared with RVEs containing 80 fibers to ensure

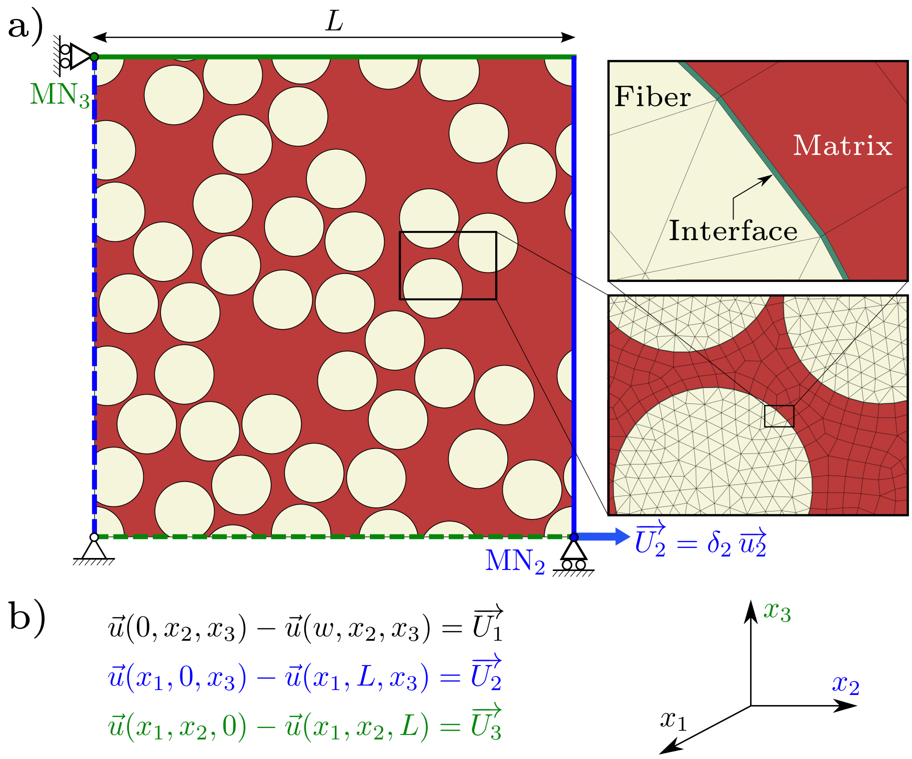

Figure 4.1: Schematic 2-D view of the model showing the detail of the fibers distribution, FEM mesh, cohesive interface and periodic boundary conditions (PBC). The transverse tension loading case along x_2 direction is illustrated.

that the size of the RVE did not influence significantly the model predictions.

4.2.1 Boundary conditions

To minimize the influence of the boundary conditions on the mechanical response of the model, *periodic boundary conditions* (PBC) were employed instead of other strategies like iso-strain or iso-stress approaches. PBC were imposed between opposite faces of the RVE to ensure the displacement continuity with the neighboring RVEs as a jigsaw puzzle. For a given RVE with dimensions of $w \times L \times L$, PBC are introduced as nodal displacement constraints between opposite RVE faces using the equations displayed in Figure 4.1b. Where x_1, x_2, x_3 are the coordinates axis ($0 \leq x_1 \leq w$, $0 \leq x_2 \leq L$, $0 \leq x_3 \leq L$) and $\overrightarrow{U_i}$ is the displacement of the master node i (with $i = 1, 2, 3$). As a result, three master nodes are defined on the three dimensional unit cell: $MN_1(w, 0, 0)$, $MN_2(0, L, 0)$, $MN_3(0, 0, L)$. Uniaxial tension and compression in both transverse directions (x_2 and x_3) can be imposed to the RVE by applying the appropriate displacements to the master nodes, see Figure 4.1a.

For instance, uniaxial tension or compression along the x_2 direction is imposed with $\overrightarrow{U_2} = (0, \pm\delta_2, 0)$, $\overrightarrow{U_1} = (u_1, 0, 0)$ and $\overrightarrow{U_3} = (0, 0, u_3)$, where δ_2 stands for the tensile or compressive displacement applied, and u_1 and u_3 the resulting lateral Poisson contractions.

Previous to the mechanical load, a homogeneous uniform thermal step is applied without external loading to reproduce the cooling down process from curing (175°C) to service temperature (15°C). This thermal step of $\Delta T = -160$°C induces a residual thermal stress microfield as a result of the mismatch in the thermo-elastic constants of fibers and matrix.

4.2.2 Constitutive models of fiber, interface and matrix

The RVE was discretized using finite elements in Abaqus/Standard (Simulia, 2013). The matrix is modeled with 8-node fully integrated brick isoparametric elements (C3D8), while the fibers are meshed with 6-node fully integrated wedge isoparametric elements (C3D6). The fiber/matrix interface debonding was simulated with 8-node cohesive isoparametric elements (COH3D8) inserted at the interfaces between fibers and matrix. Perfect and homogeneous contact between fibers and matrix was assumed without any gaps at the interface. An approximate element size of 0.5 µm was selected.

Carbon fiber

Carbon fibers were modeled as linear elastic and transversely isotropic solids. The elastic modulus in the longitudinal direction of AS4 carbon fibers was obtained experimentally as described in Section 2.1.3 through single-fiber tensile tests, while the properties in the transverse direction were taken from the literature (Herráez et al., 2015). Carbon fiber nonlinear elastic behavior in the longitudinal direction was neglected as this chapter is focused on the transverse loading of a unidirectional lamina (Curtis et al., 1968), see Section 2.1.3 for more details. In addition, fiber fracture is not taken into account in agreement with experiments carried out in AS4/8552 (González and Llorca, 2007a).

The thermoelastic properties of AS4 carbon fibers introduced in the numerical model are reported in Table 4.1.

Table 4.1: Mechanical properties of AS4 carbon fiber (Herráez et al., 2015).

E_1^f [GPa]	E_2^f [GPa]	ν_{12}^f	ν_{23}^f	G_{12}^f [GPa]	G_{23}^f [GPa]	α_1^f [10^{-6} °C^{-1}]	α_2^f [10^{-6} °C^{-1}]
231	13	0.3	0.46	11.3	4.45	-0.9	7.2

Fiber/matrix interface

Fiber/matrix interface failure was taken into account using a classical cohesive zone method, as shown in Figure 4.2a (Camanho and Davila, 2002; Turon et al., 2006, 2010)

To this end, cohesive elements are inserted at the fiber/matrix interface following a mixed-mode traction-separation law where damage onset is controlled by a quadratic stress criterion (Ogihara and Koyanagi, 2010):

$$\left(\frac{\langle t_n\rangle}{N^c}\right)^2 + \left(\frac{t_s}{S^c}\right)^2 + \left(\frac{t_t}{S^c}\right)^2 = 1 \tag{4.1}$$

where $\langle\ \rangle$ stands for McCaulay brackets defined as $\langle x\rangle = (x+|x|)/2$, t_n is the normal traction and, t_s and t_t are the shear components of the traction vector. N^c is the normal strength and S^c is the shear strength assumed to be equal in both shear directions s and t. Initially, the response of the cohesive elements is linear-elastic with a very high penalty stiffness, k_{nn}^c and k_{ss}^c, prior to damage regime initiates, δ_0. Then, linear softening is induced to represent stiffness degradation up to complete failure of the material, δ_u, see Figure 4.2a. Under mixed-mode loading, the energy dissipation is computed by means of a Benzeggagh-Kenane (BK) law as (Benzeggagh and Kenane, 1996),

$$G^c = G_n^c + \left(G_s^c - G_n^c\right) \cdot \left(\frac{2G_s}{G_n + 2G_s}\right)^{\eta_{\mathrm{BK}}^c} \tag{4.2}$$

where η_{BK}^c is the BK power exponent, G_n^c and G_s^c are the normal and shear fracture energies respectively, and G_n and G_s the reciprocal work under mixed mode propagation. Figure 4.2b illustrates the response of the constitutive model under mode I, mode II and mixed-mode conditions ($\delta_n, \delta_s \neq 0$).

Concerning the interface parameters, it will be assumed that the properties in the transverse shear direction, t, are equal to those in the longitudinal shear direction, s. Therefore, two interface strengths (N^c and S^c), two interface energies (G_n^c and

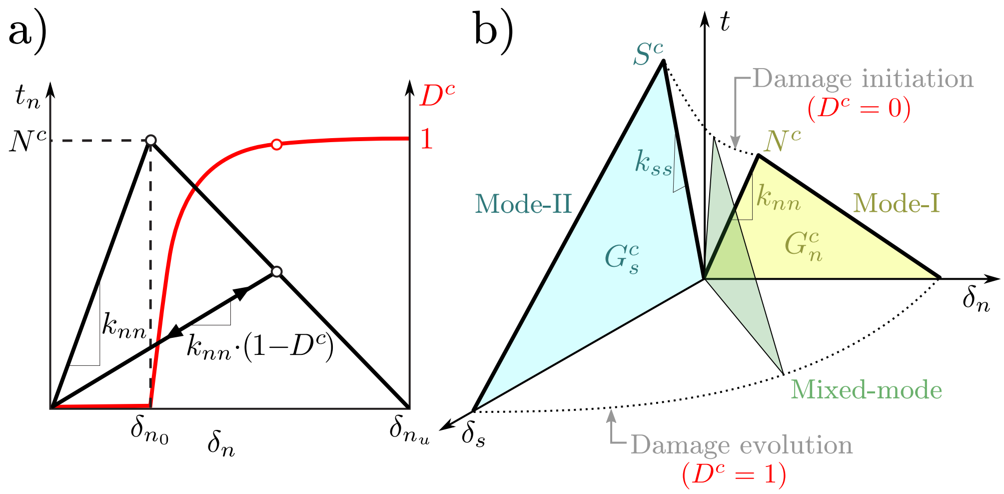

Figure 4.2: Schematic of the traction-separation curves of the cohesive law of the fiber/matrix interface: a) uniaxial loading in the normal direction showing the damage variable evolution, D^c, and b) representation of a mixed-mode case with normal and shear contributions (n and s).

G_s^c), two penalty stiffnesses (k_{nn}^c and k_{ss}^c), and the BK exponent (η_{BK}^c) need to be specified.

The penalty stiffness, k_{nn}^c and k_{ss}^c, are non-physical parameters that should be large enough to ensure displacement continuity in the absence of interface damage while minimizing convergence difficulties due to ill-conditioned stiffness matrix.

The interface shear strength, S^c, was determined experimentally from push-in tests as explained in Section 2.1.2. While the normal interface strength is set to $N^c = 2/3 \cdot S^c$ according to Ogihara and Koyanagi (2010).

Regarding the interface fracture energies, to the knowledge of the author, there are no reliable experimental methods to measure them. Setting the fracture energy values according to parametric studies that aim at reproducing macroscopic experimental results was the approach followed by Canal et al. (2012b). Nevertheless, the fracture energies obtained in this way comprise other dissipation mechanisms together with the pure interface debonding process, essentially matrix plasticity and fiber bridging. In the case of the normal separation mode, n, this is translated into an overestimation of the real interface fracture energy. For instance, assuming a value of $G_n^c = 150$ J/m^2 and linear softening, the ultimate separation at failure would be $\delta_{n_u} = 2G_n^c/N^c \approx 70$ µm, which is around ten times the carbon fiber di-

Table 4.2: Material properties of AS4/8552 fiber/matrix interface (Naya et al., 2014).

N^c [MPa]	S^c [MPa]	k^c_{nn} [GPa/µm]	k^c_{ss} [GPa/µm]	G^c_n [J/m^2]	G^c_s [J/m^2]	η^c_{BK}
42	63	100	100	2	30	1.45

ameter! In view of this, the mode I fracture energy is assumed to be $G^c_n = 2$ J/m^2. Similar values are reported in the literature (Melro et al., 2013; Vaughan and McCarthy, 2010). For the shear fracture energy, G^c_s, a value of 30 J/m^2 was assumed such that the separation at failure was $\delta_{s_u} = 1$ µm. This energy is lower than that of the matrix, representing the brittle nature of the fiber/matrix interface. Finally, from Lopes et al. (2009), the BK exponent was set to $\eta^c_{\mathrm{BK}} = 1.45$.

The interface parameters used in the simulations are presented in Table 4.2.

Epoxy matrix

The epoxy-polymer matrix is represented using the isotropic damaged/plasticity model included in Abaqus (Simulia, 2013). To summarize, the main features of this constitutive model are the pressure dependent yield surface and the distinction between tensile and compressive damage evolution. This model requires not only the definition of the uniaxial tensile and compressive mechanical response, but also the evolution of the yield surface (plasticity) and material degradation (damage). Although this model requires a complex calibration through multiaxial tests, Naya (2017) showed that from the elastic modulus, E^m, the compression yield limit, σ^m_{yc}, and the internal friction angle, ϕ^m, characterization previously shown in Section 2.1.1, the representative behavior of the polymer matrix can be captured.

Under uniaxial tension the matrix behaves as a linear elastic solid until the tensile strength value is reached, σ^m_t, which corresponds to the onset of material degradation (microcracking). Increasing the stretching leads to nucleation and coalescence of voids and microcracks inducing material softening translated into a decay in the stress, σ_t, as shown in Figure 4.3a. A linear decay in the tensile stress profile was selected in this work. Independently, a linear damage evolution law in tension was specified, $D^m_t(\tilde{\varepsilon}^{\mathrm{pl}}_t)$. Strain softening is controlled by the fracture energy of the polymer, G^m_t. However, in a finite element scheme element size regularization is performed through the characteristic element length, l^*, to minimize the influence of the mesh on the results.

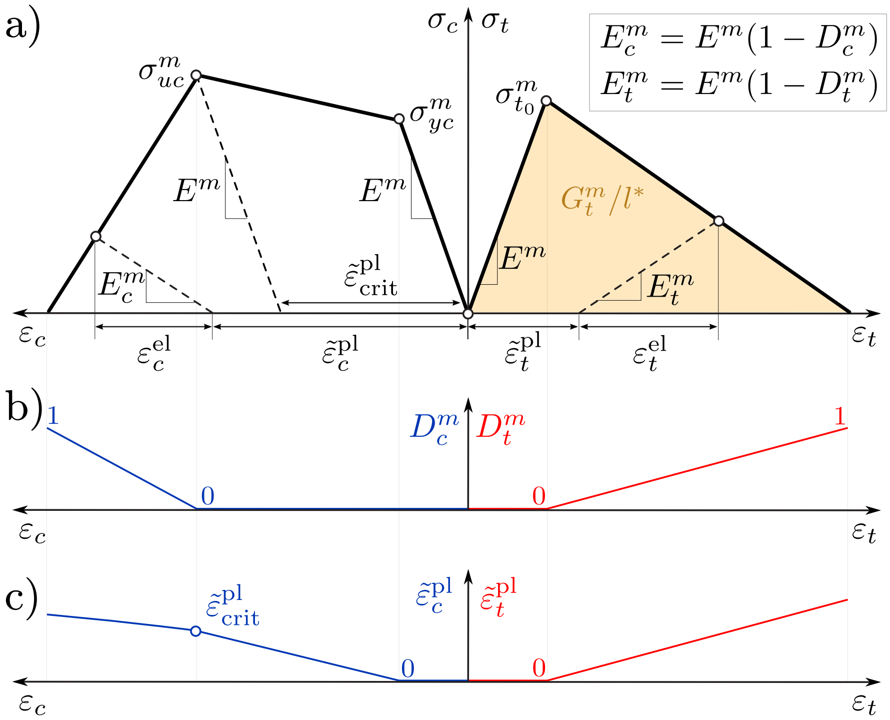

Figure 4.3: Schematics of the constitutive model of the matrix under uniaxial tension and compression: a) stress vs. strain curves, b) damage variables evolution (D_c^m and D_t^m), and c) plastic strain evolution ($\varepsilon_c^{\text{pl}}$ and $\varepsilon_t^{\text{pl}}$).

Under uniaxial compression, the response is linear and elastic up to the initial compressive yield limit, σ_{yc}^m. Then, plastic hardening takes place until the ultimate stress value is reached σ_{uc}^m at the critical plastic strain, $\tilde{\varepsilon}_{\text{crit}}^{\text{pl}}$. At this point material collapse begins by means of a decay in the stress, $D_c^m(\tilde{\varepsilon}_c^{\text{pl}})$, see Figure 4.3.

In order to describe the plastic flow and the yield surface evolution, the damaged/plasticity model requires five additional parameters: the dilation angle, ψ^m, the eccentricity, ϵ^m, the initial biaxial to uniaxial compression strength ratio, $\sigma_{b_0}/\sigma_{c_0}$, the tensile and compressive meridian yield condition ratio, K_c^m, and the viscosity, μ^m. The values selected for these parameters are shown in Table 4.4. In the absence of triaxial test data, the maximum plastic dissipation is assumed in this work. Therefore, the dilation angle is set equal to the internal friction angle, $\psi^m = \chi^m$.

For more details in the parameters selection and the constitutive equations of the matrix constitutive model, the reader is referred to Naya (2017).

Table 4.3: Parameters of the damaged/plasticity model that characterize the 8552 epoxy matrix under uniaxial tension and compression (Naya, 2017).

E^m [GPa]	ν^m	α^m [10^{-6} °C^{-1}]	$\sigma^m_{t_0}$ [MPa]	G^m_t [J/m^2]	σ^m_{yc} [MPa]	σ^m_{uc} [MPa]
5.07	0.35	52	121	90	176	180

Table 4.4: Input parameters of the matrix damaged/plasticity model defining the plastic flow and yield surface evolution (Naya, 2017).

ψ^m [°]	ϵ^m	$\sigma_{b_0}/\sigma_{c_0}$	K^m_c	μ^m
29	0.1	1.29	1.0	0.0001

4.2.3 Microstructure generation

Four different families of fiber cross sections were considered in this work as represented in Figure 4.4 including standard circular, lobular (2, 3 and 4 lobes), polygonal (3 and 4 edges) with smoothed vertices, and elliptical with 0.75 eccentricity ratio. Non-circular fibers size was selected such that the cross sectional area was equal to that of the reference circular fibers ($d_{\text{eff}} = d(\text{circular}) = 7.09$ µm for AS4 carbon fiber) for comparison purposes. The details of the non-circular fiber cross section geometries are detailed in Appendix A. An additional set of microstructures with 2-lobular and elliptical fibers aligned in the x_2 direction was considered to study the effect of cross section orientation on the overall transversal behavior of the composite material. The detailed geometry definition of the lobular and polygonal fibers is presented in Figure 4.5a and b, respectively, with the corresponding dimensions used in the simulations (fillet radii, circumscribed diameter, etc).

It was assumed that the microstructure of the composite was given by an infinite translation of the RVE along the two coordinates axis and thus the fiber positions within the RVE should keep this periodicity condition. Fiber centers were generated randomly and sequentially according to the *random sequential absorption* algorithm, RSA (Segurado and Llorca, 2002). No fiber-to-fiber contacts were included in the model and the position of each new fiber was accepted if the distance between neighboring fiber surfaces was greater than $0.05\,d$. The assumptions made on idealization of the microstructure could potentially have an impact, for instance, in fiber-to-fiber contacts resulting from a deficient resin impregnation or in a highly clustered fiber dispersions, but these effects are considered out of the scope of this work. This

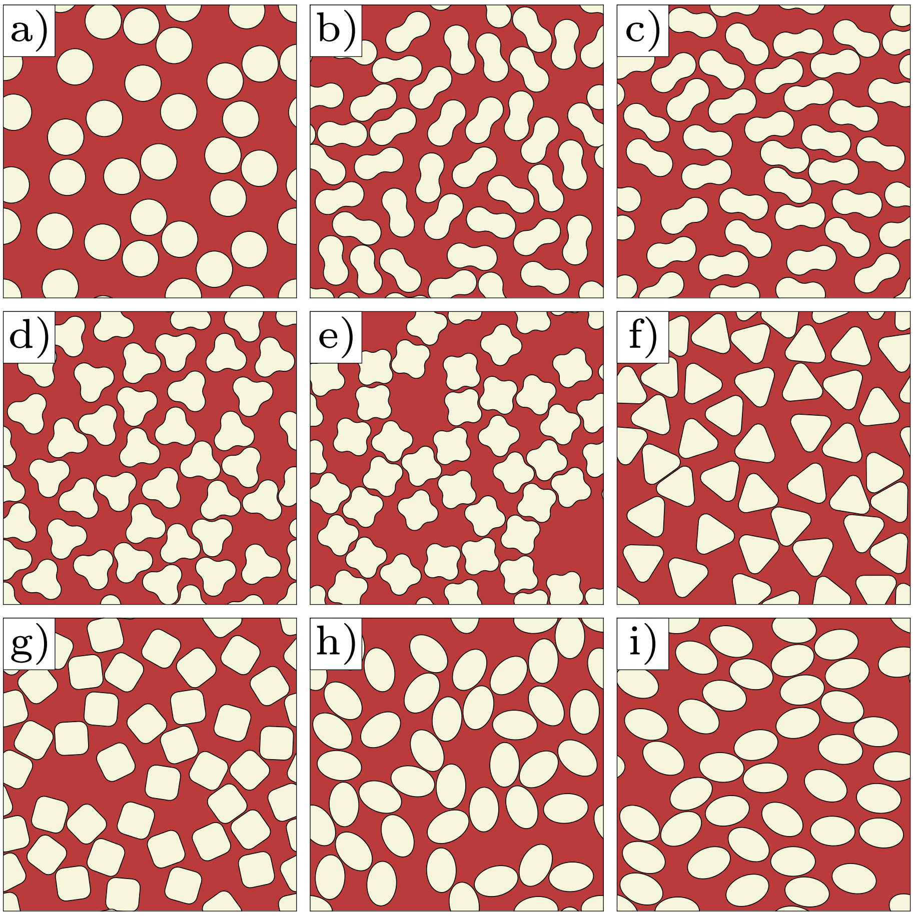

Figure 4.4: Representative volume element example of each microstructure configuration: a) circular, b) 2-lobular, c) 2-lobular aligned, d) 3-lobular, e) 4-lobular, f) 3-polygonal, g) 4-polygonal, h) elliptical and i) elliptical aligned.

restriction ensures an adequate mesh discretization of these regions (González and Llorca, 2007a; Totry et al., 2008a,b). In addition, the distance between the fiber surface and the RVE edges should be greater than $0.15\,d$ to avoid distorted finite elements during meshing. Fibers intersecting the RVE edges were split and complemented at the opposite sides of the square RVE to create a periodic microstructure. New fibers were added until the desired volume fraction of 50% was reached. The model assumed a homogeneous dispersion of fibers within the epoxy matrix and does not take into account local volume fraction variations related to the presence of fiber clusters or resin rich regions.

The microstructures generation process was carried out with the in-house developed software tool presented in Section 3.4: `Viper`.

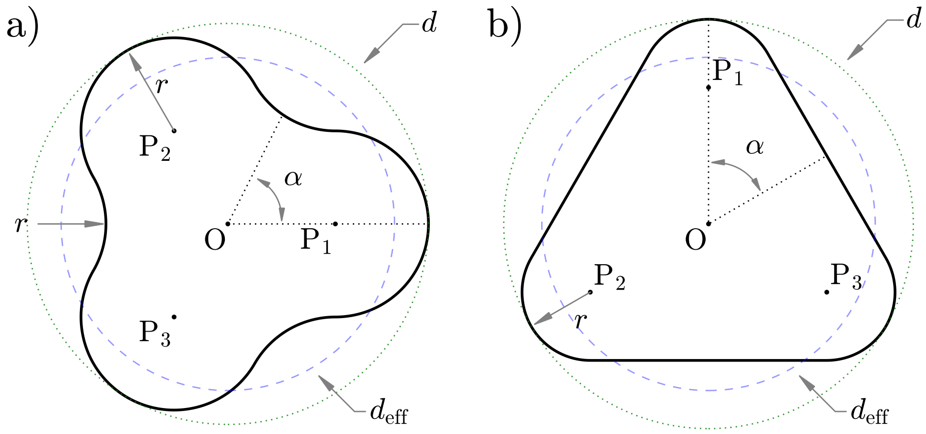

Figure 4.5: Geometry definition and dimensions for lobular and polygonal fiber sections: a) 3-lobular and b) 3-polygonal. Numerical values are shown in Table 4.5

Table 4.5: Summary of geometrical features of the lobular and polygonal sections considered in this work (see Figure 4.5).

Shape	α [°]	r/d_{eff}	d/d_{eff}
2-lobular	90	0.60	1.38
3-lobular	60	0.64	1.20
4-lobular	45	0.65	1.14
3-polygonal	60	0.20	1.23
4-polygonal	45	0.23	1.10

4.3 Transverse ply behavior prediction

Five random RVEs for each of the different configurations considered were generated for the analysis. Simulations were carried out with Abaqus/Standard (Simulia, 2013) within the framework of the finite deformations theory with the initial unstressed state as reference. In the first step, the RVE was subjected to a homogeneous temperature change of -160°C from the stress-free temperature down to service temperature which was followed by the application of the individual loading step (transverse tension or compression along x_2 or x_3 direction). In addition, simulations were performed with the same fiber distributions but without the thermal step to ascertain the effect of residual stresses on the mechanical performance of the unidirectional plies.

4.3.1 Ply thermal residual stress

Residual stresses appeared in the simulated RVEs during the thermal step due to the mismatch between the thermo-elastic constants of the fibers and the matrix. The matrix thermally shrinks more than the fibers during the temperature drop and this strain incompatibility is solved with the generation of a residual stress field at the micro level. The maximum compressive strain on the matrix and the Von Mises strain on the fibers are depicted in Figure 4.6a for a 3-lobular fibers distribution, evidencing tension and compression stress states in the matrix and the fibers respectively. Normal (t_n or interface normal stress, INS) and shear (t_s or interface shear stress, ISS) stresses are generated also at the fiber/matrix interfaces which could potentially affect the overall behavior of the unidirectional ply in the subsequent loading step. Generally speaking, high compressive normal stresses appeared between two closely neighboring fibers being then tensile normal stress distribution in this situation comparatively lower, see Figure 4.6b. In addition, interface shear stresses appeared surrounding the regions of maximum normal compressive stresses to accommodate the high normal stress gradient along the curved fiber/matrix interface, see Figure 4.6c.

The summary of the maximum interface stresses (normal and shear) attained during the cooling step for the different fiber cross sections analyzed is presented in Figure 4.7. The values, average and standard deviation, represented in the plot were obtained from the local maximum of the interface stress obtained in each of the five realizations computed being the scatter attributed to the fibers relative position and spatial distribution.

The results show that maximum normal stress values in tension 28 $\sim$ 29 MPa were attained in those microstructures containing lobular fibers and this effect was essentially attributed to the geometry of the fibers in the concave regions of their perimeter. When the fiber interfaces were flat or convex, the normal stresses were considerably reduced as compared with lobular sections (16 $\sim$ 18 MPa for polygonal and 11 $\sim$ 13 MPa for circular and elliptical). Very interestingly, the higher the number of lobes of such type of fibers, the higher the maximum interface compressive and shear stresses obtained. No significant differences of maximum residual stresses were detected in aligned microstructures (2-lobular and elliptical) when compared with equivalent random distributions.

It should be mentioned that in all cases, the interface stress level obtained was

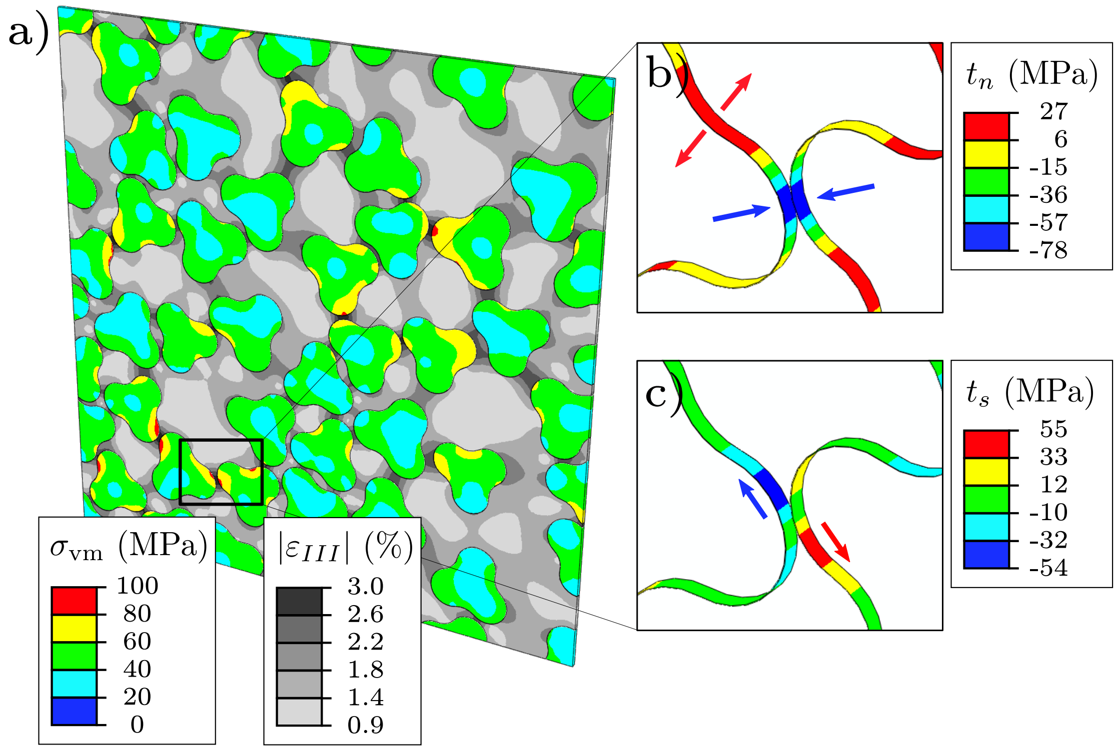

Figure 4.6: Residual stresses after thermal step in a microstructure with 3-lobular fibers: a) Maximum principal compressive strain field in the matrix (gray) and Von Mises stress in the fibers (blue-red), b) detail of interface normal stress (t_n), and c) detail of interface shear stress (t_s).

moderate and the interface damage initiation criterion was not fulfilled (eq. 4.1) being the overall behavior of the unidirectional ply elastic during the temperature drop. Previous studies have demonstrated that thermal residual stresses at the interface may critically affect mechanical response. Thermal compressive stresses provide higher transverse tensile strength (Hojo et al., 2009), while the presence of the interface shear stress contributes to the early onset of damage when transverse loading is applied (Gentz et al., 2004). In this respect, a difference in the transverse tensile strength of lobular fibers configurations is expected *a priori*.

4.3.2 Ply transverse tensile loading

The response of the unidirectional plies under transverse tension is linear and elastic up to the onset of damage which takes place at moderate transverse strain levels of $\varepsilon \simeq 1\%$. This transverse tensile failure is essentially brittle and is triggered by the localization of interface cracks at the poles of the fibers in a given section of the

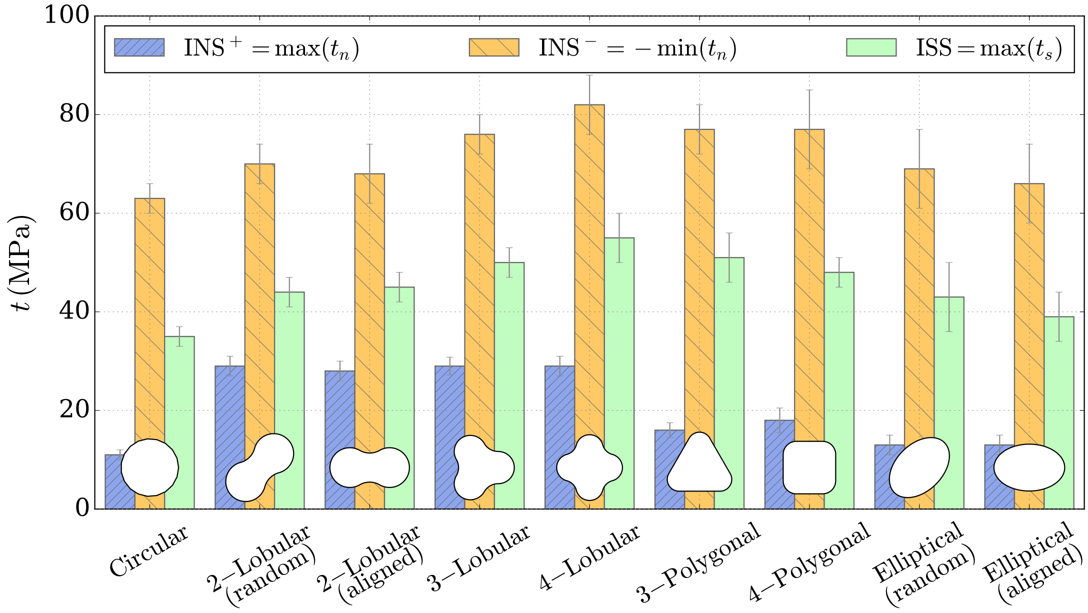

Figure 4.7: Maximum residual thermal stresses at fiber/matrix interface of AS4/8552 with $\Delta T = -160°\mathrm{C}$ for each microstructure configuration.

material. Interface cracks are rapidly localized in a narrow band which is followed by tearing of the ligaments between adjacent fibers (Canal et al., 2012a). These failure mechanisms are accurately reproduced by the RVE simulations. For instance, Figure 4.8a and b represent the final crack configuration right after failure for a homogeneous dispersion of circular and 3-polygonal fibers, respectively. Interface cracks are triggered at the fiber poles and are rapidly interconnected when tearing of matrix ligaments between fibers occurs. The failure mechanisms are the same irrespective of the shape of the fibers, although slight differences in the crack paths were observed depending on the geometry connecting the poles of the fibers as shown in Figure 4.8c and d.

The results shown in Figure 4.9a represent the transverse tensile strength, Y_t, for the RVEs containing different fiber cross sections. Circular fibers exhibited the most balanced tensile strength in both directions, x_2 and x_3, among all the fiber cross sections analyzed. This effect can be endorsed to the lower stress concentration created by the circular fibers when compared with polygonal or lobular. For instance, approximate knock-down factors of 17% and 8% are obtained for triangular and quadrilateral fibers, respectively, although this effect can be even more detrimental on the material performance depending on the fillet radii used, see Figure 4.5b.

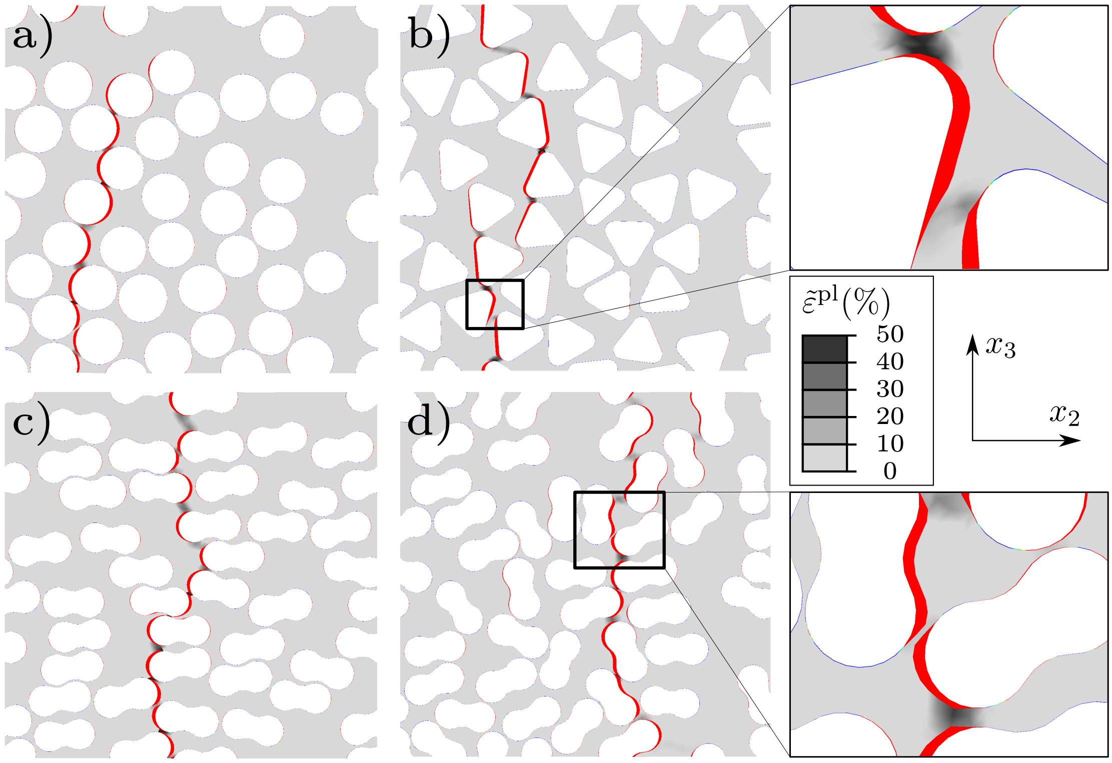

Figure 4.8: Equivalent plastic strain (gray-scaled) and interface damage (red) under transverse horizontal tension ($\varepsilon \simeq 1.0\%$): a) circular fibers, b) 3-polygonal fibers, c) 2-lobular aligned fibers, and d) 2-lobular fibers.

All configurations showed transversely isotropic behavior with the exception of the aligned 2-lobular and elliptical fibers. In both cases, the transverse strength was similar in the x_2 direction, $Y_t \approx 68$ MPa, although an important reduction in the transverse strength in the orthogonal direction x_3 can be observed (-33% and -15% for 2-lobular and elliptical, respectively). This effect can be attributed, in lobular fibers, to the initial residual tensile interface stress (INS$^+$) which prompts the earlier interface failure as compared with convex sections, as shown in Figure 4.7.

Simulations were repeated without the initial thermal step in order to ascertain the effect of residual stresses on the final transverse strength of the fibers distributions. Average values and standard deviations corresponding to all the realizations in both directions, x_2 and x_3, are depicted in Figure 4.9a. In all cases, the transverse tensile strength decreased in the absence of the thermal residual stress indicating a strong shielding effect due to their compressive nature. Very interestingly, circular and elliptical fibers presented the highest thermal residual stress effect ($+15 \sim 20\%$)

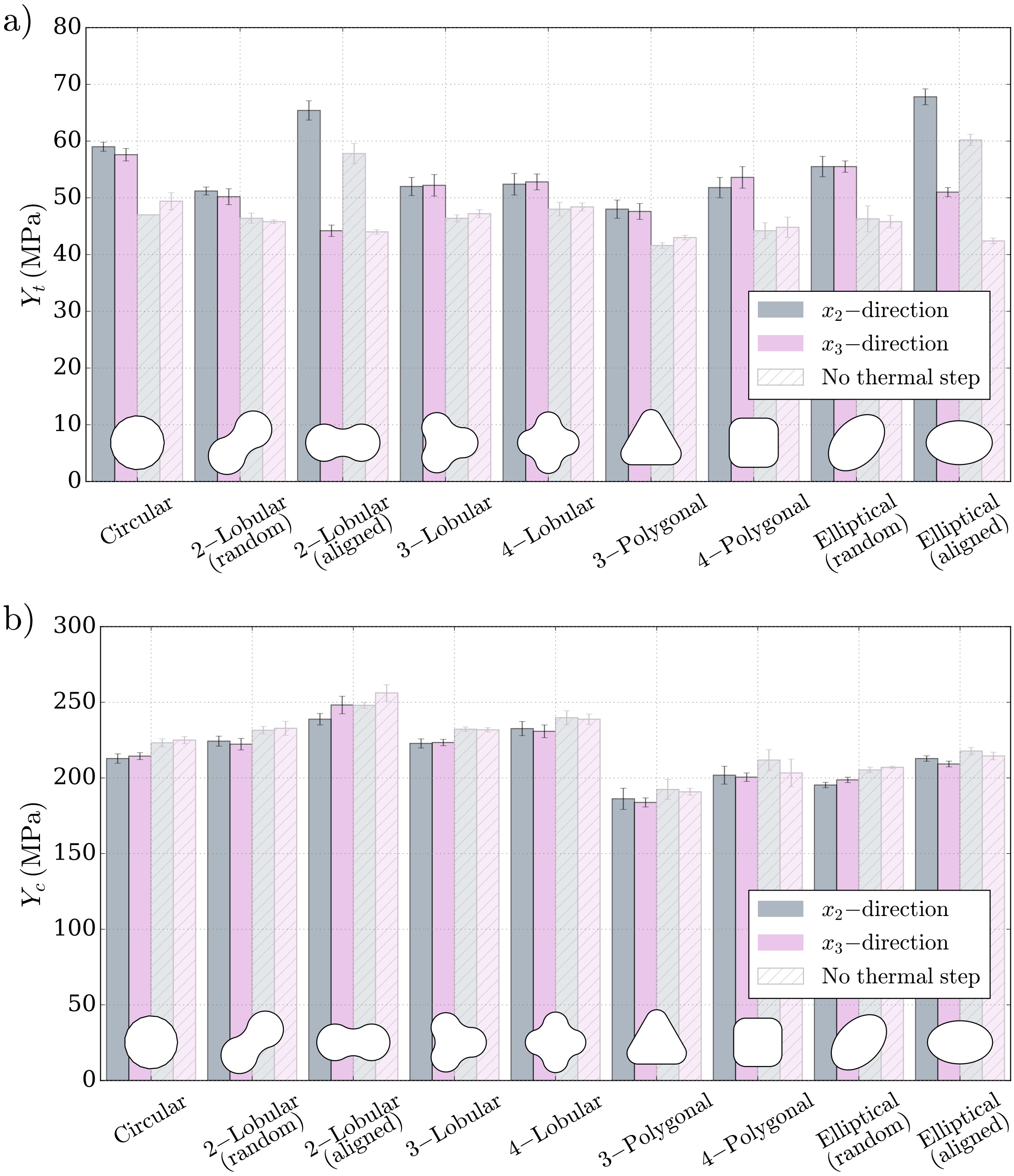

Figure 4.9: Effect of residual stresses on the transverse strength of non-circular fibers RVEs: a) tensile strength, Y_t, and b) compressive strength, Y_c.

what can be explained by the larger ratios between the compressive and tensile normal interface stress.

4.3.3 Ply transverse compressive loading

Experimental evidences demonstrated that unidirectional plies subjected to transverse compression fail after significant nonlinear deformation ($\varepsilon_c \approx 2 \sim 4\%$) by the development of matrix shear bands where severe plastic deformation and fiber/matrix interface debonding occurs. The final failure is produced through an inclined crack at $\sim 56°$ with respect to the plane perpendicular to the loading axis in the case of standard carbon/epoxy composites (González and Llorca, 2007a; Naya et al., 2017a). RVEs subjected to transverse compression failed following the aforementioned mechanisms as it is illustrated in Figure 4.10 for a homogeneous dispersion of circular, 3-polygonal and 2-lobular fibers (aligned and randomly dispersed) where the contours of accumulated plastic strain for an overall strain of $\varepsilon_c \approx 4\%$ are plotted for comparison. Interfacial voids controlled the transverse compressive strength of the material leading thus to the localization of the matrix plastic strain between adjacent fibers triggering the final percolation shear band in the matrix throughout the RVE.

Generally, the results show that microstructures with lobular fibers presented the best transverse compressive performance. This effect can be attributed to the pre-tensile residual stress induced in the lobular fibers microstructures enhancing their response under compression, see Figure 4.6. The results in terms of transverse compressive strength, Y_c, for all the fiber geometries analyzed are summarized in Figure 4.9b. All the configurations showed equivalent transversely isotropic behavior, in both directions, x_2 and x_3, of the RVE with the exception of the 2-lobular and elliptical aligned distributions which showed some degree of anisotropy caused by the alignment of the fiber cross sections.

Plastic shear bands are more intense in the case of the 3-polygonal distributions where the fibers edges are aligned with the shear bands, Figure 4.10b, jumping from fiber to fiber resulting in a final knock-down factor on the transverse compressive strength of $\sim 13\%$ when compared with the baseline circular fibers, Figure 4.9b. On the other hand, 2-lobular aligned fiber distributions exhibited the highest enhancement ($\sim 16\%$) of the transverse compression strength in both directions compared to conventional circular fibers being the shear bands more distributed within the RVE, as shown in Figure 4.10c and d.

The influence of the residual thermal stresses was limited for the case of the transverse compression for all the cases analyzed and this effect was attributed to

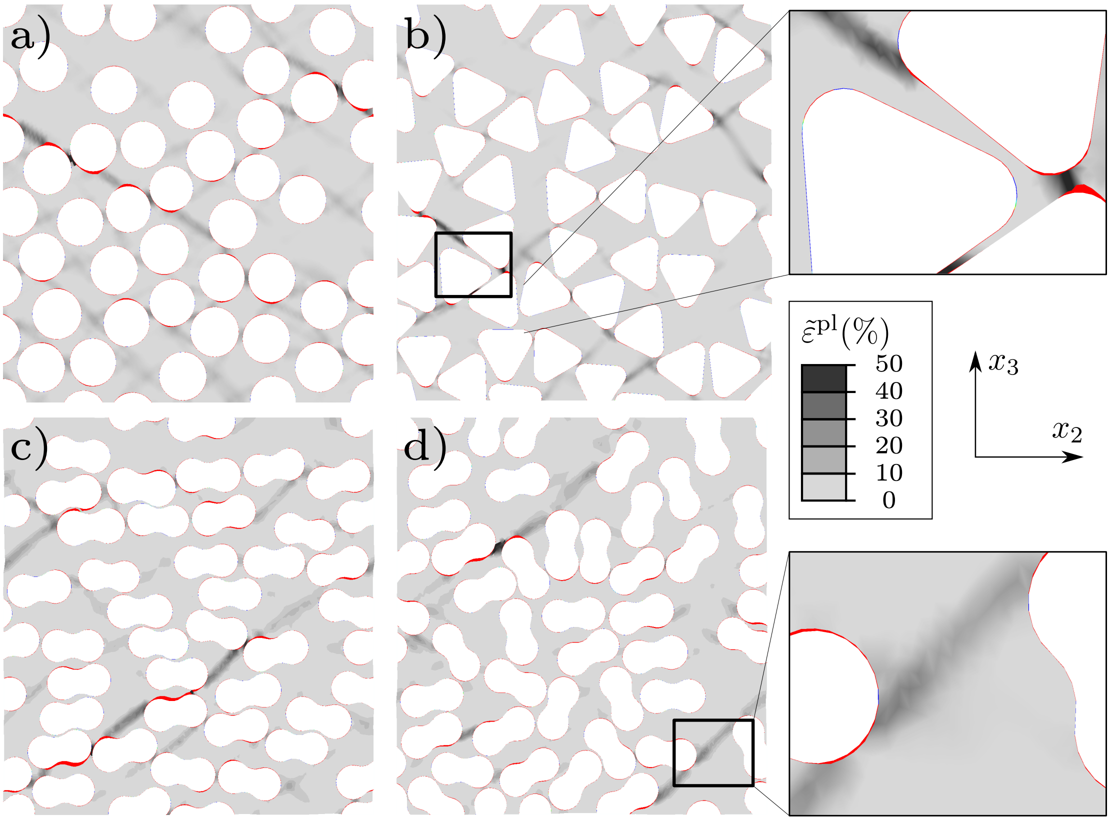

Figure 4.10: Equivalent plastic strain (gray-scaled) and interface damage (red) under transverse horizontal compression ($\varepsilon_c \simeq 4.0\%$): a) circular fibers, b) 3-polygonal fibers, c) 2-lobular aligned fibers, and d) 2-lobular randomly distributed fibers.

the fact that thermo-elastic residual stress were partially relieved due to the plastic behavior of the polymer matrix under confined compressive stress state. Shear banding occurs following the same mechanisms promoted by interface residual stresses but plastic deformation helps to reduce the subsequent effect on the compressive strength. As a result, Y_c was not strongly affected, as observed in Figure 4.9b.

4.4 Concluding remarks

The mechanical behavior of a fiber-reinforced composite lamina under transverse tension and compression has been simulated by means of computational micromechanics. This approach explicitly considers fibers distribution within the material as well as matrix, fiber and interface thermomechanical properties which are included in the simulations through the appropriate constitutive models. The simulations demonstrated the key role played by the two dominant damage mechanisms (debonding of the interface and shear band formation in the matrix) controlling the composite strength. In this work it has been observed the increase in tensile residual stresses along the concave interfaces of lobular fibers, up to 2.6 times compared to circular fibers. Under transverse tension, 2-lobular and elliptical fibers show a high orthotropic behavior when aligned reaching +10% tensile strength in the alignment direction (x_2), but it drops around $12 \sim 25\%$ in the perpendicular direction (x_3). Regarding transverse compression, all the microstructures analyzed show in-plane isotropic behavior, but those with aligned fibers. The most remarkable result is the increase of compressive strength in microstructures with lobular fibers up to +20% compared to circular fibers.

The results presented in this chapter not only show the ability of these models to reproduce the physical failure mechanisms under transverse loading, but also the potential to virtually predict the influence of design variables, such as fiber shape, on the mechanical response of a unidirectional lamina. Virtual material design opens the possibility of partially replacing or reducing costly and time-consuming experimental testing campaigns. This strategy allows the exploration of several possibilities in microstructural design such as: (i) analysis of hybrid composite microstructures, (ii) reproduction of multi-axial stress states and calculation of failure envelopes (Naya et al., 2017a), (iii) quantification of the effect of fiber volume fraction on ply properties. The coupling of this numerical tool with optimization algorithms will allow the identification of optimal microstructural configurations. Nevertheless, further validation of these techniques is required to ascertain numerical results and determine the reliability of the numerical tool.

A Numerical Framework for Small Scale Bridging Fracture Processes

5

5.1 Introduction

One of the main drawbacks limiting a wider use of fiber-reinforced polymer (FRP) composite materials is the difficulty to predict their mechanical behavior under service conditions due to the complex deformation and failure mechanisms that very often lead to well-known *black metal* design guidelines. Such complexity level is experimentally revealed at different length scales in which a FRP material is hierarchically organized, namely the ply ($10 \sim 100$ µm), the laminate ($1 \sim 5$ mm) and the structural component (~ 1 m) (Llorca et al., 2011). For instance, at the microlevel, intralaminar failure occurs due to a competition of mechanisms, triggered by the local stress state in the ply, between matrix cracking and shear banding, fiber brittle failure as well as fiber/matrix interface debonding, as shown in Chapter 4. At that length scale, the properties of the constituents as well as the spatial distribution of the reinforcement play the critical role in the fracture process although defects generated from manufacturing, such as voids, interface debonds or resin pockets, may alter this situation. These intralaminar ply mechanisms are well described in the literature and have helped considerably to develop physically based computational homogenization models (Pinho et al., 2009; Canal et al., 2012b). Such kind of models rely on the existence of a statistically *representative volume element* (RVE) whose microstructure can be generated synthetically including all relevant failure mechanisms observed in the real material (Vaughan and McCarthy, 2010). The techniques were successfully applied to predict ply strength of unidirectional plies subjected to homogeneous stress states including tension, compression, shear (González and Llorca, 2007c; Totry et al., 2010), and their combinations in a failure locus (Totry et al., 2008a), including the effect of environmental conditions (Naya et al., 2017a). To avoid artificial damage and boundary layer effects, most of the computational homogenization models make use of periodic RVEs applying homogeneous stress states through periodic boundary conditions imposed by constraining the relative displacements of pairs of opposite faces in the model.

The ability of computational homogenization models based on periodic RVEs relies on good idealizations of the current material microstructure as well as constitutive models of the constituents to explicitly reproduce damage onset and propagation and their continuous interaction (Segurado and Llorca, 2002). On the other hand, their major drawback is the inability to describe material softening after the occurrence of strain localization. To overcome such limitation, models including detailed descriptions of the microstructure of the material in the *fracture process zone* (FPZ) can be used to deal with localized crack propagation problems where material toughness determination is required. The region out of the fracture process zone in embedded models is formed by a homogenized material with equivalent properties of the overall elastic behavior of the composite. Embedded models were successfully applied in the past to simulate fracture of unidirectional plies from a micromechanical perspective including matrix plasticity, fiber bridging and pull out in Ti/SiC composites (González and Llorca, 2006, 2007c) and fiber/matrix interface debonding with ductile tearing of matrix ligaments (Canal et al., 2012b). However, an important problem when dealing with embedded cells is the inadequacy to represent at the same discretization level, fracture mechanisms spanning different length scales. For instance, the characteristic fracture process length for brittle epoxy matrices is $l_c \approx 20$ µm while the case of fiber toughening effects to fiber bridging cross-overs is $l_c \approx 1 - 5$ mm (Bao and Suo, 1992). Considering these important drawbacks, embedded models can be used to infer the shape of softening laws in composite materials based on the adequate description of the individual constituents failure mechanisms and their interaction during the propagation of a crack.

In this chapter, a numerical methodology based on computational homogenization to analyze fracture in heterogeneous materials under *small scale bridging* (SSB) conditions is presented. Due to the complexity of the problem, the methodology is illustrated to study the 2-D propagation of a crack in a fiber reinforced unidirectional ply, including the fiber/matrix interface debonding and the ductile tearing of the matrix ligaments between fibers as energy dissipation mechanisms. This crack propagation problem is also known as the intralaminar crack propagation under transverse tension characterized by the fracture toughness G_{2+}. The bidimensional formulation of the problem impedes the inclusion of higher length scale toughening mechanisms, as for instance, fiber bridging due to the lack of parallelism between fibers, so the material toughness and R-curve behavior obtained should be understood as lower bounds or initiation values rather than propagation over a finite crack length of some mm (Pinho et al., 2009). Homogenized softening laws for the crack propagation problem in a unidirectional ply are presented for a wide range of micromechanical parameters including constituent properties as the fiber/matrix interface and matrix plastic/damage behavior.

The chapter is organized as follows. The description of the framework is carried out in Section 5.2, where the embedded micromechanical model under small scale bridging and the corresponding homogeneous cohesive crack approach are described. In Section 5.3, the models are applied to determine the R-curve behavior and the energy equivalent softening laws for a baseline set of micromechanical parameters. The ability of computational micromechanics to address the influence of the micromechanical properties of the constituents is discussed in Section 5.4, whereas the final remarks and conclusions are drawn in Section 5.5. The work presented in this chapter was published in (Herráez et al., 2018b).

5.2 Methodology

5.2.1 An embedded cell model for crack propagation

A simulation methodology was developed to infer the R-curve behavior and investigate softening laws based on computational micromechanics to address crack propagation problems in unidirectional fiber reinforced composites. The modeling strategy was applied to study the intralaminar transverse fracture toughness of a unidirectional carbon/epoxy system AS4/8552 using as inputs the micromechanical parameters and the reinforcement distribution (Herráez et al., 2015; Naya et al., 2017a). The model was only applied to study the bidimensional crack propagation assuming the matrix tearing and fiber/matrix interface debonding as the dominant energy dissipation mechanisms. The crack front is assumed to be parallel to the fiber direction, namely x_1, and running in the plane $x_2 - x_3$ as shown in

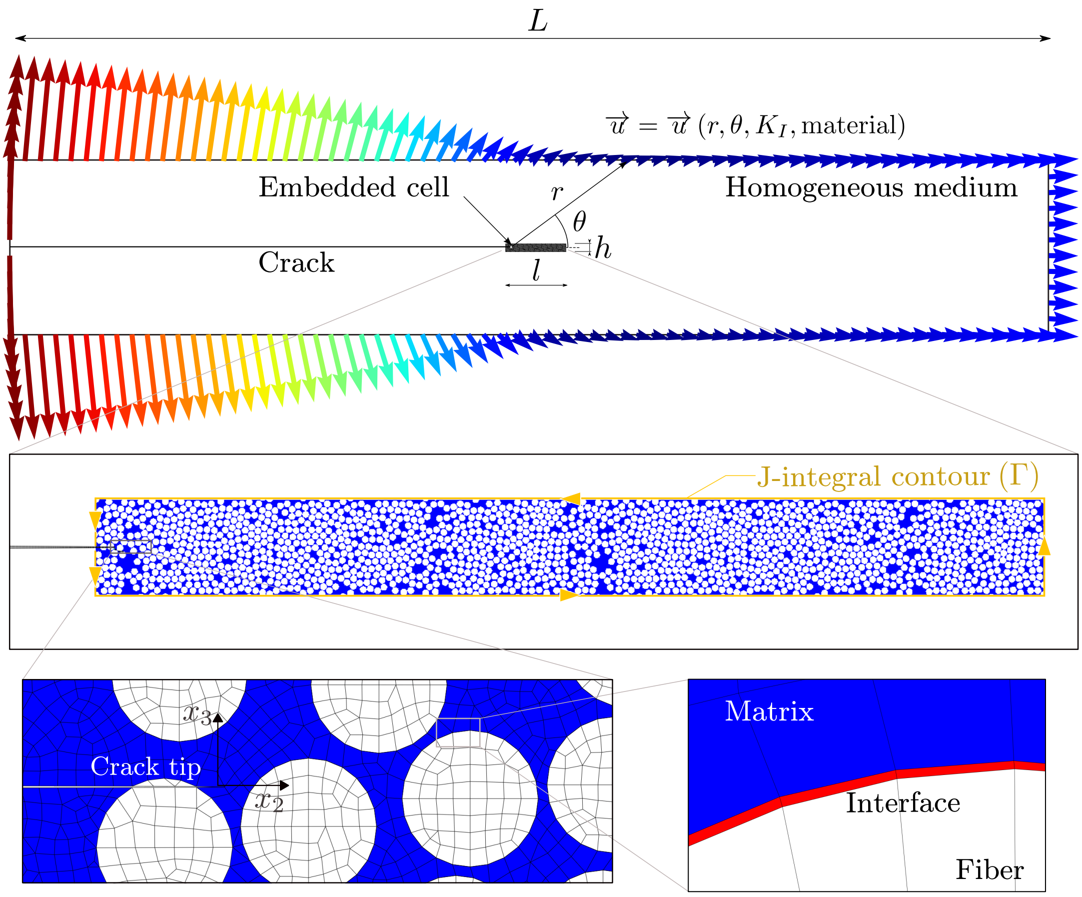

Figure 5.1: Schematic view of the model showing the displacement field (LEFM), the detail of the fibers distribution, J-integral contour Γ, FEM mesh, and cohesive interface.

Figure 5.1. The model includes the microstructure of the material, but, only in a small region close to the crack tip known as *fracture process zone* (FPZ). This detailed region of size $\ell \times h = 1500 \times 100$ µm^2 is embedded in a larger rectangular area $L \times H = 76800 \times 19200$ µm^2. This methodology allows the isolation of the crack propagation problem from any global specimen geometry effect. The microstructure used for the embedded region corresponds to a homogeneous dispersion of parallel fibers aligned in the x_1 direction, being the fiber volume fraction $V_f = 65\%$, see Figure 5.1. A typical embedded model contains over 2400 fibers with diameter 7.1 ± 0.2 µm, representative of AS4 carbon fiber as shown in Table 2.4. The rest of the model, out of the embedded region, was treated as a homogeneous transversely isotropic elastic solid whose behavior is given by any suitable homogenization scheme from the elastic constants of the constituents, fibers and matrix,

Table 5.1: Elastic properties of the AS4/8552 composite with $V_f = 65\%$ obtained through RVE computational homogenization.

E_{11} [GPa]	E_{22} [GPa]	ν_{12}	ν_{23}	G_{12} [GPa]	G_{23} [GPa]
152.3	7.17	0.32	0.48	4.1	2.42

and the volume fraction of reinforcement. The two regions of the model share the bounding nodes, so the displacement continuity is guaranteed. The width of the embedded model, h = 100 µm, was large enough to ensure the effect of the transition from heterogeneous to homogeneous solids induced negligible effects in the crack propagation process. The mesh size was set to 1 µm in the embedded region and it progressively grows along the homogeneous region up to 480 µm at the outer edges. This discretization level ensures good representation of stress fields at the microlevel while maintaining acceptable computation times. A typical baseline model is formed by 385,000 elements. Simulations were carried out using Abaqus/Standard with the implicit dynamics solving scheme using quasi-static solution settings within the framework of the finite deformations theory with the initial unstressed state as the reference one.

The whole model was discretized using a lagrangian mesh with finite elements. The matrix, fibers and the homogenized region were modeled with 4-node fully integrated quadrilateral isoparametric plane strain elements (CPE4) in Abaqus (Simulia, 2013). The fiber/matrix interface debonding was simulated with 4-node cohesive isoparametric elements (COH2D4) inserted at each of the individual fiber/matrix interfaces (Camanho and Davila, 2002; Turon et al., 2006).

The constitutive models employed by the fibers, fiber/matrix interfaces and matrix are the same as in Chapter 4 with the same properties. AS4 carbon fibers are linear elastic transversely isotropic solids. The interfaces follow a traction-separation cohesive law with linear softening with the properties shown in Table 4.2. The polymer matrix is modeled through a damaged/plasticity model brittle under uniaxial tension, but plastic under confined loading, see Table 4.3 and Table 4.4. The elastic properties of the homogenized composite region with $V_f = 65\%$ are collected in Table 5.1.

The model assumes that *small scale bridging* (SSB) conditions prevail, therefore, even if the stress field in the fracture process zone is affected by plasticity and/or damage, the overall stress in that area is dominated by the singular term $r^{-1/2}$ of the *linear elastic fracture mechanics* (LEFM). This condition is fulfilled if the characteristic length of the process zone, l_c, is small as compared with the overall dimensions of the model ($l_c \ll L, H$, Hui and Ruina (1995)) and the crack tip is far from the model edges. Under such conditions, the K_I displacement field can be imposed in the outer region of the model to simulate a crack loaded in mode I conditions. This methodology is also known as boundary layer approach and is found in the literature for the analysis of the initiation and propagation of ductile cracks (Hütter, 2013; Hossain et al., 2014). For a transversely isotropic material under plane strain conditions ($\varepsilon_{11} = 0$), the displacement field applied to the outer boundaries $\vec{u} = (u_2, u_3)$ is given by

$$\begin{Bmatrix} u_2 \\ u_3 \end{Bmatrix} = \frac{K_I}{2G_{23}} \cdot \sqrt{\frac{r}{2\pi}} \cdot (\kappa - \cos\theta) \begin{Bmatrix} \cos\frac{\theta}{2} \\ \sin\frac{\theta}{2} \end{Bmatrix} \tag{5.1}$$

where r and θ stand for the polar coordinates assuming the crack tip as the origin, K_I is the stress intensity factor in mode I, and $\kappa = 1.70$ and $G_{23} = 2.42$ GPa are material constants obtained from elastic properties of the homogenized material obtained from Table 5.1. The readers are referred to Appendix B for a more detailed description of the parameters used under plain strain conditions and the demonstration of eq. 5.1. Free stress conditions are imposed to the crack edges for $\theta = \pm\pi$, see Figure 5.1.

The model is loaded by increasing the stress intensity factor, K_I, until crack propagation (Δa) is observed. In most of the boundary layer models, the outer region where the displacement field is applied is significantly larger than the length of the propagated crack ($L \ll \Delta a$), and thus, updating the displacement field due to crack tip propagation is not required. However, if the outer region is not large enough, a mismatch between the stress intensity factor imposed through the boundary conditions and the stress intensity factor measured in the vicinity of the crack tip is observed. This effect was already reported by Hossain et al. (2014). To solve this issue, simulations were run in an incremental way by stopping the computation at a given step, i, for a given specified crack increment, namely Δa_i. Then, boundary conditions were updated assuming that the origin for the displacement field is translated in the x_2 direction the same crack increment Δa_i, being the mechanical fields imported from the previous step. More details about the differences between both approaches will be summarized in the next sections.

It should be remarked that the definition of the crack tip is somewhat arbitrary but should lie between the appearance of the first damaged element ($D > 0$) and the region where all elements are completely damaged, corresponding to the initiation of a physical crack (stress free surface). In this work, the first definition is used and the crack tip position is tracked by the direct search of the furthest damaged element in the matrix or fiber/matrix interface in the embedded cell.

The accuracy of the boundary layer approach is checked by the direct computation of the J-integral along the contour Γ of the embedded region of size $\ell \times h$. as shown in Figure 5.1. The J-integral is evaluated from the outputs of the mechanical fields obtained with the finite element model according to

$$J = \int_{\Gamma} \left(W \, dx_3 - \vec{t} \cdot \frac{\partial \vec{u}}{\partial x_2} \, ds \right) \tag{5.2}$$

where W stands for the strain energy, $\vec{u}$ for the displacement field, and $\vec{t} = \sigma \vec{n}$ the traction vector assuming $\vec{n}$ is the vector normal to the Γ contour. Under small scale bridging conditions, the stress intensity factor, K_I, imposed through the boundary layer approach and the J-integral evaluated should fulfill the Irwin relation and, therefore, $J(\Delta a) = R(\Delta a) = K_I^2(\Delta a)/E^*$ where E^* is the effective modulus in the transverse plane $x_2 - x_3$ under plain strain conditions, $E^* = E_2/(1 - \nu_{12}\nu_{21})$.

A direct comparison of the $R(\Delta a)$ results obtained with the boundary layer approach is also performed by means of a full-scale embedded cell model. In this case, the heterogeneous region containing the microstructure of the material of size $\ell \times h$ is embedded in a larger structure subjected to far field mechanical loads, Figure 5.2. To simplify the problem, the structure used corresponded with a single-edge notch test (SENT) of a panel of size $L' \times H' = 45 \times 180$ mm^2 subjected to uniaxial tension σ^∞ in the x_3 direction. The initial crack length was $a_0 = 0.05 \cdot L' = 2.27$ mm. The stress intensity factor is directly computed following the well known expression for the SENT configuration $K_I = 1.12\, \sigma \sqrt{\pi\, a}$ where a is the current crack length. The J-integral was also computed through the contour Γ containing the embedded region as described previously.

Simulation time of the SSB model was about 12 hours for the baseline case (400,000 elements), whereas the SENT model was larger (500,000 elements) and took 8 hours. However, the SENT model became unstable when the steady-state regime was reached and the simulation stopped (Δa = 900 µm), while the SSB approach remained stable during the whole process going up to Δa = 1400 µm,

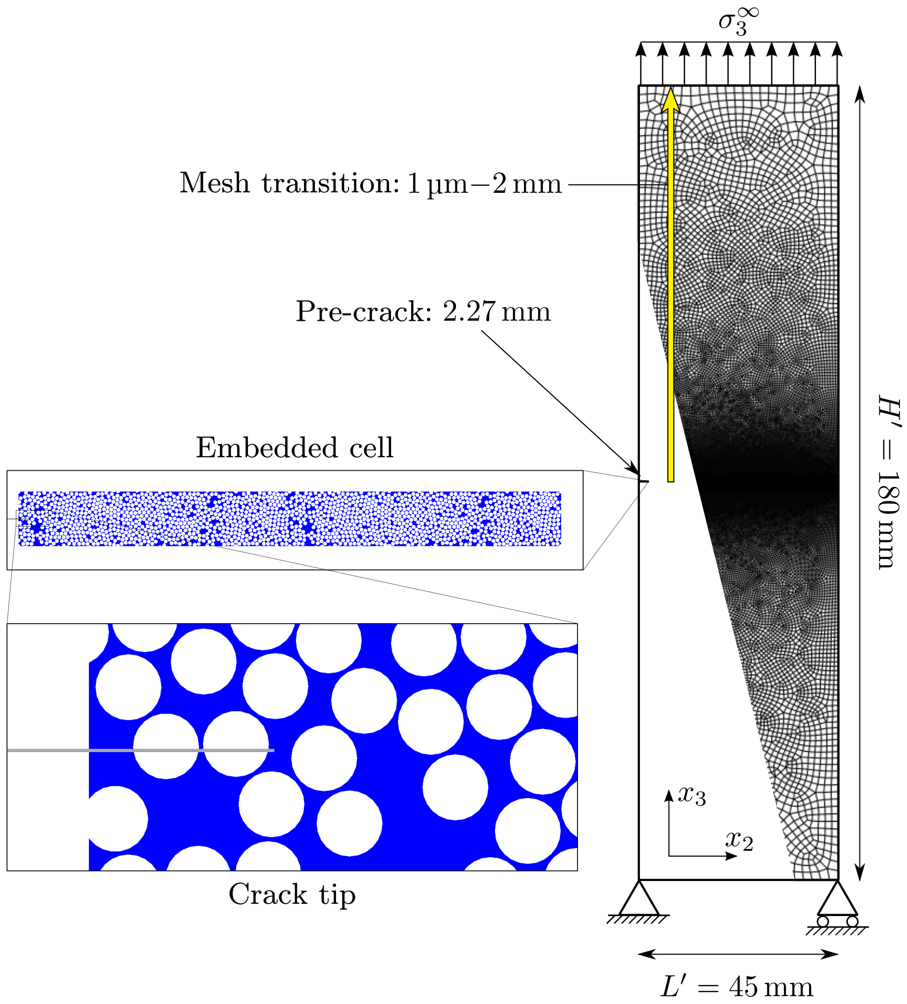

Figure 5.2: SENT (single-edge notch test) full-scale model with an initial crack $a_0 = 2.27$ mm ($a_0/L' \approx 0.05$) subjected to far-field stress σ_3^∞. Details of the embedded micromechanical model and crack tip.

see Figure 5.4. Simulations were performed using 10 cores with an Intel® Xeon® Processor E5-2680.

5.2.2 Equivalent homogeneous cohesive zone model

A homogeneous finite element model in which the fracture process zone is lumped into a single cohesive crack in the $x_3 = 0$ plane was generated in order to evaluate the response of physically sound softening laws mimicking the response of the micromechanical model, Figure 5.3. In this case, the model is constructed of two homogeneous transversely isotropic elastic solids under plain strain conditions with the elastic properties reported in Table 5.1 tied to a zero-thickness layer of cohesive

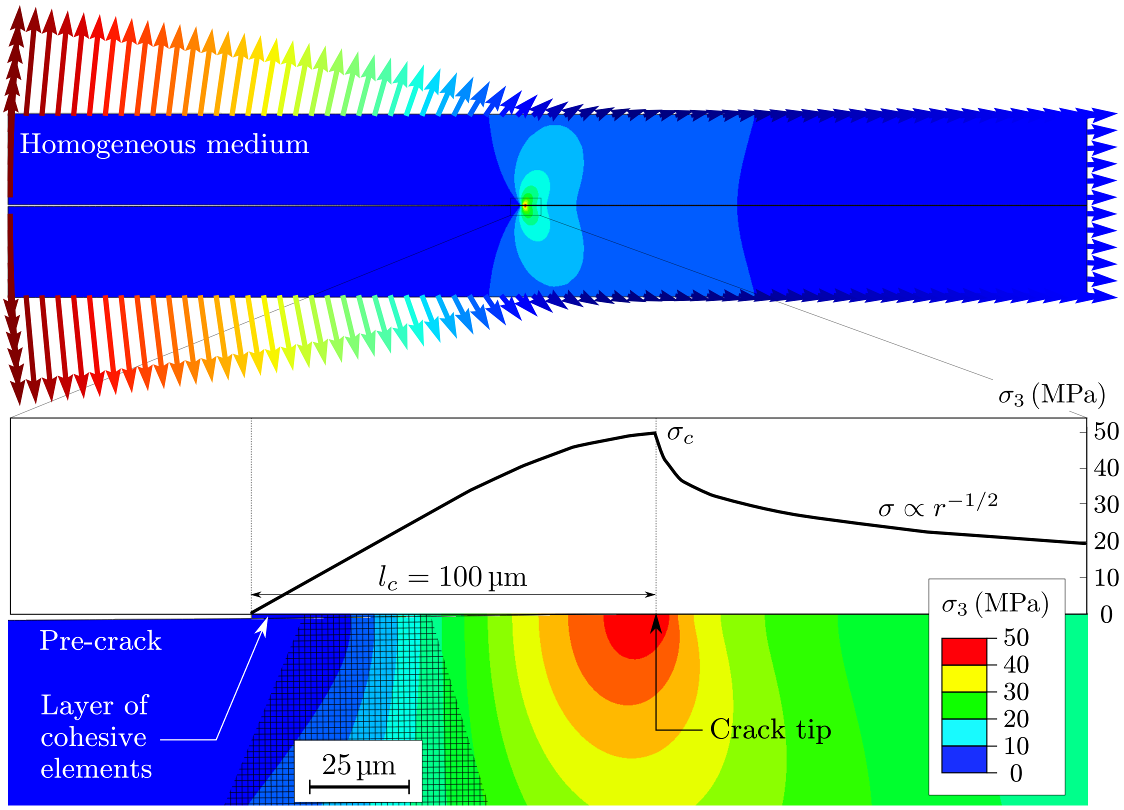

Figure 5.3: Sketch of the equivalent cohesive model for crack propagation, mode I displacement field is imposed along the boundaries of the model, and detail of the vertical stress contour field (σ_3) of the homogeneous cohesive crack model along the fracture process zone with a linear-softening traction-separation law.

elements. The total dimensions are the same as those of the embedded micromechanical model, $L \times H$, using the same boundary conditions representing the K_I displacement field of linear elastic fracture mechanics, eq. 5.1. The softening law, $\sigma(w)$, introduced in the cohesive elements (σ stress vs. w crack opening displacement) is defined by the transverse tensile strength, $Y_t = \max \sigma(w)$, toughness, $G_f = \int_0^\infty \sigma(w)\, dw$, and its softening shape (bilinear, exponential, etc.). As in the case of the elastic constants, the strength of the material, Y_t, was inferred using periodic representative volume elements through the strategy shown in Chapter 4. The remaining mechanical parameters are selected to reproduce the same $R(\Delta a)$ response, in an energy release equivalence, as the embedded model containing the explicit representation of the material microstructure.

5.3 Results

5.3.1 Fracture mechanisms and R-curve behavior

The embedded cell methodology just described was applied to determine the $R(\Delta a)$ curve for the intralaminar transverse crack propagation in AS4/8552 carbon/epoxy UD composite system. Figure 5.4 represents the $R(\Delta a)$ curves obtained for four different random realizations, namely A, B, C and D, keeping constant the volume fraction of fiber reinforcement $V_f = 65\%$ and micromechanical parameters of the constituents. As previously mentioned, the crack tip, and therefore, the definition of the crack length extension Δa, is localized by the appearance of the first damaged element in the form of, either, matrix damage or fiber/matrix interface debonding $(D > 0)$. The scatter obtained in the simulations is due to the arrangement of the fibers within the fracture process zone. The shape of the curve is similar in the four cases and is a direct consequence of the fracture mechanisms included in the simulations. Firstly, crack propagation was triggered for low energy values $G_{2+}^{\text{init}} \approx 20$ J/m^2 and this effect was associated with the generation of the first fiber/matrix debonds and/or matrix failure. Secondly, the crack progresses showing bridging by the matrix ligaments between debonded fibers that are subjected to severe plastic deformation and final ductile tearing. Once the dissipation mechanisms are exhausted, the R-curve progresses to an asymptotic value $G_{2+} \approx 50$ J/m^2 that can be considered as the intralaminar transverse fracture energy of the material, see Figure 5.4.

The fracture process zone can be visualized easily from the fracture mechanisms shown in Figure 5.5 for two different points, I and II, defined in the R-curve in Figure 5.4. An approximate fracture process zone length of $l_c \approx 400$ µm is inferred from these results which is consistent with the crack extension necessary to fully propagate a physical crack after the remaining matrix ligaments are totally broken, Figure 5.4. Under such circumstances, the fracture process zone continues its propagation in a self-similar way and the stress field translates progressively in the x_2 direction. It should be mentioned that the length of the fracture process zone is much smaller than the overall dimensions of the model $(L \approx 192\, l_c)$ which is a mandatory requirement to represent the small scale bridging conditions. Such model, with a size L and crack extension Δa, also ensures that the relative error between the stress intensity factor introduced through the boundary conditions using eq. 5.1 and the real value measured through the J-integral using eq. 5.2 around the Γ contour in the embedded region differs by less than 3%.

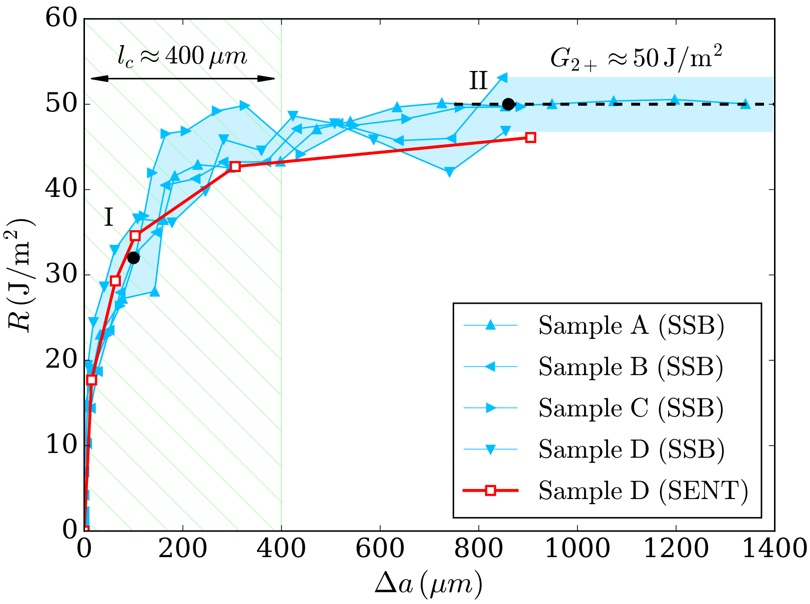

Figure 5.4: R-curve envelope obtained from four different equivalent realizations using the embedded boundary layer approach. Results with the full-scale embedded model using the SENT configuration included for comparison.

Figure 5.4 also shows the $R(\Delta a)$ curve obtained with the full-scale embedded model using the SENT specimen configuration previously described. The results in terms of energy dissipated were very similar to those obtained with the boundary layer approach and, thus, demonstrating that the small scale bridging conditions were fulfilled.

The stress field σ_3 along the crack plane $x_3 = 0$ in the fracture process zone is plotted in Figure 5.6 when the crack has propagated until $\Delta a = 860$ µm from the initial position and the applied stress intensity factor is $K_I = 0.66\,\mathrm{MPa}\sqrt{\mathrm{m}}$. The $\sigma_3(x_2)$ field in the fracture process zone was obtained by the projection of those Gauss points stresses corresponding to the finite elements running through the initial crack plane ($x_3 = 0$). Thus, the scatter observed in the stress variation is a consequence of the different materials (fibers and matrix) and their spatial distribution in the embedded region. Ahead of the crack tip, the stress shows an excellent agreement with the LEFM singular field ($r^{-1/2}$) for the given stress intensity factor $K_I = 0.66\,\mathrm{MPa}\sqrt{\mathrm{m}}$ confirming the adequacy of the imposed boundary conditions to simulate realistic small scale bridging conditions (Anderson, 2005). The results of the full-scale embedded model differ from those of the small scale only far from the

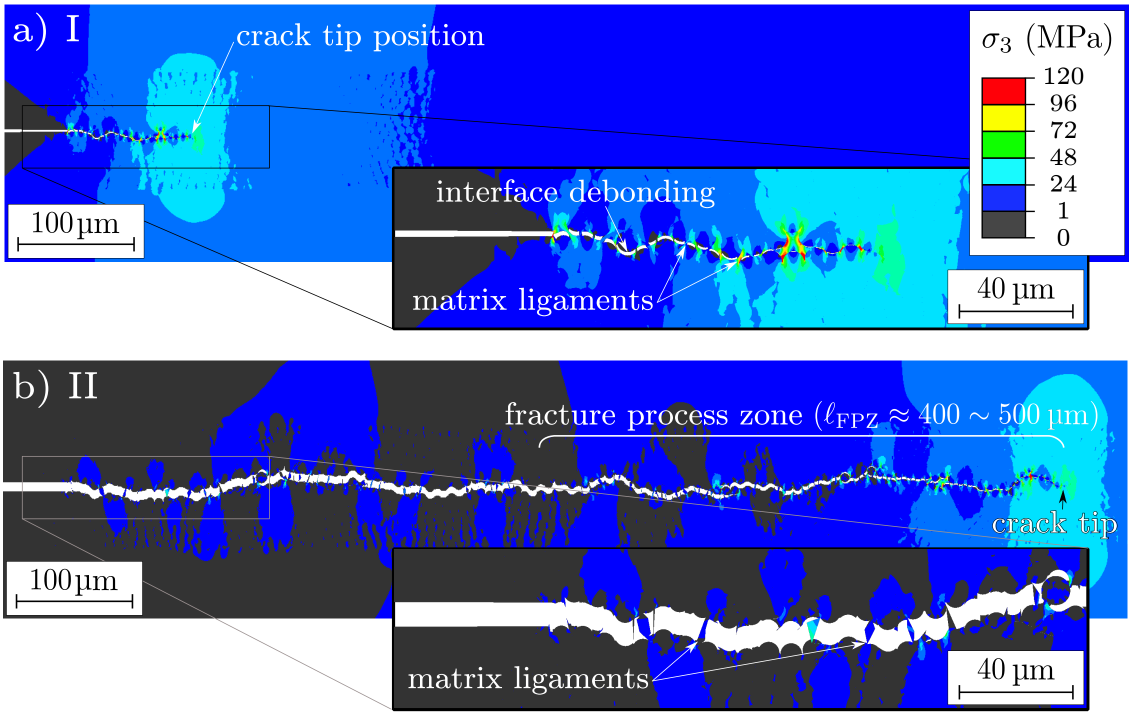

Figure 5.5: Snap-shots of the fracture mechanisms obtained with the embedded micromechanical model for the loading points I a) and II b) shown in the $R(\Delta a)$ in Figure 5.4.

crack tip when the far-field asymptotic stress $\sigma_3^\infty \approx 5$ MPa is achieved. The stress solution for the SENT and boundary layer models should be similar in a region close to the crack tip, where K_I dominates. Out of this region, autonomous zone, LEFM solution (first term of the series expansion) diverges from the SENT solution.

5.3.2 Representativeness of the embedded cell model

The baseline results of the $R(\Delta a)$ curves shown in Figure 5.4 were obtained assuming a relative size of the fracture process zone with respect to the overall dimensions of the model of $L \approx 192\ l_c$ ($l_c \approx 400$ µm) to ensure that the small scale bridging conditions are satisfied, as shown in Figure 5.6. Such results were obtained using the procedure described in the previous section by updating the BC. After a small increment of crack extension ($10 \sim 25$ µm), the K_I displacement field boundary conditions were updated assuming that the origin for the crack tip in eq. 5.1 is translated by the same amount in the x_2 direction. The procedure is then repeated for every crack increment after the R-curve achieved the steady-state conditions.

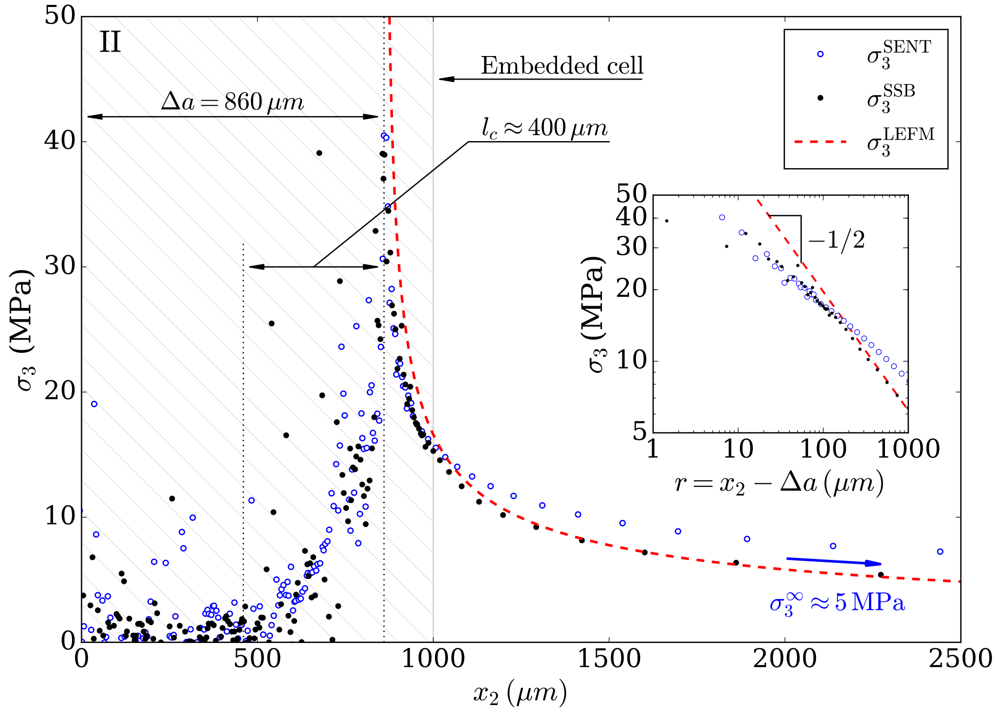

Figure 5.6: $\sigma_3(x_2)$ stress field for small scale bridging (SSB) and full-scale (SENT) models for crack tip propagation of $\Delta a = 860$ µm and a stress intensity factor applied of $K_I = 0.66$ MPa$\sqrt{\text{m}}$, corresponding to point II of the R-curves shown in Figure 5.4. Stress predictions based on linear elastic fracture mechanics theory included for comparison (LEFM). The length of the embedded cell is $l = 1000$ µm. Note the linear relation of the LEFM solution in the log-log scale plot.

The relative size of the model to the fracture process zone length L/l_c and the methodology for crack propagation deserve some additional comments. The effect of the approach updating the BC is analyzed through a new set of simulations performed with $L/l_c = 12$, 48 and 192, but without updating the boundary conditions during crack propagation. The results summarized in Figure 5.7a are compared with the baseline results previously described (see Figure 5.4). The R-curve obtained for $L/l_c = 12$ matched the baseline results only for very small crack propagations as the K_I imposed through the boundary conditions and the real values at the crack tip computed through the J-integral diverged progressively. Similar results were obtained for the larger model with $L/l_c = 192$ but data diverged after a larger crack propagation $\Delta a \approx 300$ µm. Hence, the model size relative to the fracture process zone length L/l_c needs to be previously checked if boundary conditions are not intended to be updated. On the other hand, Figure 5.7b shows the results of

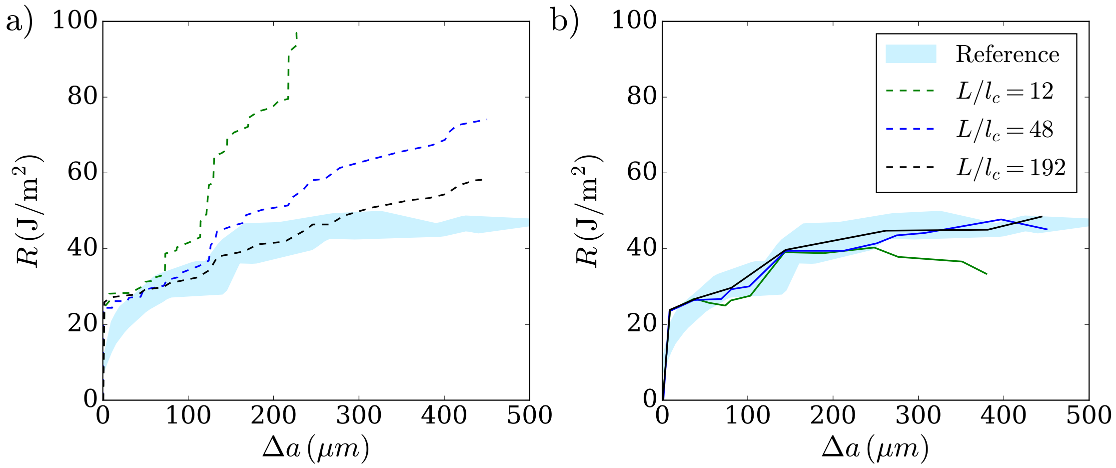

Figure 5.7: a) $R(\Delta a)$ curves obtained without updating the boundary conditions for different relative sizes of the model $L/l_c = 12, 48, 192$, b) $R(\Delta a)$ curves obtained updating the boundary conditions for different relative sizes of the model $L/l_c = 12$, 48 and 192. Baseline simulations results included for comparison.

the R-curves using the boundary conditions updated with the same relative sizes of the model $L/l_c = 12$, 48 and 192. Results obtained for $L/l_c = 48$ were similar to the baseline dimensions $L/l_c = 192$, but diverged for $L/l_c = 12$. Thus, the relative model size of $L/l_c = 192$ was accurate enough to ensure small scale bridging conditions were fulfilled.

5.3.3 Homogenized cohesive laws

The homogenized model lumping the fracture process zone in a single layer of cohesive elements presented in Section 5.2.2 is now applied to simulate the crack propagation problem. The traction vs. separation law $\sigma(w)$ is usually defined by means of the maximum stress dictating the onset of damage, Y_t, the fracture energy, G_{2+}, and the shape of the curve. The maximum stress $Y_t = 50$ MPa was determined from the numerical simulation of a model based on a periodic representative volume element (RVE) of the microstructure subjected to uniaxial transverse tension loading for the same micromechanical properties of the constituents presented previously as detailed in Chapter 4. The fracture toughness $G_{2+} = 50$ J/m^2 was obtained from the embedded model $R(\Delta a)$ curve when steady-state conditions are achieved. Even if the two previous conditions are fulfilled, the shape of the $\sigma(w)$ curve presents an additional degree of freedom related with the shape of the R-curve. To illustrate such effect, a standard linear-softening traction vs. separation law defined as

$\sigma(w) = Y_t \cdot (1 - w/w_c)$ with $w_c = 2\,G_{2+}/Y_t$ is used as shown in Figure 5.8a. The results of the homogenized cohesive model are presented in Figure 5.8b. Naturally, the results match perfectly the steady-state toughness of the embedded model but the homogenized crack resistance curve does not fit the embedded cell model fracture response in the whole Δa range.

The results in Figure 5.8 also include the R-curve derived by the direct integration of the cohesive law, $R(\Delta a) = \int_0^{\Delta a} \sigma(x)\,dx$, assuming a linear relation between the crack length extension, Δa, and the crack opening displacement, $w = w_c/l_c\,\Delta a$, (Foote et al., 1986; Sørensen and Jacobsen, 1998) as,

$$R(\Delta a) = \begin{cases} R(\Delta a) = G_{2+} \frac{\Delta a}{l_c} \left(2 - \frac{\Delta a}{l_c}\right) & \Delta a < l_c \\ R(\Delta a) = G_{2+} & \Delta a \geq l_c \end{cases} \tag{5.3}$$

where l_c is the fracture process length and it follows the well-known relation found in the literature, $l_c = \gamma\,G\,E/\sigma^2$, with $0 < \gamma \leq 1$ depending on the analytical model selected (Dugdale, 1960; Hillerborg et al., 1976; Bao and Suo, 1992). Thus, once $\Delta a = l_c$, the steady-state toughness $R = G_{2+}$ is achieved. The results obtained by the direct integration of the cohesive law assuming a linear relation for the crack opening displacement match the results obtained with the homogeneous cohesive model corroborating the accuracy of this hypothesis (Figure 5.8b).

A non-conventional cohesive law is required to improve the fitting of the embedded model R-curve. In this work, different approaches were attempted to obtain an approximate cohesive law that would result in the R-curve obtained by means of micromechanics, such as trapezoidal (Irwin, 1957; Dugdale, 1960; Bilby et al., 1963; Tada et al., 2000), with linear hardening (Budiansky et al., 1988; Suo et al., 1992), following a power law (Cox, 1993), based upon phenomenological damage mechanisms (Llorca and Elices, 1990), bilinear softening (Dávila et al., 2009; Morel et al., 2010) or more complex linear piecewise behavior (Sills and Thouless, 2015). A different strategy was presented by Hong and Kim (2003) which consists of extracting an arbitrary cohesive law from the elastic far-fields of the embedded micromechanical model through the field projection method (FPM), nevertheless, linear-softening cohesive laws will be assumed in this work as they provide reasonable balance between representativity and easiness of implementation in a constitutive model (CDM, traction-separation law...).

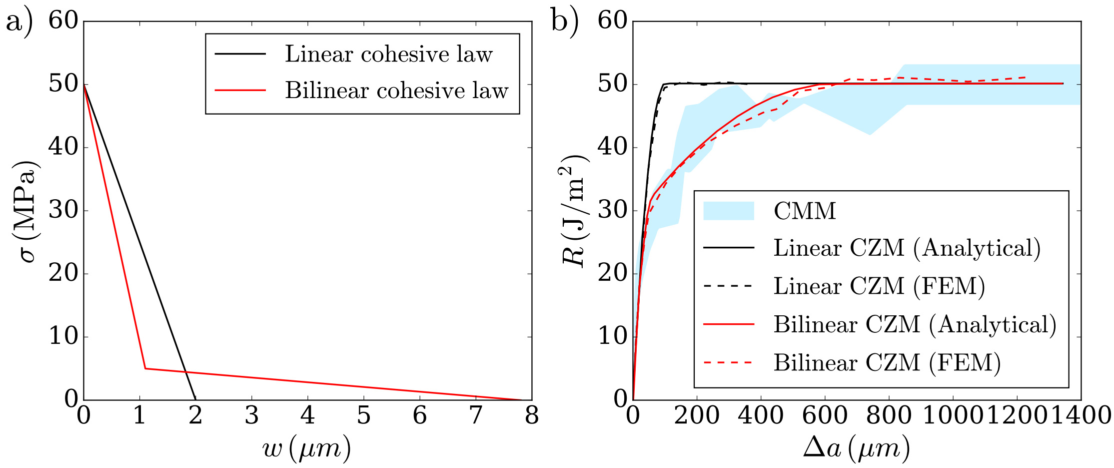

Figure 5.8: a) Linear and bilinear cohesive laws for homogenized models, and b) comparison of the $R(\Delta a)$ curves obtained with the homogenized cohesive model using linear and bilinear laws with the micromechanics embedded cell approach. Analytical results obtained by direct integration of the cohesive laws also included for comparison.

Two well differentiated cohesive zones and fracture energies are observed in the R-curves (see Figure 5.4). Hence, a bilinear softening law based on the work of Dávila et al. (2009), is proposed in order to capture the fracture process more accurately than the simple linear softening law previously shown. The bilinear softening law is described through the superposition of two linear cohesive laws, namely BCL_1 and BCL_2 (bilinear cohesive law, BCL), with complimentary strength and fracture toughness values, Figure 5.9a. The strength and toughness of the two cohesive laws are defined as fractions of Y_t and G_{2+}, respectively, as $\sigma_{c_1} = n\, Y_t$, $\sigma_{c_2} = (1-n)\, Y_t$ and $G_1 = m\, G_{2+}$ and $G_2 = (1-m)\, G_{2+}$. Following this approach, the strength and toughness are directly obtained by the summation of the individual contributions of the linear cohesive laws as $Y_t = \sigma_{c_1} + \sigma_{c_2}$ and $G_{2+} = G_1 + G_2$. The factors n and m range in the interval $(0, 1)$ and are used to control the shape of the bilinear cohesive law. They can be derived by least square minimization using the $R(\Delta a)$ curves obtained with the micromechanical model. However, the minimization process through the homogenized finite element model is computationally very expensive and simplified expressions as eq. 5.3 are very valuable for fitting purposes. In this work, a bilinear piecewise relation for the direct integration of the cohesive law as in Figure 5.9b is proposed, according to

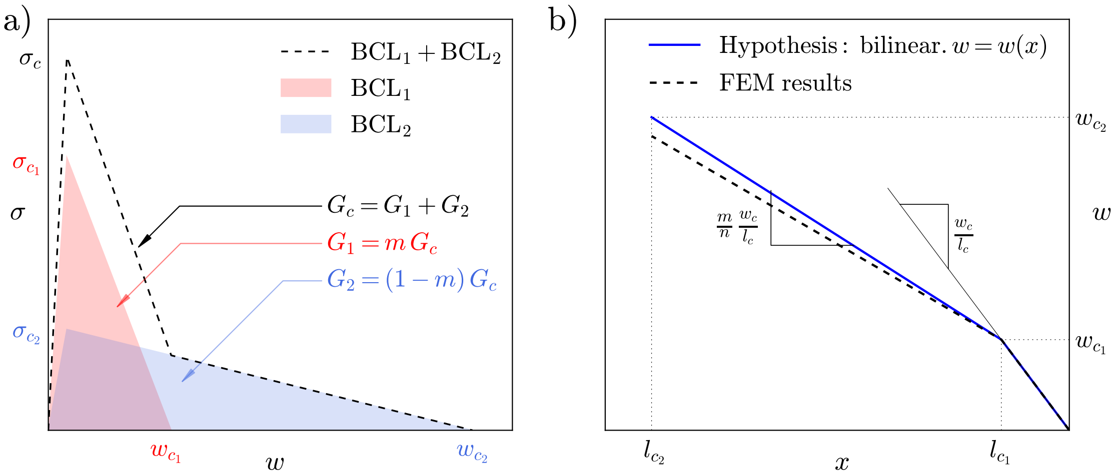

Figure 5.9: Schematics representation of: a) two linear softening cohesive laws and their superposition adapted from Dávila et al. (2009), and b) crack-separation profile: hypothesis and FEM results.

$$w(\Delta a) = \begin{cases} \frac{w_c}{l_c}\Delta a & \Delta a < l_{c_1} \\ \frac{m}{n}\frac{w_c}{l_c}(\Delta a - l_{c_1}) + \frac{w_c}{l_c}\, l_{c_1} & \Delta a \geq l_{c_1} \end{cases} \tag{5.4}$$

where $l_{c_1} = l_c \cdot m/n$ and $l_{c_2} = l_c \cdot (m/n + (n-m)/(m(1-n)))$ are the fracture process zone length associated with BCL_1 and BCL_2, respectively. The integration of the traction-separation laws along the observed crack-separation profile yields the R-curve expression in eq. 5.5.

$$R(\Delta a) = \begin{cases} R_1(\Delta a) + R_2^A(\Delta a) & \Delta a < l_{c_1} \\ R_1^T + R_2^A(l_{c_1}) + R_2^B(\Delta a) & l_{c_1} \leq \Delta a < l_{c_2} \\ R_1^T + R_2^T = G_{2+} & \Delta a \geq l_{c_2} \end{cases} \tag{5.5}$$

where,

$$R_1(\Delta a) = n\,\frac{\Delta a}{l_c}\left(2 - \frac{n}{m}\frac{\Delta a}{l_c}\right)\cdot G_{2+} \tag{5.6a}$$

$$R_2^A(\Delta a) = (1-n)\,\frac{\Delta a}{l_c}\left(2 - \frac{1-n}{1-m}\frac{\Delta a}{l_c}\right)\cdot G_{2+} \tag{5.6b}$$

$$R_2^B(\Delta a) = (1-n)\frac{m}{n}\,\frac{(\Delta a - l_{c_1})}{l_c}\left(2(1-C) - C\frac{(\Delta a - l_{c_1})}{l_c}\right)\cdot G_{2+} \tag{5.6c}$$

$$R_1^T = R_1(l_{c1}) = m\cdot G_{2+} \tag{5.6d}$$

$$R_2^T = R_2^A(l_{c1}) + R_2^B(l_{c2}) = (1-m)\cdot G_{2+} \tag{5.6e}$$

with $C = (m\cdot(1-n))/(n\cdot(1-m))$. In these equations, $m \leq n$, otherwise the values must be switched as $m := 1-m$ and $n := 1-n$. The coefficients m and n of the former expressions are determined by least squares fitting of the R-curves obtained with the embedded micromechanical model (see baseline results in Table 5.2). The final cohesive law is presented in Figure 5.8a and the results of the R-curves obtained with the homogenized cohesive model and with the direct integration of the cohesive law are compared in Figure 5.8b. The difference between both approaches, homogenized cohesive model and direct integration of the cohesive law, are almost negligible indicating the bilinear law approximation for the crack opening displacements is very accurate. Not surprisingly, the results obtained with the bilinear cohesive law clearly fit the predicted R-curves indicating the good representativeness of the fracture process zone by means of the bilinear softening law.

The advantage of the multi-mechanism softening law approach presented in this work is the ability to provide a direct quantification of the energy partition between mechanisms. For instance, the initial brittle behavior of the fiber/matrix interface can be endorsed to the first linear cohesive law, being the fracture process zone length and fracture energy $l_{c_1} = 61$ µm and $G_1 = 25.2$ J/m^2. This fracture process zone length is consistent with the region along which fiber/matrix debonding takes place, close to the crack tip, as observed in Figure 5.5a. On the other hand, the behavior due to the plastic/damage tearing of the matrix ligaments between debonded fibers is associated to the second cohesive law in which the fracture process length and fracture energy were $l_{c_2} = 664$ µm and $G_2 = 24.8$ J/m^2, respectively, see Figure 5.5b. Thus, if steady-state propagation conditions are fulfilled, then the energy partition

Table 5.2: Details of the cohesive laws obtained by least-square fitting of the $R(\Delta a)$ curves obtained with the embedded micromechanical model.

G^c [J/m^2]	G^m [J/m^2]	m	n	l_{c_1} [µm]	l_{c_2} [µm]	G_1 [J/m^2]	G_2 [J/m^2]	G_1/G_2
2	90	0.505	0.873	61	664	25.2	24.8	1.016
8	90	0.650	0.870	141	634	58.5	31.5	1.857
20	90	0.635	0.870	276	1354	114.3	65.7	1.739
2	135	0.330	0.770	56	812	20.5	41.5	0.494
2	200	0.098	0.452	38	1180	8.1	74.9	0.108

between mechanisms for this case $G_1/G_2 = 1.016$ and energy dissipation is equally attributed to both aforementioned mechanisms.

5.4 Discussion

5.4.1 Effect of the constituents properties

One of the main benefits of computational micromechanics is the ability to predict the mechanical behavior of the composite material when the properties of the constituents are changed, and, thus, enabling the virtual screening of the material prior to its manufacturing. In this section, the model described previously is applied to ascertain the effect of the constituents, mainly the toughness of the fiber/matrix interface G^c, and the toughness of the matrix G^m, on the final homogenized behavior of the UD composite material[1]. Three different realizations with the same volume fraction $V_f = 65\%$ were carried out using a set of values for $G^c = 1, 2, 4, 6, 8, 10$ and 20 J/m^2, and matrix, $G^m = 40, 90, 135, 200$ and 300 J/m^2. The corresponding results of the R-curves are plotted in Figure 5.10b and d, respectively, being the baseline values those obtained with G^c = 2 J/m^2 and G^m =90 J/m^2 (plotted in light blue in the graph). In addition, the results for the steady-state toughness G_{2+} as a function of G^c and G^m are shown in Figure 5.10a and c including also the corresponding values of the fracture process zone length, l_c, obtained by the direct observation of the numerical model.

[1]In this chapter G^c corresponds to the fracture energy of the interface under mode I (G^c_t), whereas G^m is the fracture energy of the matrix under longitudinal tension (G^m_t).

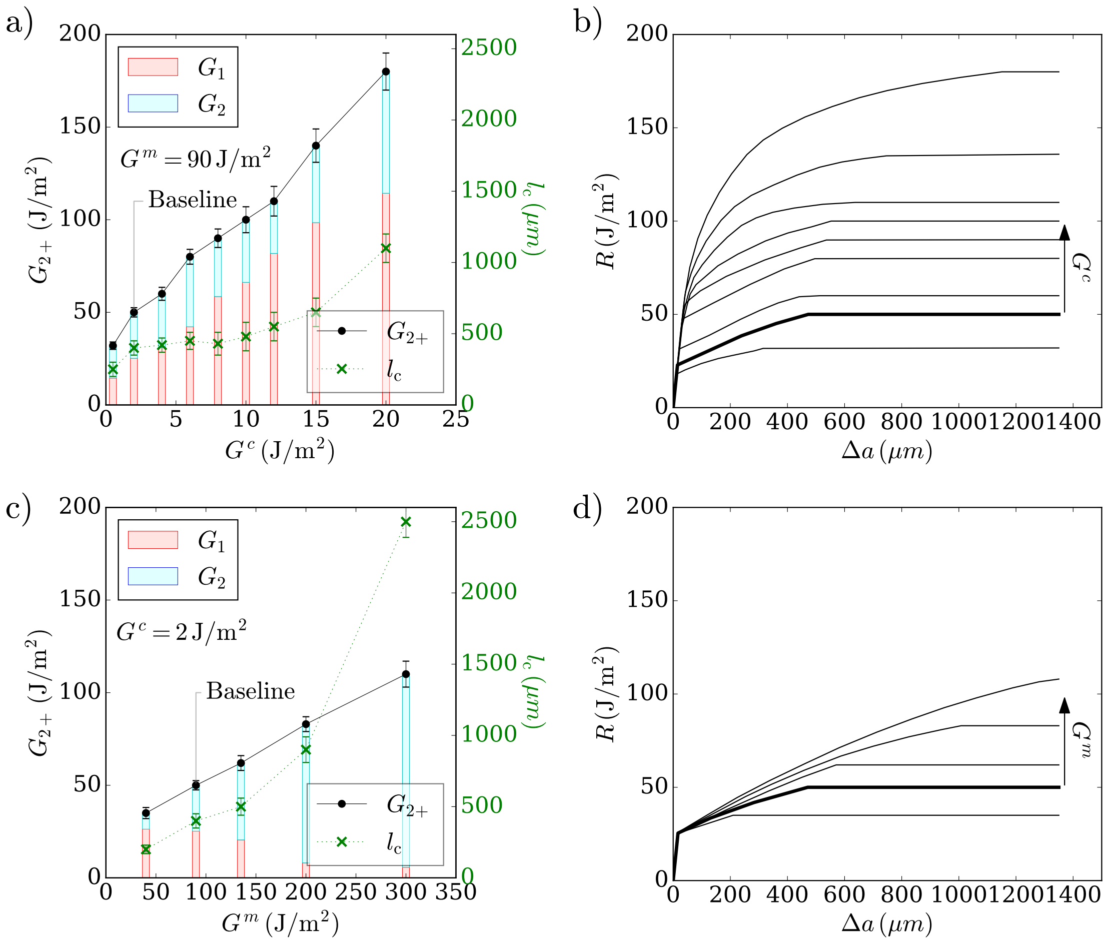

Figure 5.10: Steady-state toughness G_{2+}, G_1 and G_2 energy contributions, and fracture process length l_c for: a) interface toughness variations G^c, c) matrix toughness variations G^m. R-curves for: b) interface toughness variations, d) matrix toughness variations. The curves were obtained fitting the numerical R-curves with the bilinear cohesive law (eq. 5.5).

The results indicate that a tough interface is critical to enhance energy dissipation (Barthelat et al., 2007), specially in the first stages of the process for small crack increments ($\Delta a \leq 50$ µm), as observed in Figure 5.10b. This effect can be attributed to the onset of damage that is triggered by fiber/matrix decohesion ahead of the notch tip. If fiber/matrix interface debonding is delayed, because of the higher G^c, then, more volume of material is able to contribute to dissipate energy in the neighborhood of the crack tip enhancing the fracture energy, and not only those fibers close to the crack plane. Improving the interface toughness G^c from 2 to 20 $\mathrm{J/m^2}$ produced an increase of the steady-state fracture energy from 50 to 175 $\mathrm{J/m^2}$

while the length of the fracture process zone changed from ~ 400 µm to ~ 1200 µm, as shown in Figure 5.10a. The simulations also point out that the influence of the matrix toughness on the steady-state fracture energy, G_{2+}, is not as effective as in the case of the fiber/matrix interface debonding, Figure 5.10c. For instance, changing the matrix toughness G^m from 90 to 300 J/m^2 produces an improvement from 50 to 110 J/m^2 and the fracture process zone length l_c increases from 400 to 1200 µm. This effect is due to the damaged matrix ligaments that are less effective to shield the crack tip, so the effectiveness of improving the matrix toughness is only observed for larger crack propagation as compared with the fiber/matrix interface.

Another major benefit of computational micromechanics is the ability to provide the homogenized constitutive behavior of the composite material that can be used to study its behavior at an upper length scale. This is the case, for instance, of the cohesive laws obtained by the least squares fitting the R-curves computed with the embedded micromechanical model. Figure 5.11b shows the results of such cohesive laws obtained for the baseline properties and for interface toughness enhancements of $G^c = 8$ and 20 J/m^2, and matrix $G^m = 135$ and 200 J/m^2, fitting the overall behavior presented in Figure 5.11a.

The direct inspection of the cohesive laws obtained deserves additional comments. Firstly, the strength values of the cohesive laws are kept constant and equal to the transverse tensile strength of the material ($Y_t = 50$ MPa), as obtained from the analysis of periodic RVEs, Figure 5.11b. It should be argued that the effect of the fiber/matrix interface and matrix toughness on the transverse tensile strength of the UD composite material is negligible as this value is essentially controlled by the fiber/matrix interface strength that triggers the brittle final failure of the composite (Naya et al., 2017a). Secondly, the cohesive law is clearly modified by changing the values of the fiber/matrix interface toughness, Figure 5.11b. This modification allows the material to sustain higher stress levels, specially close to the crack tip, and therefore, dissipating additional energy through the neighboring matrix ligaments between debonded fibers. The effect aforementioned is also corroborated by observation of the deformed configurations close to the crack tip in Figure 5.11f and g, and the comparison with the baseline configuration presented in Figure 5.5. If fiber/matrix toughness is enhanced, e.g. $G^c = 20$ J/m^2, more fiber debonds are observed around the crack tip while in the case of the baseline configuration, they are localized close to the fracture plane ($x_3 = 0$) not affecting significantly the neighboring fibers. In such case, the fracture process zone of the BCL$_1$, associated with fiber/matrix debonding mechanisms, shows a clear increase from 61 to 276 µm, being the energy dissipated under steady-state conditions 3.6 times the baseline value, Table 5.2, and Figure 5.11g.

If the matrix toughness is improved, $G^m = 200$ J/m^2, the energy dissipated in the crack tip region due to fiber/matrix interface debonding is even lower, $G_1 = 8.1$ J/m^2 as compared with the $G_1 = 25.2$ J/m^2 obtained with the baseline material, and the ratio between both mechanisms is considerably low $G_1/G_2 = 0.108$. For this reason, the R-curves show a significant progressive increase from the low values observed for the initiation to the final steady-state regime, Figure 5.11a. In these cases, the crack length should be very large ($\sim$ 1200 µm) to fully exhaust this mechanism and attain the steady-state conditions.

5.4.2 Effect of the fiber volume fraction

The effect of the fiber volume fraction, V_f, on the steady-state toughness is analyzed by testing embedded cells with a different amount of fibers. In Figure 5.12a, it is shown that a composite with a lower fraction of reinforcement is able to dissipate more energy, for instance, for $V_f = 50\%$, the increase in toughness compared to the reference ($V_f = 65\%$) is $\sim$ 15 J/m^2 (+30%). Similarly, if the fiber volume fraction is increased up to 70%, G_{2+} drops $\sim$ 5 J/m^2 (-10%). This effect is explained through the size of the matrix ligaments between debonded fibers, as the fiber volume fraction increases, the distance between them becomes smaller, such that the load sustained by the matrix is lower (Ghayoor et al., 2018).

The fiber arrangement that maximizes the size of the matrix ligaments is the hexagonal packing which enables virtual volume fractions up to 90%. This arrangement provides an upper bound for the intralaminar toughness, for instance, for the 50% fiber reinforcement case, G_{2+} rises up to 90 J/m^2 (+80%), as shown in Figure 5.12a. The load level around the crack tip with the hexagonal packing (Figure 5.12b) is notably higher than with the random dispersion of fibers (Figure 5.12c) inducing more diffused damage during crack propagation. In similar fashion to the present work, the effect of fiber dispersion was considered for toughness prediction in brittle particle-reinforced ceramics in the analytical model developed by Li and Zhou (2013).

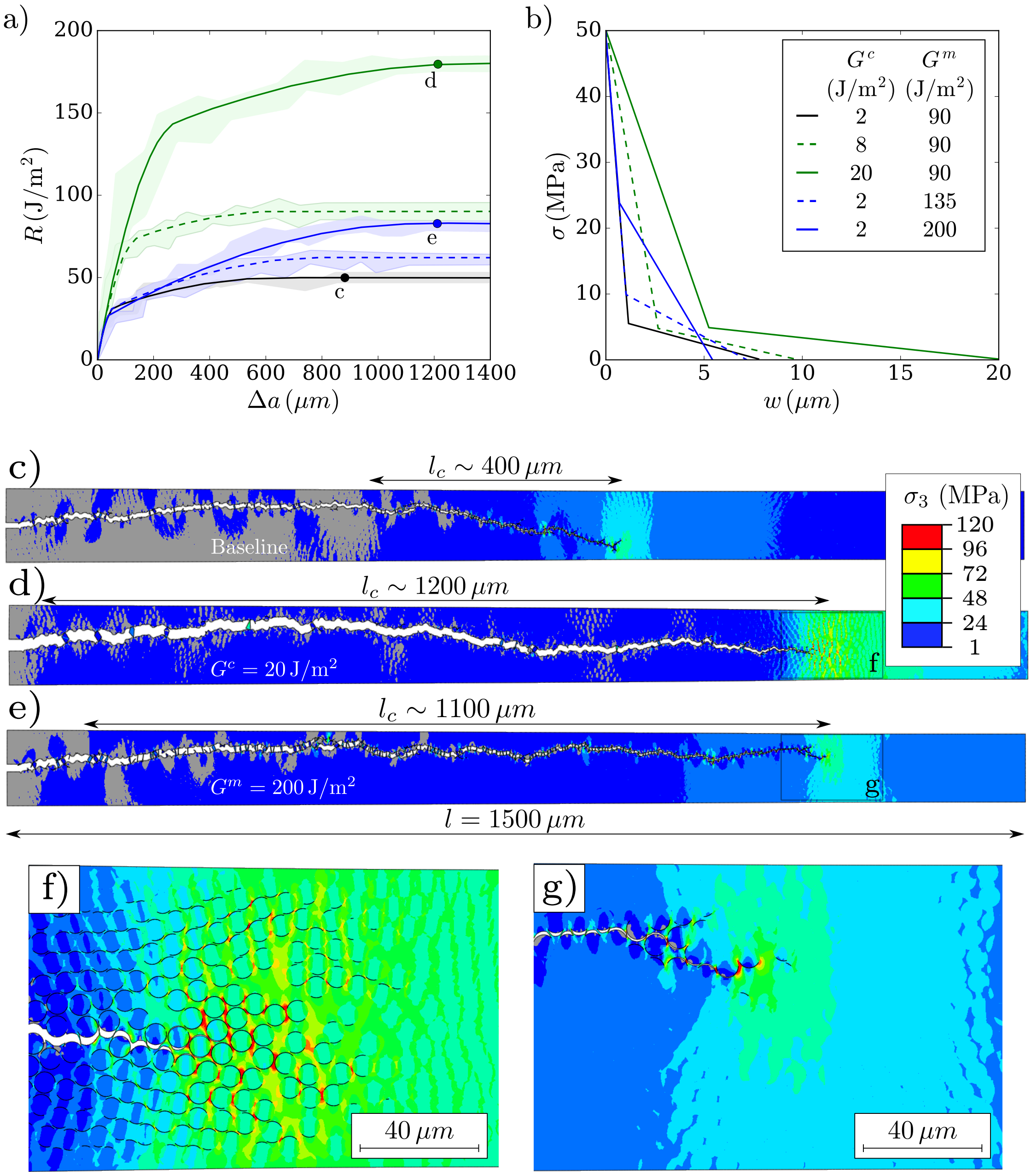

Figure 5.11: a) R-curves obtained with the embedded micromechanical model for baseline properties showing the effect of interface toughness $G^c = 2, 8$ and 20 J/m^2 and matrix toughness $G^m = 90, 135$ and 200 J/m^2. b) Bilinear cohesive laws obtained by least-squares fitting of the R-curves obtained with the embedded micromechanical model. Screenshots of the fracture process zone indicated in a): c) $G^c = 2$ J/m^2 (baseline), d) $G^c = 20$ J/m^2, e) $G^m = 200$ J/m^2. Details of the process zone close to the crack tip for: f) $G^c = 20$ J/m^2 and g) $G^m = 200$ J/m^2. Black lines in f) and g) represent fiber/matrix debonds.

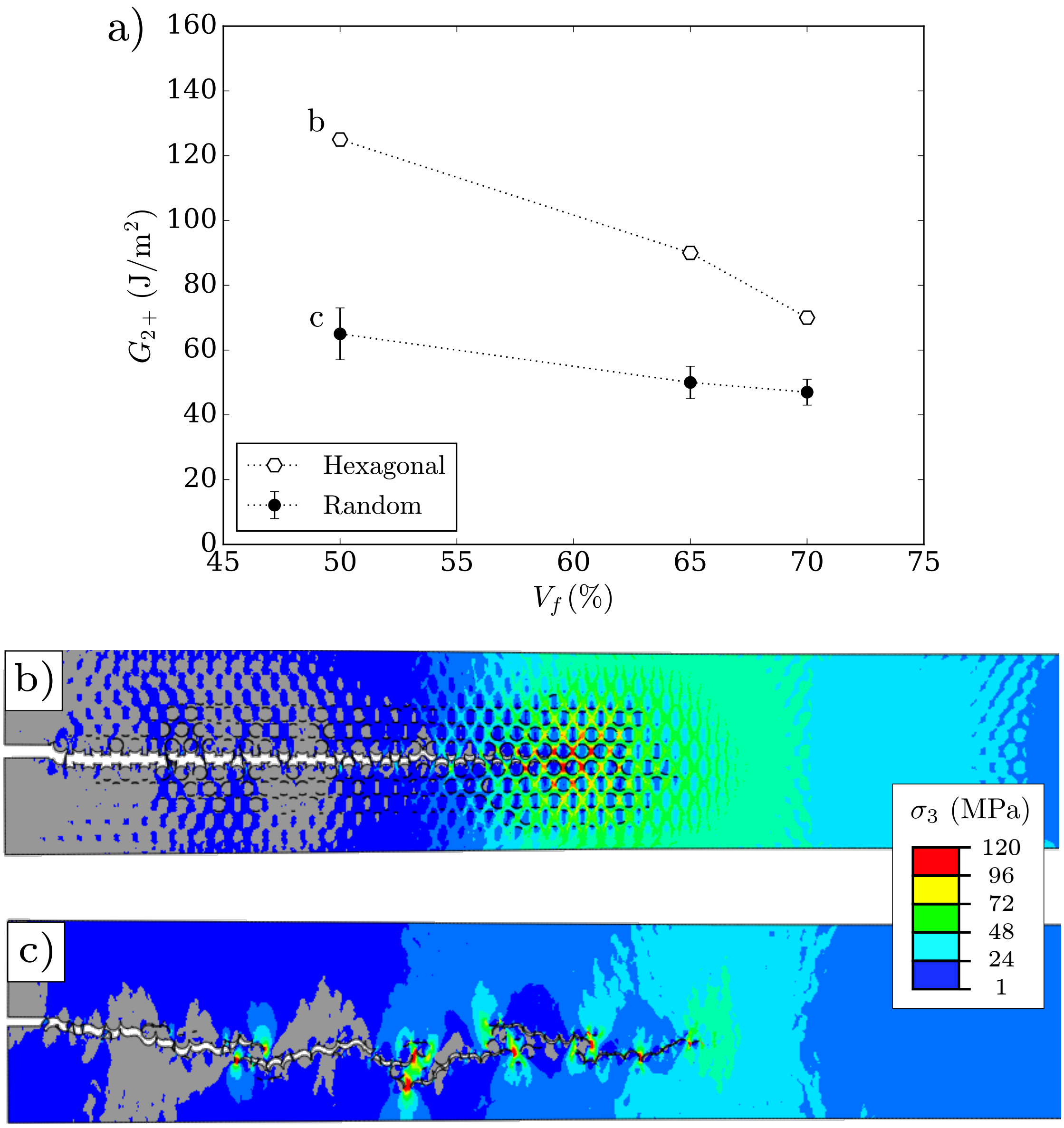

Figure 5.12: a) Steady-state toughness G_{2+} for different fiber volume fractions V_f considering an hexagonal fiber pattern and a random distribution of fibers. b) Detail of the fracture process zone for $V_f = 50\%$ with an hexagonal packing of fibers and c) with a random distribution at the steady-state crack propagation stage.

5.5 Concluding remarks

The fracture behavior of unidirectional fiber reinforced composites and the associated damage mechanisms were studied by means of computational micromechanics. The results were applied to a UD AS4/8552 carbon epoxy composite, this system is widely employed in structural applications in aerospace applications. A bidimensional modeling scheme was used to determine the intraply fracture behavior when a crack grows in the x_2-direction perpendicular to the fibers only accounting for fiber/matrix debonding and matrix plastic/damage mechanisms as the main contributions to the dissipation and fracture mechanisms. Other important effects attributed to larger scale fiber bridging were not taken into account in the model as the characteristic length associated to them, of a few mm in length, is much larger than the close tip mechanisms studied in this work ($l_c \approx 400$ µm for the baseline configuration). Thus, the steady-state fracture toughness obtained following the methodology described in this chapter should be understood as the crack tip toughness which is representative of the effects operating at the micro scale. Representative crack propagation toughness values for AS4/8552 were obtained experimentally through DCB tests (double cantilever beam) and are in the order of $250 \sim 300$ J/m^2.

The fracture behavior was simulated by means of an embedded micromechanical model. Within this approach, the actual microstructure of the composite with the corresponding mechanisms was only included in the fracture process zone ($\ell \times h$), while the remaining model of size $L \times H$ was assumed to be homogeneous with linear elastic behavior. The mechanical properties associated to each of the constituents (fibers, matrix and interfaces) were reported in previous chapters. Displacement fields associated with the K_I linear elastic fracture mechanics stress intensity factor were applied to the external boundaries of the model and allowed to determine the R-curves under the small scale bridging hypothesis. This condition was a compromise between the length of the fracture process zone and the model dimensions ($l_c \ll L$). For the baseline properties, the steady-state fracture energy was $G_{2+} \approx 50$ J/m^2, associated with a fracture process length of $l_c \approx 400$ µm.

In addition, a homogeneous model using a cohesive zone model to track the crack propagation was developed in order to establish an energy equivalence with the micromechanical embedded cell approach. A bilinear homogenized cohesive law corresponding to fiber/matrix debonding and matrix damage/tearing was least-square fitted to the R-curves resulting from the CMM model. It was found that the steady-state fracture energy was mainly dependent on the interface toughness while enhancing matrix toughness was less effective. These findings were corroborated by the direct inspection of the damage patterns close to the crack tip. When the fiber/matrix interface toughness is increased, more damage by fiber/matrix debonding is observed close to the crack tip allowing the resin to sustain additional stresses in this area, improving as a result the fracture energy of the composite. Fiber dispersion also plays a fundamental role as increasing the distance between adjacent fibers, the remaining matrix ligaments are capable of sustaining higher load levels, thus, enhancing the toughness of the composite.

The framework presented is embedded into the multiscale research line of the Composite Materials Group (IMDEA Materials) and shows up as a potential means to characterize the fracture response of an FRP taking into account the micromechanical features of the composite material. Two general possibilities are envisioned from the methodology presented. Firstly, the potential to homogenize the material behavior by means of a cohesive law representing the actual fracture mechanisms of the material, transferring information between length scales (micro and meso), as for instance, in a homogeneous constitutive model used in the analysis of angle ply laminates (i.e. computational mesomechanics). Secondly, enabling a simple way to optimize properties (strength and toughness) of heterogeneous materials by means of virtual tests performed prior to material manufacturing.

Fiber Kinking: From Micro to Mesomechanics

6

6.1 Introduction

The strong anisotropy and heterogeneity of unidirectional fiber-reinforced composites cause very different failure mechanisms depending on the load state. In this chapter, the fiber kinking phenomenon, which is known as the failure mechanism that takes place when the fibers are loaded under longitudinal compression, is analyzed (Schultheisz and Waas, 1996).

6.1.1 Objective and outline

The aim of this chapter is to compare and validate a mesoscale *continuum damage mechanics* (CDM) model developed by A.C. Bergan (Structural Mechanics and Concepts Branch at NASA Langley Research Center) to capture fiber kinking with a high fidelity *computational micromechanics* (CMM) model based on Naya et al. (2017b). The CMM model is used to assess the relative significance of various model features and assumptions in order to improve the understanding of the mechanics of the fiber kinking process. While the CMM model is a powerful tool for analyzing the mechanics of the kinking process, its small scale precludes application to typical structures. Therefore, the CMM model is exploited to interrogate the assumptions of the mesoscale model for fiber kinking.

This chapter is organized as follows. An initial review of the state of the art is done in Section 6.2. In Section 6.3, the main features of the CDM model are presented: fiber kinking theory (FKT), element decomposition, and model verification. The finite element (FE) micromechanical models are presented in Section 6.4:

the single-fiber kinking model, multi-fiber kinking model, and the in-plane shear model. Results from the CMM and CDM models are compared in Section 6.5. A parametric study on the influence of the fiber/matrix interface taking advantage of the micromechanical model developed is shown in Section 6.6. Finally, concluding remarks are presented in Section 6.7, summarizing the ability to derive the micromechanical parameters from the CMM model to feed the mesoscale model, and the representativity of fiber kinking phenomenon by the CDM model.

6.2 State of the art

Numerous evidences of the fiber kinking mechanism are found in the literature, e.g. Piggott and Harris (1980); Kyriakides et al. (1995); Waas and Schultheisz (1996); Pimenta et al. (2009a). Fiber kinking takes place in most high fiber volume fraction composite materials: as compressive loading increases, fibers rotate and matrix undergoes shear deformation, at some load level the matrix cannot support the shear stress and the system becomes unstable (Budiansky and Fleck, 1993), see Figure 6.1a. This shear instability is translated into a localized shear band (i.e. kink band) with fibers misaligned by an angle $\varphi = \varphi_0 + \gamma$ where φ_0 represents initial imperfections and γ is the shear strain. The kink band has a width w_{kb} and propagates along the specimen at an angle β, as shown in Figure 6.1a. After the sudden drop of load, there is a stress plateau during which the kink band first propagates normal to the fiber direction and then under certain conditions grows wider in the fiber direction, as shown in Figure 6.1b. The widening of the kink band along the fibers is referred to as band broadening (Budiansky et al., 1998; Vogler and Kyriakides, 1999).

Several reviews of analytical, numerical, and experimental investigations into fiber kinking are available in the literature (Camponeschi, 1987; Schultheisz and Waas, 1996; Waas and Schultheisz, 1996; Naik and Kumar, 1999). As such, only a few of the most relevant works on modeling fiber kinking are reviewed here. Brief reviews of analytical models, finite element based mesoscale models, and finite element based micromechanical models are given in the following three sections.

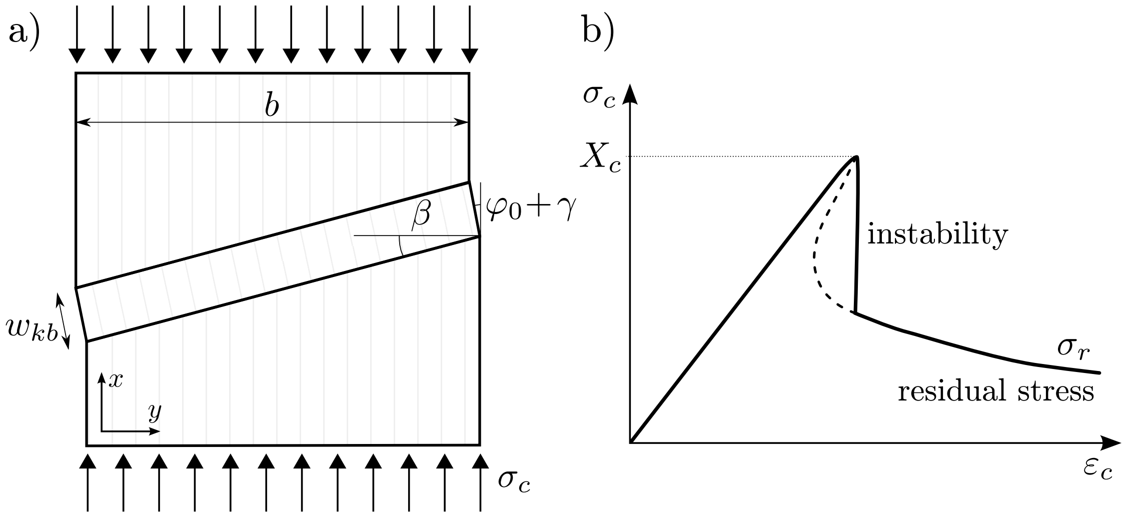

Figure 6.1: Illustration of the fiber kinking phenomenon in a unidirectional fiber-reinforced composite: a) geometry idealization and b) typical stress-strain curve under pure longitudinal compression.

6.2.1 Analytical models for fiber kinking

One of the first analytical expressions found for longitudinal compressive strength X_c of fiber-reinforced composites is given by Rosen (1965)

$$X_c = \frac{G_m}{1 - V_f} \approx G \tag{6.1}$$

where G_m is the shear modulus of the matrix, V_f is the fiber volume fraction, and G is the shear modulus of the composite lamina. This expression was derived assuming fiber kinking is an elastic buckling phenomenon, the fibers are inextensible, $\beta = 0$, and $\varphi_0 = 0$. According to Budiansky (1983), relaxing Rosen's analysis to account for $\beta \neq 0$ and $\varphi_0 \neq 0$ still overpredicts experimentally measured compressive strength. Initial fibers misalignment φ_0 of an infinitely long band of fibers ($b \to \infty$) was included by Argon (1972) assuming rigid perfectly-plastic shear behavior

$$X_c = \frac{\tau_Y}{\varphi_0} \tag{6.2}$$

where τ_Y is the yield shear stress of the composite.

The influence of defects on the compressive failure of a fiber reinforced composite was experimentally observed by Chaplin (1977) who noted that in case of elastic microbuckling, failure should occur along the full width of the lamina simultaneously, while that was not the case in his experiments.

In these first analytical expressions found in the literature, eqs. 6.1 and 6.2, compressive failure was assumed to be triggered by fiber microbuckling. For typical high-fiber-volume-fraction composites, strength was overestimated by 1.5 to 5 times the experimental values (Schultheisz and Waas, 1996). Budiansky (1983) proposed combining the nonlinear shear response of the matrix and the fibers misalignment in an analytical model. In his initial work, he considered an elastic perfectly-plastic composite with yield strain $\gamma_Y = \tau_Y / G$ under longitudinal shear and inextensible fibers. For $\beta = 0$, equilibrium considerations are used to derive

$$X_c = \frac{\tau_Y}{\gamma_Y + \varphi_0} = \frac{G}{1 + \varphi_0 / \gamma_Y} \tag{6.3}$$

Wisnom (1990) derived a similar expression using a micromechanical approach. Later, Budiansky extended eq. 6.3 to consider strain hardening in the nonlinear shear response of the ply (Budiansky and Fleck, 1993) using a Ramberg-Osgood law (Ramberg and Osgood, 1943)

$$\gamma = \frac{1}{G} \cdot (\tau + \mathrm{sign}(\tau) \cdot \alpha \cdot |\tau|^{\eta}) \tag{6.4}$$

where G is the elastic shear modulus of the composite, and η and α are material parameters of the Ramberg-Osgood model. For eq. 6.4, the closed-form solution for the longitudinal compressive strength based on Budiansky and Fleck (1993) is

$$X_c = \frac{G}{1 + \eta \cdot \alpha^{1/\eta} \cdot \left(\frac{G \cdot \varphi_0}{\eta - 1} \right)^{\frac{\eta - 1}{\eta}}} \tag{6.5}$$

The expressions proposed by Budiansky (1983) and Budiansky and Fleck (1993) are referred to as *fiber kinking theory* (FKT). Pinho et al. (2005) generalized FKT to any nonlinear shear response and 3-D stress states within the LaRC04 criterion.

A simple approximation was proposed by Hsu et al. (1998) for calculating the complete stress-strain curve using FKT where axial stress is defined by

$$\sigma_c(\gamma) = \frac{\tau(\gamma)}{\gamma + \varphi_0} \tag{6.6}$$

and the corresponding axial strain is

$$\varepsilon_c(\gamma) = \varphi_0\gamma + \frac{\gamma^2}{2} + \frac{\sigma_c(\gamma)}{E_1} \tag{6.7}$$

given any φ_0 and $\tau(\gamma)$, with the longitudinal elastic modulus of the ply, E_1. The stress-strain curve calculated using eqs. 6.6 and 6.7 includes the unstable post-peak response that can be represented by the dotted line in Figure 6.1b.

Barbero (1998) derived an expression for strength using the principal of total potential energy, finally arriving at

$$X_c = G\left(\frac{\chi}{0.21} + 1\right)^{-0.69} \tag{6.8}$$

after introducing a numerical approximation. In eq. 6.8, $\chi = G\tilde{\varphi}_0/\tau_u$ is a dimensionless constant that characterizes the compressive strength, with $\tilde{\varphi}_0$ being the standard deviation of φ_0. The nonlinear shear behavior of the ply is assumed to be described by

$$\tau(\gamma) = \tau_u \tanh\left(\frac{G\gamma}{\tau_u}\right) \tag{6.9}$$

where the shear modulus, G, and the parameter τ_u define the response. It is emphasized that eq. 6.8 is not empirical. Rather, the numerical values are nondimensional and arise from the approximation used as a simplification for the exact solution.

Experimental investigations have reported variation in strength with specimen length (Kyriakides et al., 1995; Smoot, 1982), which is a trend that is not accounted for in eqs. 6.1-6.3 and 6.5. Lagoudas et al. (1991) introduced an energy based formulation considering both macroscale and microscale factors that accounts for the role of specimen length L on strength

$$X_c = w_{\mathrm{kb}}\sqrt{\frac{2V_f E_x}{\pi d L}\tau_{Y_m}\varphi_c} \tag{6.10}$$

where V_f is the fiber volume fraction, E_x is the longitudinal modulus of the laminate, d is the fiber diameter, τ_{Y_m} is the shear yield stress for the matrix only, and φ_c is the misalignment of the fibers at maximum compressive load. Wisnom and Atkinson (1997) suggested that strain gradient effects may also explain the variations in experimental measurements.

Fleck et al. (1995) proposed the *bending theory* of fiber kinking, which uses couple stress theory to account for fiber bending and the wavelength of initial fiber misalignments while maintaining a ply-level homogenization. The analysis shows that fiber bending and imperfection wavelength have a negligible effect on strength prediction. However, consideration of fiber bending is required to predict the kink band width. The authors found that the kink band width is relatively insensitive to material properties, and falls in the range $10 < w_{\mathrm{kb}}/d < 15$ for typical carbon/epoxy composites. The couple stress approach includes a bending moment per unit area, and this results in a stress tensor that is not symmetric.

Budiansky et al. (1998) extended his previous work and used couple stress theory to derive expressions for the behavior of kink bands after their formation. The rotation angle of fibers at fracture φ_{ff} is found to be

$$\varphi_{\mathrm{ff}} = \left(\frac{2\tau_Y}{E_1}\right)^{1/3} \tag{6.11}$$

where it is noted that $\varphi_{\mathrm{ff}} > \varphi_c$. An expression for the band broadening stress, which is referred to as the residual stress herein, is also given in Budiansky et al. (1998)

$$\sigma_r = \frac{2\tau_L}{\sin(2\beta)} \tag{6.12}$$

where τ_L is the shear stress associated with large rotations (the approximation $\tau_L = 2\tau_Y$ is suggested). The parameter β was left unspecified since no simple explanation for the range of experimentally reported values of $10° < \beta < 30°$ was available (Jelf and Fleck, 1992).

Moran et al. (1995) proposed an expression for the residual stress based on an energy balance and preservation of volume under the assumption of $\varphi = 2\beta$

$$\sigma_r = \frac{1}{2\sin^2\beta} \int_0^{2\tan\beta} \tau(\gamma)\, dx \tag{6.13}$$

where $\tau(\gamma)$ is the nonlinear stress-strain law in shear. Moran suggested a trilinear curve for $\tau(\gamma)$. The resulting expression for σ_r is minimized with respect to β. Moran demonstrated that this approach yields reasonable values for both β and σ_r for ductile matrix composites. However, other authors have questioned the validity of the $\varphi = 2\beta$ assumption, e.g. Vogler and Kyriakides (1999). It is noted that Moran's approach can be extended to strain hardening shear nonlinearity curves such as eq. 6.4 using numeric integration.

Moran's model is one of the very few analytical models that determine β; most models require β to be specified as an input parameter. Schapery (1995) proposed that β is set by a balance between satisfying a matrix tensile failure criterion and shear instability. Despite these efforts, no consensus has been reached for predicting analytically σ_r or β.

In contrast to the aforementioned homogenized models, a micromechanical approach has been taken by others. Hahn and Williams (1984) derived a model based on equilibrium of an initially misaligned fiber in a matrix with shear nonlinearity. Effendi et al. (1995) added considerations for fiber failure and showed that low-strength fibers with small imperfections fail by fiber compression, while composites with larger imperfections failed by fiber kinking.

Pimenta et al. (2009b) built on the approach used by Hahn and Williams (1984) to derive a closed-form expression for the longitudinal compression strength and predict the post-failure response of a unidirectional lamina. The model developed is based on the equilibrium of an imperfectly-aligned fiber loaded in compression and bending, and supported in shear by an elastic perfectly-plastic matrix. An initial fiber misalignment given by $y_0(x) = \bar{y}_0 \cdot (1 - \cos(\pi x/L))$ is assumed where the fiber axis is along the x-direction and the parameters $\bar{y}_0$ and L define the initial imperfection. The expression derived for the compressive strength is

$$X_c = \tau_Y \frac{G_m^{2\mathrm{D}} d + \frac{\pi^2}{L^2} E_f I_f}{\tau_Y + \pi \frac{\bar{y}_0}{L} G_m^{2\mathrm{D}}} \left(\frac{V_f^{2\mathrm{D}}}{A_f} \right) \tag{6.14}$$

where subscript $_f$ indicates quantities associated with the fibers and $_m$ refers to matrix quantities. In eq. 6.14, $G_m^{2\mathrm{D}} = G_m/(1 - V_f^{2\mathrm{D}})$ with $V_f^{2\mathrm{D}} = d/(d + t_m)$, wherein t_m is the thickness of the matrix layers in the 2-D approximation. Assuming that fiber failure is governed by maximum compressive stress, w_{kb} is obtained from the analysis by identifying the location along the fiber where the maximum stress criterion is satisfied. The trends predicted from this model were found to be consistent with the bending theory for fiber kinking (Fleck and Jelf, 1995).

While these analytical models provide great insight and utility, they lack the ability to analyze particular structural configurations and ignore many details of the kinking process. For these reasons, several numerical approaches have been proposed using finite elements (FE) methods. The FE modeling approaches that are relevant to the present work are reviewed in the following two sections.

6.2.2 Modeling fiber kinking at the mesoscale using FE

A variety of FE modeling approaches for fiber kinking in a homogenized lamina (i.e. mesoscale) have been proposed. Wisnom (1993) introduced superposing beam elements on a continuum mesh where the beam elements represent the fibers and the continuum mesh represents the matrix. The study showed the importance of considering fiber rotation, shear nonlinearity in the matrix, and bending of the fibers in order to make accurate predictions of fiber kinking. Wisnom pointed out that most commercial FE codes lack the ability to represent fiber rotation and fiber bending in a homogenized mesoscale model, and thus require techniques such as the beam superposition approach to predict fiber kinking. Other authors have used Wisnom's approach to study the effects of the distribution of fiber misalignment (Lemanski and Sutcliffe, 2012; Sutcliffe, 2013) and fiber packing (Zhang et al., 2016).

In order to account for fiber bending in homogenized mesoscale models, Fleck and Shu (1995) used Cosserat theory (also termed micropolar theory), which is a higher order continuum theory that introduces stress couples into the constitutive law. The model was used to explore the FKT assumption of an infinitely long band ($b \to \infty$ in Figure 6.1a) of misaligned fibers. Finite element simulations using the 2-D couple stress based model showed the effect of the size of the initial imperfection where, as b increases from zero to infinity, the strength decreases from the value predicted by eq. 6.1 to the asymptote predicted by the 1-D couple stress model in Fleck and Jelf (1995). This model has been extended to study the effect of multiaxial loading (Shu and Fleck, 1997), strain gradient effects (Fleck and Liu, 2001), and random fiber waviness (Liu, 2004). Hasanyan and Waas (2018) proposed calibration procedures to define the unconventional material property inputs for their model based on couple stress theory using micromechanical models. These higher order continuum approaches show tremendous promise, but their usage remains limited since they depart from standard conventions in structural analyses (e.g., using an unsymmetrical stress tensor).

In contrast to the efforts to model fiber kinking directly, some authors have used phenomenological constitutive laws that resemble the characteristic fiber kinking response shown in Figure 6.1b. In these approaches, the constitutive laws are described by model input parameters that define the residual stress σ_r and fracture toughness. Careful selection of model parameters enables spectacular simulations of damage for complex structures (McGregor et al., 2008; Pinho et al., 2012; Joseph et al., 2017, 2018; Davidson et al., 2018). However, the predictive capability of these approaches is limited due to the requirement for calibration at the structural scale.

Approaches based on FKT where the fiber rotation and shear nonlinearity are carefully modeled provide an appealing alternative. Basu et al. (2006) formulated one such model using Schapery theory (Schapery, 1990) and tracking the misaligned fiber direction by integrating the increment in shear strain. Good agreement for strength as predicted by a 2-D model similar to that of Kyriakides et al. (1995) was achieved. Feld et al. (2012) proposed augmenting an existing CDM model with an additional term based on a rheological model to account for fiber kinking. Davidson and Waas (2017) used Hill's anisotropic plasticity to model out-of-plane kinking. By introducing thin regions representing resin-rich layers between the plies, predictions with $\beta > 0$ were obtained. Bergan and Leone (2016) proposed a model based on fiber kinking theory that uses the deformation gradient decomposition (DGD) method to account for the coupling between longitudinal splitting and fiber kinking. The model predictions show that large rotations and shear nonlinearity dominate the response. Likewise, Gutkin and Pinho (2015), Gutkin et al. (2016) and Costa et al. (2017) introduced a model based on fiber kinking theory and a physically-based constitutive law for shear nonlinearity. The authors demonstrated that the model is capable of predicting the compression strength and residual stress. These methods are attractive since they are physically based on the mechanics of fiber kinking, while avoiding the complications of high order theories. The mesoscale model presented herein adopts this approach.

6.2.3 Microscale FE modeling of fiber kinking

Numerical micromechanical models of fiber kinking have offered important insights on the topic. By explicitly modeling the fiber and matrix individually in a *representative volume element* (RVE) and accounting for material and geometric nonlinearity, the fiber kinking process can be simulated numerically. Some of the first of such models were developed by Kyriakides et al. (1995) consisting of a 2-D representation with a layered composite of alternating elastic fibers and, J_2 flow theory elasto-plastic matrix. The layers followed a sinusoidal curve representing the ply imperfections (φ_0). These models were among the first to predict the sequence of events leading to the formation of kink bands and realistic values for the kink band angle, β, determined by fiber failure.

One of the first 3-D micromechanical FE models for fiber kinking was developed by Hsu et al. (1998) in order to assess the limitations of 2-D models. The model used a hexagonal fiber pattern with 60 elastic, isotropic fibers and J_2 flow theory elasto-plastic behavior for the matrix. The authors demonstrated that 2-D and 3-D models were in good agreement for predictions of X_c when separate 2-D and 3-D RVEs were used to the calibrate the plasticity parameters to the same test data for the shear stress-strain response. The authors noted that the matrix shear response resulting from the calibration differs for the 2-D and 3-D models. Furthermore, the matrix shear response is not equivalent to measurements for neat resin. In contrast to the good agreement for strength, the post-peak predictions for the two models differ: the 3-D model predicts larger values for w_{kb} and β. In the same study, the FE models were compared with analytical FKT predictions. While the strength predictions were in good agreement, the FKT predicted larger values for the residual stress, σ_r. Thus the authors highlighted the complications of accurate prediction of the post-peak regime. As such, the authors modified the 3-D model in a follow up study on the propagation behavior of already-formed kink bands, where β was explicitly modeled (Hsu et al., 1999). Reasonable agreement was demonstrated with Budiansky's band broadening stress (eq. 6.12).

Fiber kinking initiation and kink band propagation transverse to the fibers was systematically tested and simulated by Vogler et al. (2001) and Vogler and Kyriakides (2001). Experimental tests were carried out holding a constant longitudinal compressive load while applying a progressive shear load under displacement control. In this manner, kink band propagation along the width of the specimen was noticeably more stable. It was observed that kink band rotation, β, was insensitive to the initial imperfection features. The numerical model considered a Drucker-Prager model for the matrix to account for inelastic dilation and sensitivity to hydrostatic pressure which were found to affect the post-peak regime of the composite, especially the β angle.

Yerramalli and Waas (2004) developed a 3-D model with 37 fibers that accounted for fiber orthotropy and J_2 incremental theory of plasticity for the matrix. As before, an RVE with shear loads was used to calibrate the nonlinear shear curve. By comparing the results obtained using isotropic fibers, consideration of fiber orthotropy was shown to reduce the post-peak residual stress σ_r. Examination of the stresses in the fibers showed that high shear strains in the fibers would likely lead to failure and that smaller diameter fibers may break before fiber kinking occurs.

A number of 2-D micromechanical models have been developed building on the foundational efforts described above to study different features and parameters affecting the fiber kinking phenomenon. Gutkin et al. (2010a) analyzed the failure envelopes for fiber reinforced composites under combined longitudinal compression and in-plane shear ($\sigma_{11} - \tau_{12}$) through a single-fiber 2-D model employing periodic boundary conditions (PBC). This study showed two types of failure mechanisms: shear-driven fiber failure and kink-band formation, which were confirmed in the complementary experimental work (Gutkin et al., 2010b). Interaction between fiber kinking and fiber/matrix debonding (splitting) was investigated by Prabhakar and Waas (2013) using a multiple-fiber 2-D model which incorporated a cohesive zone model between the fibers and the matrix. The results suggested that it may be important to consider both fiber kinking and matrix splitting for accurate prediction of compressive strength.

Modern computational resources have enabled massive multi-fiber 3-D micromechanical models. Bai et al. (2015) developed one such model and subjected it to a triaxial stress state including longitudinal compression. The model results show the same sequence of events as other authors, with plasticity in the matrix being the most dominant factor leading to kinking. A hybrid FE model of a 3-D cross-ply laminate section was developed by Bishara et al. (2017b) with the longitudinal plies represented through a single row of fibers as in Bishara et al. (2017a), while the 90° plies are modeled by means of a homogeneous CDM model. This multiscale model was able to capture several failure mechanisms including fiber kinking formation in the 0° plies, subsequent delamination between adjacent plies, and matrix cracking in the 90° plies.

Recently, Naya et al. (2017b) developed a 3-D micromechanical model generated by extruding a fiber distribution along a sinusoidal curve representing the initial fiber misalignment, φ_0. The model consists of fibers oriented in the extrusion direction, a pressure-dependent polymer matrix and a cohesive interaction in the fiber/matrix interface accounting for friction. The application of periodic boundary conditions, as in Gutkin et al. (2010a), permits the model to be simplified to a single-fiber system. The model predictions were found to be in good agreement with experimental measurements.

6.3 Continuum Damage Mechanics Model (CDM)

The main features of the mesoscale constitutive model developed by Bergan and Leone (2016) to capture the fiber kinking failure mechanism are presented in this section.

The CDM model employs geometric nonlinearity and shear nonlinearity based on Budiansky's fiber kinking theory (Budiansky, 1983; Budiansky and Fleck, 1993; Budiansky et al., 1998) with $\beta = 0$. The model includes the kinematics of the fiber kinking process by tracking fiber misalignment throughout loading. The characteristic constitutive response shown in Figure 6.3b is not directly prescribed in the model. Instead, the response is a result of the shear nonlinearity and large rotation of the fiber direction. The model is formulated in the context of continuum damage mechanics (CDM) and integrated into the existing code `CompDam` (Leone et al., 2018), which is a CDM code for predicting damage in carbon fiber reinforced polymer laminates. The deformation gradient decomposition (DGD) method is used for accurate representation of the kinematics of the kink band and fiber misalignments (Leone, 2015).

This model was implemented in Abaqus/Explicit as a VUMAT (Simulia, 2013). The main input parameters of the model, apart from the elastic properties (E_1, E_2, G_{12}, ν_{12}, ν_{23} and c_l), are the nonlinear shear curve through the Ramberg-Osgood parameters (G, η and α), the initial fiber misalignment (φ_0) and the kink band width (w_{kb}).

In the following sections, the main features of the CDM model are briefly described.

6.3.1 Compressive strength: Fiber kinking theory (FKT)

As previously described in Section 6.2.1, the *fiber kinking theory* (FKT) was initially proposed by Budiansky (1983) for an elastic-perfectly plastic composite material under shear. Later, it was generalized for a nonlinear shear response (Budiansky and Fleck, 1993), in particular, deriving the closed-form solution for a Ramberg-Osgood type shear curve (see eq. 6.5) and incorporated the effect of additional shear loading (τ_{12}). Pinho et al. (2005) extended this approach to any nonlinear shear response and introduced the effect of transverse loading (σ_{22}) and 3-D stress states.

FKT is based on the inability of the material to sustain the shear stress induced by the compressive load due to the initial misalignment of the fibers, φ_0, leading to an unstable state. The shear stress in the rotated fiber frame is

$$\tau'_{12} = \frac{\sigma_c}{2} \sin(2\varphi) \tag{6.15}$$

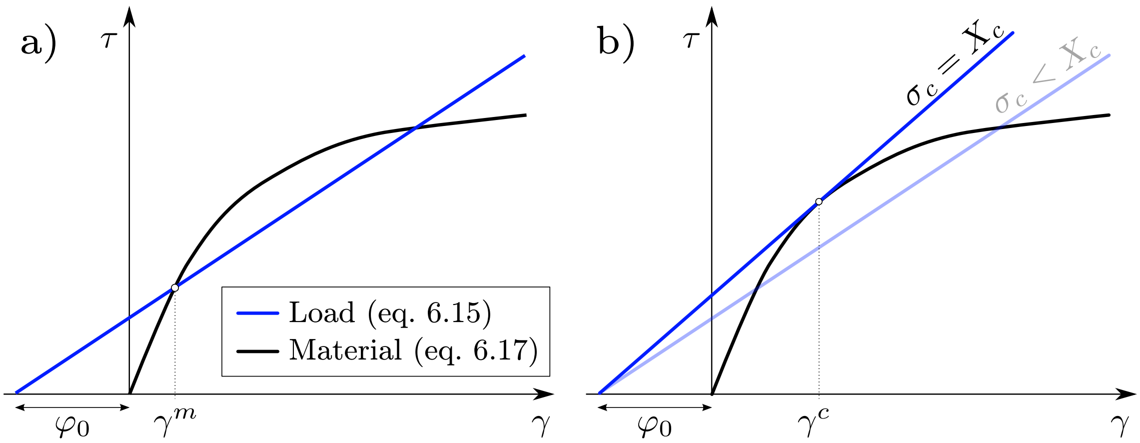

Figure 6.2: a) Shear stress-strain curves representing the nonlinear material response (eq. 6.17) and the induced shear stress due to compressive loading (eq. 6.15), b) Instability point representation, $\sigma_c = X_c$. Adapted from Pinho et al. (2005).

where σ_c is the longitudinal compressive stress and φ the sum of an initial misalignment, φ_0, with the fiber rotation due to loading, γ'_{12}

$$\varphi = \varphi_0 + \gamma'_{12} \tag{6.16}$$

From the constitutive law, the shear stress-strain relationship is represented as

$$\tau'_{12} = f_{CL}(\gamma'_{12}) \tag{6.17}$$

where f_{CL}, in the case of a Ramberg-Osgood expression is the inverse function of eq. 6.4 (Ramberg and Osgood, 1943).

In summary, eq. 6.17 represents the material response, while eq. 6.15 embodies the load applied. The graphical representation of each term is shown in Figure 6.2a, where the black line stands for the constitutive law of the material in shear and the blue line depicts the loading term. For the loading case shown in Figure 6.2a, the loading curve intersects the material curve revealing the shear strain in the rotated fiber frame, γ^m. However, as σ_c increases, the slope of the blue curve grows proportionally and eventually it becomes tangent to the black curve at $\gamma = \gamma^c$, as illustrated in Figure 6.2b. At this point, instability is reached and the the material is unable to sustain higher compressive load, $\sigma_c = X_c$. The analytical solution can be analytically expressed as

$$f_{CL}(\gamma^c) = \frac{1}{2} X_c \sin[2(\varphi_0 + \gamma^c)] \tag{6.18}$$

$$\left.\frac{\partial f_{CL}}{\partial \gamma}\right|_{\gamma^c} = X_c \cos[2(\varphi_0 + \gamma^c)] \tag{6.19}$$

where the unknowns are either the compressive strength, X_c, or the initial fiber misalignment, φ_0, and the shear strain to failure, γ^c. Therefore, for a given shear curve, f_{CL}, there is a biyective relation between the compressive strength and the initial fiber misalignment: $X_c(\varphi_0)$ and $\varphi_0(X_c)$.

6.3.2 Initial misalignment angle

The compressive strength of the ply was introduced within the CDM model by means of the initial misalignment angle, φ_0, which accounts for fiber misalignments and other manufacturing anomalies that may contribute to fiber kinking initiation. The initial fiber misalignment is calculated by rearranging eq. 6.5 as

$$\varphi_0 = \frac{\eta - 1}{G_{12}} \cdot \left(\frac{G_{12} - X_c}{X_c \, \eta \, \alpha^{\frac{1}{\eta}}} \right)^{\frac{\eta}{\eta - 1}} \tag{6.20}$$

such that φ_0 is fully defined in terms of material property inputs. The dependence of the present model on X_c as a material property input could be eliminated by considering experimentally measured fiber misalignments.

6.3.3 Mesh objectivity and decomposition

Material models that exhibit strain-softening behavior are susceptible to mesh sensitivity when strain localizes. In conventional CDM models, this deficiency is often addressed with Bažant's crack band theory in which the energy dissipated is scaled by the element size (Bazant and Oh, 1983). In the present model, there is no crack surface on which traction goes to zero and therefore the crack band theory is not applicable. Nonetheless, there is an inherent mesh sensitivity since the model includes a strain-softening response leading to strain localization in a band of elements after the strength is reached. Recently, Costa et al. (2017) identified this mesh sensitivity as it relates to modeling fiber kinking and recommended two options for ensuring mesh objectivity. The method used herein is analogous to the strain decomposition method proposed by Costa et al. (2017) and is an adaption following previous work by Bergan and Leone (2016).

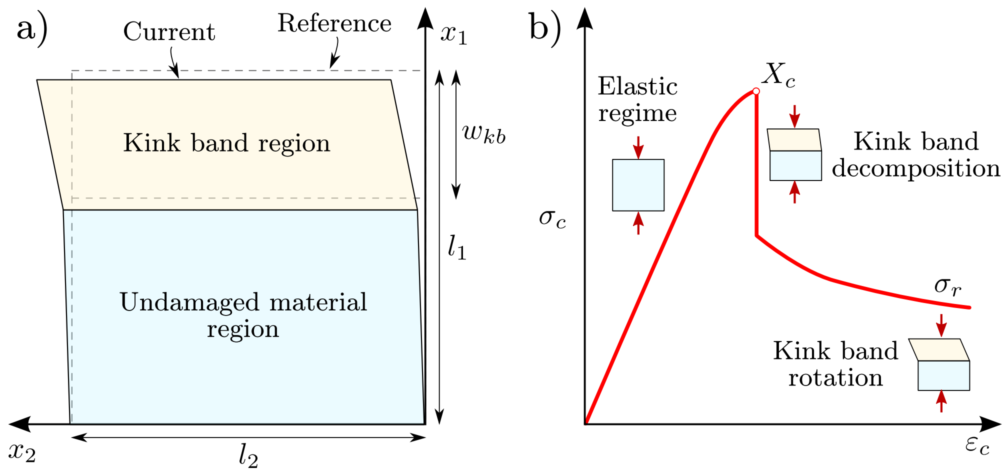

Figure 6.3: Schematic representation of the CDM model: a) decomposition into the kink band and the undamaged region, and b) representation of the stress-strain curve under longitudinal compression.

When the plastic strain becomes non-negligible, the decomposition is performed. In the decomposed element, shear nonlinearity is enabled in the kink band region, whereas in the undamaged material region the shear response is linear. The kink band width, w_{kb}, is assumed to be smaller than the element size in the x_1-direction, l_1. The relative kink band size is defined as $\omega_{\text{kb}} = w_{\text{kb}}/l_1$. When $\omega_{\text{kb}} \leq 0.95$, the element is decomposed into an undamaged region and a kink band region, as shown in Figure 6.3a, in order to preserve mesh objectivity. When $\omega_{\text{kb}} > 0.95$, the kink band width is close to the element size, so the material model described above is applied directly without decomposition of the element. When the element is decomposed, the deformation gradient decomposition (DGD) approach is used to enforce continuity and equilibrium between the undamaged and kink band regions (Leone, 2015; Bergan and Leone, 2016).

6.3.4 Determination of the kink band width

While the model includes fiber rotation, bending of the fibers is ignored. As a result of this assumption, w_{kb} cannot be predicted by the model since w_{kb} is set when the fibers break under high local bending stresses (Budiansky, 1983; Steif, 1990; Gutkin et al., 2010b). As such, w_{kb} is an input parameter for the model and must be obtained from micromechanical analysis or experimental measurements.

Values reported in the literature for different carbon/epoxy composites are summarized in Table 6.1. Some of the results correspond to experimental observations through microscopy and other methods like high resolution X-Ray Computed Tomography (XCT) (Bergan and Garcea, 2017).

Budiansky (1983) derived an expression for w_{kb} by accounting for rigid-perfectly plastic shear nonlinearity and inextensional bending of perfectly aligned fibers using a couple-stress formulation. Assuming $\beta = 0$, w_{kb} is

$$\frac{w_{\mathrm{kb}}}{d} = \frac{\pi}{4}\left(\frac{E_1}{2\tau_Y}\right)^{1/3} \tag{6.21}$$

where d is the fiber diameter and τ_Y is the shear yield stress. Budiansky suggested a kink band width of about 12 fiber diameters for typical carbon/epoxy materials. The kink band width predicted through eq. 6.21 for the materials analyzed in this chapter, AS4/8552 and IM7/8552, is shown in Table 6.1, where $\tau_Y = 95$ MPa is determined from the Ramberg-Osgood shear curve using a 5% offset, the diameter of AS4 carbon fiber is reported in Table 2.4 and the diameter of IM7 is 5.2µm (Hexcel, 2018b). Herein, the kink band width of the CDM model was set to 100 and 50 µm for AS4/8552 and IM7/8552 respectively, which is on the order of values reported in the literature, see Table 6.1.

6.3.5 Material properties

Two material systems, AS4/8552 and IM7/8552, are considered in the demonstration of the CDM and CMM models. The material properties for the CDM model are listed in Table 6.2.

The fiber-direction moduli, E_1, reported in Table 6.2 are the tensile values measured on the interval 0.1% and 0.3% strain. Often, separate values for E_1 are reported for tension and compression for a piecewise linear representation. Nevertheless, a continuous function with a single parameter, c_l, is used herein to consider the nonlinear elastic response of carbon fibers as described previously in Chapter 2. The analogous expression to eq. 2.3 at the ply scale is

$$E_1^* = E_1(1 + c_l\, \varepsilon_{11}) \tag{6.22}$$

where c_l is the nonlinearity coefficient for the ply and is an additional material property to be obtained from test data. A least squares fit of experimental data reported by Peterson and Murphey (2016) was used to obtain $c_l = 11$ from IM7/8552

Table 6.1: Values of w_{kb} reported in the literature.

Reference	Method	Material system	w_{kb} (µm)
Budiansky (1983)	Analytical 2-D, eq. 6.21	AS4/8552	59
		IM7/8552	45
Jelf and Fleck (1992)	Exp. data fitting	AS4/8552	67
		IM7/8552	51
Svensson et al. (2016)	Microscopy	HTS/RTM6	200
Hapke et al. (2011)	Microscopy	T700/977-2	55
Jumahat et al. (2010)	Microscopy	HTS40/977-2	80
Gutkin et al. (2010b)	Microscopy	T800/924	50
Pinho et al. (2006)	Microscopy (CCT)	T300/913	70
Soutis (1996)	Microscopy	T800/924C	55
Bergan and Garcea (2017)	In situ X-Ray CT	IM7/8552	25
Pimenta et al. (2009b)	Analytical 2-D	T800/924	250
Zobeiry et al. (2015)	Microscopy (CCT)	IM7/8552	50
Laffan et al. (2012)	Microscopy (4PBT)	IM7/8552	25
Bai et al. (2015)	3-D micromechanical FE	AS4/3501	49
Naya et al. (2017b)	3-D micromechanical FE	AS4/8552	120

Table 6.2: Material properties for the CDM model: AS4/8552 (Marlett et al., 2011) and IM7/8552 (Wanthal et al., 2017).

Material	E_1 [GPa]	E_2 [GPa]	G_{12} [GPa]	ν_{12}	ν_{23}	α [MPa$^{1-\eta}$]	η	X_c [MPa]	c_l	w_{kb} [µm]
AS4/8552	131.6	9.24	4.83	0.30	0.45	$2.86\ 10^{-11}$	6.49	1480	12.2	100
IM7/8552	152.7	8.7	5.16	0.32	0.45	$4.06\ 10^{-9}$	5.4	1731	11.0	50

unidirectional specimens. Whereas for the case of AS4/8552, experimental single-fiber tests were conducted to obtain the nonlinearity parameter at the fiber-scale, c_f, as shown in Section 2.1.3. This value was related to the lamina through the rule of mixtures, $c_l = V_f \cdot c_f$, where $V_f = 60\%$ is the fiber volume fraction (Peterson and Murphey, 2016). Following this procedure, the value obtained for AS4/8552 was $c_l = 12.2$.

6.3.6 Model verification

Analyses were conducted using a model with a single isoparametric hexahedral element with reduced integration (C3D8R, Simulia (2013)) subjected to uniform end shortening in the longitudinal direction in order to verify the constitutive behavior of the model. Boundary conditions were imposed to prevent hourglassing modes of deformation. The element had a uniform edge length of 0.15 mm. A smooth-step was applied with a duration of 0.1 and uniform mass scaling with a factor of 10^5. Rayleigh damping was used to limit vibrations which occur as a result of the large load drop when the strength is reached. The value of the Rayleigh damping coefficient, α_R, was chosen so as to minimize the vibration without changing the global response.

The stress vs. strain results predicted by the CDM model are shown in Figure 6.4a for the IM7/8552 material system. The compressive stress, σ_c, is calculated from the reaction force divided by the element cross-sectional area, $\sigma_c = F_1/(l_2\, l_3)$. Likewise, the compressive strain is obtained from the end shortening displacement $\varepsilon_c = u_1/l_1$. The stress vs. strain results with the CDM model are shown as the solid black line. The linear stiffness calculated using E_1 is denoted by the dotted line. The strength is shown on the plot as the horizontal blue line labeled X_c. The results from FKT, eqs. 6.6 and 6.7, are shown as the dashed line. The results show that the model reproduces the initial stiffness in good agreement with the linear stiffness at small strains. At larger strains, the model predicts that the stiffness degrades as the peak strength is approached. The stiffness reduction is primarily a result of the fiber nonlinearity, described by eq. 6.22. Nevertheless, geometric nonlinearity also contributes to the stiffness reduction. The strength from the model is in very good agreement with the input property, where it can be observed that the model just slightly over predicts the input value of X_c by 1.5%. Once the strength is reached, a snap-back phenomenon occurs as shown for the FKT results. Since the present model is not capable of predicting the snap-back behavior, the model response has an abrupt drop followed by some vibration. The vibrations are mostly suppressed by the Rayleigh damping. Afterwards, the dynamic effects from the abrupt load drop dissipate at around 1.8% strain, towards an asymptotic residual stress level, σ_r. A range of σ_r is calculated using eq. 6.12 with shear stress $\tau_L = 95$ MPa (at 5% strain) and $\beta = 12°$ to $16°$ based on experimental measurements (Bergan and Garcea, 2017). While the present model predicts slightly lower residual stress than FKT, the range for σ_r from eq. 6.12 superimposed on Figure 6.4 shows very good

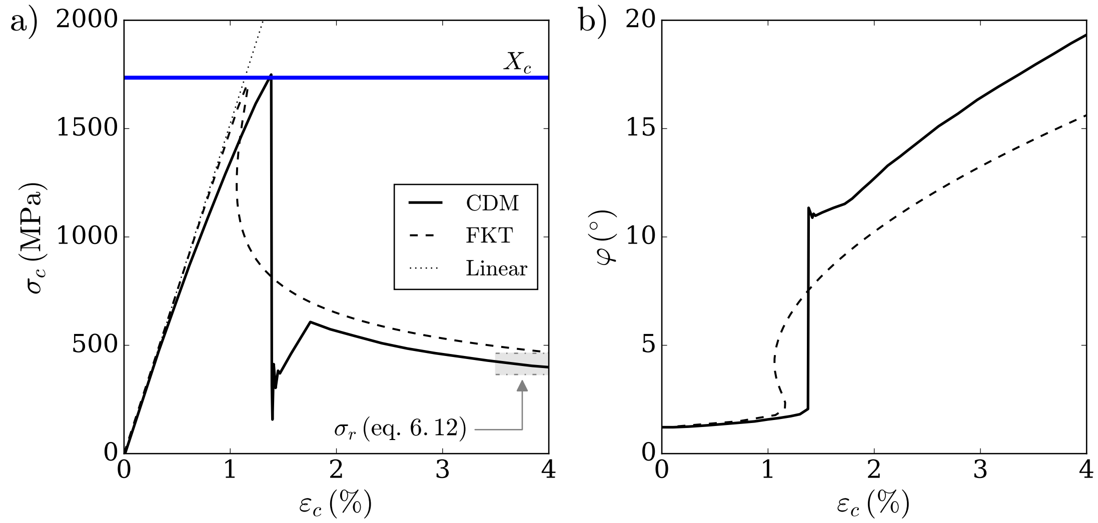

Figure 6.4: Constitutive response of the mesoscale model obtained from a single element analysis for IM7/8552.

agreement with the results from the CDM model. The fiber rotation vs. strain curves are read in Figure 6.4b. The fiber rotation in the current CDM model, φ, shows that the initial misalignment at no load leads to slight rotation up to the point where the strength is reached. At that point large fiber rotation suddenly occurs, and it continues to grow as the model approaches the residual stress in the post-peak regime. This behavior is also captured by the FKT model (Hsu et al., 1998). It should be emphasized that the constitutive response described in this paragraph and the accompanying figure are outcome of the model, not prescribed directly. As a result, the model has the ability to account for several aspects of FKT, such as the relationship between the initial misalignment angle (φ_0), compressive strength (X_c), and residual stress (σ_r).

Other verification models, assessing the effect of the kink band width and the element decomposition are not shown in this thesis, but are described in detail in Herráez et al. (2018a).

6.4 Computational Micromechanics Model (CMM)

A 3-D single-fiber computational micromechanics (CMM) model is used to assess the relative significance of various features and assumptions of the relatively coarse mesoscale model in order to improve the understanding of the mechanics of the fiber kinking process. In this section, the micromechanical finite element model is described including the geometry, discretization, and material properties. Experimental measurement and calibration undertaken to define some of the most critical material properties are described. This section concludes with verification examples that demonstrate the behavior of the CMM.

6.4.1 3-D RVE for fiber kinking

During the last three decades, a variety of micromechanical models have been developed to represent the fiber kinking process. The aim of this work is to study the initiation and evolution of the fiber kinking process, including kink band broadening (Moran et al., 1995; Budiansky et al., 1998) in the post-failure regime. As such, there is no need to use a multiple-fiber model that could capture kink band propagation. Instead, a single-fiber 3-D model with periodic boundary conditions is employed based on Naya et al. (2017b).

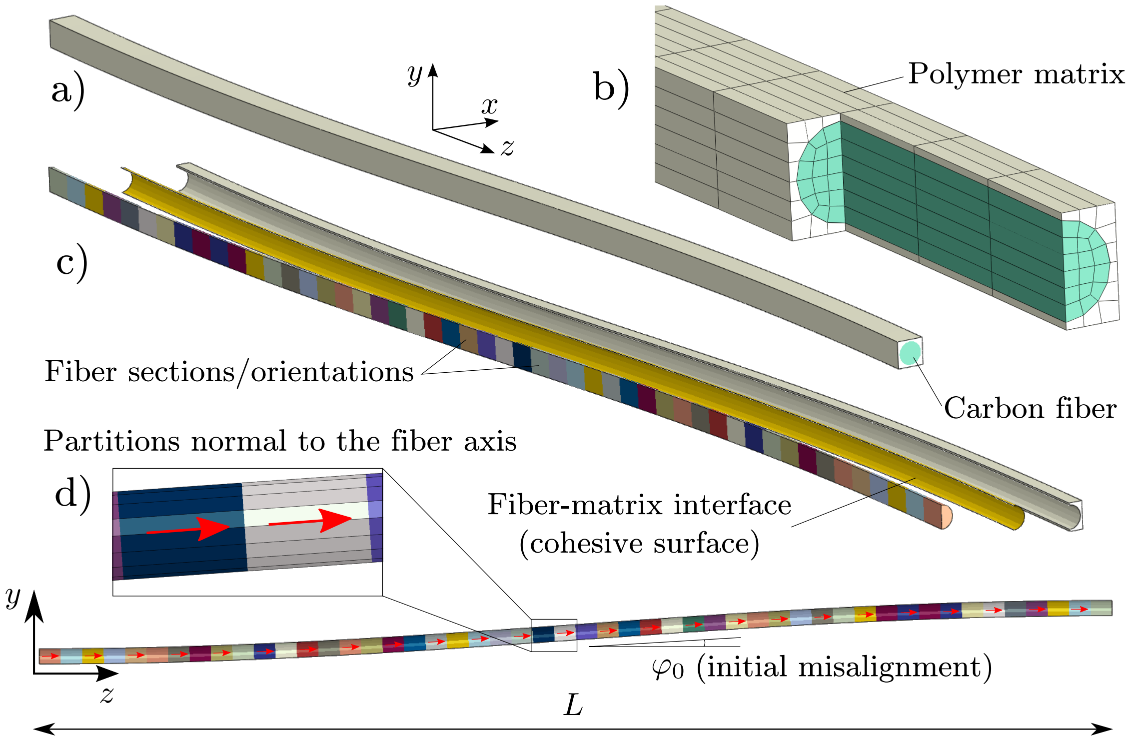

Figure 6.5: Illustration of a) the single-fiber 3-D model, b) detail of the mesh, c) exploded cut view of the model, and d) side view with detail of the longitudinal mesh and material orientation. Adapted from Naya et al. (2017b).

The model represents a 3-D single carbon fiber extruded in the longitudinal direction (z) along the half wavelength of a sine curve of length L, with an initial misalignment, φ_0, following eq. 6.23, as shown in Figure 6.5. Due to the anisotropic behavior of the carbon fiber, reinforcement sections were oriented according to its local misalignment along the fiber axis according to eq. 6.24 as shown in Figure 6.5d.

$$y(z) = L\,\frac{\varphi_0}{\pi} \cdot \left(1 - \cos\left(\pi\frac{z}{L}\right)\right) \tag{6.23}$$

$$y'(z) = \varphi_0 \cdot \sin\left(\pi\frac{z}{L}\right) \tag{6.24}$$

The fiber diameter is d and a fiber volume fraction $V_f = 60\%$ is assumed, leading to a square RVE of side $w = d/2 \cdot \sqrt{\pi/V_f}$. The model is discretized using finite elements in Abaqus/Standard (Simulia, 2013). Both, matrix and fiber, are modeled with 8-node fully integrated isoparametric elements (C3D8). The in-plane mesh size is set such that there are six elements along the fiber diameter, while in the longitudinal direction it is 10 µm, as shown in Figure 6.5b. The model length is $L = 500$ µm with partitions in the longitudinal direction normal to the fiber axis, as shown in Figure 6.5d. The model length was selected based on a preliminary study, as described in Section 6.4.4.

A single-fiber model requires a special definition of the boundary conditions, as free boundaries would promote Euler buckling of the fiber, largely underestimating the strength of the composite. Periodic boundary conditions (PBC) appear as the most adequate solution. Gutkin et al. (2010a) showed that PBC can be applied on single-fiber models for longitudinal compressive strength prediction (X_c) at the expense of inducing $\beta = 0°$. PBC are applied on the lateral faces of the model, while the model ends are subjected to isostrain conditions to introduce the longitudinal compressive load. For details on the description of the PBC, the reader is referred to Section 4.2.1.

A homogeneous thermal step with a temperature drop, ΔT, was applied without external loading prior to the loading step to consider the residual thermal stresses induced by the cool-down from the curing temperature. This thermal step induces a residual thermal stress field as a result of the mismatch between the thermoelastic constants of fibers and matrix. The accurate simulation of the cool-down process is hardly predictable due to the dependency of the thermoelastic properties of the constituents on the temperature, specially in the case of the matrix. For the sake of simplicity, constituents properties are assumed to be constant with the temperature, and it is the magnitude ΔT what is tuned to provide a reasonable estimation of the residual stress level as described in Section 6.4.3.

6.4.2 Material models for the fiber, matrix, and interface

The model consists of two phases, fiber and matrix, and a cohesive interaction which represents the fiber/matrix interface. Although, the constitutive material models are similar to those described in Chapters 4 and 5, there exist some differences which are pointed out in this section.

Carbon fiber

The carbon fiber was modeled as a transversely isotropic solid considering elastic nonlinearity and inelastic damage. Elastic nonlinearity of carbon fibers in the longitudinal direction is reported in the literature (Montagnier and Hochard, 2005) and typically the longitudinal elastic modulus is modeled as a linear function of the longitudinal strain (Kowalski, 1988; Peterson and Murphey, 2016; Le Goff et al., 2017) as considered herein by means of eq. 2.3

Fiber failure is given by a maximum stress criterion either in longitudinal tension, $\sigma_{11}^f \leq X_t^f$, or compression, $\sigma_{11}^f \geq -X_c^f$ and subsequent damage based on a CDM scheme (Maimi et al., 2008). The details of the numerical implementation of the user subroutine for the carbon fiber constitutive behavior can be found in Appendix C. AS4 fiber tensile and compressive strengths, X_t^f and X_c^f, were characterized in Sections 2.1.3 and 2.2.2 respectively. Longitudinal properties of the AS4 carbon fibers were experimentally obtained as described in Section 2.2. The IM7 carbon fibers were not characterized for availability reasons. Instead, the compressive strength of IM7 fiber was obtained from the literature (Gutkin et al., 2010a), whereas the nonlinear parameters, E_1^{0f} and c_f, were scaled from the ply-scale values, E_1 and c_l, by means of the rule of mixtures as $c_f = c_l/V_f = 18.3$ (Peterson and Murphey, 2016) and $E_1^{0f} = E_1/V_f = 256$ GPa. The thermoelastic constants introduced in the constitutive model of the carbon fibers, AS4 and IM7, are gathered in Table 6.3.

Fiber/matrix interface

Fiber/matrix debonding is taken into account by means of a cohesive crack approach similar to that described in Section 4.2.2. Nevertheless, since friction is included in the interface constitutive behavior, a surface-to-surface master-slave interaction

Table 6.3: Material properties of linear and nonlinear models of AS4 and IM7 carbon fibers. Note the AS4 fiber properties are the same as those in Chapters 2, 4 and 5 (Tables 2.4, 2.6, 2.3 and 4.1).

	Fiber	AS4	IM7
Nonlinear	E_1^{0f} [GPa]	211.5	253
	c_f	18.7	18.3
Linear	E_1^{0f} [GPa]	231	276
	c_f	0	0
	E_2^f [GPa]	12.9	11.9
	ν_{12}^f	0.3	0.3
	ν_{23}^f	0.46	0.46
	G_{12}^f [GPa]	11.3	11.6
	G_{23}^f [GPa]	4.45	3.97
	X_c^f [GPa]	3.5	3.8
	X_t^f [GPa]	4.0	5.0
	α_1^f [°C^{-1}]	-0.9 10^{-6}	-0.6 10^{-6}
	α_2^f [°C^{-1}]	7.1 10^{-6}	5.2 10^{-6}
	d [µm]	7.1	5.1

with cohesive contact behavior was employed (Simulia, 2013), instead of the approach based on cohesive elements followed in Chapters 4 and 5. Isotropic Coulomb friction through a single coefficient, μ^c, is enabled at cohesive damage initiation. The shear stresses caused by friction at the interface, τ_μ, are ramped proportional to the cohesive damage variable D^c, and can be defined as

$$\tau_{\mu^c} = \mu^c\, D^c\, \langle -\sigma_n \rangle \tag{6.25}$$

where $\langle -\sigma_n \rangle$ represents the compressive normal stress component at the interface. Thus, once the interface is completely debonded ($D^c = 1$), the surface interaction is exclusively controlled by friction, i.e. $\tau_\mu = \mu^c \langle -\sigma_n \rangle$. The fiber/matrix interface parameters used in the simulations are presented in Table 6.4. The strengths (N^c, S^c) and friction coefficient (μ^c) were calibrated as described in Section 6.4.3.

Table 6.4: Material properties of fiber/matrix interface based on Naya (2017) and calibrated as described in Section 6.4.3.

N^c [MPa]	S^c [MPa]	E^c_{nn} [GPa]	E^c_{ss} [GPa]	G^c_n [J/m^2]	G^c_s [J/m^2]	η_{BK}	μ^c
57	85	100	100	7	81	1.45	0.4

Polymer matrix

The polymer matrix is modeled through the damaged/plasticity model described in Section 4.2.2 with the same mechanical properties as used in Chapter 4 and 5, and shown in Table 4.3. Nevertheless, the value for the dilation angle, ψ^m, assumed in Table 4.4, was determined by means of the calibration procedure described in Section 6.4.3.

6.4.3 In-plane shear response

The mesoscale model requires the nonlinear stress vs. strain relation under in-plane shear loading, $\tau_{12} = \tau_{12}(\gamma_{12})$, to derive the compressive strength of the composite. Ideally, the parameters that define the shear response of the ply are obtained from an experimental test that isolates the behavior of a single ply subjected to large shear deformations. However, in the absence of such test data, the ASTM D3518 test of a $\pm 45°$ laminate subjected to longitudinal tensile loading (ASTM D3518, 2013) is used to define the shear nonlinearity behavior. The $\pm 45°$ laminate test data smears a wide variety of damage mechanisms into a single stress-strain curve, including mechanisms such as large fiber rotations and delamination, which are not desirable to include in the shear nonlinearity characterization. Nonetheless, the $\pm 45°$ laminate is the most common source of material input data available for the mesoscale model. Therefore, a new micromechanical model was designed in order to represent the stress state of a $\pm 45°$ laminate subjected to a tensile test, thus combining the in-plane shear stress parallel and perpendicular to the fibers direction simultaneously. This approach facilitates a one-to-one comparison between the mesoscale and micromechanical models of the fiber kinking mechanism. It must be remarked that the nonlinear shear curve of the ply, $\tau_{12}(\gamma_{12})$, is an input of the mesoscale CDM model and plays a crucial role in the fiber kinking phenomenon.

An RVE of a $\pm 45°$ laminate, as shown in Figure 6.6a, was developed with the

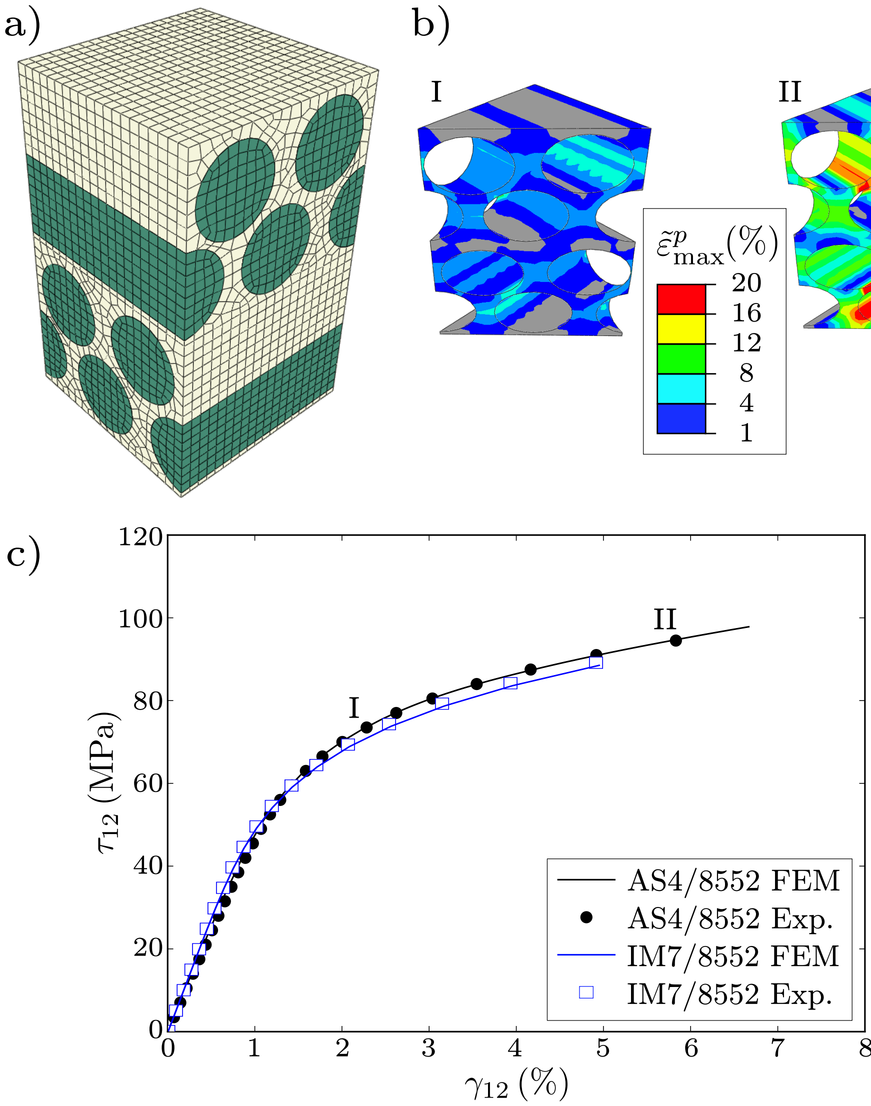

Figure 6.6: a) RVE of the ±45° finite elements model, b) cut views of the numerical model displaying the plastic strain field in the matrix at the points, I and II, indicated in c shear stress-strain experimental curves of AS4/8552 Marlett et al. (2011) and IM7/8552 Wanthal et al. (2017) with the numerical curves of the micromechanical FE model.

parameters and modeling approach described in the previous section. Under in-plane shear loading, the model is initially linear elastic until longitudinal fiber debonding is triggered followed by matrix shear yielding, which progressively increases, see Figure 6.6b. The dilation angle of the matrix, $\psi^m = 15°$, the fiber/matrix interface strengths, N^c, S^c (see Table 6.4), and the effective temperature drop, $\Delta T = 85°\text{C}$, were adjusted by trial-and-error to reproduce the experimentally measured shear stress-strain response. The final response produced from the $\pm 45°$ micromechanical RVE, and the experimentally measured response of a $\pm 45°$ laminate are nearly identical as shown in Figure 6.6c. The parameters for the Ramberg-Osgood curves reproducing the shear curve of the materials are found in Table 6.2.

6.4.4 Model verification

This section describes some analyses that verify the CMM modeling parameters and demonstrate the characteristics of the model predictions. The behavior of the fiber is assumed as linear and elastic ($c_f = 0$) with no damage. The initial fiber misalignment is taken as $\varphi_0 = 1.5°$.

Verification of model parameters

Verification studies were conducted to investigate the influence of the model length, model size, and periodic boundary conditions for the CMM. These analyses were carried out for an AS4 carbon fiber.

To analyze the effect of the boundary conditions on the model representativity, two models were compared. The first model consists of the single-fiber model with periodic boundary conditions described in Section 6.4.1. The second model consists of a vertical array of 3-D fibers extruded along a sine curve as in the single-fiber model, eq. 6.23, but in this case periodic boundary conditions are only applied on the lateral faces $x = 0, l_x$ of the model; the top and bottom faces are free (Hsu et al., 1999; Vogler et al., 2001; Bishara et al., 2017a). An increasing number of fibers was considered in this latter model ranging from 50 up to 400. A schematic representation of the model is presented in Figure 6.7a.

A 2-D model was also developed for comparison purposes, as shown in Fig. 6.7b, based on the work of other authors in the literature (Vogler et al., 2001; Pimenta et al., 2009a; Prabhakar and Waas, 2013; Wind et al., 2014). Nevertheless, since the shear response was calibrated using a 3-D micromechanical model, the equivalence with a 2-D model is not guaranteed.

The results indicate that the predictions of the compressive strength with the single and multiple-fiber models are in good agreement with FKT, as shown in Figure 6.8a. As the number of fibers increases in the multiple-fiber models, the strength approaches the strength predicted by the single-fiber model, as shown in Figure 6.8b. The limiting case of an infinite number of fibers is equivalent to the

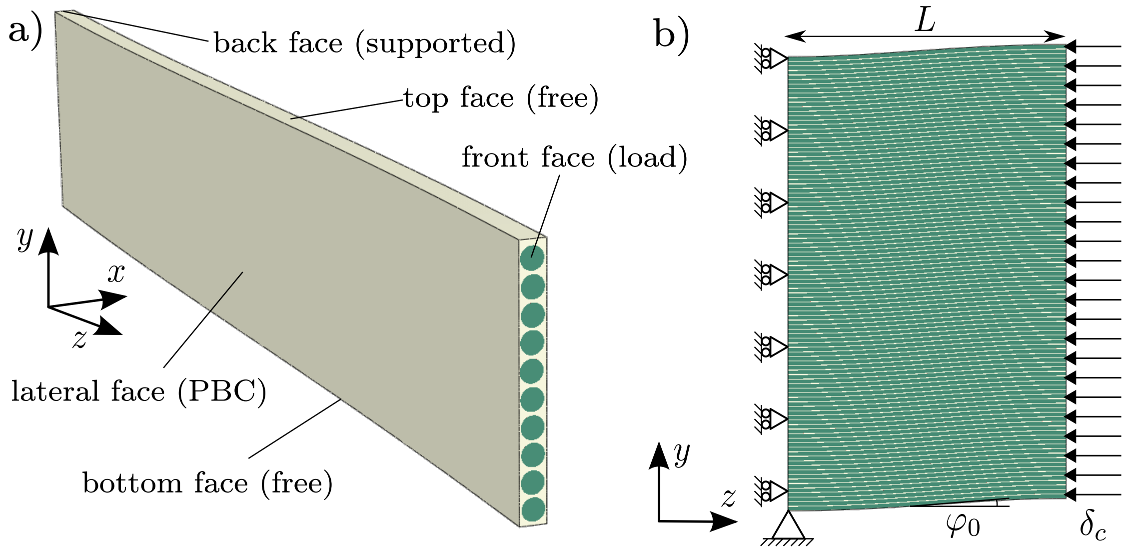

Figure 6.7: a) Multiple-fiber 3-D model consisting of 10 fibers and b) side view of a multiple-fiber 2-D model with 100 fibers illustrating the boundary conditions and initial misalignment angle of the fibers.

single-fiber model with periodic boundary conditions, which is in excellent agreement with FKT.

The effect of the model length was assessed by running single-fiber 3-D models

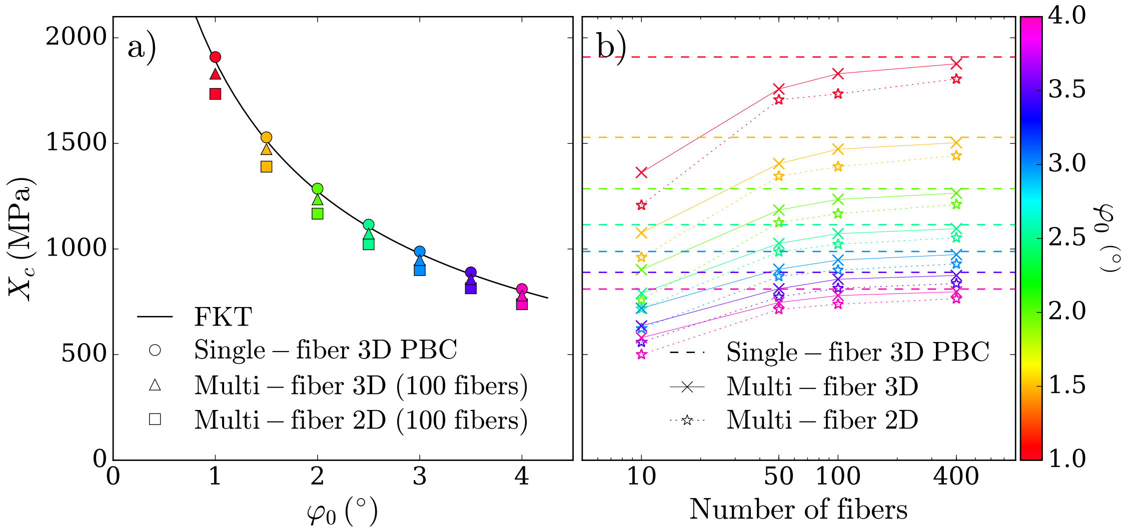

Figure 6.8: Sensitivity curves comparing a) the analytical solution from FKT, eq. 6.5, with the numerical results from different FE models and b) the effect of the number of fibers included in the multi-fiber models.

with the following length values: 200, 300, 500, 750 and 1000 µm. The longitudinal mesh size was kept constant at 10 µm. The stress-strain curves for $\varphi_0 = 1.5°$ with the different length values are shown in Figure 6.9a. A convergent trend towards the strength predicted by FKT is observed in Figure 6.9a as the model length increases. The error in strength between the CMM and FKT is below 2% for $L \geq 500$ µm. Comparing the kink band rotation (maximum, $\varphi^{\max}$, and average, φ^{avg}) in Figure 6.9b, the kinematic behavior is equivalent regardless of the fiber length. In Figure 6.9c, it is observed that the kink band width at fiber kinking initiation was very similar, around 100 µm, for all the model lengths analyzed. The maximum band broadening increases with the model length, as the fiber is longer and fiber failure, which may limit band broadening, is not considered in these analyses. Nevertheless, the relative kink band size is identical in all cases, $w_{\text{kb}}/L = 0.7$, as shown in Figure 6.9d. These results show that the kink band width at initiation only depends on the fiber diameter, d, but the band broadening after the kink has formed is affected by the far-field boundary conditions.

Based on these analyses, the single-fiber 3-D model with periodic boundary conditions and $L = 500$ µm was selected as the most suitable and representative model to analyze the fiber kinking phenomenon in terms of stress-strain curve and kink band kinematics. This version of the CMM model is used as the nominal configuration throughout the remainder of this report.

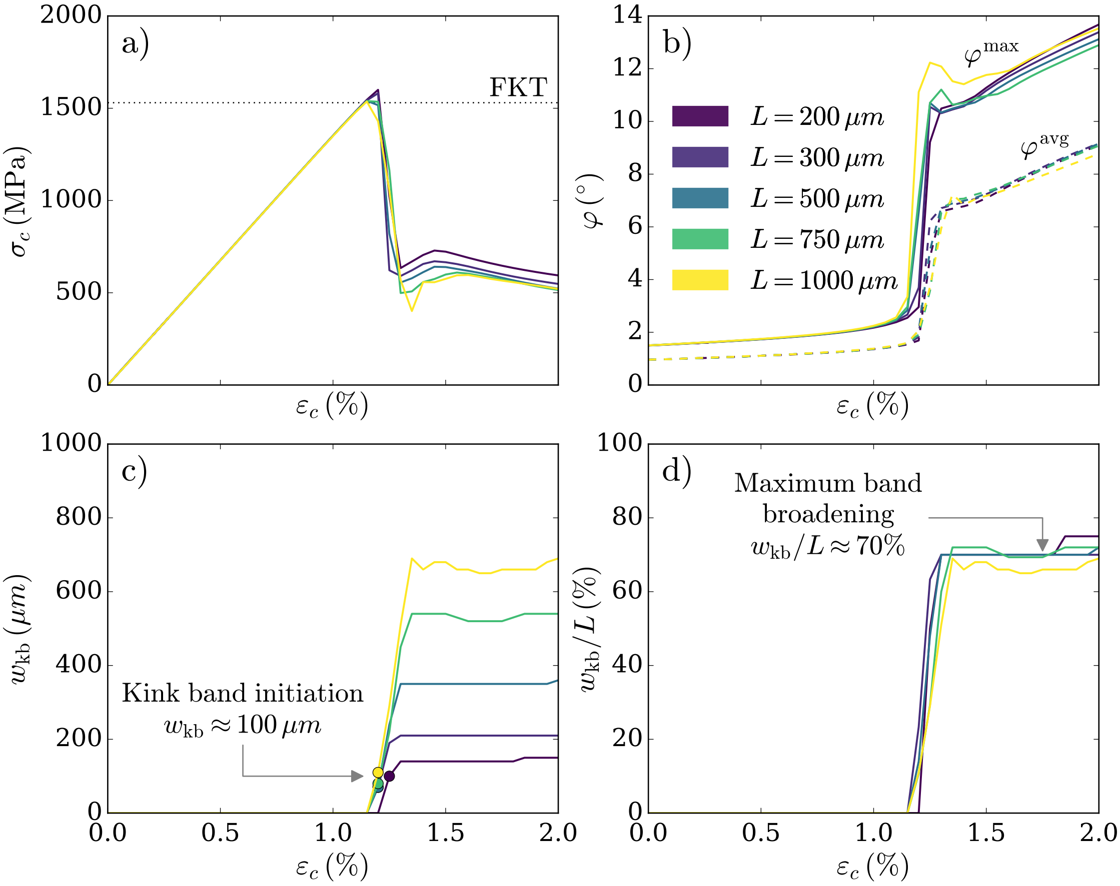

Figure 6.9: a) Stress-strain curves for the single-fiber 3-D model with $\varphi_0 = 1.5°$ for different model lengths, L; b) kink band rotation, maximum and average, $\varphi^{\max}$ and φ^{avg}; c) kink band width, w_{kb}; and d) relative kink band size, w_{kb}/L.

Sequence of events in the kinking process

The sequence of events observed in the CMM model is illustrated in Figure 6.10. As the compressive load increases, σ_c, the shear stress along the matrix grows due to the fiber initial misalignment (eq. 6.15) and starts yielding along a narrow band at the center of the imperfection (point i). The yielded region continues spreading in the longitudinal direction until the yield band is wide enough to promote local rotation of the fiber (point ii), leading to the formation of a kink band (point iii). The same sequence of events prior to fiber kinking was observed by Davidson and Waas (2014). Fiber rotation originates a sudden drop in load carrying capacity and results in the kink band, which corresponds to the region where the matrix has deformed plastically. This region is bounded by the fiber sections with the highest bending stresses. The fiber/matrix interface also participates by triggering the kinking of the fiber. When the interface is damaged, the fiber cannot transfer part of the shear load to the matrix resulting in premature kinking failure.

Due to the single-fiber model design and the periodic boundary conditions, once the kink band appears it is assumed that it has already propagated simultaneously across the whole ply. Therefore, transverse propagation cannot be observed with this model. Instead, as the compressive strain, ε_c, increases the kink band keeps growing along the fiber direction. This phenomenon is known as band broadening, and can be observed experimentally once the kink band has fully propagated across the specimen (Moran et al., 1995). Band broadening is accompanied by progressive fiber rotation, while the compressive stress gradually decreases. This sequence of events is also observed with periodic models including several fibers (Naya et al., 2017b).

Neither the tensile nor compressive strengths of the fiber are reached for the model parameters considered here. Small values of initial misalignment do result in fiber damage, as discussed later in Section 6.5.2. For small values of initial misalignment, $\varphi_0 < 1°$, the fibers fail under pure compression resulting in a constant compressive strength value, X_c, regardless of φ_0 (Gutkin et al., 2010a). However, fiber breakage was not observed in the models with initial misalignment higher than 1°, neither at fiber kinking initiation, nor during kink band broadening. Such predictions seem unrealistic since nearly all experimental observations of kink bands show broken fibers. It can be concluded, then, that more realistic failure models for the fibers are required to address this deficiency.

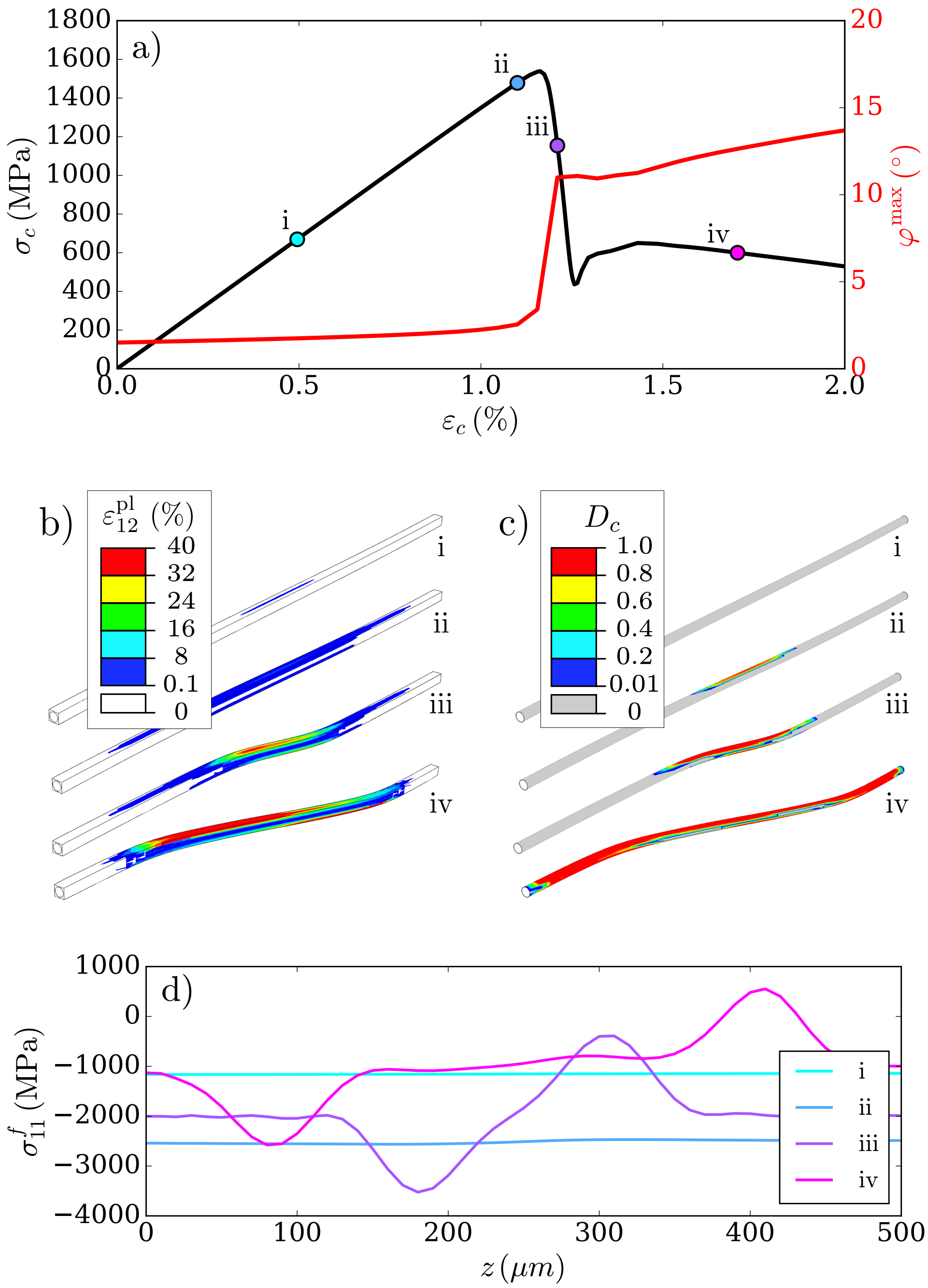

Figure 6.10: Summary of the sequence of events prior to and after fiber kinking for AS4/8552 with $\varphi_0 = 1.5°$: a) compressive stress vs. strain curve including maximum fiber rotation, $\varphi^{\max}$; b) plastic shear deformation of the matrix at the points indicated in (a); c) fiber/matrix interface damage evolution; and d) longitudinal stress along the surfaces with the highest bending stresses of the fiber.

Kink band angle

The use of periodic boundary conditions in the CMM single-fiber model forces the kink angle, β, to be zero (Gutkin et al., 2010a). Since the model predicts the residual stress, σ_r, the effective kink band angle can be estimated by rearranging eq. 6.12 as

$$\tilde{\beta} = \frac{1}{2} \arcsin\left(\frac{2\tau_L}{\sigma_r}\right) \tag{6.26}$$

Using eq. 6.26 with the residual stress values from the CMM ranging between 600 and 400 MPa from fiber kinking initiation up to 3% strain (as shown in Figure 6.9a) and assuming a shear yield stress $\tau_L = 95$ MPa (at 5% strain in Figure 6.6b), the resulting effective kink angle is found to be between 9° and 14°. This range for $\tilde{\beta}$ agrees well with values reported in an experimental study carried out in parallel through X-Ray computed tomography observation of fiber kinks in IM7/8552 (Bergan and Garcea, 2017).

For the sake of completeness, a 3-D multiple fiber model was used to measure the kink band angle, β. The model is similar to the 3-D multiple-fiber model described in Section 6.4.4, but includes an inhomogeneous initial misalignment on one of the efges to trigger fiber kinking following the approach of Vogler et al. (2001). To improve the stability of the problem, loading is applied in two steps (Vogler et al., 2001). First, a constant compressive stress, σ_c, in the fibers direction is applied up to a subcritical level. Then, an in-plane shear load, τ_{12}, is increased until fiber kinking takes place. The kink band initiates on the free edge where the larger initial misalignment is located and propagates across the model with a β angle of 12° and a constant band width, $w_{\text{kb}} = 100$ µm, as shown in Figure 6.11. The values for β and w_{kb} are in good agreement with the values obtained from the single-fiber model.

Some kink band angle values reported in the literature for carbon reinforced composites are shown in Table 6.5. Although a variety of experimental techniques were employed to promote the fiber kinking failure mechanism, it is observed that typical values of β are found between 10° to 20° in most cases, agreeing reasonably well with the results of the 3-D multiple-fiber numerical model and the experimental observations from Bergan and Garcea (2017).

From the shear stress-strain curve, Moran's energy-based analytical model (Moran et al., 1995) is able to predict the residual stress and the β angle for fiber kinking assuming there is no change of volume in the material, thus $\varphi = 2\beta$. The values

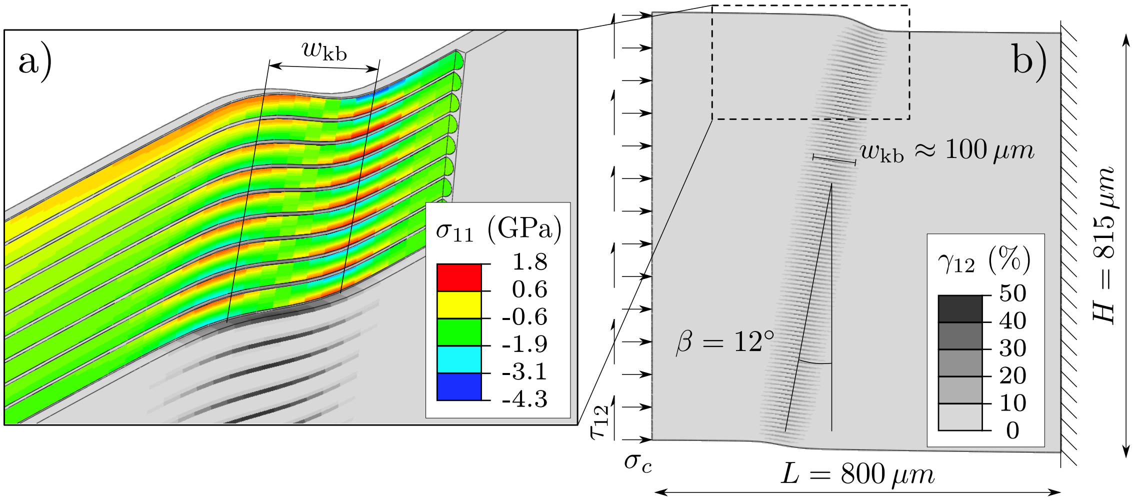

Figure 6.11: Multiple-fiber 3-D model based on Vogler et al. (2001) to obtain the kink angle, β, of AS4/8552, showing a) detail view of the strain field along the fibers in the kink band and b) shear deformation of the matrix highlighting the β angle and the w_{kb} along with the model geometry and boundary conditions.

obtained from this model using the Ramberg-Osgood shear stress-strain curve (substituting eq. 6.4 in eq. 6.13 and minimizing with respect to β) are similar for both AS4/8552 and IM7/8552, due to the similar shear behavior. The predicted residual stress, σ_r, is around 300 MPa, with $\beta = 40°$. Although the estimation for σ_r is reasonable when compared to the results of the models presented in this work, the kink band angle is not in good agreement with the CMM. This mismatch is likely a result of the fact that the CMM includes compressibility of the matrix and is therefore not restricted to Moran's assumption of $\varphi = 2\beta$. It also should be noted that using the residual stress from the CMM predictions, $\sigma_r = 400$ MPa, in Moran's model results in $\beta \approx 18°$, which is in much better agreement. Vogler et al. (2001) showed that β depends on the pressure sensitivity and dilation of the matrix, which may explain the difference between the present numerical model and Moran's analytical model.

Table 6.5: Kink band angle values reported in the literature from experiments and numerical models.

Reference	Method	Material system	β [°]
Jelf and Fleck (1992)	Experimental	AS4/PEEK	16
Couque et al. (1993)	Experimental	Carbon/PEEK	20-30
Fleck and Jelf (1995)	Experimental	Carbon/epoxy	10-15
Moran et al. (1995)	Experimental	Carbon/PEEK	12-22
Kyriakides et al. (1995)	Experimental	AS4/PEEK	12-16
Kyriakides et al. (1995)	Experimental	AS4/PEEK	10-12
Vogler and Kyriakides (2001)	Experimental	AS4/PEEK	12-15
Vogler et al. (2001)	Numerical	AS4/PEEK	5-17
Pinho et al. (2006)	Experimental	Carbon/epoxy	22-28
Lee and Soutis (2007)	Experimental	IM7/8552	5-30
Pimenta et al. (2009a)	Numerical	Carbon/epoxy	8-10
Bishara et al. (2017a)	Numerical	Carbon/epoxy	14-17
Bergan and Garcea (2017)	Experimental	IM7/8552	15-25

6.5 Correlation between the mesoscale and micromechanical models

The predictions of the micromechanical model (CMM) were compared with the predictions of the mesoscale model (CDM) to understand the role of the simplifying assumptions in the latter. In this section, the micromechanical model assumes the fiber behaves as a nonlinear elastic solid ($c_f \neq 0$) considering tensile and compressive failure, except where noted. The mesoscale finite element model is composed of one cubic C3D8R element with an edge length of 0.15 mm. The material properties used in the mesoscale analysis are provided in Table 6.2. In both analyses, end shortening displacements in the longitudinal direction were prescribed.

Additionally, analytical models from the literature are compared with the CMM and CDM results where applicable (e.g. stress-strain curves, compressive strength sensitivity curves and fiber/kink band rotation). The assumptions followed to characterize the shear response of the material are fundamental to the prediction of fiber kinking for all of the models considered. The characteristic shear curves for the different models considered are shown in Figure 6.12. Argon's expression, eq. 6.2,

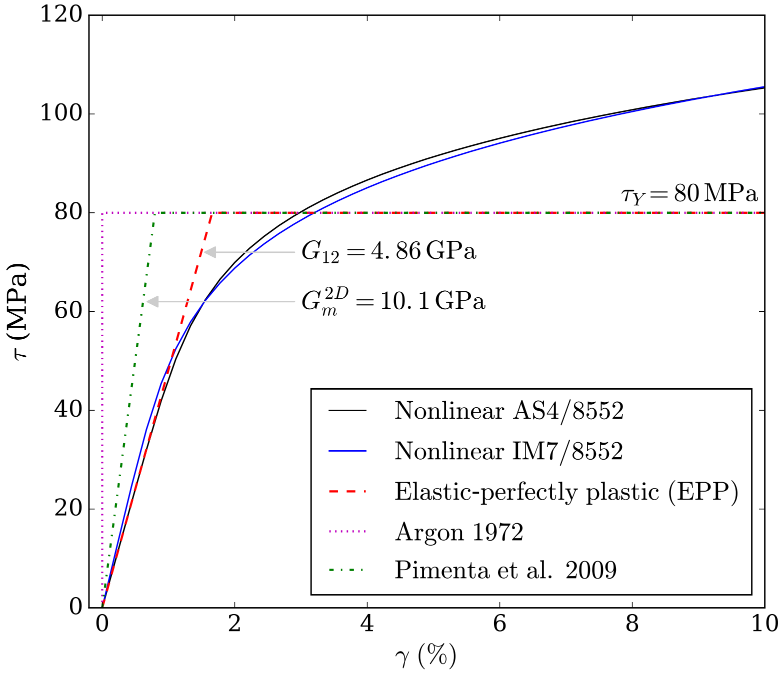

Figure 6.12: Experimental nonlinear shear curves for AS4/8552 and IM7/8552 and simplified curves of other models: perfectly-plastic of Argon's model (Argon, 1972), elastic perfectly plastic (EPP) and Pimenta's model with a modified shear modulus, G_m^{2D} (Pimenta et al., 2009b).

considers the matrix as a rigid perfectly-plastic solid (Argon, 1972). A value of 80 MPa was assumed as the yield limit of the matrix under shear. On the other hand, Pimenta's model assumes an elastic-perfectly plastic (EPP) response in shear for the matrix and is based upon micromechanical features such as fibers packing and fibers cross section (Pimenta et al., 2009b). The shear modulus is defined as $G_m^{2\mathrm{D}} = G_m/(1 - V_f^{2\mathrm{D}}) = 10.06$ GPa, and the shear yield limit is set to $\tau_Y = 80$ MPa. Fiber kinking theory does not need to simplify the shear response of the material, for this reason a more representative constitutive nonlinear response can be used. For comparison, an EPP shear response will be analyzed applying the FKT approach with $\tau_Y = 80$ MPa using eq. 6.3.

6.5.1 Stress vs. strain response

The predicted stress-strain curves for a variety of initial fiber misalignments, φ_0 of 1.5, 2, 2.5, 3, and 4° indicate a remarkable agreement between the results of the two models (CDM and CMM), as shown in Figure 6.13a for AS4/8552. The compressive

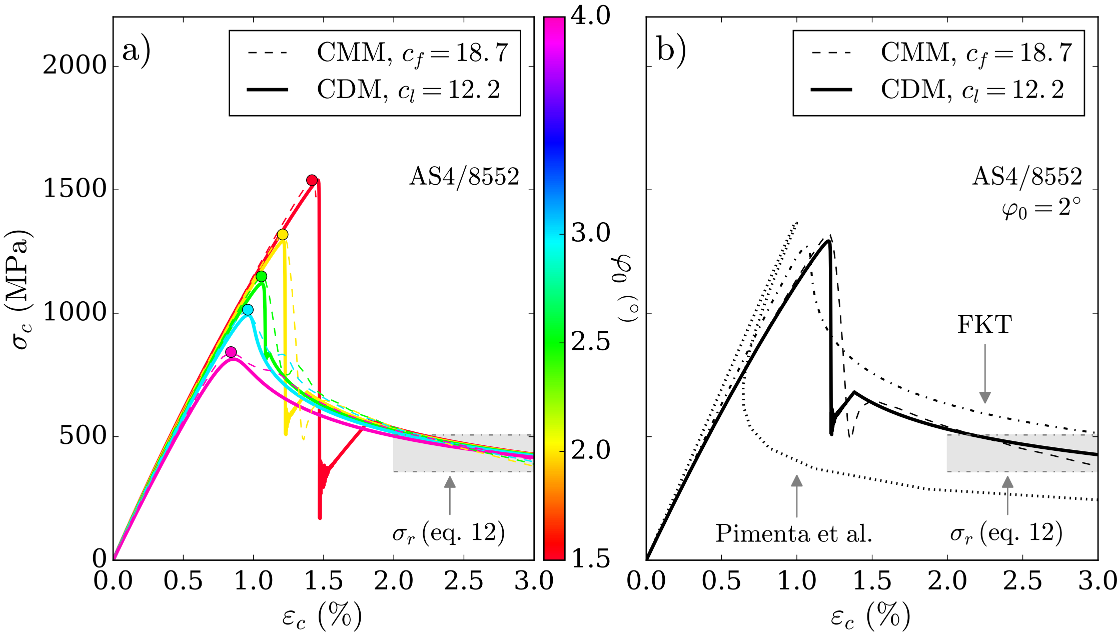

Figure 6.13: Stress-strain curves for the CMM and CDM models of AS4/8552 including nonlinear response of the fibers (c_l, $c_f \neq 0$ in eqs. 6.22 and 2.3) for a) a range of initial fiber misalignments ($\varphi_0 = 1.5$, 2, 2.5, 3 and 4°), and b) comparison with analytical models of the literature: FKT (Hsu et al., 1998) and Pimenta et al. (2009b) for $\varphi_0 = 2°$. Residual crushing stress, σ_r, is estimated from eq. 6.12.

stress, σ_c, is the nominal stress calculated as the reaction force divided by the original area, and the compressive strain, ε_c, is the end shortening divided by the original length. Both models predict the initial elastic response, strength, subsequent collapse, and finally a non-zero residual stress. Since the energy released during instability is large for small values of φ_0, some vibrations are predicted by both models immediately after the instability. The transition from a strong instability (snap-back) to a smooth response occurs between $\varphi_0 = 2.5°$ and 3° for both material systems. The value of φ_0 at which the transition to snapback occurs can be estimated from FKT as the smallest value of φ_0 for which there exists a local maximum of eq. 6.7. The results in Figure 6.13a illustrate that both models predict a dependence of the peak load on φ_0 whereas the predicted residual stress, σ_r, is independent of φ_0, which is consistent with fiber kinking theory. Some authors like Moran et al. (1995) proposed the residual stress to be a material property. A range of σ_r calculated using eq. 6.12 is superimposed on Figure 6.13 showing very good agreement with the models predictions. The values reported in an experimental investigation on IM7/8552 (Bergan and Garcea, 2017), were used in eq. 6.12 (shear strength at 5%

strain $\tau_L = 95$ MPa and $\beta = 12°$ to $16°$). The residual stress is expected to follow an asymptotic trend at large uniaxial compressive strain ($\varepsilon_c > 20\%$) as shown in the material model developed by Gutkin et al. (2016), which yields an asymptotic value around 230 MPa for another carbon fiber reinforced epoxy resin (HTS45/LY556). The excellent agreement between the two models for strength, subsequent instability, and residual stress suggests that the most significant features of the kinking process are captured by the relatively simple mesoscale model. Furthermore, the agreement between the two models demonstrates that ignoring fiber bending appears to be a reasonable assumption for relatively small carbon fibers with large wavelength misalignments. Similar results were obtained from both CDM and CMM models for IM7/8552 material system.

Of the analytical models, only Hsu's augmentation of FKT (Hsu et al., 1998) and Pimenta et al. (2009b) provide a complete stress vs. strain response. The results obtained from these two models are plotted next to the CMM and CDM curves in Figure 6.13b for $\varphi_0 = 2°$. Regarding Pimenta's model, it is observed that the stiffness of the system is constant up to the peak-load because it does not include the nonlinear elastic behavior of the fiber. The strength predicted by this model through eq. 6.14 is slightly different as it considers a linear-elastic perfectly-plastic response of the composite material under shear, instead of the more realistic strain-hardening shear response employed by the CMM and CDM models. A compromise value for the yield limit under shear, τ_Y, was selected for comparison with the rest of the models in terms of compressive strength and residual stress ($\tau_Y = 80$ MPa). During fiber kinking, the snap-back phenomenon is captured because the analytical model is not displacement-controlled. A lower residual stress, σ_r, is predicted compared to the other models. The main feature responsible for the difference in σ_r is the shape of the shear curve. In the analytical model, the absence of strain hardening makes the residual stress level lower. This effect is also noticed in the kinematics of the problem, as discussed in Section 6.5.3. On the other hand, Hsu's model predicts the same compressive strength, since it is based on FKT applied to the same nonlinear shear curve, but the stiffness of the composite up to collapse is slightly higher as the fiber modulus is assumed to be constant. The residual stress predicted agrees very well with the CDM and CMM models.

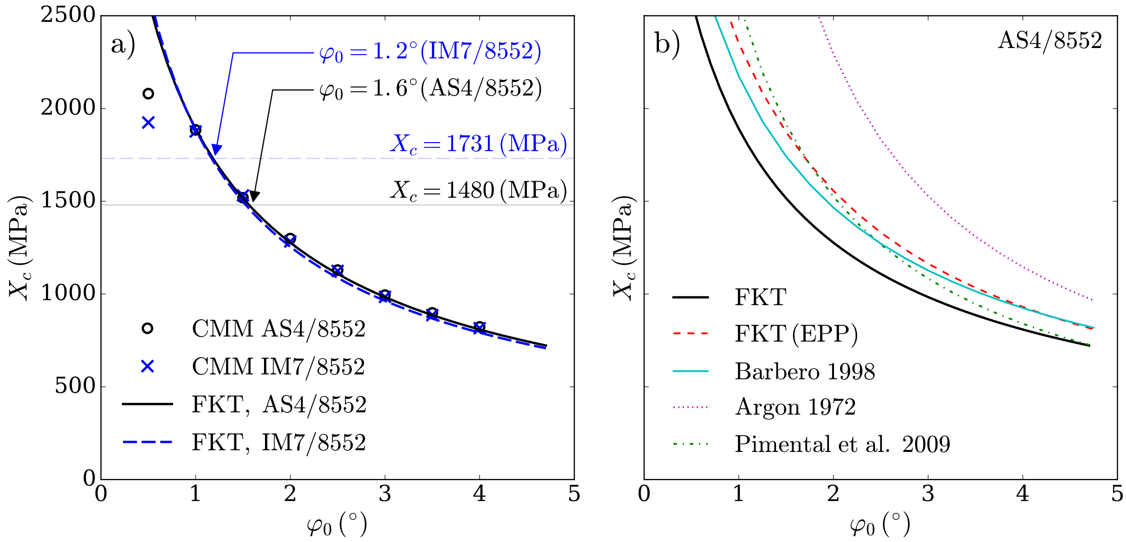

Figure 6.14: Compressive strength sensitivity curves, X_c vs. φ_0: a) comparison of the CMM results and FKT predictions, and b) comparison of the strength predicted FKT by various analytical models for AS4/8552 (Argon, 1972; Budiansky, 1983; Barbero, 1998; Pimenta et al., 2009b).

6.5.2 Imperfection sensitivity curves

The compressive strength, X_c, predicted by FKT, eq. 6.5, and the CMM single-fiber model are shown in Figure 6.14a as a function of φ_0 for AS4/8552 and IM7/8552. Very good agreement is observed between the two models for $\varphi_0 \geq 1°$, which is attributed to the similarity of the nonlinear shear response in the two models (Figure 6.6). Though not shown, the predictions by the mesoscale model are identical to the FKT results, as is expected since the mesoscale model is based on FKT. The strength sensitivity curve provides a one to one relation between X_c and φ_0, such that, for the typical compressive strengths of the materials addressed in this work (horizontal lines in Figure 6.14a), a representative value of φ_0 is obtained: 1.2° and 1.6° for IM7/8552 and AS4/8552 respectively.

For very small values of initial misalignment, $\varphi_0 < 1°$, the CMM model predicts fiber failure due to pure longitudinal compression, instead of fiber kinking. A cut-off strength point is found at $X_c = V_f \cdot X_c^f$, yielding 2100 and 1920 MPa for AS4/8552 and IM7/8552 respectively.

Imperfection sensitivity functions, $X_c(\varphi_0)$, predicted by other analytical models are shown in Figure 6.14b. All the models predict a critical effect of the initial misalignment, φ_0, on the compressive strength of the unidirectional fiber-reinforced composite, X_c. The sensitivity to the initial misalignment, $\partial X_c/\partial\varphi_0$, is more critical for the low misalignments range. Argon's model predicts the highest strength for the range of misalignments considered, going to infinity for the limit $\varphi_0 = 0°$. The two FKT predictions show the effect of the Ramberg-Osgood shear curve as compared with the EPP shear curve. In both cases, FKT has an upper limit $X_c(\varphi_0 = 0) = G_{12}$. Pimenta's model is very close to the solution obtained from the equivalent EPP shear curve by means of FKT. The assumptions and strategy followed by Pimenta could be extended for different nonlinear shear curves as proposed by the author (Pimenta et al., 2009b). Finally, the analytical model developed by Barbero (1998) reads a similar strength-misalignment trend, for this case a half-normal statistical distribution of the fibers misalignment was assumed with zero mean and standard deviation of φ_0.

6.5.3 Fiber rotation

The fiber rotation angle, φ, is shown in Figure 6.15a as a function of the longitudinal strain for φ_0 ranging from 1.5° to 4° for AS4/8552. Since $\varphi = \varphi(z)$ in the CMM, two definitions for φ are plotted for comparison with the fiber rotation predicted by the CDM model, labeled φ_{CDM} in the figure. The maximum fiber rotation in the CMM takes place at $z = L/2$ and is denoted as $\varphi^{\text{max}}_{\text{CMM}}$. The average rotation of the kinked fiber is calculated from the transverse deflection at the end of the fiber, u_y, and the kink band width, w_{kb}, as $\varphi^{\text{avg}}_{\text{CMM}} = \tan^{-1}(u_y/w_{\text{kb}})$. In all cases, the fiber misalignment shows slight rotation ($\varphi \approx \varphi_0$) prior to the strain at which the peak load is attained. When the critical strain corresponding to the peak load is reached, the fiber rotates rapidly into the kinked configuration, which is seen as the abrupt change in φ in Figure 6.15a at $\varepsilon_c \approx 1\%$. The rotation is much more abrupt for small imperfections than for large initial misalignments. Under yet higher strains (in the strain regime that corresponds with the residual stress, $\varepsilon_c \geq 1.5\%$) the fibers continue to rotate at a constant rate with increasing ε_c. The fiber rotation predicted by the CDM is bounded by the average and maximum φ from the CMM. It could be argued that φ_{CDM} should match $\varphi^{\text{max}}_{\text{CMM}}$ since both represent the critical or maximum fiber misalignment. The difference between φ_{CDM} and $\varphi^{\text{max}}_{\text{CMM}}$ is most likely due to considerations of fiber bending and periodic boundary conditions in the CMM, both of which affect the fiber rotation and are not included in the CDM. Nonetheless, the agreement between the two models is remarkable and, thus, highlights further efficacy of the relatively low-fidelity mesoscale model at

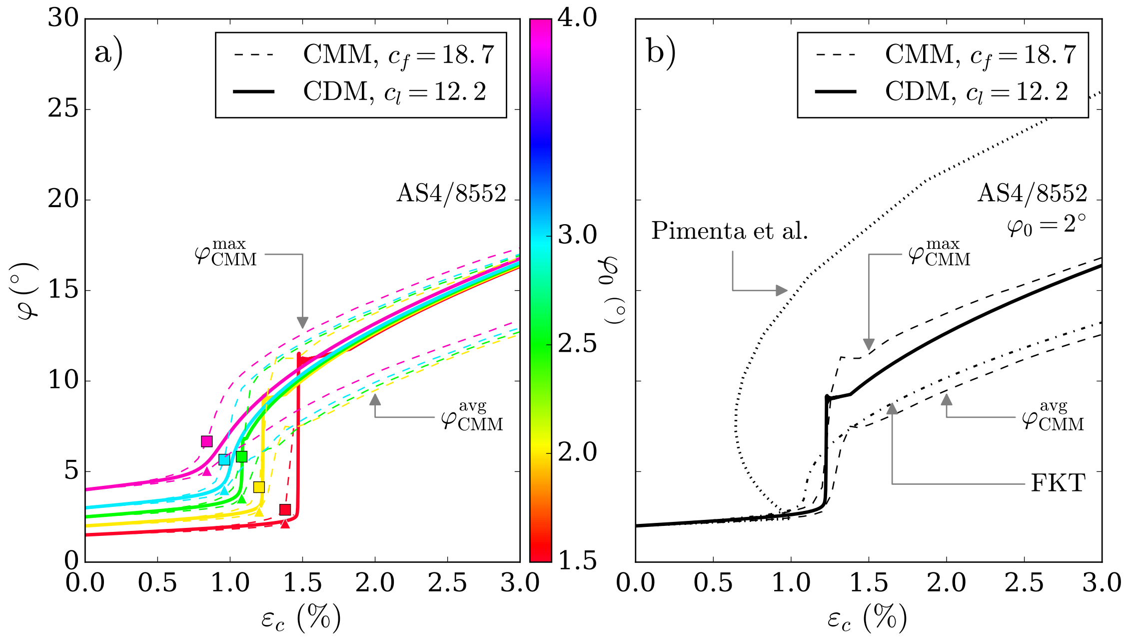

Figure 6.15: Fiber rotation curves for the CMM and CDM models of AS4/8552 including nonlinear response of the fibers (c_l, $c_f \neq 0$ in eqs. 6.22 and 2.3) for a) a range of initial fiber misalignments ($\varphi_0 = 1.5$, 2, 2.5, 3 and 4°), and b) comparison with analytical models of the literature: FKT (Hsu et al., 1998) and Pimenta et al. (2009b) for $\varphi_0 = 2°$.

representing the large rotations associated with the fiber kinking process as predicted by the high-fidelity micromechanical model. Similar results were obtained from both, CDM and CMM, models for IM7/8552 material system.

Results from the model proposed by Pimenta et al. (2009b) are included in Figure 6.15b displaying the maximum rotation of the fiber during kinking. In qualitative terms, the same features are represented: fiber rotation is negligible up to the point when the fiber kinking mechanism is triggered. Then, sudden rotation of the fibers happens during snap-back. Finally, under large compressive strains, the fibers keep rotating gradually. However, quantitatively, the analytical predictions for φ rise beyond 20° at $\varepsilon = 2\%$; which is much higher than $\varphi \approx 14°$ predicted by the mesoscale and micromechanical models at the same strain level. The main simplification of the analytical model consists of assuming an elastic perfectly-plastic shear response of the matrix. By ignoring strain-hardening, the analytical model underestimates the shear stiffness at large strains and, therefore, overpredicts φ. Nevertheless, the analytical estimate of the fiber rotation by the FKT model is equivalent to the average fiber rotation obtained from the micromechanical model, $\varphi^{\mathrm{avg}}_{\mathrm{CMM}}$, see Figure 6.15b.

It is important to notice that Hsu's analytical model (Hsu et al., 1998) employs the characteristic Ramberg-Osgood nonlinear shear curve which is introduced in the CDM model, see Figure 6.6c.

6.5.4 Fiber nonlinearity

The effect of fiber nonlinearity on the mechanical response of the CMM and CDM models is illustrated in Fig. 6.16. Both models account for fiber nonlinearity and therefore show a pre-peak reduction in stiffness. The resulting compressive strength, X_c, is not affected. However, fiber nonlinearity increases the strain to failure from 1% to 1.2% for AS4/8552 with $\varphi_0 = 2°$ in both models. Kink band rotation is not affected once the fiber kinking phenomenon is triggered, following the same rotation rate ($\partial\varphi/\partial\varepsilon_c$).

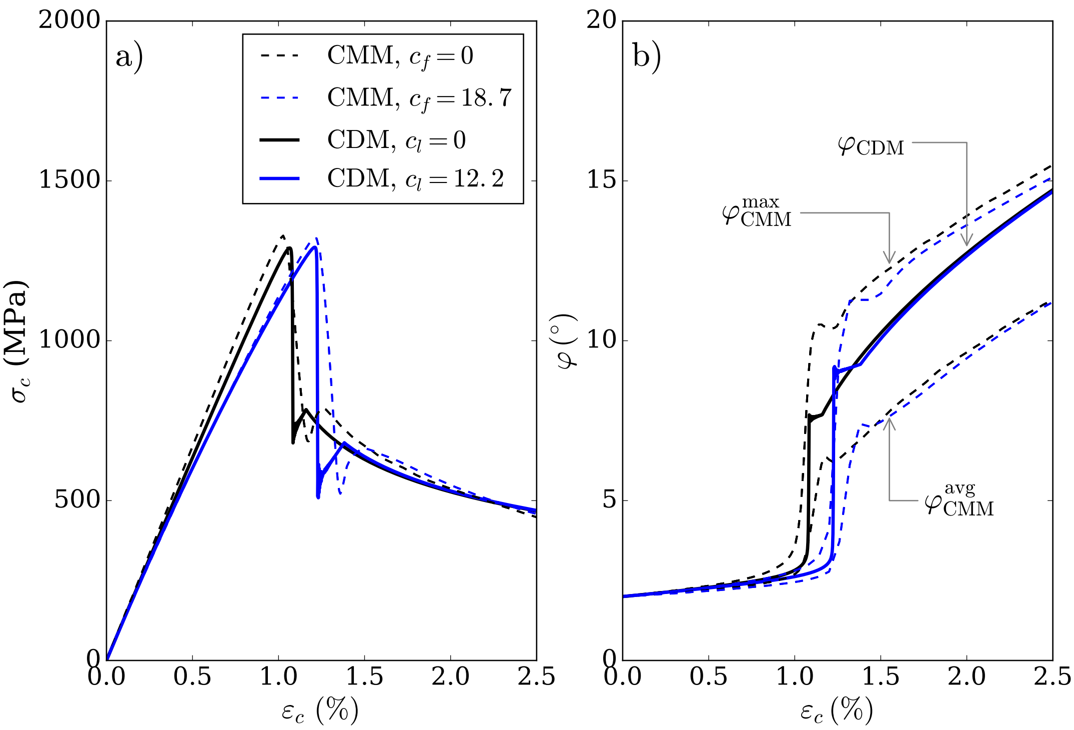

Figure 6.16: Comparison of the CMM and CDM models for AS4/8552 with and without nonlinearity of the fibers for $\varphi_0 = 2°$: a) stress-strain curves and b) fiber rotation.

Table 6.6: Comparison of kink band width values, w_{kb}.

Material	CDM	CMM	Eq. 6.21	Fleck and Jelf (1995)	Pimenta et al. (2009b)
	[μm]	[μm]	[μm]	[μm]	[μm]
AS4/8552	100	90 – 120	50	85	62 – 118
IM7/8552	50	50 – 70	38	70	48 – 93

6.5.5 Kink band width

The kink band width, w_{kb}, was computed with the micromechanical model as the distance between the points with the highest bending stress along the fiber at the maximum load applied, following Pimenta et al. (2009b). The CMM shows $w_{kb} \propto d$, as reported in the literature (Budiansky, 1983; Jelf and Fleck, 1992). The results for w_{kb} predicted by the CMM model are presented in Table 6.6, and compared with the results of other analytical models from the literature which consider fiber bending (Budiansky, 1983; Fleck and Jelf, 1995; Pimenta et al., 2009b).

The CDM model does not consider fiber bending, as detailed in Section 6.3, so a kink band width value must be specified as input of the model. The values employed in the CDM model are reported in Table 6.6 and are based on the CMM results, analytical models from the literature (Budiansky, 1983; Fleck and Jelf, 1995) and experimental observations (Table 6.1). The selection of w_{kb} has an important effect on the post-peak response of the model as shown in Figure 6.17. Wider kink bands arrest kink band rotation (see Figure 6.17b), thus enhancing the residual stress sustained by the material during the softening regime. Most of the band rotation occurs abruptly during the load drop right after the peak stress is reached.

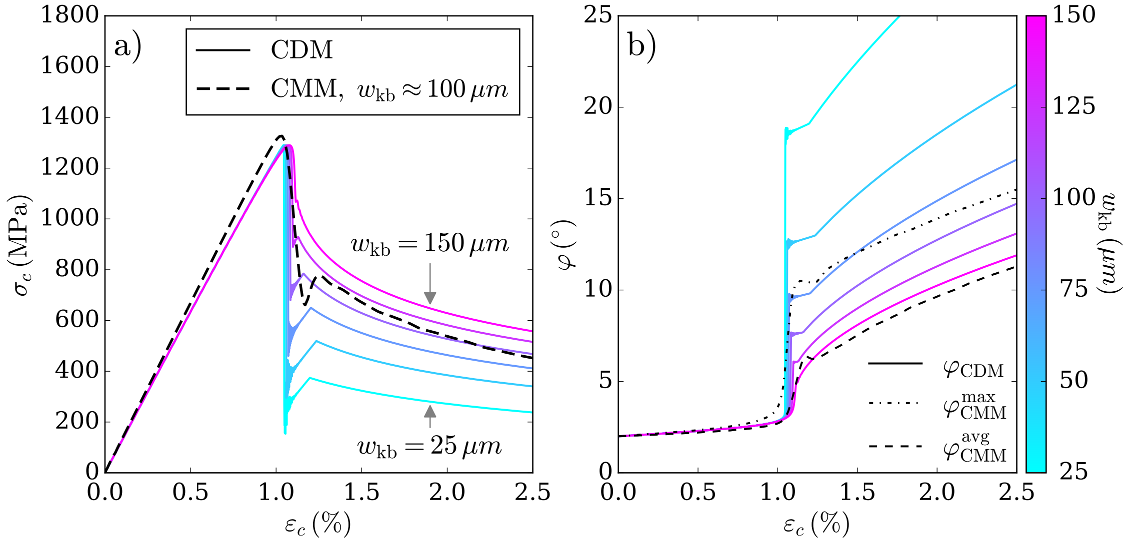

Figure 6.17: Effect of the kink band width, w_{kb}, on the CDM constitutive model: a) stress-strain curve and b) kink band rotation. Curves obtained for AS4/8552 system with $\varphi_0 = 2°$ and $c_l = c_f = 0$.

6.6 Parametric study with the micromechanical model

Taking advantage of the CMM single-fiber model presented in Section 6.4.1, a parametric study to analyze the effect of the fiber/matrix interface strength on the fiber kinking mechanism was carried out. For the sake of efficiency, the results shown in this section do not include fiber nonlinearity, $c_f = 0$, nor fiber failure.

6.6.1 Effect of fiber/matrix cohesive interface

A parametric study on the fiber/matrix cohesive interface strength was carried out to analyze its effect on the fiber kinking mechanism. To this end, the single-fiber CMM model with an initial misalignment of $\varphi_0 = 2°$ was simulated for different interface shear strengths, $S^c = 21$, 63, 85 and 300 MPa. The baseline case with $S_0^c = 85$ MPa corresponds to the results presented in Section 6.5 and the interface properties of Table 6.4. For the other interface shear strength cases, the normal strength and fracture energies were scaled accordingly. The case where $S^c = 300$ MPa, represents a perfect interface model. The fiber/matrix friction coefficient was kept constant, $\mu^c = 0.4$, except where noted. It should be remarked that the interface shear strength employed as baseline in this chapter was selected by fitting the nonlinear shear curve of the ply, see Section 6.4.3 for a more detailed explanation.

The results of this analysis are summarized in Figure 6.18. A low interface

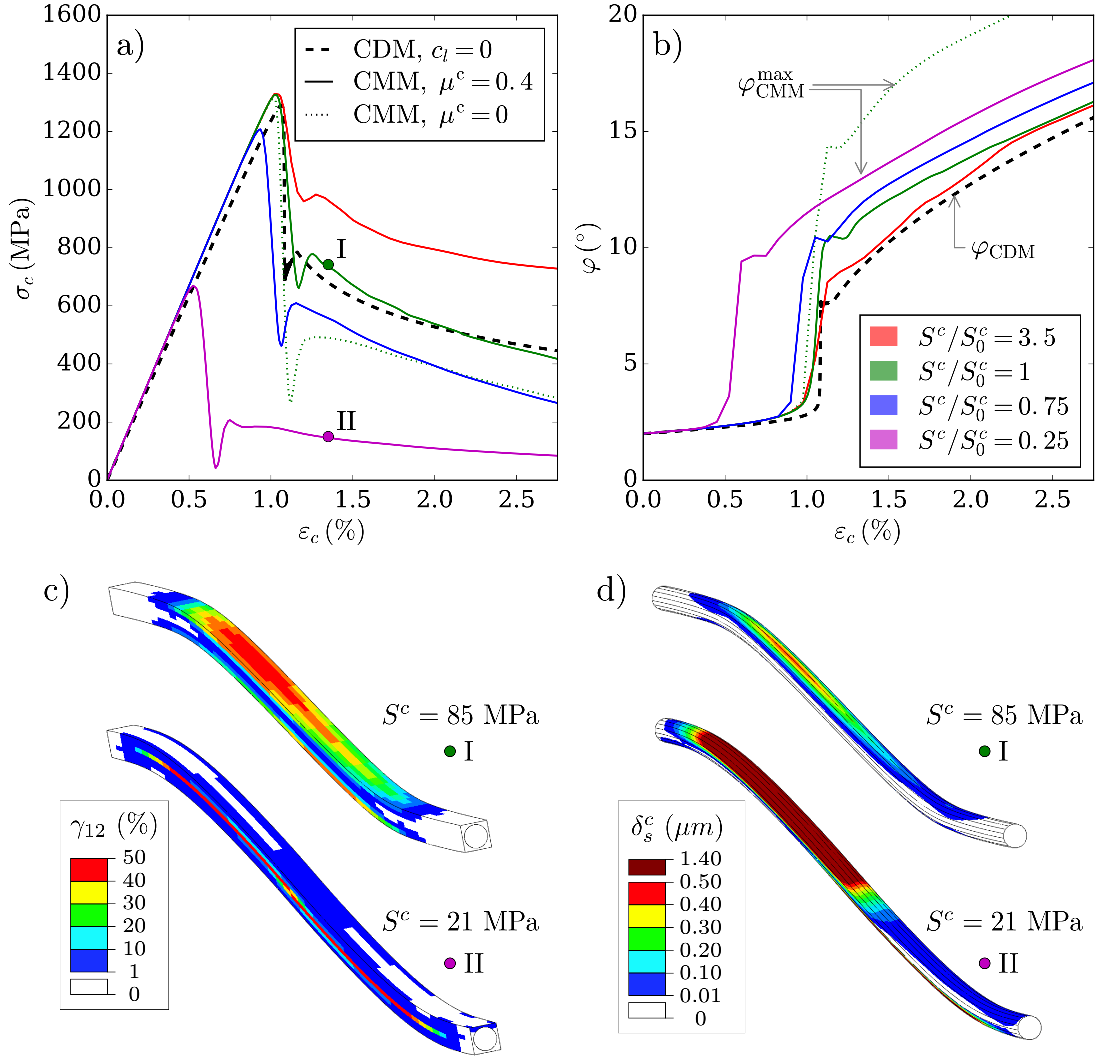

Figure 6.18: Effect of fiber/matrix interface shear strength of AS4/8552 with $\varphi_0 = 2°$: a) stress-strain curves and b) fiber rotation curves. Snapshots of the FE models at $\varepsilon_c = 1.35\%$ plotting c) the shear strain, γ_{12}, and d) the interface shear slippage in the longitudinal direction, δ_s^c.

strength triggers fiber kinking earlier reducing the compressive strength as shown in Figure 6.18a for the cases with $S^c = 21$ MPa and 63 MPa. On the other hand, when the interface shear strength is higher than the shear yield limit of the matrix, $S^m = 80$ MPa, then fiber kinking is activated by matrix shear instability regardless of the interface strength. For this reason, considering a perfect interface does not increase the compressive strength of the material.

The residual stress, σ_r, is not only dependent on the matrix yield limit in shear,

S^m, but also on the ability of the interface to transfer load between the matrix and the fiber. A strong interface is able to sustain the shear loads on the interface and promotes the plastic shear deformation of the matrix as shown in Figure 6.18c for the case with $S^c = 85$ MPa. On the other hand, if the interface is weak, it fails prematurely and the matrix slips along the fiber when the interface shear stress overcomes the interface shear strength, preventing plastic deformation of the matrix. In Figure 6.18d, it is observed the interface shear slippage in the longitudinal direction, δ_s^c, is much higher for the weak interface case, going up to 1.4 µm, compared to 0.5 µm for the stronger interface (85 MPa) over a larger fiber surface. According to this hypothesis, the perfect interface case can be employed as an upper bound of σ_r as it further exploits the potential of the matrix to dissipate plastic energy through shear deformation.

The effect of a frictionless interface was observed after the load drop due to fiber kinking. Although, friction does not participate until the fiber/matrix interface is damaged, it plays a role arresting fiber rotation during the post peak regime. In absence of friction, fiber rotation can only be arrested by fiber bending and matrix hardening due to the hydrostatic pressure induced by φ, thus fiber rotation in the CMM model with $\mu^c = 0$ is higher as shown in Figure 6.18b. The additional fiber rotation results in a lower residual stress, $\sigma_r = 395$ MPa as compared to 540 MPa of the baseline case at $\varepsilon_c = 2\%$.

6.7 Concluding remarks

A high-fidelity computational micromechanics model (CMM) was developed to widen the understanding of the fiber kinking mechanism and to assess the extent to which the mesoscale continuum damage mechanics (CDM) model captures the key features of fiber kinking (Herráez et al., 2018a).

The computationally efficient CMM finite element model consists of a 3-D single-fiber that was previously demonstrated to capture the representative phenomena of fiber kinking. The model considers nonlinearity in the fiber, matrix plasticity, and fiber/matrix interface debonding as well as geometric nonlinearity. The most significant difference between the CMM and CDM models as related to fiber kinking is that the CMM includes fiber bending whereas the mesoscale model does not. The CMM predicts that fiber kinking occurs with the following sequence of events: i) yielding in the matrix begins in a narrow band near the maximum misalignment, well before peak load; ii) then, under increasing load, yielding in the matrix spreads in the longitudinal direction until the yielded region is large enough to promote local rotation of the fiber; iii) next, instability due to fiber rotation and matrix yielding leads to the formation of the kink band; and iv) finally, the rotation of the fibers is arrested once the angle becomes large enough. The kinking process predicted by the CMM is in good agreement with other micromechanical models in the literature (Davidson and Waas, 2014).

The CDM model based on the fiber kinking theory was developed by A.C. Bergan from NASA Langley Research Center (Bergan and Leone, 2016). This model has a stress-strain response that includes a sharp drop due to the onset of fiber kinking, followed by a nonzero residual stress. Furthermore, the mesoscale model tracks the fiber rotation through the kinking response such that longitudinal shortening deformation is coupled with shearing deformations. These characteristics arise from consideration of material nonlinearity in the shear stress-strain behavior and large fiber rotations. Thus, the constitutive response is not prescribed directly. Rather, it is a result of the fundamental material and geometric nonlinearities that contribute to the fiber kinking process. Verification studies demonstrated that the mesoscale model reproduces strength, fiber rotation, and residual stress in excellent agreement with fiber kinking theory. The mesoscale model makes use of the deformation gradient decomposition (DGD) technique to enable mesh objectivity. The reader is referred to Herráez et al. (2018a) for a detailed description of the implementation of the CDM model.

Correlations between the microscale and mesoscale models serve as a basis for assessing the representativity of the fiber kinking process achieved by the mesoscale model. In this work it is also explored the potential of an efficient single-fiber model to capture, not only the failure initiation due to fiber kinking, but also the phenomena observed during the post peak regime (fiber rotation, kink band generation and broadening, residual stress...). To focus the comparisons on the characteristics of the two models instead of differences in input properties, the CMM was calibrated with the same shear nonlinearity response used in the mesoscale model. The comparison between the mesoscale and microscale models was made through the analysis of the corresponding stress-strain curves (σ_c vs. ε_c) and the kinematics of fiber kinking (φ vs. ε_c). Analyses were also conducted to study the influence of the kink band width w_{kb} and the kink band angle β.

The elastic response of the microscale and mesoscale models showed very good agreement, both with and without consideration for elastic nonlinearity in the fibers. It was noted that the coefficients of fiber nonlinearity for the microscale and mesoscale models are related by the rule of mixtures. The strength predicted by the two models is a function of the initial misalignment angle and is nearly identical for $1° < \varphi_0 < 4°$. Small values of φ_0 lead to fiber compression failure, which is only accounted for in the CMM. Fiber kinking occurs as an instability due to interaction between fiber rotation and shear nonlinearity of the material. The two models predict similar values of strain for the onset of the instability.

The residual stress, σ_r, predicted by the two models is in excellent agreement, with both models showing a slight decay under increasing compressive strain. It was demonstrated that the value of σ_r is a function of the width of the kink band and fiber rotation. Despite the fact that the mesoscale model does not include fiber bending, the results for fiber rotation (φ vs. ε_c) throughout the kinking process show excellent agreement between both models. Both models show a jump in the fiber rotation at the onset of fiber kinking, followed by the progressive rotation of the fiber as the compressive strain increases.

The kink angle β is assumed to be zero in both models. While experimental measurements uniformly show nonzero values for β (see Table 6.5) the two models are nonetheless able to capture the residual stress level in good agreement with models in the literature that account for $\beta \neq 0$. An effective $\tilde{\beta}$ angle can be estimated through eq. 6.12 yielding 10° to 15°, which is in agreement with an experimental study carried out through X-ray CT in IM7/8552 (Bergan and Garcea, 2017). A multi-fiber micromechanical 3-D model based on Vogler et al. (2001) was employed to verify the β angle estimation. The multi-fiber model yielded $\beta = 12°$, supporting the estimation using eq. 6.12, and is in good agreement with experimental measurements (Bergan and Garcea, 2017).

The mesoscale CDM model requires the kink band width w_{kb} as an input parameter. This value may be estimated from analytical models that consider fiber bending like Budiansky (1983) and Fleck and Jelf (1995), measured experimentally (Bergan and Garcea, 2017) or computed numerically using micromechanical models like the CMM model presented based on recent work of Naya et al. (2017b).

The correlation between the results of the mesoscale and micromechanical models is remarkable in terms of strength, post-peak residual stress, and fiber rotation. The quality of the correlation indicates that the significant features of the kinking process are included in the relatively simple mesoscale model. The CMM model validates the

CDM model considering fiber kinking is extremely hard to study experimentally in a controlled manner. Recovering the *bottom-up multiscale* approach, the CMM single-fiber model is a very efficient approach to represent the fiber kinking phenomenon and can be used to extract parameters for a homogenized model, herein the CDM model, like the residual stress level, and the kink band width.

A parametric analysis was conducted using the CMM to explore opportunities to improve longitudinal compression strength. It was shown that the fiber/matrix interface properties (stress transfer between the fibers and the matrix) not only have an important effect on the compressive strength, X_c, but also play a major role on the residual crushing stress, σ_r. If the interface is very weak, the fiber slides during kinking and the matrix is not deformed plastically. Hence, the accurate characterization of the interface properties arises as a crucial task to feed micromechanical models to achieve representative results. Fiber/matrix friction only has a positive effect on σ_r, reducing fiber rotation through the additional interface shear stress introduced by the friction coefficient.

The results of this chapter, together with a more detailed description of the CDM constitutive model implementation, and an application case in a mesoscale virtual test have been published in Herráez et al. (2018a).

Conclusions

7

7.1 Closing of the thesis

During the last years, the Composite Materials Group (CMG) at IMDEA Materials has focused its work towards the development of a full description of the mechanical response of composite laminated materials through a bottom-up multiscale approach (Llorca et al., 2011; Lopes et al., 2016). This thesis is embedded within the microscale framework of this multiscale approach and is focused not only in the development of novel virtual micromechanical models, but also on the experimental characterization of the constituents at the micro-level.

In particular, the aim of this work was the development of numerical micromechanical models in order to improve our understanding of some of the failure mechanisms exhibited by unidirectional fiber-reinforced composites, especially in terms of damage propagation, and the transfer of this information towards the mesoscale level of analysis. Complementary, an experimental procedure to characterize the longitudinal properties of the reinforcement constituent, i.e. the fibers, was presented. The main conclusions achieved during this work are drawn along the following paragraphs.

- Within the framework of the multiscale analysis research line of the CMG, the mechanical characterization of the reinforcement phase, the fibers, remained as a pending task. State-of-the-art techniques were employed to measure the longitudinal properties of different types of fibers (carbon, glass and aramid). In this regard, *ex situ* single-fiber tensile tests were carried out on FIB-notched fibers to obtain their effective tensile fracture toughness, G_t^f, while unnotched specimens were dedicated to characterize the elastic response of the fibers in the longitudinal direction (Herráez et al., 2016a). In the case of carbon fibers, the characteristic nonlinear elastic response was fitted through a single-parameter model, c_f. Besides, a new technique to measure the longitudinal compressive strength of fibers, X_c^f, was designed: micropillars were FIB-milled on the cross section of fibers within a composite ply and then compressed by nanoindentation until failure. The results obtained by means of experimental micromechanics agree reasonably with other experimental techniques (Oya and Johnson, 2001; Kant and Penumadu, 2013) from the literature or the consequent ply-scale properties (Peterson and Murphey, 2016).

- An efficient and versatile methodology for the generation of periodic microstructures with arbitrary fiber shapes and sizes, which is able to achieve very high fiber volume fractions, was implemented. In fact, a user interface implementing this generation algorithm (`Viper`), plus other state-of-the-art algorithms were developed in order to facilitate and speed up the pre-processing stage of micromechanical analysis.

- A numerical framework to evaluate fracture processes in quasi-brittle materials, based upon *small scale bridging* conditions (SSB), was developed (Herráez et al., 2018b). The main benefit of this framework is the ability to provide geometry-independent crack resistance curves (R-curves), through the application of the displacements field associated with the K_I linear elastic fracture mechanics stress intensity factor. This framework was applied to the study of the intralaminar fracture behavior of a crack growing in the direction transverse to the fibers for a carbon/epoxy UD ply, G_{2+}. Moving towards a homogenized mesomechanics scheme, a traction-separation cohesive law was analytically derived from the R-curve obtained with the micromechanical model, and validated numerically by guaranteeing that the fracture behavior was properly captured at the meso level. The SSB framework shows a high potential to homogenize the fracture process of the material by means of a cohesive law by lumping the actual damage mechanisms of the microstructure, thus, enabling the transference of information between length scales, micro and meso, as for instance, in a mesoscale constitutive model used to represent individual composite plies (e.g. LaRC04, `CompDam`, Falcó et al. (2018)).

- The failure mechanism of fiber kinking was studied from a computational micromechanics perspective (Herráez et al., 2018a). The great influence of the nonlinear in-plane shear response of the composite ply on the fiber kinking mechanism was corroborated, as stated by the analytical models available in the literature (Pinho et al., 2005). The CMM model was successfully employed to assess the extent to which a mesoscale continuum damage mechanics (CDM) model, developed by A.C. Bergan (Bergan and Leone, 2016), captures the key features of fiber kinking.

To sum up, the numerical methods/models presented in this thesis are promising in terms of virtual characterization of the damage and fracture processes of FRPs. Nevertheless, further experimental validation of these techniques is required to ascertain numerical results and determine the reliability of these tools, since they are intended to be the main source of input parameters for the mesoscale constitutive models.

7.2 Proposed future research

In spite of the experimental effort carried out by CMG, together with that of this thesis; there are still important gaps in terms of constituent properties characterization that are crucial to enhance the accuracy of micromechanical models.

Continuing with the previous classification of experimental and computational developments, the recommended future works are the following.

- The most elusive constituent to be experimentally characterized is the fiber/matrix interface. A number of features, namely the normal strength, N^c, fracture energies, G_n^c, G_s^c, and the friction coefficient, μ, have not been measured yet and they play a fundamental role on the interface debonding failure mechanism. The FIB technique shows up as an opportunity to design *in situ* experimental configurations to measure the parameters that are missing.

- Characterization of the matrix under tensile loading should be performed through *in situ* microtests in order to understand the failure mechanisms of the polymer matrix at the microlevel, together with defects distribution.

- Motivated by the numerical models developed to study the fiber kinking phenomenon, a better comprehension of the fibers failure under shear loads is mandatory. New experimental techniques could be developed to introduce, in a controlled manner, a measurable shear stress field along the fiber up to failure.

Some of the computational future works that arise naturally from this thesis are the following:

- The CMM strategy allows the exploration of innumerable possibilities in microstructural design such as: analysis of hybrid composite microstructures (Swolfs et al., 2014), reproduction of multi-axial stress states and calculation of failure envelopes (Naya et al., 2017a), and quantification of the effect of fiber volume fraction on ply properties (Ghayoor et al., 2018), among others.

- The *small scale bridging* (SSB) framework presents a great potential to characterize the different fracture modes not only of a fiber-reinforced polymer, but also other quasi-brittle heterogeneous materials. In a few years, other 3-D fracture mechanisms like the translaminar crack propagation (González and Llorca, 2006) could be explored with this technique considering a rather large number of fibers.

- The applicability of the SSB framework should be illustrated for mesoscale showcases, to demonstrate the representativity of the cohesive laws derived by this method compared to the standard linear ones as in Dávila et al. (2009).

To conclude, application of computational micromechanics shows up as an ideal numerical technique not only to evaluate elastic and strength properties, but also failure mechanisms and damage propagation processes in great detail. Indeed, CMM is perfectly suited to provide the input parameters required by phenomenological mesoscale constitutive models, e.g. LaRC04 (Pinho et al., 2006), `CompDam` (Leone et al., 2018), Falcó et al. (2018).

Non-circular fibers geometry

A

Various non-circular cross sections were designed based on a literature review in this research field (Edie et al., 1986; Edie and Stoner, 1993; Edie and Dunham, 1989). These fiber cross sections have been implemented within an in-house developed user-interface: `Viper` (see Section 3.4).

The non-circular fiber cross sections described in detail in this appendix are the following: lobular, C-shaped, elliptical, and smoothed polygonal. Each of these sections are defined by at least one shape parameter (e.g. number of edges) and its area, by means of the effective diameter, d_{eff}. The effective diameter of a non-circular fiber, d_{eff}, is defined as the diameter of the circular fiber whose cross section is equivalent. Whereas the diameter of a non-circular fiber, d, is defined as the circumscribing diameter of the cross section, i.e. for a circular fiber $d = d_{\text{eff}}$.

A *lobular* fiber is univocally defined by the number of lobes, n_l, and the effective diameter, d_{eff}. The number of lobes must be larger or equal to 2. As an example, a lobular fiber with $n_l = 4$ is shown in Figure A.1a. The following expressions determine the geometrical features sketched in Figure A.1b to reproduce a lobular cross section.

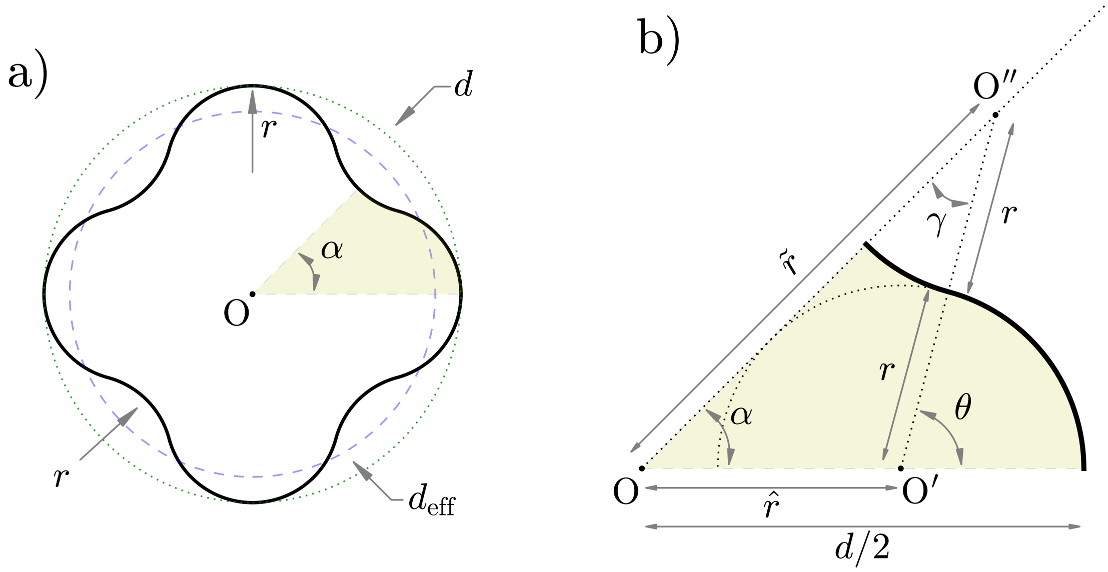

Figure A.1: a) Drawing of the lobular fiber with 4 lobes ($n_l = 4$) and b) detail of the lobular fiber unit cell.

$$\alpha = \frac{\pi}{n_l} \tag{A.1a}$$

$$d = d_{\text{eff}} \sqrt{\frac{\pi}{\frac{n_l}{(1+\csc\alpha)^2} \cdot (\cot\alpha + \sqrt{3} + \alpha)}} \tag{A.1b}$$

$$\gamma = \frac{\pi}{6} = 30^\circ \tag{A.1c}$$

$$r = \frac{d}{2(1+\csc\alpha)} \tag{A.1d}$$

$$\hat{r} = r \cdot \csc\alpha \tag{A.1e}$$

$$\tilde{r} = r \cdot (\cot\alpha + \sqrt{3}) \tag{A.1f}$$

The perimeter of a lobular fiber is,

$$P = \frac{\pi \cdot d \cdot n_l}{1+\csc\alpha}\left(\frac{1}{n_l} + \frac{1}{3}\right) \tag{A.2}$$

And the section can be calculated as

$$A = n_l \cdot r^2 \cdot (\cot\alpha + \sqrt{3} + \alpha) \tag{A.3}$$

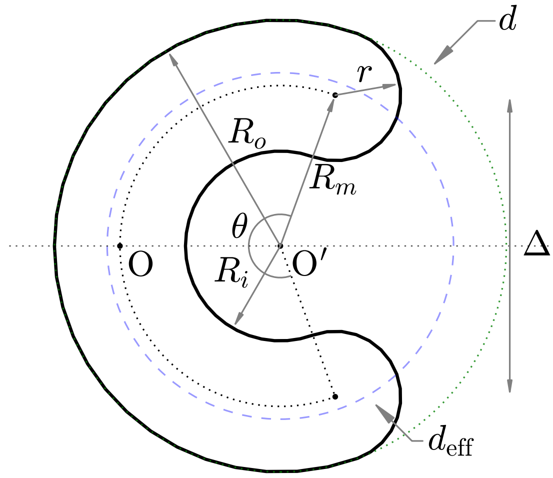

Figure A.2: Drawing of a C-shaped fiber with $\theta = 220°$ and $\xi = 0.4$.

The *C-shaped* fiber is the most complex section designed in this work. Apart from the effective diameter, it requires two parameters: the angular amplitude (θ) and the hollowness ratio (ξ). A drawing with the main annotations of a C-shaped section is shown in Figure A.2. The parameters of the C-shaped fibers considered in Section 3.3.1 are $\theta = 90°$ and $\xi = 0.1$.

$$d = d_{\text{eff}} \sqrt{\frac{\pi}{\frac{\theta}{2}(1-\xi^2) + \frac{\pi}{4}(1-\xi)^2}} \tag{A.4a}$$

$$R_o = \frac{d}{2} \tag{A.4b}$$

$$\xi = \frac{R_i}{R_o} \tag{A.4c}$$

$$R_m = \frac{1}{2}(R_o + R_i) \tag{A.4d}$$

$$r = \frac{1}{2}(R_o - R_i) \tag{A.4e}$$

The perimeter and area of a C-shaped cross section are calculated as,

$$P = \theta \cdot (R_o + R_i) + 2\pi r \tag{A.5}$$

$$A = \frac{d^2}{4} \cdot \left[\frac{\theta}{2}(1-\xi^2) + \frac{\pi}{4}(1-\xi)^2\right] \tag{A.6}$$

To prevent the C-shaped section from self-intersecting when $\theta > 180°$, the following condition must be fulfilled by the parameters selected:

$$\Delta > 2r \Rightarrow \sin\frac{\theta}{2} > \frac{1-\xi}{1+\xi} \tag{A.7}$$

An *elliptical* fiber is described by the eccentricity parameter, ϵ, and the effective diameter. Figures A.3a and b show the sketch of an ellipse indicating its main features: semi-major axis (a), semi-minor axis (b), focal distance (c), foci (F_1, F_2) and center (O). The eccentricity of an ellipse is defined as the ratio between the focal distance, c, and the semi-major axis, a, i.e. $\epsilon = c/a$, and is bounded between 0 (circle) and 1 (infinitely long ellipse). The eccentricity of the elliptical fibers considered in Section 3.3.1 is 0.75.

$$d = d_{\text{eff}} \cdot (1-\epsilon^2)^{-1/4} \tag{A.8a}$$

$$a = \frac{d}{2} \tag{A.8b}$$

$$b = a \cdot \sqrt{1-\epsilon^2} \tag{A.8c}$$

The perimeter of an ellipse can be approximated by the expression of Ramanujan

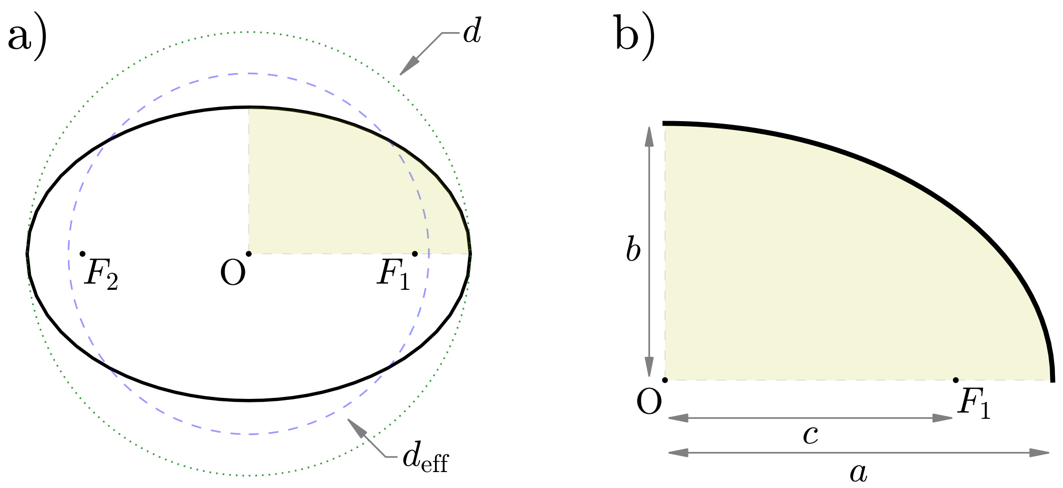

Figure A.3: a) Drawing of a elliptical fiber with $\epsilon = 0.75$ and b) detail of the geometry.

(1914) as,

$$P \approx \pi \cdot \left[3(a+b) - \sqrt{(3a+b)(a+3b)}\right] \tag{A.9}$$

And the area of an ellipse is given by,

$$A = \pi \cdot a \cdot b = \pi a^2 \sqrt{1-\epsilon^2} \tag{A.10}$$

A *smoothed polygonal* (spolygon) cross section is defined by the number of edges, n_e, the smoothing ratio, χ, and the effective diameter, d_{eff}. The number of edges must be larger or equal to 3 ($n_e \geq 3$), whereas the smoothing ratio, defined as the ratio between the curvature radius R and the apothem a, is comprised between 0 and 1 ($0 < \chi < 1$). As an example, a smoothed polygonal section with $n_e = 4$ and $\chi = 0.5$ is plotted in Figure A.4a. The smoothing ratio of the spolygon fibers considered in Section 3.3.1 is 0.3.

The following equations describe the explicit relations among the auxiliary geo-

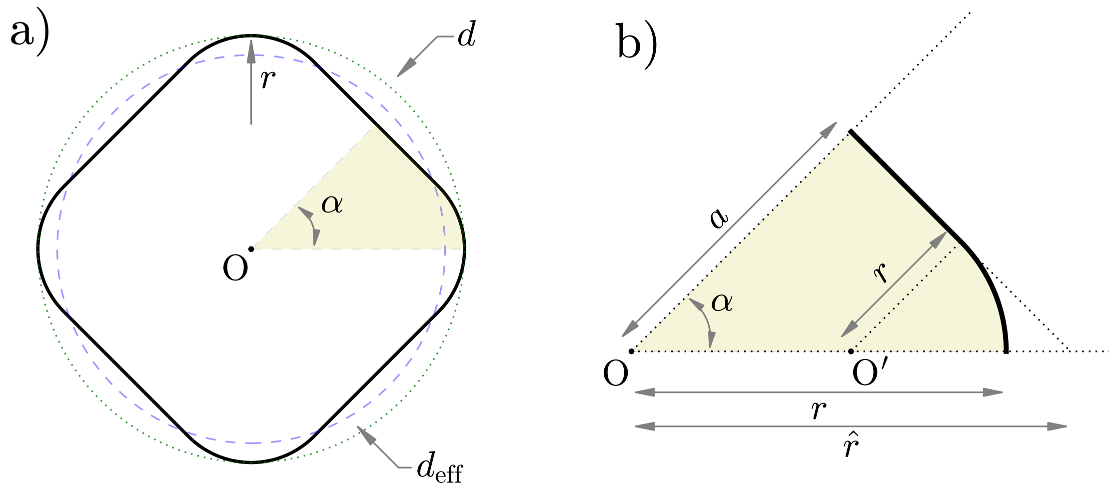

Figure A.4: a) Drawing of a smoothed polygonal fiber with 4 edges ($n_e = 4$, $\chi = 0.5$) and b) detail of the geometry.

metrical data shown in Figure A.4b and the input parameters ($n_e,\ \chi,\ d_{\text{eff}}$).

$$\alpha = \frac{\pi}{n_e} \tag{A.11a}$$

$$\chi = \frac{r}{a} \tag{A.11b}$$

$$d = d_{\text{eff}} \sqrt{\frac{\pi}{\frac{n_e}{2}\sin 2\alpha - \chi^2 \cdot (n_e \cdot \tan\alpha - \pi)}} \tag{A.11c}$$

$$r = \frac{d}{2} \tag{A.11d}$$

$$\hat{r} = \frac{r}{1 - \chi \cdot (1 - \cos\alpha)} \tag{A.11e}$$

The perimeter of an Spolygon fiber is,

$$P = n_e \cdot d \cdot [(1 - \chi) \cdot \sin\alpha + \chi \cdot \alpha] \tag{A.12}$$

And the section can be calculated as

$$A = \frac{d^2}{4} \cdot \left[\frac{n_e}{2}\sin 2\alpha - \chi^2 \cdot (n_e \cdot \tan\alpha - \pi)\right] \tag{A.13}$$

B Linear elastic fracture mechanics solution for a transversely isotropic solid

The displacements field around the crack tip under mode I in a linear elastic solid is derived solving the constitutive equation of the material, $\varepsilon = \mathbf{S} \cdot \sigma$. Firstly, the strain components, ε, are obtained from the derivatives of the displacements field, u. Then, the compliance tensor, $\mathbf{S}$, which is the inverse of the stiffness tensor, $\mathbf{S} = \mathbf{Q}^{-1}$, is given by the constitutive response of the material, in this case it is shown for an elastic transversely isotropic material ($a = Q_{11} = Q_{22},\ b = Q_{12},\ c = Q_{66}$). Finally, the stress vector, σ, is derived from Westergaard's stress function (Westergaard, 1939).

$$\underbrace{\begin{Bmatrix} \frac{\partial u_x}{\partial x} \\ \frac{\partial u_y}{\partial y} \\ \frac{1}{2}\left(\frac{\partial u_x}{\partial y} + \frac{\partial u_y}{\partial x}\right) \end{Bmatrix}}_{\varepsilon} = \underbrace{\frac{1}{c\left(a^2 - b^2\right)} \begin{bmatrix} ac & -bc & 0 \\ -bc & ac & 0 \\ 0 & 0 & a^2 - b^2 \end{bmatrix}}_{\mathbf{S}} \underbrace{\begin{Bmatrix} \operatorname{Re} Z - y \operatorname{Im} Z' \\ \operatorname{Re} Z + y \operatorname{Im} Z' \\ -y \operatorname{Re} Z' \end{Bmatrix}}_{\sigma} \tag{B.1}$$

where $Z(z^*) = K_I / \sqrt{2\pi z^*}$, with z^* being a complex representation in polar coordinates of a material point referred to the crack tip and can be written as $z^* = re^{i\theta}$. Integrating the first two components of eq. B.1 and transforming Z and y into polar coordinates the full displacements field is obtained,

$$\begin{Bmatrix} u_x \\ u_y \end{Bmatrix} = \frac{K_I}{2G} \cdot \sqrt{\frac{r}{2\pi}} \cdot (\kappa - \cos\theta) \begin{Bmatrix} \cos\frac{\theta}{2} \\ \sin\frac{\theta}{2} \end{Bmatrix} \tag{B.2}$$

where G and κ are material properties as defined in Table 5.1. The *energy release rate* (G_I) is related with the *stress intensity factor* (K_I) through Irwin's equation (Irwin, 1957) as $G_I = K_I^2/E^*$, where E^* follows the expression shown in Table B.1 for isotropic and transversely isotropic materials under the hypothesis of plane strain.

Table B.1: Parameters for isotropic and transversely isotropic materials under plane strain assumption.

	Isotropic	Transversely isotropic[a,b]
a	$\frac{E\cdot(1-\nu)}{(1+\nu)(1-2\nu)}$	$\frac{1-\nu_{pz}\nu_{zp}}{E_p E_z \Delta}$
b	$\frac{E\nu}{(1+\nu)(1-2\nu)}$	$\frac{\nu_p-\nu_{pz}\nu_{zp}}{E_p E_z \Delta}$
c	$\frac{E}{1+\nu}$	$\frac{E_p}{1+\nu_p}$
κ	$3-4\nu$	$\frac{3-\nu_p-4\nu_{pz}\nu_{zp}}{1+\nu_p}$
G	$\frac{E}{2\cdot(1+\nu)}$	$\frac{E_p}{2\cdot(1+\nu_p)}$
E^*	$\frac{E}{1-\nu^2}$	$\frac{E_p}{1-\nu_{pz}\nu_{zp}}$

[a]The isotropy plane (2-3) and its normal (1) are represented by $_p$ and $_z$ respectively
[b]$\Delta = (1+\nu_p)\cdot(1-\nu_p-2\nu_{pz}\nu_{zp})/(E_p^2 E_z)$

Continuum Damage Mechanics model for fiber failure

C

To consider the fiber failure under longitudinal loading and the nonlinear elastic response in the longitudinal direction typical of carbon fibers, a 3-D *continuum damage mechanics* model (CDM) was developed. This model is based on the work of Maimi et al. (2008) and is implemented as a UMAT in Abaqus/Standard (Simulia, 2013). The material is considered transversely isotropic with the following compliance matrix,

$$\mathbf{S} = \begin{bmatrix} \frac{1}{(1-D)E_1^f} & \frac{-\nu_{12}^f}{E_1^f} & \frac{-\nu_{12}^f}{E_1^f} & 0 & 0 & 0 \\ & \frac{1}{(1-D)E_2^f} & \frac{-\nu_{23}^f}{E_2^f} & 0 & 0 & 0 \\ & & \frac{1}{(1-D)E_2^f} & 0 & 0 & 0 \\ & & & \frac{1}{(1-D)G_{12}^f} & 0 & 0 \\ & \text{sym} & & & \frac{1}{(1-D)G_{12}^f} & 0 \\ & & & & & \frac{1}{(1-D)G_{23}^f} \end{bmatrix} \tag{C.1}$$

where E_1^f and E_2^f are the longitudinal and transverse elastic moduli respectively, ν_{12}^f and ν_{23}^f are the longitudinal and transverse Poisson ratios, and G_{12}^f and G_{23}^f are the longitudinal and transverse shear moduli. Transverse isotropy of the material is verified with $G_{23}^f = E_2^f/2/(1+\nu_{23}^f)$. A single damage variable is represented by D.

Nonlinear elasticity in the longitudinal direction of the fiber is included in the constitutive model including another parameter, c_f, as shown in eq. C.2.

$$E_1^f = E_1^{0f} \cdot (1 + c_f \cdot \varepsilon_{11}) \tag{C.2}$$

where E_1^{0f} is the tangent longitudinal elastic modulus of the fiber when $\varepsilon_{11} = 0$, and $c_f > 0$ is the nonlinear parameter. These parameters were obtained fitting experimental curves from single-fiber tensile tests as described in Chapter 2. Under uniaxial loading, the expression for the longitudinal stress results from integrating eq. C.2.

$$\sigma_{11}(\varepsilon_{11}) = \int_0^{\varepsilon_{11}} E_1^f(\varepsilon)d\varepsilon = E_1^{0f} \cdot \left(\varepsilon_{11} + \frac{c_f}{2} \cdot \varepsilon_{11}^2\right) \tag{C.3}$$

Care must be taken when selecting the compressive strength of the fiber, X_c^f, as it is a concave quadratic function and its lower bound for X_c^f is $X_c^f > E_1^{0f}/2\ c_f$.

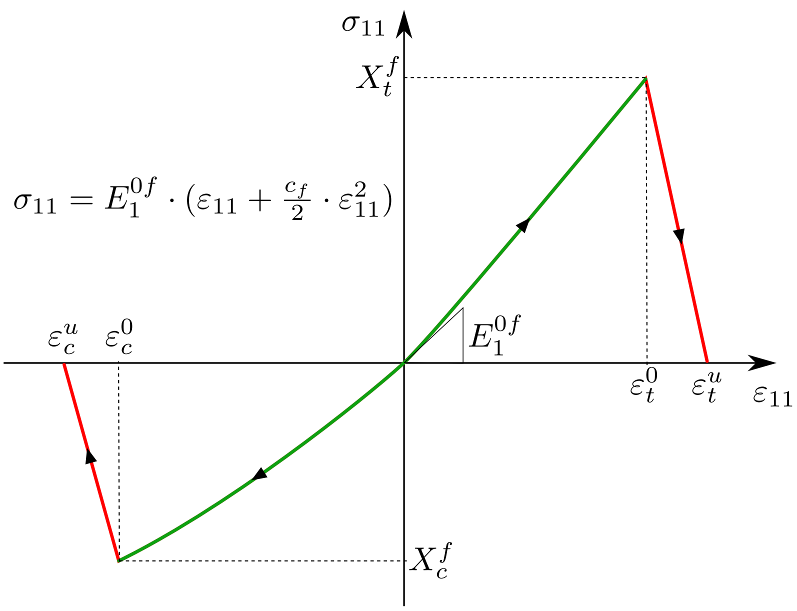

Figure C.1: Stress vs. strain curve of the constitutive model of the fiber under uniaxial longitudinal loading: nonlinear elastic response (green line) until damage onset followed by linear softening (red lines).

The damage variable, D, lumps longitudinal damage distinguishing between tensile, D_{1+}, and compressive loading, D_{1-}.

$$D = \begin{cases} D_{1+} & , \ \varepsilon_{11} \geq 0 \\ D_{1-} & , \ \varepsilon_{11} < 0 \end{cases} \tag{C.4}$$

Two damage activation functions are required to represent longitudinal damage under tension:

$$\begin{aligned} F_{1+} &= \phi_{1+} - r_{1+} \leq 0 \\ F_{1-} &= \phi_{1-} - r_{1-} \leq 0 \end{aligned} \tag{C.5}$$

where ϕ_M are the loading functions under longitudinal tension ($M = 1+$ or t) and compression ($M = 1-$ or c), and r_M are the elastic domain thresholds, which are initially set to 1 (undamaged) and increase with damage. A maximum stress criterion governs damage initiation either in tension or compression as:

$$\begin{aligned} \phi_{1+} =& \frac{\tilde{\sigma}_{11}}{X_t^f} \\ \phi_{1-} =& -\frac{\tilde{\sigma}_{11}}{X_c^f} \end{aligned} \tag{C.6}$$

The evolution of the elastic domain thresholds, r_M, is expressed by the Kuhn-Tucker conditions preventing damage healing of the material.

$$\dot{r}_M \geq 0; \ F_M \leq 0; \ \dot{r}_M F_M = 0 \tag{C.7}$$

These conditions are guaranteed updating the elastic domain thresholds as,

$$\begin{aligned} r_{1+}^i =& \max(r_{1+}^{i-1}, \ r_{1-}^{i-1}, \ \phi_{1+}) \\ r_{1-}^i =& \max(r_{1-}^{i-1}, \ \phi_{1-}) \end{aligned} \tag{C.8}$$

where i represents the current increment and $i-1$ is the previous increment. In this manner, tensile damage in the material does not penalize the ability of the constitutive model to hold compressive loads.

The damage evolution laws are defined to implement linear strain softening under tensile and compressive loads as,

$$
\begin{aligned}
\bar{\varepsilon}_M &= r_M \frac{X_M^f}{E_{11}^f} \\
D_M &= \frac{\varepsilon_M^u \cdot (\bar{\varepsilon}_M - \varepsilon_M^0)}{\bar{\varepsilon}_M \cdot (\varepsilon_M^u - \varepsilon_M^0)}
\end{aligned}
\tag{C.9}
$$

where $\bar{\varepsilon}_M$ is the equivalent longitudinal strain for tension ($M = 1+$) or compression ($M = 1-$), ε_M^u is the ultimate strain, ε_M^0 is the strain at damage initiation for tension or compression (see Figure C.1).

Mesh objectivity is achieved through a crack band regularization by tuning the ε_M^u as a function of the element size, l^*, following Bazant's scheme (Bazant and Oh, 1983) as,

$$
\varepsilon_M^u = \frac{2\,G_M}{X_M \cdot l^*}
\tag{C.10}
$$

where G_M is the fracture energy in longitudinal tension or compression, X_M is the tensile or compressive strength and l^* is the characteristic length of the element.

The convergence of the solving algorithm requires the computation of the material tangent constitutive tensor, $\mathbf{C}_T$, as:

$$
\mathbf{C}_T = \mathbf{S}^{-1} : (\mathbf{I} - \mathbf{M})
\tag{C.11}
$$

where $\mathbf{S}$ is the compliance constitutive tensor (eq. C.1), $\mathbf{I}$ is the identity tensor and the tensor $\mathbf{M}$ is:

$$
\mathbf{M} = \frac{1}{(1-D)^2} \frac{\partial D}{\partial \varepsilon_{11}}
\begin{bmatrix}
\frac{\sigma_{11}}{E_1^f} & 0 & 0 & 0 & 0 & 0 \\
\frac{\sigma_{22}}{E_2^f} & 0 & 0 & 0 & 0 & 0 \\
\frac{\sigma_{33}}{E_2^f} & 0 & 0 & 0 & 0 & 0 \\
\frac{\tau_{12}}{G_{12}^f} & 0 & 0 & 0 & 0 & 0 \\
\frac{\tau_{13}}{G_{12}^f} & 0 & 0 & 0 & 0 & 0 \\
\frac{\tau_{23}}{G_{23}^f} & 0 & 0 & 0 & 0 & 0
\end{bmatrix}
\tag{C.12}
$$

where the damage variable derivative is,

$$\frac{\partial D}{\partial \varepsilon_{11}} = \frac{\varepsilon_M^u \cdot \varepsilon_M^0}{\bar{\varepsilon}_M^2 \cdot (\varepsilon_M^u - \varepsilon_M^0)} \tag{C.13}$$

The integration of the constitutive model follows the work flow presented by Maimi et al. (2008):

1. Read the strain and the strain increment. $\varepsilon^i,\ \Delta\varepsilon^i$
2. Compute the effective stress. $\tilde{\sigma}^i = \mathbf{S}_0^{-1} : \varepsilon^i$
3. Compute the loading functions. $\phi_M^i(\tilde{\sigma}^i)$
4. Compute the threshold values. $r_M^i(r_M^{i-1}, \phi_M^i)$
5. Compute the damage variables. $D_M^i(r_M^i)$
6. Compute the nominal stress tensor. $\sigma^i = (\mathbf{S}^i)^{-1} : (\varepsilon^i + \Delta\varepsilon^i)$
7. Compute the tangent constitutive tensor. $\mathbf{C}_T^i = (\mathbf{S}^i)^{-1} : (\mathbf{I} - \mathbf{M}^i)$

References

ABOUDI, J. (1989). *Micromechanical Analysis of Composites by the Method of Cells. Applied Mechanics Reviews*, **42**, p. 193.

ABOUDI, J. (2004). *The generalized method of cells and high-fidelity generalized method of cells micromechanical models - A review. Mechanics of Advanced Materials and Structures*, **11**, pp. 329–366.

AGEORGES, C., FRIEDRICH, K., SCHÜLLER, T., and LAUKE, B. (1999). *Single-fibre Broutman test: Fibre-matrix interface transverse debonding. Composites Part A: Applied Science and Manufacturing*, **30**, pp. 1423–1434.

ALLEN, S.R. (1987). *Tensile recoil measurement of compressive strength for polymeric high performance fibres. Journal of Materials Science*, **22**, pp. 853–859.

ANDERSON, T. (2005). *Fracture Mechanics. Fundamentals and Applications.* CRC Press, 3rd edition.

AOKI, S., MORIYA, Y., KISHIMOTO, K., and SCHMAUDER, S. (1996). *Finite element fracture analysis of WC-CO alloys. Engineering Fracture Mechanics*, **55**, pp. 275–287.

ARGON, A. (1972). *Fracture of Composites.* In *Treatise on Materials Science & Technology*, volume 1. pp. 79–114.

ASTIZ, M.A. (1986). *An incompatible singular elastic element for two- and three-dimensional crack problems. International Journal of Fracture*, **31**, pp. 105–124.

ASTM C1557-14 (2014). *Standard Test Method for Tensile Strength and Young's Modulus of Fibers.* In *Annual Book of ASTM Standards.* ASTM International, West Conshohocken, PA.

ASTM D1577-07 (2012). *Standard Test Methods for Linear Density of Textile Fibers.* In *Annual Book of ASTM Standards.* ASTM International, West Conshohocken, PA.

ASTM D3518 (2013). *Standard Test Method for In-Plane Shear Response of Polymer Matrix Composite Materials by Tensile Test of a 45 Laminate.* In *Annual Book of ASTM Standards.* ASTM International, West Conshohocken, PA.

ASTM D4018-17 (2017). *Standard Test Methods for Properties of Continuous Filament Carbon and Graphite Fiber Tows.* In *Annual Book of ASTM Standards.* ASTM International, West Conshohocken, PA.

Bai, X., Bessa, M.A., Melro, A.R., Camanho, P.P., Guo, L., and Liu, W.K. (2015). *High-fidelity micro-scale modeling of the thermo-visco-plastic behavior of carbon fiber polymer matrix composites. Composite Structures*, **134**, pp. 132–141.

Bao, G. and Suo, Z. (1992). *Remarks on crack-bridging concepts. Applied Mechanics Review*, **45**, pp. 355–366.

Barbero, E.J. (1998). *Prediction of Compression Strength of Unidirectional Polymer Matrix Composites. Journal of Composite Materials*, **32**, pp. 483–502.

Barthelat, F., Tang, H., Zavattieri, P.D., Li, C.M., and Espinosa, H.D. (2007). *On the mechanics of mother-of-pearl: A key feature in the material hierarchical structure. Journal of the Mechanics and Physics of Solids*, **55**, pp. 306–337.

Bascom, W.D. and Jensen, R.M. (1986). *Stress Transfer in Single Fiber/ Resin Tensile Tests. The Journal of Adhesion*, **19**, pp. 219–239.

Basu, S., Waas, A., and Ambur, D. (2006). *A macroscopic model for kink banding instabilities in fiber composites. Journal of Mechanics of Materials and Structures*, **1**, pp. 979–1000.

Bazant, Z. and Oh, B. (1983). *Crack Band Theory for Fracture of Concrete. Matériaux et Construction*, **16**, pp. 155–177.

Bazant, Z. and Planas, J. (1997). *Fracture and size effect in concrete and other quasibrittle materials.* CRC Press.

BECKERT, W. and LAUKE, B. (1998). *Critical discussion of the single-fibre pull-out test: Does it measure adhesion? Composites Science and Technology*, **57**, pp. 1689–1706.

BENCOMO-CISNEROS, J., TEJEDA-OCHOA, A., GARCÍA-ESTRADA, J., HERRERA-RAMÍREZ, C., HURTADO-MACÍAS, A., MARTÍNEZ-SÁNCHEZ, R., and HERRERA-RAMÍREZ, J. (2012). *Characterization of Kevlar-29 fibers by tensile tests and nanoindentation. Journal of Alloys and Compounds*, **536**, pp. S456–S459.

BENSSOUSAN, A., LIONS, J.L., and PAPANICOLAU, G. (1978). *Asymptotic Analysis for Periodic Structures.* North Holland, Amsterdam.

BENZEGGAGH, M. and KENANE, M. (1996). *Measurement of mixed-mode delamination fracture toughness of unidirectional glass/epoxy composites with mixed-mode bending apparatus. Composites Science and Technology*, **56**, pp. 439–446.

BERGAN, A. and GARCEA, S. (2017). *In-situ observations of longitudinal compression damage in carbon-epoxy cross-ply laminates using fast Synchrotron radiation computed tomography.* In *American Society for Composites Thirty-Second Technical Conference.* West Lafayette, Indiana.

BERGAN, A. and LEONE, F. (2016). *A Continuum Damage Mechanics Model to Predict Kink-Band Propagation Using Deformation Gradient Tensor Decomposition.* In *ASC 31st Technical Conference.* Williamsburg, Virginia.

BERRYMAN, J.G. (1985). *Measurement of spatial correlation functions using image processing techniques. Journal of Applied Physics*, **57**, pp. 2374–2384.

BESAG, J. (1977). *Comments on Ripley's paper. Journal of the Royal Statistical Society*, **B39**, pp. 193–195.

BILBY, B.A., COTTRELL, A.H., and SWINDEN, K.H. (1963). *The Spread of Plastic Yield from a Notch. Proceedings of the Royal Society of London A: Mathematical, Physical and Engineering Sciences*, **272**, pp. 304–314.

BISHARA, M., ROLFES, R., and ALLIX, O. (2017a). *Revealing complex aspects of compressive failure of polymer composites - Part I: Fiber kinking at microscale. Composite Structures*, **169**, pp. 105–115.

Bishara, M., Vogler, M., and Rolfes, R. (2017b). *Revealing complex aspects of compressive failure of polymer composites - Part II: Failure interactions in multidirectional laminates and validation. Composite Structures*, **169**, pp. 116–128.

Böhm, H. (1998). *A short introduction to the basic aspects of continuum micromechanics.* Technical report, Institute of Lightweight Design and Structural Biomechanics (ILSB), Vienna University of Technology.

Bowyer, A. (1981). *Computing Dirichlet tessellations. The Computer Journal*, **24**.

Broutman, L. (1969). *Measurement of the fiber-polymer matrix interfacial strength.* In *Interfaces in composites: a symposium presented at the Seventy-First annual meeting, American Society for Testing Materials*, volume 452. ASTM International, San Francisco, CA.

Budiansky, B. (1983). *Micromechanics. Computers & Structures*, **16**, pp. 3–12.

Budiansky, B., Amazigo, J.C., and Evans, A.G. (1988). *Small-scale crack bridging and the fracture toughness of particulate-reinforced ceramics. Journal of the Mechanics and Physics of Solids*, **36**, pp. 167–187.

Budiansky, B. and Fleck, N. (1993). *Compressive failure of fibre composites. Journal of the Mechanics and Physics of Solids1*, **41**, pp. 183–211.

Budiansky, B., Fleck, N., and Amazigo, J. (1998). *On kink-band propagation in fiber composites. Journal of the Mechanics and Physics of Solids*, **46**, pp. 1637–1653.

Bullegas, G., Pinho, S.T., and Pimenta, S. (2016). *Engineering the translaminar fracture behaviour of thin-ply composites. Composites Science and Technology*, **131**, pp. 110–122.

Bulsara, V.N., Talreja, R., and Qu, J. (1999). *Damage initiation under transverse loading of unidirectional composites with arbitrarily distributed fibers. Composites Science and Technology*, **59**, pp. 673–682.

Buryachenko, V.A., Pagano, N.J., Kim, R.Y., and Spowart, J.E. (2003). *Quantitative description and numerical simulation of random microstructures of* *composites and their effective elastic moduli. International Journal of Solids and Structures*, **40**, pp. 47–72.

Camanho, P. and Davila, C. (2002). *Mixed-Mode Decohesion Finite Elements for the Simulation of Delamination in Composite Materials.* Technical Report June.

Camanho, P.P., Davila, C.G., and de Moura, M.F. (2003). *Numerical Simulation of Mixed-Mode Progressive Delamination in Composite Materials. Journal of Composite Materials*, **37**, pp. 1415–1438.

Camponeschi, E. (1987). *Compression of composite materials: A review. US Navy AD-A189 272.* Technical report, David Taylor Research Center, Bethesda, MD.

Canal, L., González, C., Molina-Aldareguía, J., Segurado, J., and Llorca, J. (2012a). *Application of digital image correlation at the microscale in fiber-reinforced composites. Composites Part A: Applied Science and Manufacturing*, **43**, pp. 1630–1638.

Canal, L.P., Llorca, J., González, C., and Segurado, J. (2012b). *Intraply fracture of fiber-reinforced composites: Microscopic mechanisms and modeling. Composites Science and Technology*, **72**, pp. 1223–1232.

Catalanotti, G. (2016). *On the generation of RVE-based models of composites reinforced with long fibres or spherical particles. Composite Structures*, **138**, pp. 84–95.

Catto, E. (2017). *Box2D. A 2D Physics Engine for Games.*

Chamis, C. (1983). *Simplified Composite Micromechanics Equations for Hygral, Thermal and Mechanical Properties.* In *Conference of the Society of Plastics Industry.* Houston, Texas, United States.

Chand, S. (2000). *Carbon fibers for composites. Journal of Materials Science*, **35**, pp. 1303–1313.

Chaplin, C.R. (1977). *Compressive fracture in undirectional glass-reinforced plastics. Journal of Materials Science*, **12**, pp. 347–352.

Cheng, M., Chen, W., and Weerasooriya, T. (2005). *Mechanical Properties of Kevlar® KM2 Single Fiber. Journal of Engineering Materials and Technology*, **127**, p. 197.

Costa, S., Gutkin, R., and Olsson, R. (2017). *Mesh objective implementation of a fibre kinking model for damage growth with friction. Composite Structures*, **168**, pp. 384–391.

Couque, H., Albertini, C., and Lankford, J. (1993). *Failure mechanisms in a unidirectional fibre-reinforced thermoplastic composite under uniaxial, in-plane biaxial and hydrostatically confined compression. Journal of Materials Science Letters*, **12**, pp. 1953–1957.

Cox, H.L. (1952). *The elasticity and strength of paper and other fibrous materials. British Journal of Applied Physics*, **3**, pp. 72–79.

Cox, B.N. (1993). *Scaling for bridged cracks. Mechanics of Materials*, **15**, pp. 87–98.

Cui, L. and O'Sullivan, C. (2003). *Analysis of a triangulation based approach for specimen generation for discrete element simulations. Granular Matter*, **5**, pp. 135–145.

Curtis, G., Milne, J., and Reynolds, W. (1968). *Non-Hookean behaviour of strong carbon fibres. Nature*, **220**, pp. 1024–1025.

Davidson, P., Joseph, A., and Waas, A. (2018). *Multi Scale Progressive Damage and Failure Analysis of Bolted Joints*. In *59th AIAA/ASCE/AHS/ASC Structures, Structural Dynamics, and Materials Conference*. Kissimmee, FL.

Davidson, P. and Waas, A. (2014). *Mechanics of kinking in fiber-reinforced composites under compressive loading. Mathematics and Mechanics of Solids*, **21**, pp. 1–18.

Davidson, P. and Waas, A. (2017). *The effects of defects on the compressive response of thick carbon composites: An experimental and computational study. Composite Structures*, **176**, pp. 582–596.

Dávila, C.G. (2005). *Failure Criteria for FRP Laminates. Journal of Composite Materials*, **39**, pp. 323–345.

Dávila, C., Jaunky, N., and Goswami, S. (2003). *Failure Criteria for FRP Laminates in Plane Stress*. In *44th AIAA/ASME/ASCE/AHS/ASC Structures, Structural Dynamics and Materials Conference*. Norfolk, VA, pp. 5379–5389.

Dávila, C.G., Rose, C.A., and Camanho, P.P. (2009). *A procedure for superposing linear cohesive laws to represent multiple damage mechanisms in the fracture of composites. International Journal of Fracture*, **158**, pp. 211–223.

DeTeresa, S.J. (1985). *The Axial Compressive Strength of High Performance Polymer Fibers.*

Diggle, P.J. (1983). *Statistical analysis of spatial point patterns.* Academic Press, London.

Drucker, D.C. and Prager, W. (1952). *Soil mechanics and plastic analysis or limit design. Quarterly of Applied Mathematics*, **10**, pp. 157–165.

Dugdale, D. (1960). *Yielding of steel sheets containing slits. Journal of the Mechanics and Physics of Solids*, **8**, pp. 100–104.

Dvorak, G.J. (1992). *Transformation Field Analysis of Inelastic Composite Materials. Proceedings: Mathematical and Physical Sciences*, **437**, pp. 311–327.

Edie, D.D. and Dunham, M.G. (1989). *Melt Spinning Pitch-based Carbon Fibers. Carbon*, **27**, pp. 647–655.

Edie, D., Fain, C., Robinson, K., Harper, A., and Rogers, D. (1993). *Ribbon-shape carbon fibers for thermal management. Carbon*, **31**, pp. 941–949.

Edie, D., Fox, N., Barnett, B., and Fain, C. (1986). *Melt-spun non-circular carbon fibers. Carbon*, **24**, pp. 477–482.

Edie, D. and Stoner, E. (1993). *Carbon–Carbon Materials and Composites.* Elsevier.

Effendi, R.R., Barrau, J.J., and Guedra-Degeorges, D. (1995). *Failure mechanism analysis under compression loading of unidirectional carbon/epoxy composites using micromechanical modelling. Composite Structures*, **31**, pp. 87–98.

Falcó, O., Ávila, R.L., Tijs, B., and Lopes, C.S. (2018). *Modelling and simulation methodology for unidirectional composite laminates in a Virtual Test Lab framework. Composite Structures*, **190**, pp. 137–159.

Feder, J. (1980). *Random sequential adsorption. Journal of Theoretical Biology*, **87**, pp. 237–254.

Feld, N., Allix, O., Baranger, E., and Guimard, J.M. (2012). *A micromechanics-based mesomodel for unidirectional laminates in compression up to failure*. *Journal of Composite Materials*, **46**, pp. 2893–2909.

Fiedler, B., Hojo, M., Ochiai, S., Schulte, K., and Ando, M. (2001). *Failure behavior of an epoxy matrix under different kinds of static loading*. *Composites Science and Technology*, **61**, pp. 1615–1624.

Fleck, N.A., Deng, L., and Budiansky, B. (1995). *Prediction of Kink Width in Compressed Fiber Composites*. *Journal of Applied Mechanics*, **62**, p. 329.

Fleck, N.A. and Jelf, P.M. (1995). *Deformation and failure of a carbon fibre composite under combined shear and transverse loading*. *Acta Metallurgica Et Materialia*, **43**, pp. 3001–3007.

Fleck, N.A. and Liu, D. (2001). *Microbuckle initiation from a patch of large amplitude fibre waviness in a composite under compression and bending*. *European Journal of Mechanics - A/Solids*, **20**, pp. 23–37.

Fleck, N. and Shu, J.Y. (1995). *Microbuckle initiation in fibre composites : A finite element study*. *Journal of the Mechanics and Physics of Solids*, **43**, pp. 1887–1918.

Foote, R.M.L., Mai, Y.W., and Cotterell, B. (1986). *Crack growth resistance curves in strain-softening materials*. *Journal of the Mechanics and Physics of Solids*, **34**, pp. 593–607.

Fukuda, H., Yakushiji, M., and Wada, A. (1999). *A loop test to measure the strength of monofilaments used for advanced composites*. *Advanced Composite Materials*, **8**, pp. 281–291.

Gentz, M., Armentrout, D., Rupnowski, P., Kumosa, L., Shin, E., Sutter, J., and Kumosa, M. (2004). *In-plane shear testing of medium and high modulus woven graphite fiber reinforced/polyimide composites*. *Composites Science and Technology*, **64**, pp. 203–220.

Ghayoor, H., Hoa, S.V., and Marsden, C.C. (2018). *A micromechanical study of stress concentrations in composites*. *Composites Part B: Engineering*, **132**, pp. 115–124.

Ghossein, E. and Lévesque, M. (2012). *A fully automated numerical tool for a comprehensive validation of homogenization models and its application to spherical particles reinforced composites. International Journal of Solids and Structures*, **49**, pp. 1387–1398.

Gong, J., Chen, Y., and Li, C. (2001). *Statistical analysis of fracture toughness of soda-lime glass determined by indentation. Journal of Non-Crystalline Solids*, **279**, pp. 219–223.

González, C. and Llorca, J. (2006). *Multiscale modeling of fracture in fiber-reinforced composites. Acta Materialia*, **54**, pp. 4171–4181.

González, C. and Llorca, J. (2007a). *Mechanical behavior of unidirectional fiber-reinforced polymers under transverse compression: Microscopic mechanisms and modeling. Composites Science and Technology*, **67**, pp. 2795–2806.

González, C. and Llorca, J. (2007b). *Numerical simulation of the fracture behavior of Ti/SiC composites between 20 °C and 400 °C. Metallurgical and Materials Transactions A: Physical Metallurgy and Materials Science*, **38**, pp. 169–179.

González, C. and Llorca, J. (2007c). *Virtual fracture testing of composites: A computational micromechanics approach. Engineering Fracture Mechanics*, **74**, pp. 1126–1138.

Guinea, G., Rojo, F., and Elices, M. (2004). *Stress intensity factors for internal circular cracks in fibers under tensile loading. Engineering Fracture Mechanics*, **71**, pp. 365–377.

Gusev, A.A., Hine, P.J., and Ward, I.M. (2000). *Fiber packing and elastic properties of a transversely random unidirectional glass/epoxy composite. Composites Science and Technology*, **60**, pp. 535–541.

Gutkin, R., Costa, S., and Olsson, R. (2016). *A physically based model for kink-band growth and longitudinal crushing of composites under 3D stress states accounting for friction. Composites Science and Technology*, **135**, pp. 39–45.

Gutkin, R. and Pinho, S.T. (2015). *Combining damage and friction to model compressive damage growth in fibre-reinforced composites. Journal of Composite Materials*, **49**, pp. 2483–2495.

GUTKIN, R., PINHO, S., ROBINSON, P., and CURTIS, P. (2010a). *Micromechanical modelling of shear-driven fibre compressive failure and of fibre kinking for failure envelope generation in CFRP laminates. Composites Science and Technology*, **70**, pp. 1214–1222.

GUTKIN, R., PINHO, S.T., ROBINSON, P., and CURTIS, P.T. (2010b). *On the transition from shear-driven fibre compressive failure to fibre kinking in notched CFRP laminates under longitudinal compression. Composites Science and Technology*, **70**, pp. 1223–1231.

HADLEY, D.W., WARD, I.M., and WARD, J. (1965). *The Transverse Compression of Anisotropic Fibre Monofilaments. Proceedings of the Royal Society of London.Series A.Mathematical and Physical Sciences*, **285**, pp. 275–286.

HAHN, H.T. and TSAI, S.W. (1973). *Nonlinear Elastic Behavior of Unidirectional Composite Laminae. Journal of Composite Materials*, **7**, pp. 102–118.

HAHN, H. and WILLIAMS, J. (1984). *Compression failure mechanisms in unidirectional composites.* Technical report, NASA TM-85834, NASA Langley Research Center, Hampton, VA.

HAPKE, J., GEHRIG, F., HUBER, N., SCHULTE, K., and LILLEODDEN, E.T. (2011). *Compressive failure of UD-CFRP containing void defects: In situ SEM microanalysis. Composites Science and Technology*, **71**, pp. 1242–1249.

HASANYAN, A. and WAAS, A. (2018). *Compressive failure of fiber composites: a homogenized, mesh independent model.* In *59th AIAA/ASCE/AHS/ASC Structures, Structural Dynamics, and Materials Conference*. Kissimmee, FL.

HASHIN, Z. (1980). *Failure Criteria for Unidirectional Fiber Composites. Journal of Applied Mechanics*, **47**, p. 329.

HASHIN, Z. and SHTRIKMAN, S. (1963). *A variational approach to the theory of the elastic behaviour of multiphase materials. Journal of the Mechanics and Physics of Solids*, **11**, pp. 127–140.

HAWTHORNE, H.M. and TEGHTSOONIAN, E. (1975). *Axial compression fracture in carbon fibres. Journal of Materials Science*, **10**, pp. 41–51.

Herráez, M., Bergan, A., González, C., and Lopes, C. (2018a). *Modeling Fiber Kinking at the Microscale and Mesoscale*. Technical report, NASA TP (submitted), Hampton, VA.

Herráez, M., Fernández, A., Lopes, C.S., and González, C. (2016a). *Strength and toughness of structural fibres for composite material reinforcement. Philosophical Transactions of the Royal Society A: Mathematical, Physical and Engineering Sciences*, **374**, p. 20150274.

Herráez, M., González, C., and Lopes, C. (2018b). *A numerical framework to analyze fracture in composite materials: From R-curves to homogenized softening laws. International Journal of Solids and Structures*, **134**, pp. 216–228.

Herráez, M., González, C., Lopes, C., de Villoria, R.G., Llorca, J., Varela, T., and Sánchez, J. (2016b). *Computational micromechanics evaluation of the effect of fibre shape on the transverse strength of unidirectional composites: An approach to virtual materials design. Composites Part A: Applied Science and Manufacturing*, **91**, pp. 484–492.

Herráez, M., Mora, D., Naya, F., Lopes, C.S., González, C., and Llorca, J. (2015). *Transverse cracking of cross-ply laminates: A computational micromechanics perspective. Composites Science and Technology*, **110**, pp. 196–204.

Herráez, M., Naya, F., González, C., Monclús, M., Molina-Aldareguía, J., Lopes, C., and Llorca, J. (2017). *Microscale Characterization Techniques of Fibre-Reinforced Polymers.* In P.W.R. Beaumont, C. Soutis, and A. Hodzic, eds., *The Structural Integrity of Carbon Fibre Composites.* Springer International Publishing, Cham, pp. 283–299.

Herrera-Franco, P. and Drzal, L. (1992). *Comparison of methods for the measurement of fibre/matrix adhesion in composites. Composites*, **23**, pp. 2–27.

Hexcel (2013). *HexPly® 8552 Epoxy Matrix Properties.*

Hexcel (2018a). *HexTow® AS4.*

Hexcel (2018b). *HexTow® IM7.*

Hill, R. (1963). *Elastic properties of reinforced solids: Some theoretical principles. Journal of the Mechanics and Physics of Solids*, **11**, pp. 357–372.

Hillerborg, A., Modéeer, M., and Petersson, P.E. (1976). *Analysis of Crack Formation and Crack Growth by Means of Fracture Mechanics and Finite Elements. Cement and Concrete Research*, **6**, pp. 773–781.

Hitchon, J. and Phillips, D. (1979). *The dependence of the strength of carbon fibres on length. Fibre Science and Technology*, **12**, pp. 217–233.

Hojo, M., Mizuno, M., Hobbiebrunken, T., Adachi, T., Tanaka, M., and Ha, S.K. (2009). *Effect of fiber array irregularities on microscopic interfacial normal stress states of transversely loaded UD-CFRP from viewpoint of failure initiation. Composites Science and Technology*, **69**, pp. 1726–1734.

Hong, S. and Kim, K.S. (2003). *Extraction of cohesive-zone laws from elastic far-fields of a cohesive crack tip: A field projection method. Journal of the Mechanics and Physics of Solids*, **51**, pp. 1267–1286.

Honjo, K. (2003). *Fracture toughness of PAN-based carbon fibers estimated from strength–mirror size relation. Carbon*, **41**, pp. 979–984.

Hossain, M.Z., Hsueh, C.J., Bourdin, B., and Bhattacharya, K. (2014). *Effective toughness of heterogeneous media. Journal of the Mechanics and Physics of Solids*, **71**, pp. 15–32.

Hsu, S.Y., Vogler, T.J., and Kyriakides, S. (1998). *Compressive Strength Predictions for Fiber Composites. Journal of Applied Mechanics*, **65**, p. 7.

Hsu, S.Y., Vogler, T., and Kyriakides, S. (1999). *On the axial propagation of kink bands in fiber composites : Part II analysis. International Journal of Solids and Structures*, **36**, pp. 575–595.

Hui, C.Y. and Ruina, A. (1995). *Why K? High order singularities and small scale yielding. International Journal of Fracture*, **72**, pp. 97–120.

Hunt, M.A., Saito, T., Brown, R.H., Kumbhar, A.S., and Naskar, A.K. (2012). *Patterned Functional Carbon Fibers from Polyethylene. Advanced Materials*, **24**, pp. 2386–2389.

Hütter, G. (2013). *Multi-Scale Simulation of Crack Propagation in the Ductile-Brittle Transition Region. Engineering, Energy Universit, Technische Freiberg, Bergakademie.*

IRWIN, G. (1957). *Analysis of stresses and strains near the end of a crack traversing a plate. Journal of Applied Mechanics*, **24**, pp. 361–364.

JELF, P.M. and FLECK, N.A. (1992). *Compression Failure Mechanisms in Unidirectional Composites. Journal of Composite Materials*, **26**, pp. 2706–2726.

JOSEPH, A., DAVIDSON, P., and WAAS, A. (2017). *Intra-inter Crack Band Model (I2CBM) for Progressive Damage and Failure Analysis of Bolted Joints.* In *58th AIAA/ASCE/AHS/ASC Structures, Structural Dynamics, and Materials Conference*. Grapevine, TX.

JOSEPH, A., DAVIDSON, P., and WAAS, A. (2018). *Failure analysis of composite multi-bolt joints using intra-inter crack band model (I2CBM).* In *59th AIAA/ASCE/AHS/ASC Structures, Structural Dynamics, and Materials Conference*. Kissimmee, FL.

JUMAHAT, A., SOUTIS, C., JONES, F.R., and HODZIC, A. (2010). *Fracture mechanisms and failure analysis of carbon fibre/toughened epoxy composites subjected to compressive loading. Composite Structures*, **92**, pp. 295–305.

KANT, M. and PENUMADU, D. (2013). *Fracture behavior of individual carbon fibers in tension using nano-fabricated notches. Composites Science and Technology*, **89**, pp. 83–88.

KELLY, A. and TYSON, W. (1965). *Tensile properties of fibre-reinforced metals: Copper/tungsten and copper/molybdenum. Journal of the Mechanics and Physics of Solids*, **13**, pp. 329–350.

KIM, J.K., BAILLIE, C., and MAI, Y.W. (1992). *Interfacial debonding and fibre pull-out stresses. Journal of Materials Science*, **27**, pp. 3143–3154.

KIM, J.K. and MAI, Y.W. (1998). *Measurements of interface/interlaminar properties.* In *Engineered Interfaces in Fiber Reinforced Composites*. Elsevier Science Ltd, Oxford, pp. 43–92.

KOWALSKI, I. (1988). *Characterizing the Tensile Stress-Strain Nonlinearity of Polyacrylonitrile-Based Carbon Fibers.* In J. Whitcomb, ed., *Composite Materials: Testing and Design (Eighth Conference)*. American Society for Testing and Materials, Philadelphia, pp. 205–216.

KYRIAKIDES, S., ARSECULERATNE, R., PERRY, E.J., and LIECHTI, K.M. (1995). *On the compressive failure of fiber reinforced composites. International Journal of Solids and Structures*, **32**, pp. 689–738.

LAFFAN, M., PINHO, S., ROBINSON, P., IANNUCCI, L., and MCMILLAN, A. (2012). *Measurement of the fracture toughness associated with the longitudinal fibre compressive failure mode of laminated composites. Composites Part A: Applied Science and Manufacturing*, **43**, pp. 1930–1938.

LAGOUDAS, D.C., TADJBAKHSH, I., and FARES, N. (1991). *A New Approach to Microbuckling of Fibrous Composites. Journal of Applied Mechanics*, **58**, pp. 473–479.

LE GOFF, E., BOIS, C., and WARGNIER, H. (2017). *A progressive intra- and inter-laminar damage model to predict the effect of out-of-plane confinement on pin-bearing behaviour of laminated composites. Journal of Composite Materials*, **51**, pp. 433–450.

LEE, J. and SOUTIS, C. (2007). *A study on the compressive strength of thick carbon fibre-epoxy laminates. Composites Science and Technology*, **67**, pp. 2015–2026.

LEMANSKI, S. and SUTCLIFFE, M. (2012). *Compressive failure of finite size unidirectional composite laminates with a region of fibre waviness. Composites Part A: Applied Science and Manufacturing*, **43**, pp. 435–444.

LEONE, F.A. (2015). *Deformation gradient tensor decomposition for representing matrix cracks in fiber-reinforced materials. Composites Part A: Applied Science and Manufacturing*, **76**, pp. 334–341.

LEONE, F., BERGAN, A., and DÁVILA, C. (2018). *CompDam - Deformation Gradient Decomposition (DGD).*

LI, Y. and ZHOU, M. (2013). *Prediction of fracturess toughness of ceramic composites as function of microstructure: II. analytical model. Journal of the Mechanics and Physics of Solids*, **61**, pp. 489–503.

LIU, D. (2004). *Compressive strength of fibre composites with random fibre waviness. Journal of the Mechanics and Physics of Solids*, **52**, pp. 1481–1505.

LIU, Y. and KUMAR, S. (2012). *Recent Progress in Fabrication, Structure, and Properties of Carbon Fibers. Polymer Reviews*, **52**, pp. 234–258.

Llorca, J. and Elices, M. (1990). *Fracture resistance of fiber-reinforced ceramic matrix composites. Acta Metallurgica et Materialia*, **38**, pp. 2485–2492.

Llorca, J., González, C., Molina-Aldareguía, J.M., Segurado, J., Seltzer, R., Sket, F., Rodríguez, M., Sádaba, S., Muñoz, R., and Canal, L.P. (2011). *Multiscale modeling of composite materials: a roadmap towards virtual testing. Advanced materials*, **23**, pp. 5130–47.

Lopes, C., Camanho, P., Gürdal, Z., Maimí, P., and González, E. (2009). *Low-velocity impact damage on dispersed stacking sequence laminates. Part II: Numerical simulations. Composites Science and Technology*, **69**, pp. 937–947.

Lopes, C.S., González, C., Falcó, O., Naya, F., Llorca, J., and Tijs, B. (2016). *Multiscale virtual testing: the roadmap to efficient design of composites for damage resistance and tolerance. CEAS Aeronautical Journal*, **7**, pp. 607–619.

López Jiménez, F. and Pellegrino, S. (2012). *Failure of Carbon Fibers at a Crease in a Fiber-Reinforced Silicone Sheet. Journal of Applied Mechanics*, **80**, p. 011020.

Lucarini, S. and Segurado, J. (2018). *On the accuracy of spectral solvers for micromechanics based fatigue simulations. Computational Mechanics*, **Submitted**.

Macturk, K.S., Eby, R.K., and Adams, W.W. (1991). *Characterization of compressive properties of high-performance polymer fibres with a new microcompression apparatus. Polymer*, **32**, pp. 1782–1787.

Maimi, P., Mayugo, J., and Camanho, P. (2008). *A Three-dimensional Damage Model for Transversely Isotropic Composite Laminates. Journal of Composite Materials*, **42**, pp. 2717–2745.

Mandell, J., Chen, J., and McGarry, F. (1980). *A microdebonding test for in situ assessment of fibre/matrix bond strength in composite materials. International Journal of Adhesion and Adhesives*, **1**, pp. 40–44.

Manders, P.W. and Chou, T.W. (1983). *Variability of Carbon and Glass Fibers, and the Strength of Aligned Composites. Journal of Reinforced Plastics and Composites*, **2**, pp. 43–59.

Marlett, K., Ng, Y., and Tomblin, J. (2011). *Hexcel 8552 AS4 Unidirectional Prepreg at 190 gsm & 35 % RC Qualification Material Property Data Report. Niar.*

Marshall, D.B. (1984). *An Indentation Method for Measuring Matrix-Fiber Frictional Stresses in Ceramic Composites. Journal of the American Ceramic Society*, **67**, pp. C–259–C–260.

McGregor, C., Zobeiry, N., Vaziri, R., and Poursartip, A. (2008). *A Constitutive Model for Progressive Compressive Failure of Composites. Journal of Composite Materials*, **42**, pp. 2687–2716.

Melro, A.R., Camanho, P.P., Andrade Pires, F.M., and Pinho, S.T. (2013). *Micromechanical analysis of polymer composites reinforced by unidirectional fibres: Part I-Constitutive modelling. International Journal of Solids and Structures*, **50**, pp. 1906–1915.

Melro, A., Camanho, P., and Pinho, S. (2008). *Generation of random distribution of fibres in long-fibre reinforced composites. Composites Science and Technology*, **68**, pp. 2092–2102.

Miller, B., Muri, P., and Rebenfeld, L. (1987). *A microbond method for determination of the shear strength of a fiber/resin interface. Composites Science and Technology*, **28**, pp. 17–32.

Miwa, M., Tsushima, E., and Takayasu, J. (1991). *Axial compressive strength of carbon fiber with tensile strength distribution. Journal of Applied Polymer Science*, **43**, pp. 1467–1474.

Molina-Aldareguía, J.M., Rodríguez, M., González, C., and Llorca, J. (2011). *An experimental and numerical study of the influence of local effects on the application of the fibre push-in test. Philosophical Magazine*, **91**, pp. 1293–1307.

Montagnier, O. and Hochard, C. (2005). *Compression Characterization of High-modulus Carbon Fibers. Journal of Composite Materials*, **39**, pp. 35–49.

Moran, P.M., Liu, X.H., and Shih, C.F. (1995). *Kink band formation and band broadening in fiber composites under compressive loading. Acta Metallurgica Et Materialia*, **43**, pp. 2943–2958.

Morel, S., Lespine, C., Coureau, J.L., Planas, J., and Dourado, N. (2010). *Bilinear softening parameters and equivalent LEFM R-curve in quasibrittle failure. International Journal of Solids and Structures*, **47**, pp. 837–850.

Mori, T. and Tanaka, K. (1973). *Average stress in matrix and average elastic energy of materials with misfitting inclusions. Acta Metallurgica*, **21**, pp. 571–574.

Mortell, D.J., Tanner, D.A., and McCarthy, C.T. (2017). *A virtual experimental approach to microscale composites testing. Composite Structures*, **171**, pp. 1–9.

Mueller, M., Pejchal, V., Žagar, G., Singh, A., Cantoni, M., and Mortensen, A. (2015). *Fracture toughness testing of nanocrystalline alumina and fused quartz using chevron-notched microbeams. Acta Materialia*, **86**, pp. 385–395.

Naik, N. and Kumar, R.S. (1999). *Compressive strength of unidirectional composites: evaluation and comparison of prediction models. Composite Structures*, **46**, pp. 299–308.

Naito, K., Tanaka, Y., Yang, J.M., and Kagawa, Y. (2008). *Tensile properties of ultrahigh strength PAN-based, ultrahigh modulus pitch-based and high ductility pitch-based carbon fibers. Carbon*, **46**, pp. 189–195.

Naya, F. (2017). *Prediction of mechanical properties of unidirectional FRP plies at different environmental conditions by means of computational micromechanics.* Ph.D. thesis, Universidad Politécnica de Madrid.

Naya, F., González, C., Lopes, C., Van der Veen, S., and Llorca, J. (2014). *Combined Multiscale Simulations in Fiber-reinforced Composites.* In *ECCM16 - 16th European Conference on Composite Materials*, 22-26 June 2014. Seville (Spain).

Naya, F., González, C., Lopes, C., Van der Veen, S., and Pons, F. (2017a). *Computational micromechanics of the transverse and shear behavior of unidirectional fiber reinforced polymers including environmental effects. Composites Part A: Applied Science and Manufacturing*, **92**, pp. 146–157.

Naya, F., Herráez, M., Lopes, C., González, C., Van der Veen, S., and Pons, F. (2017b). *Computational micromechanics of fiber kinking in unidirec-*

tional FRP under different environmental conditions. Composites Science and Technology, **144**, pp. 26–35.

Ochiai, S., Kuboshima, S., Morishita, K., Okuda, H., and Inoue, T. (2010). *Fracture toughness of Al2O3 fibers with an artificial notch introduced by a focused-ion-beam. Journal of the European Ceramic Society*, **30**, pp. 1659–1667.

Ogihara, S., Imafuku, Y., Yamamoto, R., and Kogo, Y. (2009). *Application of FIB technique to introduction of a notch into a carbon fiber for direct measurement of fracture toughness.* In *Journal of Physics: Conference Series*, volume 191. p. 012009.

Ogihara, S. and Koyanagi, J. (2010). *Investigation of combined stress state failure criterion for glass fiber/epoxy interface by the cruciform specimen method. Composites Science and Technology*, **70**, pp. 143–150.

Oh, J.H., Jin, K.K., and Ha, S.K. (2006). *Interfacial Strain Distribution of a Unidirectional Composite with Randomly Distributed Fibers under Transverse Loading. Journal of Composite Materials*, **40**, pp. 759–778.

Ohsawa, T., Miwa, M., Kawade, M., and Tsushima, E. (1990). *Axial compressive strength of carbon fiber. Journal of Applied Polymer Science*, **39**, pp. 1733–1743.

Oliphant, T.E. (2007). *Python for Scientific Computing. Computing in Science & Engineering*, **9**, pp. 10–20.

Oliver, W. and Pharr, G. (1992). *An improved technique for determining hardness and elastic modulus using load and displacement sensing indentation experiments. Journal of Materials Research*, **7**, pp. 1564–1583.

Oya, N. and Johnson, D.J. (2001). *Longitudinal compressive behaviour and microstructure of PAN-based carbon fibres. Carbon*, **39**, pp. 635–645.

Panar, M., Avakian, P., Blume, R.C., Gardner, K.H., Gierke, T.D., and Yang, H.H. (1983). *Morphology of poly(p-phenylene terephthalamide) fibers. Journal of Polymer Science: Polymer Physics Edition*, **21**, pp. 1955–1969.

Park, S.J., Seo, M.K., and Shim, H.B. (2003). *Effect of fiber shapes on physical characteristics of non-circular carbon fibers-reinforced composites. Materials Science and Engineering: A*, **352**, pp. 34–39.

Park, S.J., Seo, M.K., Shim, H.B., and Rhee, K.Y. (2004). *Effect of different cross-section types on mechanical properties of carbon fibers-reinforced cement composites. Materials Science and Engineering A*, **366**, pp. 348–355.

Pathan, M.V., Tagarielli, V.L., Patsias, S., and Baiz-villafranca, P.M. (2017). *A new algorithm to generate representative volume elements of composites with cylindrical or spherical fillers. Composites Part B*, **110**, pp. 267–278.

Peterson, M.E. and Murphey, T.W. (2016). *High Strain Flexural Characterization of Thin CFRP Unidirectional Composite Lamina. American Society for Composites Thirty-First Technical Conference.*

Phoenix, S. and Skelton, J. (1974). *Transverse Compressive Moduli and Yield Behavior of Some Orthotropic, High-Modulus Filaments. Textile Research Journal*, **44**, pp. 934–940.

Piggott, M. and Harris, B. (1980). *Factors affecting the compression strength of aligned fibre composites.* In *Advances in Composite Materials*. Elsevier, pp. 305–312.

Pimenta, S., Gutkin, R., Pinho, S., and Robinson, P. (2009a). *A micromechanical model for kink-band formation: Part I - Experimental study and numerical modelling. Composites Science and Technology*, **69**, pp. 948–955.

Pimenta, S., Gutkin, R., Pinho, S., and Robinson, P. (2009b). *A micromechanical model for kink-band formation: Part II—Analytical modelling. Composites Science and Technology*, **69**, pp. 956–964.

Pinho, S., Darvizeh, R., Robinson, P., Schuecker, C., and Camanho, P. (2012). *Material and structural response of polymer-matrix fibre-reinforced composites. Journal of Composite Materials*, **46**, pp. 2313–2341.

Pinho, S.T., Dávila, C.G., Camanho, P.P., Iannucci, L., and Robinson, P. (2005). *Failure Models and Criteria for FRP Under In-Plane or Three-Dimensional Stress States Including Shear Non-Linearity.* Technical Report February, NASA/TM-2005-213530.

Pinho, S., Robinson, P., and Iannucci, L. (2006). *Fracture toughness of the tensile and compressive fibre failure modes in laminated composites. Composites Science and Technology*, **66**, pp. 2069–2079.

PINHO, S., ROBINSON, P., and IANNUCCI, L. (2009). *Developing a four point bend specimen to measure the mode I intralaminar fracture toughness of unidirectional laminated composites. Composites Science and Technology*, **69**, pp. 1303–1309.

PRABHAKAR, P. and WAAS, A.M. (2013). *Interaction between kinking and splitting in the compressive failure of unidirectional fiber reinforced laminated composites. Composite Structures*, **98**, pp. 85–92.

PUCK, A. and SCHÜRMANN, H. (2004). *Failure analysis of FRP laminates by means of physically based phenomenological models. Failure Criteria in Fibre-Reinforced-Polymer Composites*, **3538**, pp. 832–876.

PYRZ, R. (1994). *Quantitative description of the microstructure of composites. Part I: Morphology of unidirectional composite systems. Composites Science and Technology*, **50**, pp. 197–208.

RAMANUJAN, S. (1914). *Modular Equations And Approximations to Pi. Quarterly Journal of Pure and Applied Mathematics*, **45**, pp. 350–372.

RAMBERG, W. and OSGOOD, W. (1943). *Description of Stress-Strain Curves by Three Parameters.* Technical report, National Advisory Committee for Aeronautics.

REYNOLDS, W. and SHARP, J. (1974). *Crystal shear limit to carbon fibre strength. Carbon*, **12**, pp. 103–110.

RINTOUL, M.D. and TORQUATO, S. (1997). *Reconstruction of the Structure of Dispersions. Journal of Colloid and Interface Science*, **186**, pp. 467–476.

RIPLEY, B. (1977). *Modelling Spatial Patterns. Journal of the Royal Statistical Society. Series B*, **39**, pp. 172–212.

RIPLEY, B. (1981). *Spatial Statistics.* Wiley Series in Probability and Statistics. John Wiley & Sons, Inc., Hoboken, NJ, USA.

RODRÍGUEZ, M., MOLINA-ALDAREGUÍA, J., GONZÁLEZ, C., and LLORCA, J. (2012a). *A methodology to measure the interface shear strength by means of the fiber push-in test. Composites Science and Technology*, **72**, pp. 1924–1932.

RODRÍGUEZ, M., MOLINA-ALDAREGUÍA, J., GONZÁLEZ, C., and LLORCA, J. (2012b). *Determination of the mechanical properties of amorphous materials through instrumented nanoindentation. Acta Materialia*, **60**, pp. 3953–3964.

ROSEN, B. (1965). *Mechanics of Composite Strengthening.* In Am. Soc. Metals Seminar, ed., *Fibre Composite Materials*, chapter 3.

SAUTTER, M., DIETRICH, C., POECH, M.H., SCHMAUDER, S., and FISCHMEISTER, H.F. (1993). *Finite element modelling of a transverse-loaded fibre composite effects of section size and net density. Computational Materials Science*, **1**, pp. 225–233.

SCHAPERY, R. (1990). *A theory of mechanical behavior of elastic media with growing damage and other changes in structure. Journal of the Mechanics and Physics of Solids*, **38**, pp. 215–253.

SCHAPERY, R. (1995). *Prediction of compressive strength and kink bands in composites using a work potential. International Journal of Solids and Structures*, **32**, pp. 739–765.

SCHÜLLER, T., BECKERT, W., LAUKE, B., AGEORGES, C., and FRIEDRICH, K. (2000). *Single fibre transverse debonding: Stress analysis of the Broutman test. Composites Part A: Applied Science and Manufacturing*, **31**, pp. 661–670.

SCHULTHEISZ, C.R. and WAAS, A.M. (1996). *Compressive failure of composites, Part I: Testing and micromechanical theories. Progress in Aerospace Sciences*, **32**, pp. 1–42.

SCOTT, D. (1992). *Multivariate Density Estimation: Theory, Practice, and Visualization.* John Wiley & Sons, Inc., New York.

SEGURADO, J. and LLORCA, J. (2002). *A numerical approximation to the elastic properties of sphere-reinforced composites. Journal of the Mechanics and Physics of Solids*, **50**, pp. 2107–2121.

SHIM, H., SEO, M., and PARK, S. (2002). *Thermal conductivity and mechanical properties of various cross-section types carbon fiber-reinforced composites. Journal of materials science*, **37**, p. 1881–1885.

SHU, J.Y. and FLECK, N.A. (1997). *Microbuckle initiation in fibre composites under multiaxial loading. Proceedings of the Royal Society A: Mathematical, Physical and Engineering Sciences*, **453**, pp. 2063–2083.

SIH, G.C., PARIS, P.C., and IRWIN, G.R. (1965). *On cracks in rectilinearly anisotropic bodies. International Journal of Fracture Mechanics*, **1**, pp. 189–203.

Sills, R.B. and Thouless, M.D. (2015). *Cohesive-length scales for damage and toughening mechanisms. International Journal of Solids and Structures*, **55**, pp. 32–43.

Simulia, ed. (2013). *Abaqus Analysis User's Guide. Version 6.13.*

Sinclair, D. (1950). *A Bending Method for Measurement of the Tensile Strength and Young's Modulus of Glass Fibers. Journal of Applied Physics*, **21**, pp. 380–386.

Slusarksi, K.A., Walter, M.S., Bogetti, T.A., and Wetzel, E.D. (2014). *In-plane Shear Properties of High-Performance Filaments.* In *Fracture and Fatigue, Volume 7: Proceedings of the 2013 Annual Conference on Experimental and Applied Mechanics*. Springer International Publishing, pp. 91–96.

Smith, P. and Torquato, S. (1988). *Computer simulation results for the two-point probability function of composite media. Journal of Computational Physics*, **76**, pp. 176–191.

Smoot, M. (1982). *Compressive Response of Hercules AS1 3501-6 Graphite Epoxy Composites*. Center for Composite Materials.

Sørensen, B.F. and Jacobsen, T.K. (1998). *Large-scale bridging in composites: R-curves and bridging laws. Composites Part A: Applied Science and Manufacturing*, **29**, pp. 1443–1451.

Soutis, C. (1996). *Failure of Notched CFRP Laminates Due to Fibre Microbuckling: A Topical Review. Journal of the Mechanical Behavior of Materials*, **6**.

Steif, P.S. (1990). *A model for kinking in fiber composites—I. Fiber breakage via micro-buckling. International Journal of Solids and Structures*, **26**, pp. 549–561.

Suo, Z., Bao, G., and Fan, B. (1992). *Delamination R-curve phenomena due to damage. Journal of the Mechanics and Physics of Solids*, **40**, pp. 1–16.

Sutcliffe, M. (2013). *Modelling the effect of size on compressive strength of fibre composites with random waviness. Composites Science and Technology*, **88**, pp. 142–150.

Svensson, D., Alfredsson, K.S., Stigh, U., and Jansson, N.E. (2016). *Measurement of cohesive law for kink-band formation in unidirectional composite. Engineering Fracture Mechanics*, **151**, pp. 1–10.

Swolfs, Y., Gorbatikh, L., and Verpoest, I. (2014). *Fibre hybridisation in polymer composites: A review. Composites Part A: Applied Science and Manufacturing*, **67**, pp. 181–200.

Tabor, D. (1951). *The Hardness of Metals.* Clarendon Press.

Tada, H., Paris, P., and Irwin, G. (2000). *The Analysis of Cracks Handbook.*

Tagawa, T. and Miyata, T. (1997). *Size effect on tensile strength of carbon fibers. Materials Science and Engineering: A*, **238**, pp. 336–342.

Tanaka, F., Okabe, T., Okuda, H., Kinloch, I.A., and Young, R.J. (2014). *Factors controlling the strength of carbon fibres in tension. Composites Part A: Applied Science and Manufacturing*, **57**, pp. 88–94.

Toribio, J., Álvarez, N., González, B., and Matos, J. (2009). *A critical review of stress intensity factor solutions for surface cracks in round bars subjected to tension loading. Engineering Failure Analysis*, **16**, pp. 794–809.

Torquato, S. (2002). *Random Heterogeneous Materials*, volume 16 of *Interdisciplinary Applied Mathematics.* Springer New York, New York, NY.

Torquato, S. and Stell, G. (1982). *Microstructure of two-phase random media. I. The n-point probability functions. The Journal of Chemical Physics*, **77**, pp. 2071–2077.

Tory, E., Jodrey, W., and Pickard, D. (1983). *Simulation of random sequential adsorption: Efficient methods and resolution of conflicting results. Journal of Theoretical Biology*, **102**, pp. 439–445.

Totry, E., González, C., and Llorca, J. (2008a). *Prediction of the failure locus of C/PEEK composites under transverse compression and longitudinal shear through computational micromechanics. Composites Science and Technology*, **68**, pp. 3128–3136.

Totry, E., Llorca, J., and González, C. (2008b). *Failure locus of fiber-reinforced composites under transverse compression and out-of-plane shear. Composites Science and Technology*, **68**, pp. 829–839.

Totry, E., Molina-Aldareguía, J.M., González, C., and Llorca, J. (2010). *Effect of fiber, matrix and interface properties on the in-plane shear deformation of carbon-fiber reinforced composites. Composites Science and Technology*, **70**, pp. 970–980.

Trias, D. (2005). *Analysis and Simulation of Transverse Random Fracture of Long Fibre Reinforced Composites.* Ph.D. thesis, University of Girona.

Trias, D., Costa, J., Turon, A., and Hurtado, J.E. (2006). *Determination of the critical size of a statistical representative volume element (SRVE) for carbon reinforced polymers. Acta Materialia*, **54**, pp. 3471–3484.

Tsai, C.L. and Daniel, I.M. (1999). *Determination of shear modulus of single fibers. Experimental Mechanics*, **39**, pp. 284–286.

Turon, A., Camanho, P., Costa, J., and Dávila, C. (2006). *A damage model for the simulation of delamination in advanced composites under variable-mode loading. Mechanics of Materials*, **38**, pp. 1072–1089.

Turon, A., Camanho, P., Costa, J., and Renart, J. (2010). *Accurate simulation of delamination growth under mixed-mode loading using cohesive elements: Definition of interlaminar strengths and elastic stiffness. Composite Structures*, **92**, pp. 1857–1864.

Vaughan, T. (2011). *Micromechanical Modelling of Damage and Failure in Fibre Reinforced Composites under Loading in the Transverse Plane.* Ph.D. thesis.

Vaughan, T. and McCarthy, C. (2010). *A combined experimental–numerical approach for generating statistically equivalent fibre distributions for high strength laminated composite materials. Composites Science and Technology*, **70**, pp. 291–297.

Vogler, T., Hsu, S.Y., and Kyriakides, S. (2001). *On the initiation and growth of kink bands in fiber composites. Part II analysis. International Journal of Solids and Structures*, **38**, pp. 2653–2682.

Vogler, T. and Kyriakides, S. (1999). *On the axial propagation of kink bands in fiber composites : Part i experiments. International Journal of Solids and Structures*, **36**, pp. 557–574.

VOGLER, T.J. and KYRIAKIDES, S. (2001). *On the initiation and growth of kink bands in fiber composites. Part I: Experiments. International Journal of Solids and Structures*, **38**, pp. 2639–2651.

WAAS, A.M. and SCHULTHEISZ, C.R. (1996). *Compressive failure of composites, Part II: Experimental studies. Progress in Aerospace Sciences*, **32**, pp. 43–78.

WALLENBERGER, F.T., WATSON, J.C., and LI, H. (2001). *Glass Fibres.* In *ASM Handbook Composites, 21*, chapter 21. pp. 27–34.

WANG, S., YANG, Y., ZHOU, L.M., and MAI, Y.W. (2012). *Size effect in micro-compression of epoxy micropillars. Journal of Materials Science*, **47**, pp. 6047–6055.

WANTHAL, S., SCHAEFER, J., JUSTUSSON, B., HYDER, I., ENGLESTAD, S., and ROSE, C. (2017). *Verification and validation process for progressive damage and failure analysis methods in the NASA Advanced Composites Consortium.* In *American Society for Composites Thirty-Second Technical Conference2.* West Lafayette, Indiana.

WATSON, D.F. (1981). *Computing the n-dimensional Delaunay tessellation with application to Voronoi polytopes. The Computer Journal*, **24**, pp. 167–172.

WEIBULL, W. (1939). *A Statistical Theory of the Strength of Materials.*

WESTERGAARD, H. (1939). *Bearing Pressures and Cracks. Journal of Applied Mechanics*, **6**, pp. 49–53.

WIND, J.L., STEFFENSEN, S., and JENSEN, H.M. (2014). *Comparison of a composite model and an individually fiber and matrix discretized model for kink band formation. International Journal of Non-Linear Mechanics*, **67**, pp. 319–325.

WISNOM, M.R. (1990). *The effect of fibre misalignment on the compressive strength of unidirectional carbon fibre/epoxy. Composites*, **21**, pp. 403–407.

WISNOM, M.R. (1993). *Analysis of Shear Instability in Compression Due to Fibre Waviness. Journal of Reinforced Plastics and Composites*, **12**, pp. 1171–1189.

WISNOM, M. and ATKINSON, J. (1997). *Constrained buckling tests show increasing compressive strain to failure with increasing strain gradient. Composites Part A: Applied Science and Manufacturing*, **28**, pp. 959–964.

Wongsto, A. and Li, S. (2005). *Micromechanical FE analysis of UD fibre-reinforced composites with fibres distributed at random over the transverse cross-section. Composites Part A: Applied Science and Manufacturing*, **36**, pp. 1246–1266.

Wulf, J., Steinkopff, T., and Fischmeister, H.F. (1996). *FE-simulation of crack paths in the real microstructure of an Al(6061)/SiC composite. Acta Materialia*, **44**, pp. 1765–1779.

Xia, Z., Curtin, W., and Peters, P. (2001). *Multiscale modeling of failure in metal matrix composites. Acta Materialia*, **49**, pp. 273–287.

Yang, L., Yan, Y., Ran, Z., and Liu, Y. (2013). *A new method for generating random fibre distributions for fibre reinforced composites. Composites Science and Technology*, **76**, pp. 14–20.

Yang, Y., Ye, J.C., Lu, J., Liu, F.X., and Liaw, P.K. (2009). *Effects of specimen geometry and base material on the mechanical behavior of focused-ion-beam-fabricated metallic-glass micropillars. Acta Materialia*, **57**, pp. 1613–1623.

Yerramalli, C. and Waas, A. (2004). *The Effect of Fiber Diameter on the Compressive Strength of Composites - A 3D Finite Element Based Study. Computer Modeling in Engineering and Sciences*, **6**, pp. 1–16.

Zhang, S.Y. and Dong, M.H. (2011). *Bridging Toughening and Fracture Energy of X-Type Fiber Reinforced Cementitious Composites. Advanced Materials Research*, **368-373**, pp. 419–422.

Zhang, L., Zhang, S., Jiang, Y., Tao, J., and Chen, X. (2016). *Compressive behaviour of fibre reinforced plastic with random fibre packing and a region of fibre waviness. Journal of Reinforced Plastics and Composites.*

Zobeiry, N., Vaziri, R., and Poursartip, A. (2015). *Characterization of strain-softening behavior and failure mechanisms of composites under tension and compression. Composites Part A: Applied Science and Manufacturing*, **68**, pp. 29–41.

Zweben, C. and Rosen, B. (1970). *A statistical theory of material strength with application to composite materials. Journal of the Mechanics and Physics of Solids*, **18**, pp. 189–206.